Liquid penetration into paper

Raymond John Roberts

A thesis submitted for the degree of
Doctor of Philosophy at
The Australian National University

THE AUSTRALIAN NATIONAL UNIVERSITY

August 2005

Typeset in Times by TEX and LATEX 2ε.

To get the necessary image quality it was necessary to print this thesis one page to a sheet.

Except where otherwise indicated, this thesis is my own original work.

Raymond John Roberts
10 August 2005

Rags make paper

Paper makes money

Money makes banks

Banks make loans

Loans make beggars

Beggars make rags

Author unknown, circa Eighteenth century

Acknowledgements

I acknowledge the initial overall supervision of this research while studying part time by Dr Phillip Evans, then Reader in Forestry ANU who encouraged me to undertake the project and helped set up its original scope. When Phil left ANU to take up the position of Professor and Director at the Centre for Advanced Wood Processing Department of Wood Science University of British Columbia the role of overall supervision went to Dr Mark Knackstedt Associate Professor, Department of Applied Mathematics, Research School of Physical Sciences and Engineering, ANU. I acknowledge Mark's intellectual leadership, superb editing skills and friendship.

I also acknowledge the intellectual support, supervision, assistance with experimentation and friendship of Dr Tim Senden, Senior Research Fellow, Department of Applied Mathematics, Research School of Physical Sciences and Engineering, ANU. The friendship and support of Mark and Tim especially in the last year of the project where other issues could have created difficulties with the successful completion of the project is especially acknowledged and greatly appreciated.

I also acknowledge the support of Dr Roger Heady of the Electron Microscope Unit, ANU who provided so much assistance with the Cambridge Scanning Electron Microscope especially on weekends while studying part time. I especially appreciate the way in which Roger always managed to find a slot on the SEM for me for those last minute jobs that seemed to be unending.

I also acknowledge the support of:

Mr Anthony Hyde Senior Technical Officer Department of Applied Mathematics, Research School of Physical Sciences and Engineering, ANU who gave me great assistance in the design and in liaising with the workshop in the construction of the two cryo-cell units for the CLSM.

Dr M. Bruce Lyne President of the YKI Institute in Stockholm for organising various laboratory papers used in this thesis.

Mr Ross Cunningham of the Statistical Consulting Unit, The Graduate School ANU for advice and assistance in the design of experiments and analysis of data.

Mrs Christine Donnelly of the Statistical Consulting Unit, The Graduate School ANU for advice on the use of the statistical programme Genstat.

Dr Jeff Wood of the Statistical Consulting Unit, The Graduate School ANU for statistical advice.

Ms Jocelyn Paton and Ms Carolyn Carlile, Carter Holt Harvey Panels, Tumut for their

assistance in sample acquisition and preparation.

Mr Adrian Paalvast Manager, Carter Holt Harvey Panels, Tumut who provided support while I was employed part time at CHH.

Dr Vincent Otieno-Alego for access and assistance in the use of the Raman Microscope at the University of Canberra.

Mr John Barnard, Deparment of Chemical Engineering, Monash University for his assistance with mercury intrusion porosimety.

I am indebted to my parents Ruth and Bill who provided a place for me to stay in Canberra while I studied part time.

I am also indebted to my dear sons Will and Simon who missed out on a lot of time with dad and who understood the need for their dad to undertake this project at the expense of time with them on the farm. Their love and support meant so much and is impossible for me to put into words.

I acknowledge the financial support of the Cooperative Research Centre for Functional Communication Surfaces and also BASF AG Ludwigsafen for their financial support for the project and access to their 2-photo confocal laser scanning microscope at the Central Research Laboratories. I particularly acknowledge the assistance of Dr Wolfgang Schrof Group Leader Polymer Physics BASF Ludwigshafen who enabled me to use the CLSM exclusively while in Ludwigshafen and who supplied technical assistants while there.

I acknowledge the financial help of CSR who provided a research grant to enable me to purchase a high speed video camera and who supported my part time study while I was still employed as Technical Manager at the Tumut plant.

I acknowledge the support of Carter Holt Harvey Panels when I became a full time student in employing me part time as a treater specialist.

Finally I wish to acknowledge the leadership and support of Mr Mike Alston who was my manager at Tumut. Mike was the one who started this process by telling me to ”go and do some science” to solve a problem that no-one in the world was able to shed any light on. However I mainly acknowledge and deeply appreciate the friendship he gave me all the way through and his ability to fight off the corporate diversions from above and his efforts to gain corporate support for me after the takeover of CSR Panels by CHH when I became a full time student.

I look forward to a long association with all the people mentioned above.

Abstract

The origin of this thesis lay in the production of defects associated with manufacturing LPM impregnated panels. The causes of these defects were unknown as was their exact nature. In identifying the actual nature and cause of these defects, it is necessary to research the fundamental mechanisms of fluid flow into paper as well as identifying how certain structural characteristics of paper, as well as characteristics of the penetrating liquids, affected fluid flow within paper.

To understand the affect of different liquids on impregnation into porous media, simple isotropic micromodels are used to quantify the effects of surface tension and contact angle on the rate of fluid flow. The use of the Lucas-Washburn equation is questioned.

Using cryo-SEM and a newly developed technique of cryo 2-photon confocal laser scanning microscopy, the actual mechanisms of fluid flow in unsized paper are identified. These are due primarily to the advance of the wetting fluid in the form of bulk liquid films along channels formed by fibre overlaps. This is in contrast to the common description of fluid penetration, where the primary flow mechanism is based on the bulk filling of pores. These channels, formed by fibre overlaps are shown to form a highly interconnected dense network of flow paths which efficiently transport the wetting fluid. The flow rates associated with penetration along a number of potential flow paths within the fibre web are calculated. The experimentally observed penetration rate is consistent with a film flow process through inter-fibre channels which is significantly slower than a penetration process dominated by meniscus flow through pores. In addition the mechanism of fluid flow in internally sized papers is presented.

The effects of different fillers on paper structure, flow path morphologies and imbibition rate are also quantified. Laboratory papers with different types and amounts of filler are studied using SEM and cryo-SEM and a newly developed technique of high speed video microscopy to quantify such effects.

Contents

List of Figures

List of Tables

Chapter 1

Introduction

This chapter introduces the thesis. The background to the research is described including its aims, practical applications, scope, methods of study as well as the structure of the thesis. An overview of the industrial process of resin impregnation of decor paper is presented here and the key steps in the manufacture of low pressure melamine panels are described.

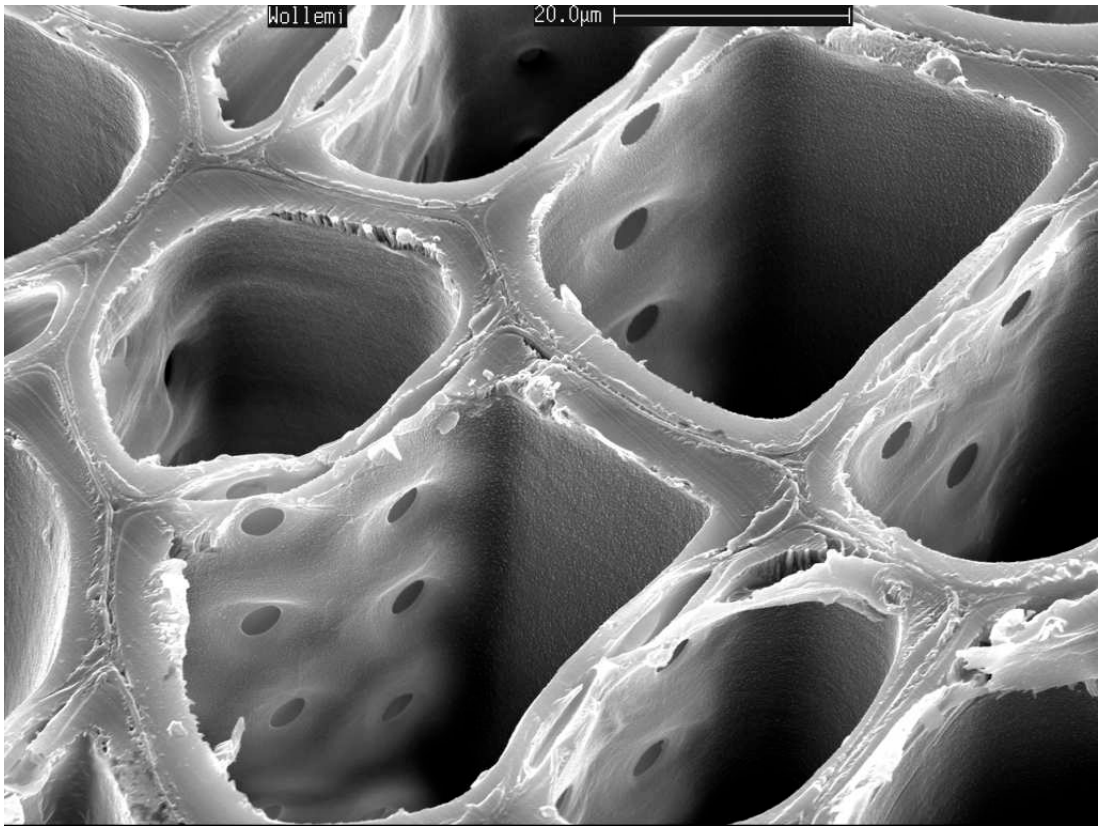

From where it all comes; transverse section of softwood tracheids from Wollemi Pine, Wollemia nobilis with alternate biseriate pitting. Photo courtesy Dr Roger Heady, Electron Microscope Unit, ANU.

1.1 Introduction to the thesis

Decorative melamine panels are ubiquitous in the modern interior. The durability and chemical resistance of these panels is due to a 100-200 μm layer of resin impregnated paper. The surprising lack of information and depth of understanding of the production of this resin impregnated paper has led to the body of work which constitutes this thesis. From the requirement to better understand this process arose a broader need to understand the physics behind liquid penetration in paper.

The use of amino resin impregnated and coated decor papers laminated onto wood composite panels is widespread throughout the world in furniture, cabinet-making, partitioning of offices and for flooring. The first reference to the process of manufacturing low pressure melamine (LPM) laminates was by Seidl (1949) who described overlays for laminating veneer and plywood including descriptions of the resins used. Decorative overlays were described as being made from special papers of high resin content that are moulded into a dense infusible plastic, typical of the "familiar plastic table top". The purpose of these overlays was to produce a highly serviceable and appealing surface of attractive color or design.

Enzenberger (1961, 1968) was the first to describe the process of impregnation of decor papers, and lamination using melamine formaldehyde (MF) resins. Adam and Kamutski (1993) referred to the original patents for the production of melamine resins by Cassella, Ciba and Henkel in 1935 and described in detail the attributes of MF resins in their cross-linked state which make them suitable for LPM laminates. A good description of the manufacture and use of UF and MF resins is given in Pizzi (1983a,b) and Jalbert (1991).

The origin of this thesis lay in the author's industrial experience in managing a commercial LPM production facility and specifically the problem that was frequently encountered, the presence of numerous surface defects in MF coatings. This problem is commonplace throughout the world in factories making the product. The causes and nature of these surface defects in LPM laminates which gives them a mottled, milky appearance with poor stain and abrasion resistance were unknown.

Little has been published on what factors control the "treatability" of decor paper. Suppliers of resins, decor papers and the treating machines are unable to provide useful insights into the physics of saturation at both a macro and microscopic level. Many raw papers, however, perform differently and take up different amounts of resin during saturation. Some papers are anecdotally "difficult to saturate" and tend to produce more rejects during laminating in short cycle LPM presses.

There is a paucity of information in the public arena about the process of LPM resin impregnation and most of the literature available is provided by suppliers of paper, resins or treaters, and cannot be regarded as impartial.

1.2 Brief overview of LPM manufacturing process

The production of LPM coated panel board occurs in three stages, firstly the manufacture of the substrate, either particleboard or medium density fibreboard (MDF). This is followed by treatment of the decor paper with resins (impregnation and coating) and finally pressing of the treated paper onto the substrate (laminating). This thesis commences by investigating problems resulting from fluid imbibition in the first stage of the treatment of the decor papers (described below).

1.2.1 First stage of treating; impregnation of decor paper with urea formaldehyde resin

Initially decor paper is impregnated with a urea formaldehyde (UF) resin by passing the paper under very slight tension over the top of a pre-wetting roller, the bottom third of which is in a bath containing UF resin (Figures 1.1 & 1.2). The film of resin picked up on the roller is transferred onto the bottom side of the paper, and the resin penetrates into the paper. The paper then travels over a series of rollers to give the resin time to migrate from one side to the other and displaces air from the paper. The paper is then completely immersed in a resin bath to wet the top-side of the paper (Figure 1.1) and it is then dried to a specific moisture content in a series of ovens. If the paper is dipped into the resin bath too soon after the pre-wetting rollers, a layer of air could be trapped in the core thereby preventing the paper from being adequately saturated with the UF resin.

This thesis relates to the part of the process where the paper comes into contact with the pre-wetting roller to just before it is dipped into the resin bath after the first sky roller and, in fact, probably only to the first metre of travel of the paper after contact with the pre-wetting roller. This constitutes about 0.5 s or a fraction of a percent of the whole process time, yet it is during this stage that the success or failure of the whole process is ordained. Surprisingly this critical part of the process has been and remains the least understood part of the whole process of manufacturing LPM panels.

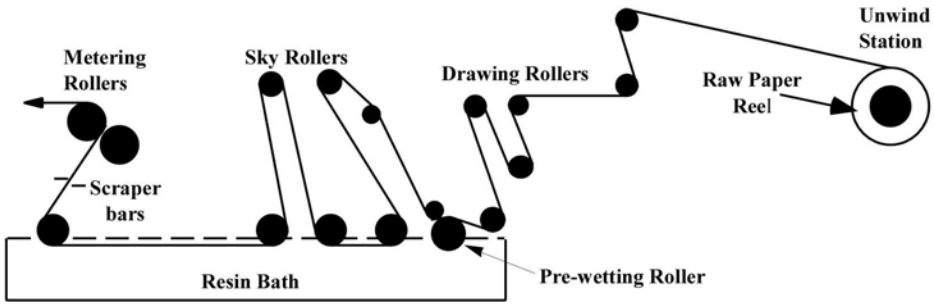

***Figure 1.1**: Schematic representation of the UF resin impregnation stage of a paper treater.*

1.2.2 Second stage of treating; coating with melamine formaldehyde resins

The next stage of the treatment process involves coating the saturated and dried UF resin impregnated paper with a melamine formaldehyde (MF) resin. This is usually done by applying the resin onto the paper using gravure rollers. A gravure roller contains thousands of small trapezoidal cells that fill when the roller passes through a resin bath. The excess resin is scraped off the roller so that the desired quantity of resin remains in the cells of the roller. As the paper travels over the other side of the roller, the resin is transferred to the paper. The quantity of resin transferred is very accurately controlled by the differential between the circumferential speed of the gravure roller and the line speed of the paper. The resin is then smoothed over the paper by a series of wire and smoothing rollers. The paper is finally dried in a series of accurately controlled convection ovens. The treated paper is then ready for laminating onto the panel substrate to produce the final product.

1.2.3 Consequences of inadequate penetration of resin at first stage

The aim of the first stage of the treatment process is to fill the void spaces (pores) of the paper with relatively inexpensive UF resin solids so that a minimal amount of the more expensive MF resin is used in the second stage to coat the paper. The MF resin is substantially more durable than UF resin and must contiguously cover the surface (Adam and Kamutski, 1993). Melamine impregnated paper is ten times more impermeable than paper treated with UF resin alone (Ebrahimzadeh, 1998). However, if MF resin flows into voids in the paper remaining after UF resin treatment, then insufficient MF resin may remain on the surface of the paper to effectively coat it. Defects in LPM may occur as a result of this mechanism because the MF resin used to treat decor paper is formulated to flow just prior to full cure in order to achieve the desired textured finish on the surface of the panel. To overcome this problem it has often been necessary to add excess MF resin to the paper to ensure there will be enough on the surface to provide a good protective coating. This is expensive and can lead to longer pressing cycles with consequential lost production and possible over-cure of the coating resin.

The resulting economic loss from the production of rejects or increased use of MF resin is considerable *i.e.*, A$40 per board, annualised at over A$500,000 for an average sized factory alone. This estimate does not include the cost of lost production. The industry in Australia produces approximately 41 million square metres per annum of saleable product and a conservative estimate of the costs of defect production in Australia alone would be close to A$5 million, assuming a conservative defect rate of about 1%. Plants that both treat and laminate worldwide number in the hundreds and therefore the economic losses caused by this problem probably approaches hundreds of millions of dollars.

Figure 1.2: *Images of pre-wetting roller, closeup on the left and showing the positions of the sky rollers on the right. Note that only the bottom third of the pre-wetting roller is in the resin bath. The roller rotates against the travel of the paper enabling a film of resin on the roller to come into contact with the paper. Arrows denote the direction of movement of the paper and the prewetting roller.*

1.3 Aim and purpose of research

It is proposed that excessive consumption of MF resin during the process of manufacturing laminated paper overlays, and defects in the overlay are caused by inadequate filling of paper voids with UF resin during the first stage of the treatment process. There is a large gulf between industry practice and our current understanding of the saturation process of decor paper. After reviewing the field it was clear that substantial progress in this area could only occur via a greater understanding of fluid flow in paper over short time spans. Thus the thesis focusses on the kinetics of capillary penetration of wetting liquids into porous media, after preliminary research (in Chapters 3 & 4) which examines the inter-relationships between resin saturation and paper properties and the generation of defects in laminated paper overlays. An understanding of fluid penetration processes is a prerequisite to obtaining a better understanding of all product-converting processes which involve contact between paper and fluids. In order to gain an understanding of fluid penetration into paper it is necessary to realistically characterize paper pore morphology in 3D within the fibre web, and obtain a fundamental understanding of the physical processes which dictate fluid movement and fluid-solid interactions during penetration.

1.4 Structure of the thesis

In addition to this chapter, the thesis is comprised of 8 chapters as follows;

Chapter 2 is primarily a review of the literature of treatment of decor papers, the techniques used to study fluid flow in paper and previous research into fluid flow in paper. Most previous research on the latter is based on the Lucas-Washburn theory (Lucas, 1918; Washburn, 1921), of the penetration of liquids into porous materials where the rate of penetration is a function of the balance between surface tension forces and viscous drag. Interfacial contact angle is assumed to be constant and the pore morphology is reduced to an equivalent cylindrical pore. It has long been recognized that Lucas-Washburn over simplifies the morphology of paper, which, in reality, is a geometrically complex material made up of a cellulose fiber matrix in many cases modified with a consolidated mass of pigment and binder. A critique of the Lucas-Washburn theory also forms part of Chapter 2.

Chapter 3 discusses the experimental identification of the causes and nature of the defects in pressed LPM is examined experimentally. The effect of level of UF resin saturation and paper type on defects in the MF coating is examined. Scanning electron microscopy (SEM)[1] was used to examine the morphology of defects and Raman microscopy was used to study the distribution of MF resin in the paper.

Chapter 4 examines the physical characteristics and fluid imbibition behaviour (simulating conditions at the pre-wetting roller) of nine different decor papers. The level of defects in the pressed papers (reported earlier in Chapter 3) are related to these characteristics. Relationships between imbibition and physical characteristics are also established.

Chapter 5 reports on studies of the effects of liquid contact angle and surface tension on imbibition into simple model systems thus removing the confounding effect of the structural complexity of real paper. Mechanisms of fluid transport are presented.

Chapter 6 reports on attempts to identify the actual mechanisms of fluid flow in both unsized and sized papers using cryo-SEM and a newly developed technique involving cryo 2-photon confocal laser scanning microscopy (CLSM).

Chapter 7 reports on extensions of the studies covered in Chapters 3, 4, 5 & 6 into more complex paper systems. This involves papers with different filler types and amounts, two different fluid types, and modifications of the surface energy of the papers using plasma treatment to remove any chemical heterogeneity on the paper surface. This enables the determination of the impact of fillers on the morphology of pores within the paper structure and on its effects on fluid imbibition.

Chapter 8 discusses extensions of the work presented in Chapter 7 enabling identification of the causes of the paper effects on saturation demonstrated with the decor papers in Chapters

[1]The term 'SEM' is used to indicate both the process (*i.e.* scanning electron microscopy) and the equipment (*i.e.* scanning electron microscope). This is in accordance with common practice in the field of electron microscopy and is used throughout this thesis accordingly.

3 & 4.

Chapter 9 concludes the thesis by discussing the main findings of the thesis in relation to the aims and introduces areas of future research.

Each chapter is preceded by a concise introductory paragraph. Where new experimental techniques have been developed, details are included as Appendices. To show fluid flow in paper there are many SEM and 2-photon CSLM images of (cryo) fluid flow. A pair of anaglyphic 3D glasses are included for viewing the stereo CLSM images in Chapter 6. Also attached in the back of the thesis is a CD containing movies of the sequences of images obtained using 2-photon CLSM, a wetting sequence obtained using high speed video microscopy from Chapter 7 as well as a reconstructed micro-computed tomography data-set referred to in Chapter 9. Published and presented papers arising from the thesis are included as Appendices to the thesis.

Chapter 2

Literature review

This chapter reviews the literature on the treatment of decor papers, the experimental methods used to study fluid flow in paper and previous research on fluid flow in paper. Its purpose is to allow the reader to understand material presented in subsequent experimental chapters. It is not intended to be a comprehensive review of fluid-paper interactions.

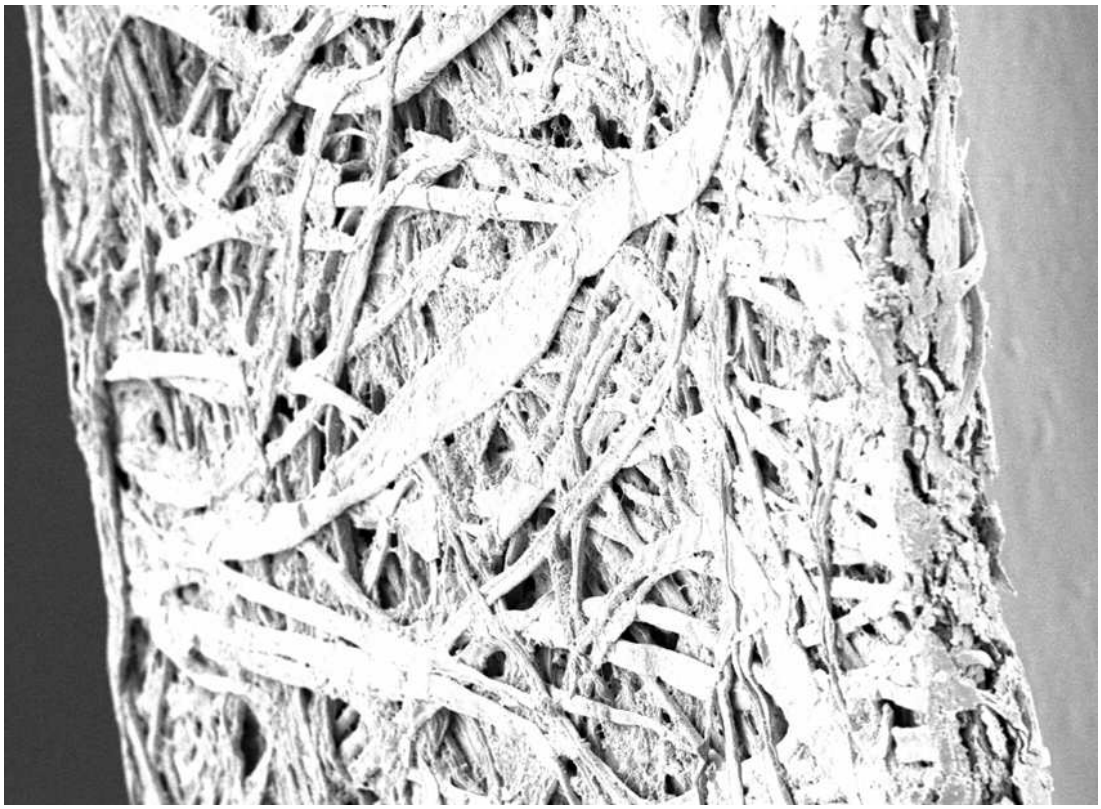

An image of copy paper using a field emission scanning electron microscope (FESEM)

2.1 Previous research into resin impregnation of decor papers

Arledter (1957) examined the factors affecting the penetration of paper by oil and resin. He concluded that any penetration test method based on perception of the human eye, or any method which did not use test solutions with precisely controlled temperatures and viscosities could not yield reliable test data, particularly if the same paper was compared at different times and by different observers. Arledter (1957) found that the time of resin penetration in different papers varied between 0.5 to 1000 seconds and judgement as to when the end point of penetration was reached varied for different observers by a wide margin. He stated that resin solvents should be removable from the impregnated paper structure without excessive resin migration and without leaving closed air voids. The purpose of Arledter's insightful paper was to firstly determine the best methods or instruments to determine the resin penetration rate of absorbent papers in general, secondly to investigate what test solutions or test methods were most suitable for measuring treating performance of absorbent papers and finally to inter-relate paper structure factors, resin penetration rate and resin pick up. Even today these areas are worthy of study as our understanding of the absorption of liquids by paper is incomplete.

Cussons (1997) in an unpublished report has provided the best outline of what happens during the resin impregnation process of decor paper in a commercial treater. He discussed various paper and liquid effects on treating. He stated that most decor papers had pore size distributions of 2-50 μm and that flow of resin mainly occurred in the region > 10 μm. Cussons (1997) stated that only 50% of the total void volume in decor paper is filled with resin using standard treatment methods and pore size distribution is the most important factor affecting resin impregnation.

Schnieder (1997a) divided resin impregnation of decor papers into four stages:

1. Phase 1-10 milliseconds when surface pores fill.

2. Phase 2; 10-80 ms, fiber walls swell after first contact with resin i.e. they absorb water. The resin solution then penetrates the pores very quickly.

3. Phase 3; 80-400 ms, absorption slows down. After 100 ms the resin strikes through, which means that it reaches the backside of the paper. After 400 m/s 80% of the pores are full and paper has reached it's final thickness.

4. Phase 4; 400-2000 ms, the rate of absorption slows down with saturation being reached after 2000 m/s.

There were no details in the study as to how she identified within-fibre imbibition.

Defects in LPM panels occur as a result of two fluid flow problems during treating and pressing, firstly insufficient flow of UF resin into the decor paper and secondly the excessive

flow of MF resin into the paper during pressing (Chapter 3) Therefore the rest of this review focusses on fluid flow and the methodology to measure and model fluid flow in paper.

2.2 Review of experimental methods used in the thesis

2.2.1 SEM in the study of liquids and paper

SEM is used to image raw and resin impregnated papers (Chapters 3, 7 & 8) and cryo-SEM, a new technique involving freezing of the sample immediately after liquid contact, is used to study the imbibition of aqueous solutions into paper (Chapters 6 & 7).

Oliver and Mason (1976) described the use of SEM to study stationary and moving liquid drops on paper surfaces and demonstrated the effect of surface roughness on the morphology of the liquid droplets. Molten drops of polythene and polymethylmethacrylate were applied to paper and the process of spreading and solidification of the droplet was observed. Solid droplets were mounted on a stub, gold coated and imaged. Morphological changes in droplets were complicated by contraction in their volume during solidification. The authors concluded that the complicated structure of paper and limitations of SEM prevented qualitative analysis of the morphology of liquid drops applied to paper.

Forsberg and Lepoutre (1994) used environmental scanning electron microscopy (ESEM) to observe moderate structural changes at the surface of paper fibres as water condensed onto the surface in a high moisture environment. They stated that cellulosic fibers are sensitive to moisture during printing with offset or water-based gravure inks, and interactions between water and paper can lead to undesirable changes in the paper structure. The purpose of their study was therefore to study the roughening phenomenon *in-situ*. They found a roughening of the paper surface but made no comments on the distribution of fluids nor imbibition mechanisms. Using this technique the authors were unable to obtain a “snapshot” of the mechanisms of imbibition in paper because as soon as the water condensed it would have imbibed into the paper almost immediately.

Liukkonen (1997) also used ESEM to examine the interaction of water with paper surfaces and found that the electron beam caused the water droplets to evaporate. Also the drops continued to grow and merge over time. Cryo-SEM has the potential to overcome problems of evaporation of the imbibing fluid and could enable the study of fluid flow in unsized papers as well as sized papers.

2.2.2 Cryo 2-photon confocal laser scanning microscopy (CLSM)

Cryo 2-photon CLSM, described in Chapter 6, was used to study the imbibition of aqueous solutions both below the surface of paper and beneath the droplet of the imbibing fluid. It was a new technique developed for this thesis.

The concepts of confocal microscopy (*single photon*) were first described in the original patent for a confocal microscope by Minsky (1957). Van der Wulp (1995) gave an excellent description of the principles of confocal laser scanning microscopy (CLSM) and stated that a 3D reconstruction of a specimen could be generated by stacking 2D optical sections collected in a series. This was the principle behind the 3D reconstructions of the two-photon CLSM images in Chapter 6. Other workers who have reviewed the principles and advantages of single photon confocal microscopy are Lemasters et al. (1993); Centonze and Pawley (1995); Inoue (1995).

Denk et al. (1989) in their patent application for a *two-photon* confocal laser scanning microscope, described some of the disadvantages of single photon CLSM which mainly centre on photo-bleaching of samples. They described the principle of two-photon excitation which allows accurate spatial discrimination and quantification of fluorescence from small volumes whose locations are defined in three dimensions. This provides a depth of field resolution comparable to that produced in confocal laser scanning microscopes (single photon) without the problem of out of focus fluorescence. "This is especially important in cases where thicker layers of cells are to be studied (for example paper fibres). Furthermore, two-photon excitation greatly reduces background fluorescence". Denk et al. (1995); Potter and Fraser (1999) also described the benefits of two-photon microscopy and the reduction of photo-bleaching throughout the specimen.

A number of workers have used CLSM to study paper. Ting et al. (1997, 2000); Lloyd and Dickson (2000); Dickson (2000a,b) used CLSM to examine changes in the fibre network and individual fibres as a result of direction compression. Jang et al. (1991) described a technique for rapidly producing cross-sectional images of wood pulp fibers based on optical sectioning using CSLM. They then used image analysis to calculate fibre properties such as cross-sectional area, perimeter, and wall thickness. Xu et al. (1997) examined fibre distribution in the z-direction of a handsheet using CSLM (single photon) and image analysis. They stated that some of the most important paper properties including printability are affected by the difference in fibre distribution in the z-direction. Jang and Seth (1998) used CLSM to study loss of lumen volume as a result of fibre processing. It is believed, however, that CLSM has not been used to study fluid flow in paper.

2.2.3 Plasma treatment of paper

Plasma treating, described in Chapter 7, was used to reduce chemical heterogeneities at paper surfaces in order to more accurately determine how the structure of paper affects fluid imbibition.

Many workers have studied the effect of plasma treatment on liquid imbibition into paper. Brown and Swanson (1971) in an early study found that a cellulose surface could be made

more hydrophilic by corona treatment. Suranyi et al. (1980) found that self sizing as proposed by Swanson and Cordingly (1959) in aged corrugating medium could be reversed by plasma treatment. The corona treatment caused a significant increase in the oxygen:carbon ratio of the medium indicating that the carbon rich surface component had been either removed or oxidised. This was consistent with the observed decrease in the wetting time after corona treatment. Cramm and Bibee (1982) also found that plasma treatment caused oxidation of the surface of paper, increasing surface energy and allowing better wetting by liquids. Bottin et al. (1984); Sapieha et al. (1988); Young et al. (1994) also examined the effects of plasma treatment on the wettability of paper.

2.2.4 Mercury intrusion porosimetry

There has been a lot of debate on the efficacy of using mercury intrusion porosimetry to determine pore size distribution in paper and coatings. It is still the most widely used method to determine "pore size" distributions in porous media such as paper. However the fundamental assumption underpinning the determination of pore sizes from intruded mercury volumes is that the pores are cylindrical. This of course is unfounded when the geometry of void spaces in paper are examined closely.

Kraske (1960) found agreement in void volumes obtained using nitrogen sorption and mercury porosimetry methods. Climpson and Taylor (1976) used transmission electron microscopy (TEM) to derive pore volume and compared the results with those obtained from the mercury intrusion method. They found that mercury intrusion resulted in much lower (pore) sizes suggesting that it did not give an accurate indication of pore dimensions.

Davis and Smith (1989) used NMR spectroscopy to analyze the pore structure of coatings. They mentioned that mercury porosimetry was not an ideal technique to measure pore sizes in paper, for the following reasons; 1, it is a destructive technique and requires assumptions about pore shape (assuming pores to be cylindrical); 2, mercury porosimetry skews the measured distribution to smaller pore sizes; 3, samples may be compressed, altering the calculations of pore size distribution.

Kettle et al. (1997) commented on the problems of using mercury porosimetry at the lowest applied pressures. At such pressures mercury is unable to correctly probe the largest pores which is a limitation when analysing uncoated papers. They stated that these large pores were very important since the liquids absorbed faster into the larger pores as described in the Lucas-Washburn equation. The use of the Lucas-Washburn equation to describe fluid flow in paper is reviewed in Section 2.4.1.

Furo and Daicic (1999) used NMR cryoporometry to investigate the pore structure of paper and paper coatings and reviewed a number of methods for determining pore size distribution of paper coatings and paper. They stated that mercury porosimetry was the favoured method,

however they pointed out its limitations, including problems in measuring small pores and its destructive effect on a soft material such as paper which could cause inaccurate determination of pore size distribution.

2.3 Testing the rate of fluid imbibition into paper

2.3.1 Testing imbibition into decor papers

Arledter (1957) examined the impregnation properties of paper products used in the plastics industry and evaluated different methods of assessing resin pickup. He was one of the first to specify the performance measurements of a technical absorbent paper where a "wanted amount of resin in the form of a solution was incorporated into a paper in such a way that the resin shall, without excessive filter effect, penetrate and distribute in the paper structure and uniformly cover all available individual surfaces and fibres in the shortest possible time". Arledter determined that none of the TAPPI (TAPPI, 1992) or American Society for Testing and Materials (ASTM) methods were relevant to the problem of measuring resin pick-up by paper. As mentioned above, Arledter (1957) concluded that any penetration test method based on perception of the human eye, or any method which did not use test solutions with precisely controlled temperatures and viscosities could not yield reliable test data.

Seiler (1957) noted there were a large number of tests available for paper, such as basis weight, density, various strength tests, ash content, moisture content and porosity which could be used to cull papers that were obviously unsuitable for applications where absorbency was required. None of the methods were able, however, to select the best paper from within a group of papers with satisfactory performance. Seiler suggested that a test based on simple penetrability[1] and saturability[2] could be used to select batches or types of paper for applications requiring saturation. He did not, however, describe such a test.

2.3.2 Review of non-optical methods to test rate of liquid imbibition into paper

Non optical methods were used in this thesis to measure rates of liquid imbibition into paper. These were based on the standard test methods referred to above (Arledter, 1957) and measured fluid flow in the *x & y* directions. The only non-optical method used to predict fluid imbibition in the *z* direction was measurement of air permeability using the Gurley method, which is still commonly used by manufacturers to predict fluid flow in saturating papers.

The most widely used non-optical fluid imbibition test over short time scales was developed by Bristow (1967). His apparatus (the Bristow Wheel) was designed to study liquid absorption

[1] Penetrability refers to the rate of strike through of a resin solution through the paper from one surface to another and as Seiler states, depends on void structure of the paper and the viscosity of the resin

[2] Saturability represents the total amount of resin which can be held by the paper and depends on the concentration of voids and capillary forces on the resin

into paper during short time intervals in the range 0 - 2 s and evolved from the nip spreading methodology of Wink and Van den Akker (1957) and Sweerman (1961) and later modified by Hung et al. (1969). The Bristow method measures the length of track for a given liquid volume with a paper sample over different speeds. Bristow (1967) described the wetting of paper by aqueous fluids as a two stage process; (firstly wetting of the surface and secondly, redistribution of the liquid away from the surface), also involving a wetting delay. The test method itself was developed as a result of the inefficiencies of the Cobb test (Cobb and Lowe, 1934; Scandinavian Pulp Paper and Board Testing Committee, 1964) & TAPPI TM 441, which measure water uptake over much longer time periods (Bristow, 1968).

2.3.3 Review of optical techniques for measuring liquid imbibition into paper

The test methods developed in Chapters 4 and 7 were based on measuring changes in reflectance of paper on the opposite side to that of an imbibing liquid. The method used in Chapter 4 used a video acquisition rate of 30 fps and that in Chapter 7 was based on high speed microscopy with an acquisition rate of 300 fps.

Price et al. (1953) developed a test method that measured the resistance of paper to penetration by liquids based on changes in the optical properties of the sheet during penetration by a test liquid. A specially designed photometer was used to measure changes in optical properties (reflectance and transmission). The test method developed became known as the Hercules size test[3] and is still used as a measure of resistance of paper to penetration by liquids. The principle of measuring optical properties of a paper sheet during liquid penetration was the basis for two test methods developed in this thesis. The Hercules test, however, measures imbibition in papers over long time scales (for sized papers) whereas the methods developed in this thesis measured imbibition over very short time scales as appropriate for a thesis relevant to resin imbibition into decor paper.

Napier (1964) also developed an apparatus for measuring liquid penetration into paper which was based on the principle that as a liquid rises under capillary forces through a sheet of paper, the light reflectance of the upper surface of the sheet decreases. Napier (1964) stated that the initial rapid rise of the liquid occurred due to fluid flow into the largest pores. When the liquid in the large pores reached the top surface of the paper, the penetration rate in the sheet as a whole decreased as smaller pores filled.

Lyne and Madsen (1964) also developed a method for measuring liquid penetration of paper that used an oscilloscope to measure decrease in reflection of a paper surface when a film of liquid was applied to the opposite side.

Windle et al. (1970) developed an optical technique for measuring the draining of water from coatings. They measured capillary penetration over millisecond time intervals, rather than

[3]TAPPI Standard T 530

extrapolating from long time data as had been done previously. A piece of paper was floated on the surface of a bath of black dye and photographed at intervals through a microscope. This idea of floating a sample of paper on a penetrating liquid for the measurement of liquid penetration forms the basis for methodology (relative reflectance technique) developed and described in Chapter 4.

Winspear (1979) in a study of the relationship of paper moisture and porosity on liquid penetration referred to the difficulty in determining end points using transverse penetration tests, especially those based on perception by the human eye. He was of the opinion that modified capillary rise tests were probably the best replacement for transverse penetration tests. Winspear (1979) used a reflectance meter and photo-electric cell and determined the end point of liquid penetration by measuring the point at which liquid strike-through caused a given drop in the reflectance of the paper surface.

Howarth and Schindler (1985) used an adaptation of the apparatus developed by Hoyland et al. (1973) to obtain a pictorial record of the fluid penetration pattern on the top side of the paper. A liquid surface was brought into contact with the under surface of a horizontal sheet of paper and the penetration of dyed water through it was recorded using a cine camera. Three measures of liquid penetration were obtained from the visual record of fluid penetration: time to first penetration, average gradient of the main body of the curve and time to 95% penetration. The percentage reflectance lost by the bottom surface becoming dyed related to the percentage area penetrated. This methodology is similar to that used in Chapter 7 except the imaging rate was slower in the previous studies *i.e.* 18 vs 300 fps .

Chen et al. (2001) used a high speed CCD camera at 200 fps to record the kinetics of droplet shape and droplet absorption based on the comparative analysis of the time needed for the droplet to disappear (as a function of droplet volume for various yarns). This study was relevant to direct imaging of droplet penetration into individual yarns rather than into a porous network *per se*.

2.4 Review of theories of fluid flow in paper

2.4.1 Bulk capillary flow theory and the use of the Lucas-Washburn equation

There is a large volume of work on the study of fluid flow in paper, a significant proportion of which refers to the Lucas-Washburn equation (Lucas, 1918; Washburn, 1921) which states that the time t required for liquid penetration into a certain capillary length l is proportional to the second power of this length and the viscosity of the liquid (Equation 2.1). Time of penetration decreases with increasing capillary radius r, with increasing surface tension γ of the penetrating liquid (decreasing angle of contact) and viscosity μ. Given the complexity of the structure of paper, earlier studies made simplifying assumptions about the geometry of

pores. Fluid flow was represented in one-dimension through single capillary models of a given pore radius, which were unconnected with each other.

$$l = 1/2[\frac{\gamma r}{\mu}]^{1/2} t^{1/2} \tag{2.1}$$

This section of the review describes such work. Later work reviewed in Section 2.4.3 describes three dimensional models where pores had more complex shapes, were connected by throats of a given radius, but where however, the mechanism of imbibition was still bulk meniscus flow.

Price et al. (1953) showed that liquid penetration into paper occurred in two stages, fast initial penetration as being capillary flow and slower secondary penetration being penetration into the fibres.

Bristow (1961) in a literature review of adhesion stated that paper was a network of capillaries between fibres. He described liquid penetration in terms of capillary flow due either to gravitational or to capillary (surface tension) forces, or the presence of an externally applied pressure or to the combination of all three. Liquid penetration in a capillary system could be described by application of Poiseuille's law for streamlined flow through a capillary.

Bristow (1961) appreciated the limitations of the Washburn equation which gives a direct correlation between the rate of penetration and the capillary radius r. This relationship was complicated by three factors: a) porosity influenced the initial wetting; b) r varies due to the swelling characteristics of cellulose and; c) the distribution of pore sizes in the network made it impossible to ascribe a single value to r. Bristow (1971) subsequently stated that in no case did sorption of water occur by the simple advance of liquid in the pores as described by the Lucas-Washburn equation, although such an equation was perhaps valid for the sorption of oil (where little or no diffusion into fibres takes place). He stated that most studies of the sorption of liquids by paper assumed that it occurred via capillary flow, although such an assumption neglects that portion of the liquid which migrates by diffusion or other processes.

Brecht (1962) recognised that simplifying assumptions such as circular pore cross-section, a pore diameter or a pore length equal to paper thickness weakened the application of the Lucas-Washburn model to describe fluid flow in paper. These problems were compounded by fibre swelling, caused by water and water vapour. The effect of such swelling on the penetration of fluids into the pores of paper has not been fully determined. Brecht (1962), in accord with Bristow (1961), stated that the Lucas-Washburn equation adequately described the penetration of oils and non-swelling liquids into paper, concluding that the only path for such penetration was capillary flow through the pores.

Verhoeff et al. (1963) examined fluid penetration into unsized papers and stated that there were two well-defined paths for penetration; capillary flow through the pores described by Lucas-Washburn, and diffusional flow through fibres, both occurring simultaneously. Such

penetration occurred so fast it was impossible to separate the two. In sized sheets they stated that diffusion through the fibres was much quicker than capillary flow and that insufficient attention had been paid to the effect of the structure of the paper web on liquid penetration. This was an insightful comment because it is the complex geometry of the void space in paper that provides the main limitation to the use of the Lucas-Washburn equation to describe fluid flow in paper.

Van den Akker and Wink (1969) concurred that the Lucas-Washburn theory was far from valid in terms of its ability to model liquid penetration of paper. The representation of paper as a bundle of circular capillary tubes on which the theory rests is too different from the complex pore system of paper (that can be visualised using optical and electron microscopy). They also stated that contact angle was not a good indicator of water resistance because the surface pores and surface roughness of the paper had an appreciable influence on the angle. This also affects the use of the Lucas-Washburn equation.

Windle et al. (1970) used optical techniques to study liquid migration from coatings into paper. They stated that regions above the average pore size were the first to wet and subsequent liquid penetration could be attributed to sideways spreading of the liquid through the paper and bulk migration through the paper sheet, presumably through the smaller pores.

Hoyland et al. (1973) stated that the basic shortcomings of the Lucas-Washburn theory were that pores in paper were not thin capillaries and that swelling of the fibres was not taken into account. They offered the following model as an alternative: After liquid had wetted the surface of the sheet, it was absorbed into the fibres and penetration proceeded along the pores. This resulted in a change in thickness of the sheet and the depth of penetration was less than that which would occur if liquid were not absorbed into the fibres. The assumption was made that the liquid advanced by bulk meniscus flow. They did not take into account, however, the effect of complex pore geometry on flow. They stated that penetration of swelling liquids into paper had four potential paths: 1) liquid penetration through the pores by capillary flow; 2) liquid movement through the pores by surface diffusion; 3) liquid movement through the fibres by various processes and; 4) vapour phase movement through the pores. The mechanism of fluid flow in paper is examined subsequently in this thesis in Chapters 6 & 7.

Oliver and Mason (1976) found that paper surfaces often contained fibres with sharp edges that significantly inhibited the spreading of a liquid. This was an interesting observation as it identifies another significant problem affecting the application of the Lucas-Washburn theory to the imbibition of liquids in paper, that of complex pore geometry (Kent and Lyne, 1989a). Oliver and Mason (1976) also stated that surface morphology of fibres had a pronounced influence on spreading and absorption behaviour of liquids which warranted further study.

Hoyland (1977) described the complexity of paper structure and the irregular distribution of pore volume within the sheet. He reviewed capillary flow models for paper, which at that time were limited by the lack of a rigorous geometrical description of the porous structure of

paper. He also found that during the initial rapid penetration of paper by liquid, little fibre swelling took place, however, as the penetration rate decreased, so large increases in sheet thickness were recorded. According to Hoyland (1977) this accounted for deviations from the Lucas-Washburn equation.

Stannet and Williams (1977) stated that two general mechanisms of water transport in cellulosic materials were possible. They were activated diffusion and capillary flow. In highly porous materials such as paper, pore flow may be accompanied by a surface "hopping" type of mechanism.

Winspear (1979) reviewed Hoyland's (1977) work and stated that when liquids penetrated paper, fibre swelling occurred and that the majority of liquid flow took place through the spaces and pores between fibres rather than through the channels within the fibres, the latter being a slower process than the former. Winspear (1979) stated that as liquid moved into paper, wider channels tended to supply liquid to narrower ones having higher suction, thereby by-passing many smaller pores. This was probably why it was thought that complete liquid saturation of paper at ordinary pressures was difficult or impossible (Cussons, 1997). Winspear (1979) examined the applicability of the Lucas-Washburn equation to the penetration of unsized papers by 'non-swelling' liquids as well as by aqueous liquids which swell cellulose. He concluded that the equation adequately described penetration of paper by "non-swelling" liquids, but it broke down when applied to liquids that swell cellulose.

Nguyen and Durso (1983) stated that as fibre webs were porous media with interconnected pores of various sizes, the liquid imbibition process was by diffusion flow in pores rather than by liquid flow described by a capillary tube model (Washburn, 1921). They believed that removing the liquid source stopped all capillary-based flow. In the case of fibre webs, however, slow movement of fluid could still occur by a redistribution from a wetter to a drier area.

Bristow (1986a) stated that even though the square root relationship in the Lucas-Washburn equation was a good approximation for the behaviour observed during the absorption of a non-swelling oil by paper, a similar linear relationship was often obtained in studies of the absorption of water and other swelling liquids resulting in the general application of the Lucas-Washburn equation for the interpretation of such behaviour. Bristow (1986a) believed this was an incorrect interpretation as a relationship between $t^{1/2}$ and fluid flow was not sufficient to justify the assumption that capillary flow was the physical mechanism involved. This was because the sorption of water into fibres occurred via a complex diffusion process, where vapour phase diffusion in the pores, surface diffusion along the fibres and bulk diffusion through the cellulosic material all played a part. Furthermore, the diffusion path was undoubtedly dependent on the network structure. The boundary between the two types of liquid uptake, (pore sorption and fibre sorption) was not strictly defined in terms of paper structure or fibre morphology. One represented simple capillary flow of liquid in pores between and within fibres, the other represented an interaction between liquid and fibre consisting essentially of sorption

into the fibre wall and a diffusion through the cellulosic material.

Eklund and Salminen (1986, 1987) studied the absorption of water from coatings into paper over short time intervals. The Lucas-Washburn equation did not satisfactorily explain their experimental results in accord with the findings of other workers (Bristow, 1967; Lyne and Aspler, 1982; Aspler et al., 1984; Aspler and Lyne, 1984). They concluded that the absorption of water by paper over short time intervals was mainly dependent on the prevailing pressure. Capillary migration (at zero pressure) was found to be dependent on temperature, suggesting that the initial steps in water transport in a non-pressurized system was via the gas phase. They stated that this occurred because the influence of temperature was of such a magnitude that changes in the viscosity and surface tension of the water were insufficient to explain the values obtained. Lepoutre (1989) also found that the absorption of water by paper over short term time periods increased much more rapidly with temperature than could be accounted for by capillary flow theory.

Eklund and Salminen (1986, 1987) also found that swelling (due to fibre sorption) would change the value of r (and could never be constant), and accordingly that some correction factor needed to be added to the Lucas Washburn equation. They also suggested that there was always air trapped in paper even in fully saturated papers. Washburn (1921) assumed that the capillary system was open and connected at both ends, and hence pressure losses due to trapped air were not part of the model. However Eklund and Salminen (1986, 1987) referred to the fact that only a very small proportion of pores were connected to both sides of the paper sheet. The authors concluded, “the counter pressure caused by compressed air at short penetration times was of such a magnitude that the water penetration at low pressures must take place according to mechanisms” other than by surface tension forces.

Chen and Scriven (1990) also found that the counter pressure of trapped air influenced liquid penetration into paper as well as the absorption of liquid by fibres, and associated swelling.

Salminen (1988) stated that the classical Lucas-Washburn model did not adequately describe water transport in the pore system of paper for three reasons;

1. Time and velocity dependence of dynamic capillary pressure: (a) the effect of penetration velocity on the formation of an advancing interface and (b) interactions between water (vapor phase) molecules and the fibre wall ahead of the capillary front. As a result the dynamic capillary pressure was not constant, as assumed in the derivation of the Lucas-Washburn model, but was dependent on the transport velocity of the liquid front as well as on the contact time between the liquid and the paper.

2. Counter pressure of air; caused by trapped air as proposed by Eklund and Salminen (1986, 1987) and referred to above.

3. Expansion of the fibre network and fibre sorption (through swelling) caused by water.

Salminen (1988) also found that diffusion was probably the most important transport mechanism in hydrophobic (sized) papers under no external pressure.[4] He made no reference to another highly significant shortcoming of the Lucas-Washburn model, caused by the effect of the complex geometry of pores and discontinuities in pore structure on rate of fluid flow (Kent and Lyne, 1989a) and (Kent and Lyne, 1989b).

Lyne (1993) divided liquid-paper interactions into the following phases: a) dynamic wetting (an interfacial adhesion phenomenon between the liquid and a solid surface) and spreading; b) capillary penetration; c) pressure penetration and; d) diffusion into the fibre wall and swelling. It was assumed that the first occurred over short time scales and the second over much longer time scales.

Aspler et al. (1993) and Aspler (1993) in describing ink penetration and spreading in paper stated that the application of the Lucas-Washburn equation to the phenomenon of ink setting had several shortcomings: 1) Measuring the sorption of a simple oil or solvent was not sufficient to model the penetration of the thin fluid phase ($3\mu l$) of a pigmented ink; 2) The assumption of uniform parallel capillaries did not come close to the reality of paper structure; 3) It was unrealistic to think that fluid viscosity would remain constant during the setting process; 4) Neither the surface tension of the ink and solid were well-defined. Zang and Aspler (1995) also questioned the use of Lucas-Washburn to describe ink flow into paper.

Marmur and Cohen (1997) investigated the rise of a liquid in filter paper and found that a single capillary model and the Lucas-Washburn equation adequately described their results. They stated that the cosine of the contact angle θ was far from unity, which was assumed in many cases. Contact angle was not meant to represent the intrinsic contact angle between the liquid and the fibres, it was the angle that would exist in a cylindrical capillary that was equivalent to the studied porous medium in terms of the kinetics of penetration.

Kornev and Neimark (2001) stated that no theory existed to quantitatively predict the initial stage of imbibition during the spontaneous penetration of a wetting liquid into the pore channels of paper. They concluded that the Lucas-Washburn equation adequately described uptake of viscous fluids into capillaries and porous solids, but it failed to describe the initial stage of penetration, which had been attributed to the neglect of fluid inertia. The authors developed a variety of regimes for spontaneous liquid penetration of paper which were characterized by different initial fluid velocities.

2.4.2 Effect of pore geometry

The Lucas-Washburn equation assumes that capillary systems have an average pore radius and it takes no account of the complexities of the pore geometry in paper, as mentioned above.

[4] This was not defined as either inter-fibre or intra-fibre diffusion.

Kent and Lyne (1989a,b) found that studies of the penetration of water or inks into paper that employed smooth capillary models were inaccurate. Nevertheless they were used because they provided information on the effective hydro-dynamic pore radius. This term was derived by applying the Lucas-Washburn equation to experimental measurements of liquid imbibition. The danger associated with such an approach is that it focusses attention exclusively on the size distribution of pores, and away from factors such as shape, discontinuity and wall rugosity. The authors introduced three such discontinuities: the step, bend and T-junction, and described the different vapour pressures that develop as liquid passes through these discontinuities. They stated that the major factor retarding capillary penetration of ink into paper after printing was the influence of pore morphology on the interfacial curvature between the advancing ink and paper. They also referred to the effect of pore geometry, especially whether pores were divergent or convergent, on contact angles.

Danino and Marmur (1994) studied the horizontal penetration of liquid in paper and stated that in a porous medium with non-uniform size distribution of pores[5], the local capillary driving force depended on pore geometry. When the amount of liquid was limited, there was a tendency for the liquid to redistribute itself by flowing from large pores into the smaller ones, as liquid penetration into small pores was slower than penetration of large ones. They stated that the Lucas-Washburn equation assumed that the rate of fluid flow was dependent on r in a smooth capillary.

2.4.3 Complex simulated three dimensional pore models of imbibition

More recent models of capillary flow in paper attempt to take into account of how the complexity of the pore structure affects imbibition rates. These models still assume bulk meniscus flow and include the simplifying assumptions that wet pore radii is equivalent to dry pore radii, there is an unlimited reservoir of liquid, flow is unidirectional and all pores act separately and are completely accessible for intrusion or drainage at all pressures (Kettle et al., 1997). Kettle et al. (1997) concluded that large pores dominated the absorption of fluid at short contact times ($<$1s), whereas smaller pores dominate the absorption over longer contact times. No account was taken of the inter-connectivity of the network, which may include the shielding or shadowing of large voids by smaller connecting voids around them.

Matthews (2000) modeled fluid permeation in porous coatings and paper. He pointed out that even in a simple capillary system where there was a well known approach to liquid flow there were many complications that were not accounted for, such as uncertainty of dynamic contact angle, exact meniscus shape, micro-roughness and cleanliness of tube's inner surface. Wetting was also affected by the development of a pre-cursive wetting film. He pointed out that these complexities were rarely addressed because there was little benefit in refining the

[5]the effective capillary radius was determined using Lucas-Washburn

mathematics of permeation into a void, if the gross dimensions of the void were wrong. To address such complexities Matthews (2000) introduced Pore-Cor[6] which was an isotropic 10 x 10 x 10 cubic lattice of cubic pores, connected by cylindrical throats subsequently modified to become double conical. This system was used to model velocity changes for wetting fluids, caused by geometry changes within void structures. It was assumed that they gave a representation of heterogeneity of surface energy. Even complex models such as these, however, do not represent the true structure of the void space of paper and assume bulk meniscus flow in the complex simulated pore shapes. Furthermore they take no account of micro-roughness of the pore wall (fibre surface). Other workers who have used a similar approach include Schoelkopf et al. (2000a,b) and Gane et al. (2000).

2.4.4 Intra-fibre flow

Intra-fibre flow occurs within the fibre itself. The two potential pathways for this flow are firstly in the fibre lumen, and secondly within the fibre wall. Intra-fibre flow of liquids is not adequately described by capillary flow models. Maloney and Paulapuro (1998) found that a significant part of the water within cell walls melted at the same temperature as bulk water and they suggested such water was located within fibre cell macropores formed when lignin was dissolved during pulping. Capitani et al. (2002) confirmed this by using NMR to study the distribution of water in fibres in dry paper. They found that water pools were surrounded by amorphous cellulose. The average dimension of the water pools were approximately 1.5 nm and the size of pores within the cellulose in fibres were up to 1.4 nm. These pores may provide a pathway for the movement of water in sized paper.

2.4.5 Fluid flow in sized papers

There has been much attention focussed on the flow of liquids in sized papers. This thesis is primarily concerned with flow in unsized and uncoated papers, but flow in sized papers was examined because of the insights it can provide into the magnitude of intra-fibre flow and the longer time scales over which this occurs.

Reaville and Hine (1967) stated that the primary pathway for fluid imbibition in sized papers was through the pores. Fluid flow was controlled by surface diffusion ahead of the water front and this was accompanied simultaneously by secondary penetration into the fibre.

Bristow (1968) found that water could not enter the pore system in sized papers, and that the only sorption that occurred was associated with diffusion into fibres. Sizing effectively prevented the entry of water into the pores and the uptake of water was solely due to fibre sorption.

[6] referred to by Kettle et al. (1997)

2.4.6 Effect of surfactants on imbibition into paper

A significant amount of work on the effect of surfactants on imbibition into paper has been done based either on adding a surfactant to the paper during manufacture to reduce any heterogeneities caused by self sizing or by actually adding surfactants to the imbibing fluid. Lyne and Aspler (1982) confirmed the observations by Bristow (1971) that addition of a surfactant to the liquid had little effect on wetting time and reported that significant reductions in wetting time could be achieved if the paper was impregnated with a surfactant. Aspler et al. (1984) found that the addition of surfactant to paper after self sizing had occurred, could restore its wettability and the rate of sorption of water. Aspler and Lyne (1984) found that improved wettability was seen as a decrease in the wetting delay resulting in an increased rate of water uptake. Surfactants added to pure cellulose fibres caused no change in wettability, whereas surfactants greatly increased the wettability of fibers previously rendered hydrophobic by wood resins. However, the presence of surfactant in water had little effect on wetting delay. Salminen (1988) studied the effect of surface tension and confirmed the findings of Aspler and Lyne (1984) *i.e.* high molecular weight surface active agents had virtually no influence on the transport velocity because the migration time of surfactant molecules to the newly formed surface was longer than the surface age in a wetting process. On the other hand, small alcohol molecules were found to be effective in lowering the dynamic surface tension of an aqueous solution. The effect of isopropanol concentration on transport was detailed and at higher concentrations the rate was faster and there was a great difference in the saturation volume for pure water and isopropanol. Zhmud et al. (2000) stated that the $t^{1/2}$ behaviour was characteristic of a diffusion-controlled process often observed for surfactant solutions in hydrophobic capillaries. However, the authors showed that the physics of these phenomena were completely different, and in the latter case, the Lucas-Washburn equation was not applicable at all.

2.4.7 Film flow

Film flow is where a thin layer of liquid advances along a surface surrounding a void under capillary pressure. The void still contains a non-wetting fluid (usually air). A number of workers referred to film-based-flow.

Phillip (1978) described the formation of films of liquid when he examined combined absorption and capillary condensation on rough surfaces.

Lyne and Aspler (1982) referred to wetting films on fibres created by the surface diffusion of water and the adsorption of water vapour. The slow production of such films on surfaces with low surface energies was explained by the wetting delay referred to by Bristow (1967), Eklund and Salminen (1986, 1987) and Lyne and Aspler (1982).

Ransohoff and Radke (1988) showed that in cylindrical capillaries occupied by a non-wetting phase, wetting liquid flow occurred in thin films. In non-circular capillaries, however,

most of the wetting liquid flow occurred in the corner regions. The two-dimensional hydrodynamic problem of wetting liquid flow along the corners of a predominantly gas-occupied non-circular pore was solved numerically. The solution was quantitatively expressed in terms of a dimensionless flow resistance, which was a function of surface viscosity, half angle of the corner of the pore and contact angle. Their results showed that increasing the contact angle or degree of roundedness of the corner diminished the available area for flow causing a greater resistance to flow.

Chen and Scriven (1990) in a study of coating paper, referred to films being formed by spontaneous imbibition through capillary action, where the interfaces were concave toward the air ahead of the front because they merged into thin films of setting liquid. Locally, the apparent contact angle with the matrix surface was zero or nearly so.

Blunt et al. (1992) used a three dimensional network model of a porous medium to compute relative permeabilities and capillary pressures in drainage and imbibition. They stated that film flow or flow along microscale roughness of the wetting phase was essential to allow the non-wetting phase to form well-connected pathways through the system. They identified two types of realistic displacement: 1) flow with trapping pores, where the wetting phase could not drain from large volumes surrounded by non-wetting fluid, and 2) no trapping, where all the wetting phase escaped along microscopic channels.

Blunt (1997) subsequently developed a three dimensional pore level network model that computed relative permeability and capillary pressure for drainage and imbibition cycles. The model accounted for wetting layers in crevices of the pore space, cooperative pore filling, different contact angles and various types of pore filling mechanisms in imbibition as described by Lenormand et al. (1983); Lenormand and Zarcone (1984); Lenormand et al. (1988). Two distinct types of mechanisms have been developed to explain the advance of liquids during pore filling. The first is piston-like, where the fluid advances in a connected front occupying the centres of the pore space. The second is where the wetting fluid flows along crevices in the pore space, filling pores in advance of the connected front. Filling of pores depends on the number of nearest neighbours that are already filled with wetting fluid. Lenormand et al. (1983); Lenormand and Zarcone (1984); Lenormand et al. (1988) first observed and described these mechanisms.

Lyne (1993) in reviewing work on the dynamic interactions of liquids with solid surfaces divided liquid-paper interactions into the following: 1) dynamic wetting, spreading and capillary penetration; 2) pressure penetration and; 3) diffusion into the fibre wall and subsequent swelling. He also stated that on a molecular level it would be improbable that a liquid would end abruptly at the three phase line as depicted by the Young-Dupre equation. In support of this suggestion he referred to work by Hardy (1919, 1936) who showed that a thin film of liquid preceded the complete spreading of a drop or bulk liquid on a solid surface. Lyne (1993) questioned whether these films behaved as normal liquids at all. He pointed out that spreading

was enhanced on rough surfaces for liquid that had contact angles less that ninety degrees, and inhibited for liquids with contact angles greater than ninety degrees. Furthermore it was suggested that spreading was enhanced along grooves and inhibited across them.

Bico and Quere (2003) mentioned that the progression of liquid inside a porous medium such as paper involves two macroscopic fronts; a main one which saturates the medium and a thinner one which could be in the form of a film, which propagates ahead of the main front using the fine structures of the porous material. This precursor being the front which pumps the liquid inside the larger ones.

Manufacturers of decor papers have always assumed that the Lucas-Washburn model can adequately describe fluid penetration into the papers. One of the fundamental aspects of this model is that time of penetration of a liquid decreases with increasing capillary radius. Thus manufacturers have long believed that a decor paper with larger pores will perform better as it will imbibe resin much more quickly than one with smaller pores. Other areas that have been taken for granted is that the air permeability of paper as measured by the Gurley method relates to how well a paper will imbibe a liquid and thus perform in a treater. In general, however, manufacturers of decor papers have been unable to relate the physical characteristics of paper to their impregnating performance. Thus this thesis focusses on these areas in order to improve the process of manufacturing decor papers for decorative underlays.

Chapter 3

The Cause of Surface Defects in Low Pressure Melamine Panels

In this chapter the nature of the defects in LPM panels is described and related to two fluid flow problems; firstly, inadequate impregnation of paper by UF resin during the first stage of treating; secondly, flow of MF resin away from the surface of the paper into voids created by inadequate impregnation of paper with UF resin. Treatment (level of saturation) effects and paper type were found to have a strong effect on the level of surface defects in LPM panels.

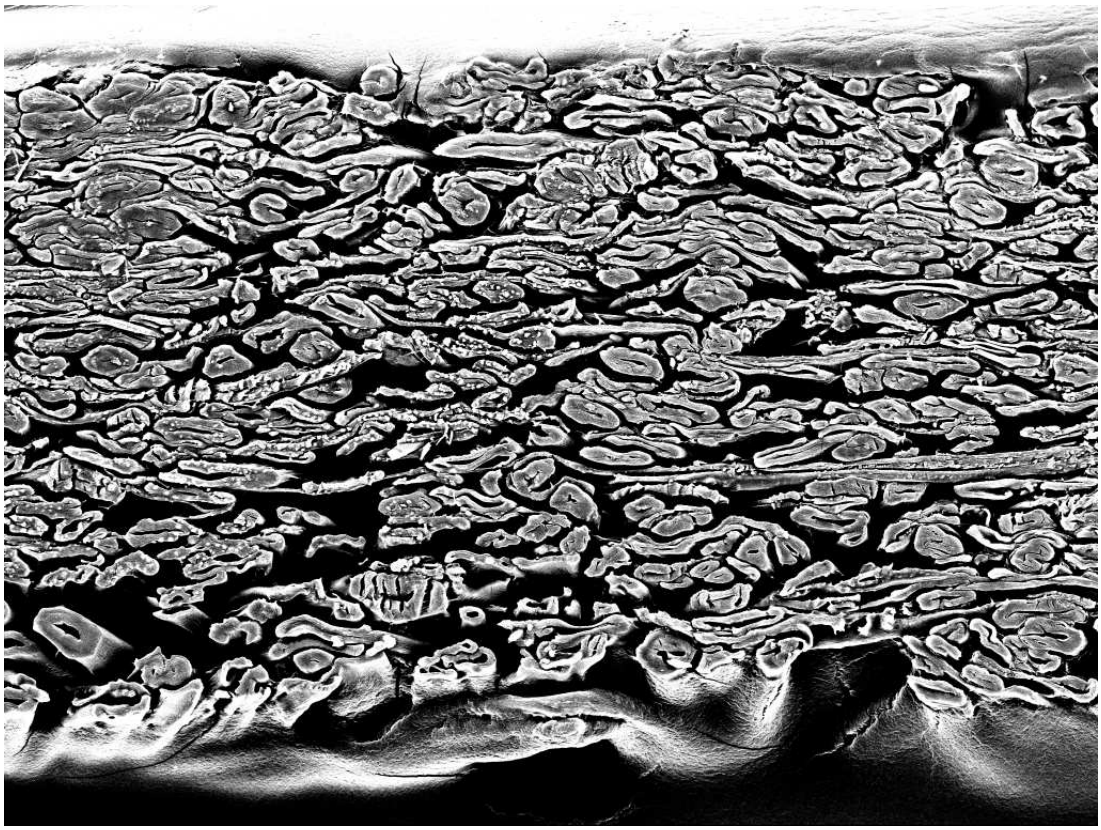

Image of the edge of Kraft underlay paper used in low and high pressure laminates.

3.1 Introduction

In Chapter 1 it was proposed that excessive consumption of MF resin during the process of manufacturing laminated paper overlays, and defects in the overlay were caused by inadequate filling of paper voids with UF resin (hereafter referred to as saturation) during the first stage of the treatment process. After the impregnation of paper with UF resin, MF resin is applied to the upper surface of the saturated paper. The MF resin is formulated to flow during pressing in order to achieve the desired finish as determined by the pattern on the particular caul plate in use before final cure (Pizzi, 1983a,b). Therefore any flow of MF resin away from the surface of the paper could result in the presence of uncoated areas or voids on the surface of papers.

The degree to which this occurs during the manufacture of paper overlays is not known. Assuming some migration of MF resin into paper, differences in the surface quality of paper overlays should reflect levels of saturation of papers by UF resin during the first stage of the treatment process. This would also mean that paper types which are more completely saturated with UF resin should have fewer open pores in the surface caused by the migration of MF resin into the core of the paper.

It is therefore hypothesised that if pores in paper are not completely filled with UF resin, then during hot pressing, the MF resin applied to the surface will flow into unfilled sub-surface pore spaces before curing has been completed, creating unfilled surface voids. It is further hypothesised that different papers will saturate to varying degrees reflecting differences in their structure, and develop different levels of surface defects. The aims of this Chapter are to test these hypotheses by determining the extent to which the level of treatment of decor papers with UF resin and paper type influences the surface quality and distribution of the MF coating on laminated pressed paper overlays.

3.2 Materials and Methods

3.2.1 Justification of techniques used

Quantification of the levels of surface defects in paper overlays was achieved using SEM. It was also possible using SEM to obtain information on the degree to which the core of the paper samples was filled by UF resin. It was more difficult, however, to determine the extent to which MF resin migrated into the paper because both cured UF and MF resins are transparent and therefore could not be visualised using either SEM or optical microscopic techniques. Labeling of resins and their subsequent identification with EDXA analysis was one possible approach to the problem, however, there was the possibility that labeled compounds could migrate away from the base resin during pressing and curing (Schnieder, 1997a). Various other techniques have been used to determine the distribution of MF resins in various substrates. Rapp et al. (1999) used Electron Energy Loss Spectroscopy (EELs) to quantify the penetration

of a melamine resin into wood cell walls. Kohl et al. (1996) described the use of differential scanning calorimetry to characterise the curing of MF resin. Gindl et al. (2002) used UV-microscopy to investigate the diffusion of melamine urea formaldehyde (MUF) resin in wood cell walls. Jayme and Rohman (1965) used infra-red microscopy and base-line evaluation of subsequent spectra to quantify the level of amino-plastic polymers in paper. A similar technique is used in this thesis to evaluate Raman spectra.

Raman microscopy has been used to identify melamine distribution in UF/MF copolymers (Schnieder, 1997a). This is possible because Raman microscopy can identify characteristic peaks in MF resins thus distinguishing them from those present in the spectra of UF resins (Hill et al., 1984; Scheepers et al., 1993, 1995).[1]

3.2.2 Selection of paper samples

Nine different saturating kraft[2] decor papers were selected from over 100 different types of paper used for the commercial production of resin impregnated overlays (Table A.1). The nine papers (identified by colour) that were selected were representative of all the different types of papers currently being treated commercially in Australia. The papers varied in their ash content, density, thickness and whether they were calendered or not (Biermann, 1996; Lyne, 1976; Lepoutre, 1976), (Table A.2). They also varied in their ease of treatment in terms of resin demand and percentage of rejects ex treater and subsequent defects after short cycle pressing (laminating). During experimentation it was crucial that all samples were correctly identified by paper type and batch as it was difficult to re-identify samples. Samples for each type were obtained from two different batches of paper, and if this was not possible, they were obtained from different paper rolls. Samples were also randomly chosen from within batches or rolls of paper. Figures 3.18, 3.19 & 3.20 show SEM images of the wetting (rough) side of all of the untreated decor papers used in experimental work in this thesis.

Figures 3.18, 3.19 & 3.20 show that all of the papers with the exception of Kraft (which is an unfilled paper) have particles of filler that impart the necessary opacity and colour to the papers. The SEM images were all taken at the same scale so it can be seen that some of the papers for example Black, Storm and Streetlight have very large open pores on the surface; compared to the very tight surface structures of Alpine White and Beech. The impact of filler on liquid uptake of the decor papers is examined further in Chapter 8.

3.2.3 Resins

In order to minimise experimental error caused by variation in the physical or chemical characteristics of resins, the same batches of UF and MF resins were used throughout the experiment.

[1] A very good description of the principles behind Raman microscopy is given by Fredericks (1996).

[2] Type of pulping process involving the use of sodium sulphate invented by Dahl in 1879 (Biermann, 1996).

Fresh resin mixes were used to treat all samples in order to eliminate any possible effects arising from ageing of the resin (Tables 3.1 & 3.2).

***Table 3.1**: Composition of the UF resin used to treat papers.*

Components of saturating resin mix	**Weight**
Borden BR110 UF resin	207g
Fentak CT12 UF catalyst (Ammonium chloride)	0.64g
Fentak F25T wetting agent (non ionic surfactants)	1.0g
Water	31.0g

***Table 3.2**: Composition of the MF resin used to treat papers.*

Components of coating resin mix	**Weight**
Borden BD829 MF resin	230g
Fentak CT218 MF catalyst (Morphylene paratoluene sulphonic acid	0.70g
Fentak F306 release agent	1.20g
Water	5.0g

3.2.4 Treatments

Paper samples measuring 300 x 300 mm square were randomly selected from each replicate with the first replicate being treated before samples from the second replicate were selected and treated.

The selected sample was placed on a clean glossy surface[3] with the decorative (smooth) side of the paper facing down. The sample was divided into three equally-sized sections; the first section was not treated with any UF resin. The second section was only given two brush coats of UF resin, approximately 25 g/m^2. The third section was brush coated with UF resin until it was completely saturated, *i.e.* when there were no visible dry spots in the paper, approximately 50 g/m^2. The paper was then turned over so that the decorative side faced up and the treatments were repeated. The sheet of Aqua Panel was cleaned and dried between each treatment.

The UF treated paper was then hung vertically in an oven (Thermoline Laboratory Oven model 060FD) at 125°C for 85 s. The paper was placed on a sheet of release paper to cool and given one brush coat of MF approximately 40 g/m^2 resin taking care to apply the same quantity of resin by using the same number of brush strokes to all of the different sections. The

[3]Laminex Aqua Panel (a high pressure laminate)

MF resin was first applied to the sections that did not contain UF resin to reduce the chance of any cross-contamination of paper with UF resin. This was, however, considered unlikely because the UF resin was fully cured before the MF resin was applied to paper sections. All hand treating was done along the machine direction of the paper. The fully treated paper was then placed in an oven (as above) and dried for 85 s. Each of the treatments was identified prior to resin saturating and coating by numbering each section with pencil.

All of the treated paper samples were then pressed on 3 mm thick MDF in a Siempelkamp test press at a temperature of 182°C for 45 s. The system hydraulic pressure used during pressing was 100 bar and given that the area of the board being pressed was 0.5 x 0.5 m the specific pressure was 0.03N m^{-2}.

The pressed samples were then prepared for surface and edge imaging by SEM, and for analysis of the distribution of MF resin in the paper by Raman microscopy.

3.2.5 Sample preparation for SEM; treated and pressed paper

A 10 mm strip was cut from each pressed sample using an 8 mm band-saw. The underside of each strip was then sanded using a 150 mm belt sander to remove as much of the underlying MDF as possible. The purpose of this was to reduce the time taken to achieve vacuum when the samples were subjected to sputter coating $(1x10^{-4}Torr)$ and SEM analysis $(1x10^{-5}Torr)$.

Individual samples measuring 10 x 10 mm were cut at random from within each of the treatment areas using hand-held, hard-backed, single-edged razor blades (GEM Stainless Steel uncoated single edge industrial blades). Samples were fixed to 12 mm diameter aluminium SEM stubs using double-sided carbon tape. All samples were individually identified with sample numbers ranging from 1 to 54, each of which represented a unique batch, paper type and resin treatment.

As pressed treated paper is a poor conductor of electricity, the specimens were rendered fully conductive by coating them with a 250 Å film of gold in order to prevent "charging" distortions of SEM images (Smith, 1959; Buchanan and Lindsay, 1962). The gold coating not only provided a conduction path to earth for beam electrons but also had the effect of improving secondary electron emission (hence improving the signal-to-noise ratio) (Heady, 1997). Gold coating was carried out in an argon gas sputter coating unit (Polaron Model E5000) (Figure 3.1) using 20 mA ion current for approximately 240 s. Electrical contact between stub and specimen was enhanced by brushing silver conducting paint (Balzers 8010 14020) around the edge of each specimen taking care not to affect specimen surfaces of interest.

3.2.6 Sample preparation for Raman microscopy

Samples measuring 10 x 5 mm were cut from the same pressed resin impregnated paper samples used for SEM examination. Preparation of samples for Raman microscopy was the same

***Figure 3.1**: Polaron Model E5000 sputter coater*

as for SEM except that the gold coating step was omitted. Glass knives made with a LKB model 7800 knifemaker (Figure 3.2) and attached to a Reichert-Jung Ultracut microtome (Figure 3.3) were used to prepare the edges of specimens. This minimised damage to the paper structure which was particularly important for samples containing little or no UF resin. 1.0 μm thick sections were microtomed from the edges of specimens until a section at least 3 mm in length had been produced. Prepared samples were attached to glass slides using *Bluetac* which was left for about 5 minutes to reduce the chance of elastic movement of the material before samples were examined under the Raman microscope. It was important to avoid touching prepared edges of samples as contamination from skin oils could have caused considerable fluorescence during imaging. After the samples had been examined with the Raman microscope they were fixed to SEM stubs and sputter coated with gold for edge imaging with SEM.

3.2.7 SEM imaging and data acquisition

The surfaces and edges of pressed, treated paper samples were examined using a Cambridge Instruments S360 Stereoscan scanning electron microscope fitted with a high brightness lanthanum hexaboride (LaB_6) electron source (Figures 3.4 & 3.5). Secondary electron and backscattered electron images were obtained (Figure 3.21).[4] The latter had the most contrast between the resin-filled and unfilled pores and hence was used for subsequent image analysis. A fila-

[4]Heady (1997) described in detail the use of the SEM used in this thesis.

***Figure 3.2**: LKB model 7800 knifemaker*

***Figure 3.3**: Reichert-Jung Ultracut microtome*

ment current of 1.9 A, a probe current of 1.21 nA and an electron accelerating voltage (EHT) of 20kV was used during imaging. All samples were viewed at magnifications of x100 for data analysis and x400 for detailed study of pore morphology. The contrast and brightness of individual images were adjusted to maximize the contrast between the unfilled pores and other areas within each image. Images were digitally recorded using a slow-scan (160 s) image acquisition system and converted to a 1024 x 768 pixel 8-bit grey scale image (PC TIFF Tagged Imaged File Format). These were then stored digitally using a PC[5] for later analysis.

One field of view was examined for each of the 54 different resin-treated and pressed samples consisting of 9 paper types, 3 resin treatments with 2 replicates. Each field of view measured 1.210 mm, x 0.905 mm. Kallmes and Corte (1960) used 1 mm paper squares during their examination of the structure of paper because the sample was of the same order of magnitude as the basic structural unit of paper, the fibre. Thus a 1 mm field of view was considered appropriate here to characterise the different treatment/paper combinations. A total of over 5,000 individual unfilled pores or voids in the surface of MF resin coated samples were analysed. The sizes of unfilled pores were quantified using Scion Image[6]. Variables measured were length, width and area of the individual unfilled pores, total unfilled pore area and number, and the ratio of the long and the short axes of the unfilled pores. The depth of the unfilled pores could not be accurately determined using SEM.

Imaging of the edges of resin impregnated paper samples was done at magnifications of 300 - 600 x depending on the thickness of the paper (Table 3.3). For edge imaging, two fields of view were selected at random for each paper/treatment combination because of the smaller fields of view compared to surface images. Figure 3.23 shows a good example of an edge image of paper with no UF treatment. Edge imaging of unfilled pores in backscattered mode did not require manual manipulation of the images within the image analysis program, providing the image had good contrast. The total area of unfilled pores to the total area of the field of view was measured for each paper type/treatment combination using the density slice function of Scion Image.

[5] ImageSlave version 2.11 1995, Meeco Holdings Pty. Ltd., Sydney

[6] An image processing and analysis program for PC's release Beta 3B, US National Institutes of Health, Scion Corporation Maryland USA 1998

***Figure 3.4**: Cambridge Instruments S360 Stereoscan scanning electron microscope*

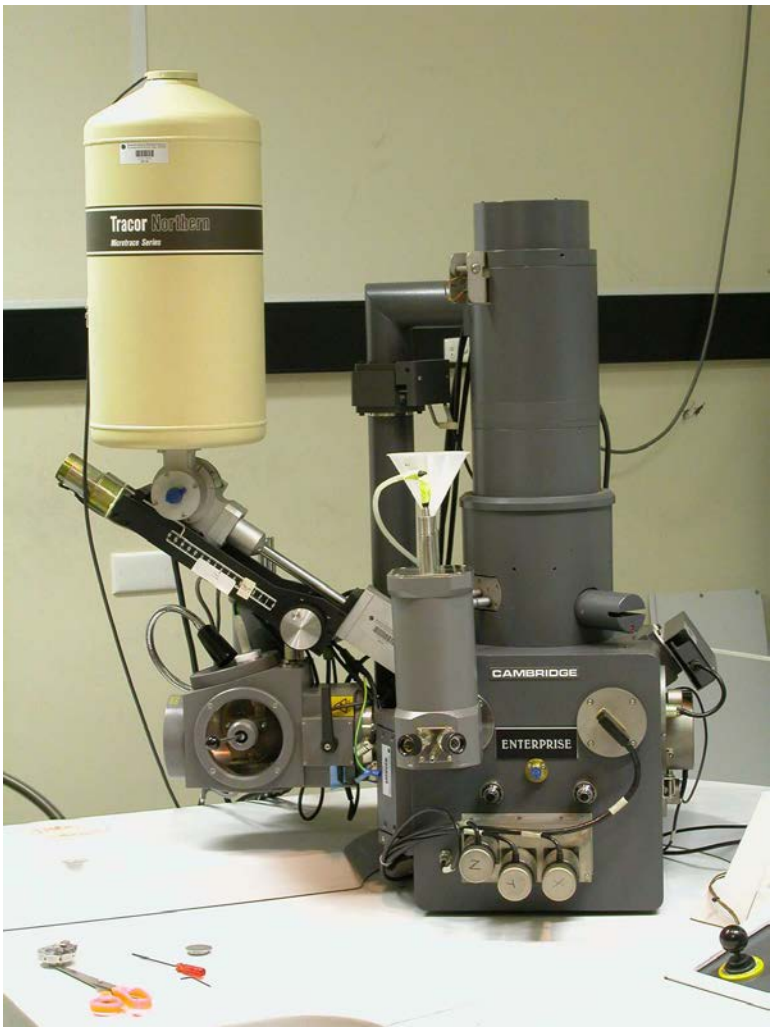

***Figure 3.5**: Closeup of the specimen chamber in the Cambridge S360 SEM*

***Table 3.3**: SEM magnifications for edge imaging of papers*

Paper type	SEM magnification
Alpine White	600
Beech	600
Black	600
Fog	600
Folkstone Grey	600
Kraft	300
New England Elm	450
Storm	500
Streetlight	400

3.2.8 Experimental design and statistical analysis of data

The aims of this Chapter are to determine the extent to which the level of treatment of decor papers with UF resin and paper type influences the surface quality and distribution of the MF coating on laminated pressed paper overlays. The effect of such fixed factors on the following response variables was examined;

1. number and proportion of unfilled pores
2. their dimensions including average, total area and variance of area, length of the major axis and ratio of major/minor axis
3. The relative intensity of the melamine peak at 975 cm^{-1} to the two titanium dioxide peaks at 448 and 610 cm^{-1}, giving the ratio of melamine to TiO_2.

The design of the experiment involved factorial principles. Random effects included roll to roll variation in paper and within paper variability and it was necessary to know whether the selection of the sample area using SEM or Raman had any effect on the results. Analysis of variance (ANOVA) for a randomised block design was used to analyse data. Some data were transformed into natural logarithms to ensure that it complied with the assumptions of ANOVA, *i.e.* normality with constant variance. Statistical computation was carried out using Genstat (Lawes Agricultural Trust). The factorial design of the experiment allowed data to be averaged across non-significant $(p > 0.05)$ effects thereby giving the experiment greater precision. Significant results are presented graphically and individual means can be compared using least significant differences $(p < 0.05)$.

3.2.9 Raman microscopy and data acquisition

3.2.9.1 Introduction

Raman microscopy has been used to study the curing of UF resin by Hill et al. (1984) who identified several spectral regions for distinguishing critical structural differences in cured and uncured UF resins (Tables A.3 & A.5). These peaks are used to identify UF resins in this Chapter.

Scheepers et al. (1993) characterized the curing of MF resins using Fourier transform (FT) Raman spectroscopy. They confirmed that MF resin formation consisted of two stages. During the first stage water insoluble melamine dissolves in formalin under alkaline conditions undergoing a series of addition reactions (Pizzi, 1983a) to create various methylolmelamines. Condensation reactions then take place to create a low molecular weight resin. At this stage, the resin is both soluble and fusible. During the second stage, the resin cures with the application of heat or an acid catalyst. During curing, further chain extension and cross-linking takes place to form an insoluble, infusible three-dimensional network. Scheepers et al. (1993) were the first to assign bands and interpret Raman spectra of MF resins and their changes during cure. All spectra of melamine-containing compounds showed an intense band at 975 cm^{-1} which was attributed to the ring breathing vibration of the triazine ring. They also found that the band at 975 cm^{-1} was not influenced by degree of methylolation. Hence it can be used to identify and examine the distribution of MF resin in impregnated and pressed decor papers. Scheepers et al. (1993) found that "MF resins have significant absorptions in the Raman range, but the absorbtions at a specific wavelength are the same for various samples. Therefore, relative band areas are not affected in a different way to the MF resins studied." Scheepers et al. (1993) claim to be the first to identify this peak, however, their claim can be challenged as Dollish et al. (1973) identified 8 frequencies for s-triazine (1,3,5-triazine) and assigned the frequency 676 cm^{-1} to "in-plane ring deformation", and ring "breathing" at 1132 and 992 cm^{-1}. They also found ring "breathing" vibrations at 1000-980 cm^{-1} for various 2,4,6 s-triazines (Tables A.4 & A.6). It was these peaks that were used to determine the level of MF resin migration and to answer the questions posed by Schnieder (1997b).

Scheepers et al. (1995) also identified the 676 cm^{-1} raman spectral band in melamine resins. The authors suggested that "it might be possible to use the intensity of the 676 cm^{-1} band for determination of the free melamine content of MF resins." "The 676 cm^{-1} ring mode vanishes upon methylolation, whereas the 975 cm^{-1} band retains constant intensity" (during and after methylolation). Both bands were assigned to deformations of the triazine ring (Scheepers et al., 1995). The authors concluded that "Raman spectroscopy can be used to determine the free melamine content in MF resins. Consequently confocal Raman microspectroscopy is able to obtain spectral information on MF resin from a small volume element" (μm scale).

***Figure 3.6**: The Renishaw model 2000 Raman microscope*

3.2.9.2 Experimental

A Renishaw model 2000 Raman microscope[7] using a near infrared laser (780 nm at 6.8 mW at 100% power output) was used to assess the distribution of melamine through treated pressed paper. Scanning was done using a 50 x objective with a scanning time of 50 s and an accumulation of 5 full scans to obtain the final spectrum (Figure 3.6).

In order to compare the amount of MF resin in the paper sample by position, paper type and UF resin treatment, the ratio of melamine to titanium dioxide within each paper was determined. This was quantified by measuring the area under the melamine peak at 975 cm^{-1} and expressing this as a ratio of the area under the two TiO_2 peaks at 448 and 610 cm^{-1} (Otieno-Alego, 2000). A similar technique was used by Sun et al. (1997) to determine the lignin to cellulose ratio in pulp samples and predict pulp Kappa numbers. Peak areas here were obtained using Igor Pro.[8] The extents of the two TiO_2 peaks were from 395-490 cm^{-1} and 545-655 cm^{-1}, and for melamine from 950-1000 cm^{-1}. The baseline was interpolated between these points for all peaks. Initially peaks were analysed with and without baseline correction (Sun et al., 1997), however, subsequently base line correction was used to remove

[7] Renishaw Raman Imaging Microscope Windows - based Raman Environment Users Notes M-8012-1894 01 Issue 1.0 Renishaw plc New Mills, Wotton-Under-Edge Gloucestershire, GL12 8JR

[8] v. 3.1.4 (1988-1998) Wavemetrics Inc).

background fluorescence as it did not affect the melamine or TiO_2 profiles for the corrected Raman spectra.

Two papers were not analysed. These were Black, because it had no detectable TiO_2 peak, and Kraft, because all samples fluoresced strongly and hence it was impossible to identify any peaks. The fluorescence in Kraft originated from the lignin because the pulp used in this paper was unbleached.

The purpose of experimentation was to determine whether there was a difference in the distribution of MF resins in papers treated with different levels of UF resin. Raman spectra were all obtained in the same plane, on the surface, half way to the middle of the paper and in the middle of the paper. The location of the line of scanning was random and orthogonal to the surface of the paper. Some dyes in the printed papers fluoresced making acquisition of data more difficult even using neutral density filters which reduced the intensity of the laser by 25%. Fluorescence even occurred when the back (non printed) side of such papers were scanned, showing that some of the ink dyes (or their solvents) had penetrated a substantial distance from the surface of the papers. It was still possible, however, to quantify the relevant melamine and titanium peaks from poorer quality spectra. The spectroscopic data (in ASCII format) were analysed using the wave analysis program Igor.

To determine whether UF resin flowed during LPM pressing, potentially resulting in intermixing with the curing MF resin, discs of paper treated only with UF resin were removed from the sample sheets and pressed. The distance that the resin flowed out from the discs was measured.

3.2.10 SEM examination of edges of raw paper

Imaging of the edges of paper was undertaken to get an estimation of porosity (pore volume) and pore structure, which was then related to the saturation performance of the paper. It was essential that the preparation of the samples was done in such a way as to minimise distortion of fibres and pore spaces. The edge imaging of paper is experimentally challenging due to its delicate structure. The technique used here was based on one developed by Williams et al. (1994) who described it as a "technique enabling imaging of raw paper edges with a SEM while avoiding the effect of dislocation or damage of fibres during normal cutting and sample preparation process". This technique was further developed by Kibblewhite and Bailey (1988) who used a similar embedding technique with BEEM[9] capsules to study fibre cross-sections, and Williams and Drummond (2000) who developed a modified technique for viewing much larger or greater numbers of samples.

James et al. (1998) used SEM to study paper cross-sectional structure. They adopted the technique described by Kibblewhite and Brookes (1977) where samples were clamped in per-

[9]Registered trade mark

spex and cut at an angle of 45° with a razor blade resulting in significant fibre damage. Dickson (2000a,b) also used resin embedding to examine cross sections of paper, however, they did not erode the resin away, but abraded sections of the whole sample and imaged samples using confocal laser scanning microscopy (CLSM), which is the technique used in Chapter 6 of this thesis.

Samples (10 x 5 mm) of all of the different papers were randomly selected from large rolls of paper. They were placed into gelatine capsules which were filled with low viscosity embedding media, (C035 Spurr's Embedding Mixture) and warmed to room temperature. In order to maximise saturation with embedding media, samples were agitated for 24 h on a IKAO Schuttler MTS 4 agitator set at 100 rpm. They were then held at 4°C for 10 days and cured at 60°C for 12 h. After curing, the resinated paper blocks were trimmed with GEM razor blades to remove excess resin and then microtomed using a Reichert Ultra Cut microtome. One micron (1.0 μm) sections were cut from the blocks, trying to produce a very smooth surface on the paper sample. The blocks were then agitated in a 1:1 solution of saturated sodium hydroxide and 100% ethanol to erode the embedding resin from the pore spaces and improve the definition of the SEM images as recommended by Williams et al. (1994). The sodium hydroxide solution was replaced after each sample to minimise contamination of subsequent samples with dissolved embedding resin. In order to erode sufficient resin from the pore spaces and to minimise the re-deposition of the resin onto the fibres, the samples were immersed and agitated in the eroding solution for at least 5 minutes. The samples were secured with tweezers with the microtomed edge of the block orientated away from the point of the tweezers. The tweezers were clamped to the block using electrical tape so that the microtomed section of the sample was protected while allowing the eroding solution access to the rest of the sample.

After erosion of the embedding resin, the samples were washed in 100% ethanol and then examined under a Nikon SM2-2T stereo microscope at 30 x magnification to determine if sufficient embedding resin had been eroded away to enable effective imaging of the void spaces below the surface of the paper. If insufficient resin had been eroded away, the cut edges of the fibre would appear rounded and smooth and for such samples the erosion process was repeated. This was necessary for the high ash papers such as Alpine White, Beech, Folkstone Grey and Fog, as the filler material found on and between the fibres appeared to make it more difficult to remove the embedding resin. This observation was relevant to the results of imbibition studies into various fillers in Chapter 7.[10] After drying the eroded samples were mounted on SEM stubs, gold coated and examined using SEM as previously described.

[10]It is shown that imbibition occurred preferentially in paper with spherical type fillers due to higher capillary pressures in the narrow channel morphologies created by adjacent filler particles. It could be inferred that the removal of resins from such paper fillers would therefore be more difficult.

3.3 Results

3.3.1 Overall effects of treatment & paper type on surface quality of paper

The significant effects of level of resin treatment and paper type, and interactions between level of resin treatment and paper type on the surface characteristics of pressed LPM are summarised in Table 3.4. In addition a graphical summary is presented for each analysis (below) clearly showing each significant effect. Each graph shows mean values plus a LSD bar *($p < 0.05$)* that can be used to assess significant differences between means.

Table 3.4: *Significant effects of, and interactions between, saturation treatment and paper type on surface defects of treated pressed samples.*

Experimental factors	**Response variables**					
	Number of pores	Variance of areas of individual pores	Total area	Average area of unfilled pores	Length of the major axis	Ratio of major/minor axis
Treatment	***	*	***	***	***	***
Paper type	*	**	**	*	*	**
Interaction T x P	NS	NS	NS	***	*	NS

(* = $p < 0.05$, ** = $p < 0.01$, *** = $p < 0.001$, *NS = not significant* $p > 0.05$)

3.3.2 Treatment effects

3.3.2.1 Surface

There was a significant effect *($p < 0.001$)* of UF resin treatment on the number of unfilled pores in the different papers (Figure 3.7). With increased levels of UF saturation there were fewer unfilled pores on the surface of paper samples, irrespective of paper type (Figure 3.7). This effect is clearly shown in a series of SEM images (Figures 3.24, 3.25, 3.26 and 3.27), each of which show three images representing no UF, low UF and normal UF resin treatment levels, respectively. Figure 3.28 shows surface voids in paper at higher magnification. Also noticeable in Figure 3.28 are "caps" of MF resin that had formed as thin lenses over surface voids during treating and had become dislodged during the process of pressing. This is a common cause of dusting in both treating and pressing and is a phenomenon that has hitherto not been well understood. Such material forms a dust that is a sensitising irritant to humans. It was previously believed that this material arose from bubbles formed due to excessive heating during the curing of the resin in the second stage ovens in the treater.

There was also a significant effect *($p = 0.012$)* of treatment on variance of areas of individual pores. With increased levels of saturation the variance of pore size was smaller (Figure 3.8).

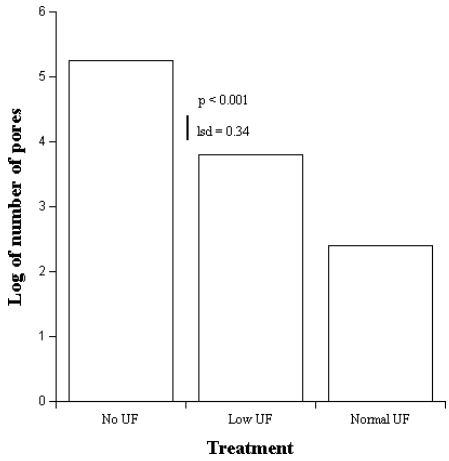

Figure 3.7: *The effect of UF saturation treatment on the total number of pores in paper samples. Error bar (LSD) represents the least significant difference ($p < 0.05$).*

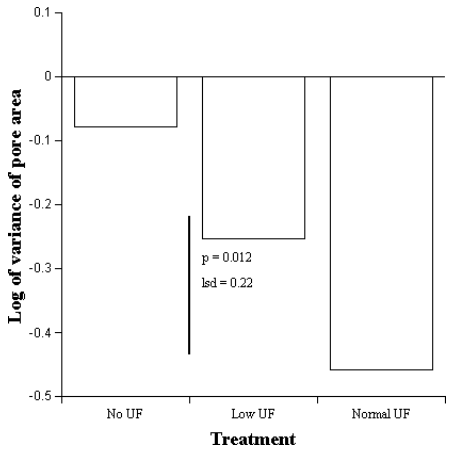

Figure 3.8*: Effect of UF saturation treatment on variance of areas of individual pores.*

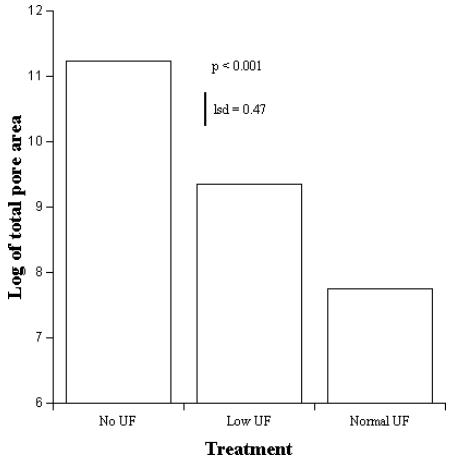

Figure 3.9*: Effect of level of UF saturation on total area of unfilled pores.*

There was a significant effect *($p < 0.001$)* of treatment on the log of the total area of unfilled pores (Figure 3.9). SEM images for Alpine White subjected to different levels of UF saturation (Figure 3.29) also suggest that with increased levels of saturation with UF resin the area of unfilled pores in papers became lower. The total area of unfilled pores is probably related to visual defects that can be observed in pressed low pressure melamine sheets, as unfilled pores on the surface would reduce the transparency of the melamine coating and also change it's light scattering characteristics. Thus the larger the area of unfilled pores in the coating the greater the probability that the panel would be rejected.

There was a significant effect *($p < 0.001$)* of treatment on the ratio of the major to the minor axis of pores (Figure 3.10). This was a measure of symmetry of unfilled voids *i.e.* the lower the ratio the greater the symmetry. This effect was also apparent in SEM images for Kraft paper samples subjected to different levels of UF treatment (Figure 3.30).

3.3.2.2 Subsurface

There was a significant effect *($p < 0.001$)* of UF resin treatment on the proportion of unfilled pores beneath the surface of the paper (Figure 3.11). It was clear that the greater the level of UF treatment the lower the amount of unfilled pores beneath the surface of the paper. For example, there was more than double the proportion of unfilled pores in paper that had received no UF treatment compared to normally treated paper. This is clearly shown in the SEM images of the edges of Streetlight pressed paper (Figure 3.38), which received no UF, low UF and normal UF saturation treatments, respectively.

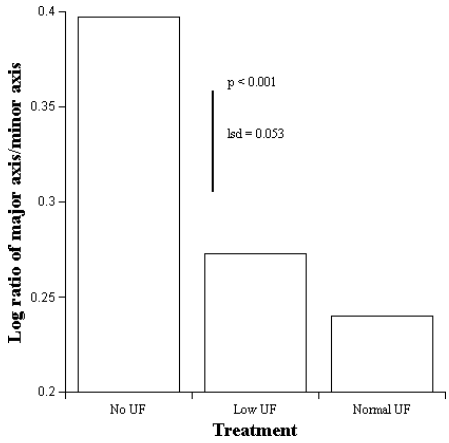

***Figure 3.10**: Effect of level of UF saturation on the ratio of the major to minor axis of unfilled pores.*

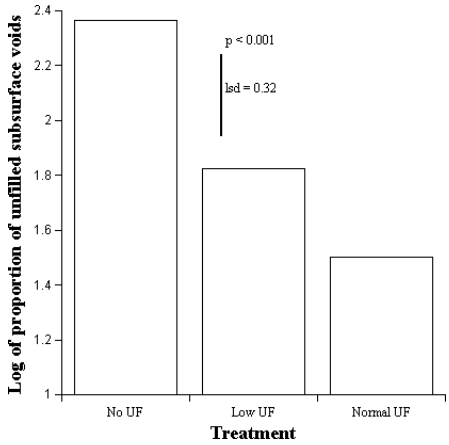

***Figure 3.11:** Effect of level of UF saturation on the ratio of the proportion of unfilled pores beneath the surface of paper in treated and pressed LPM.*

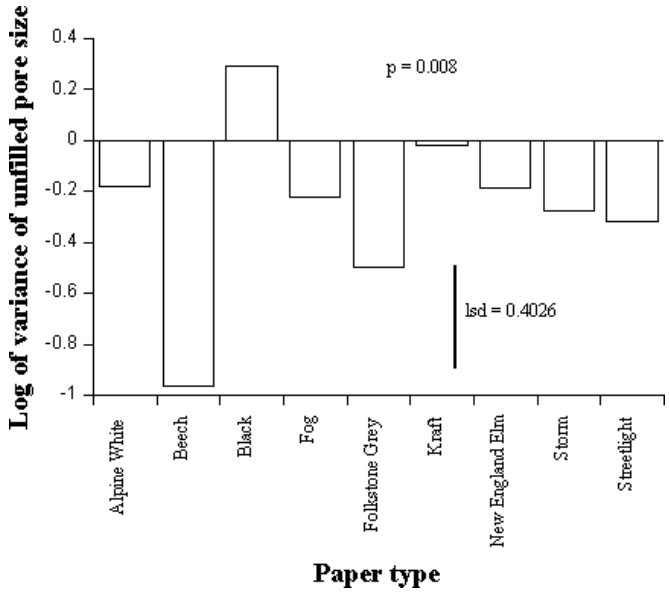

***Figure 3.12**: Effect of paper type on variance of areas of individual pores.*

3.3.3 Paper effects

3.3.3.1 Surface

There was a significant effect *(p = 0.008)* of paper type on the variance of area of unfilled pores (Figure 3.12), but no significant interaction of paper type and treatment on variance of unfilled pore area..

Irrespective of the levels of UF saturation, unfilled pore size was less variable in some papers than in others, for example Beech. Conversely unfilled pore size was more variable in Black than in all other paper types, except for Kraft (Figure 3.12). Black was the most difficult of all papers to treat and press and it was the paper that contained the lowest amount of inorganic filler. There was considerable variability in the data as is reflected by the large LSD bar, (Figure 3.12).

There was also a significant effect of paper type *(p = 0.014)* on the number of unfilled pores (Figure 3.13). Beech had significantly lower numbers of unfilled pores than all other papers except for Folkstone Grey which in turn had significantly lower numbers of unfilled pores than papers such as Fog, Kraft, New England Elm, Streetlight and Storm.

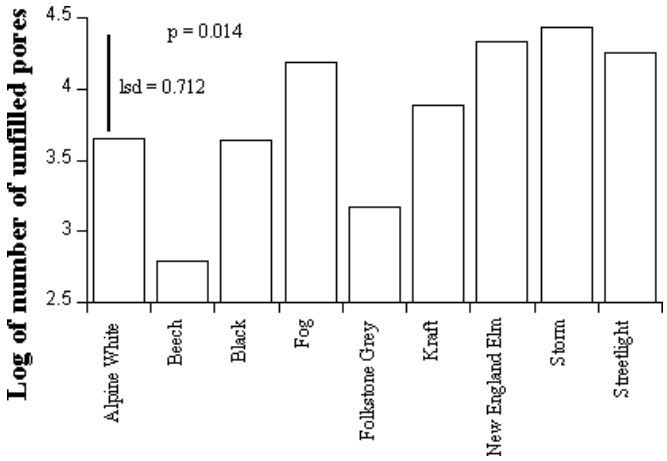

***Figure 3.13**: Effect of paper type on total numbers of unfilled pores.*

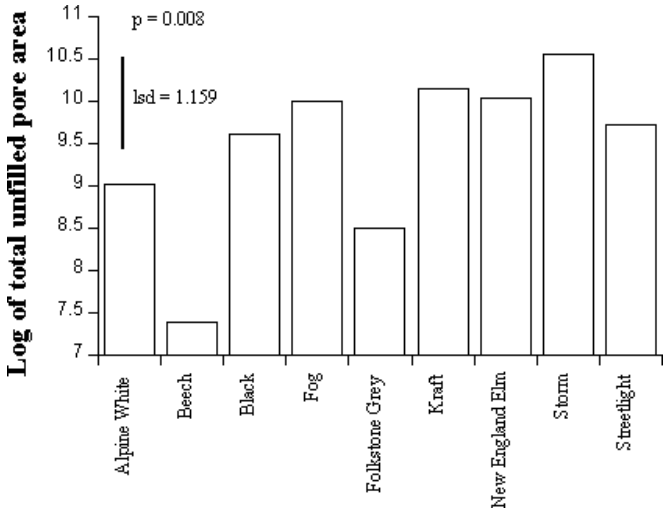

***Figure 3.14**: Effect of paper type on total area of unfilled pores.*

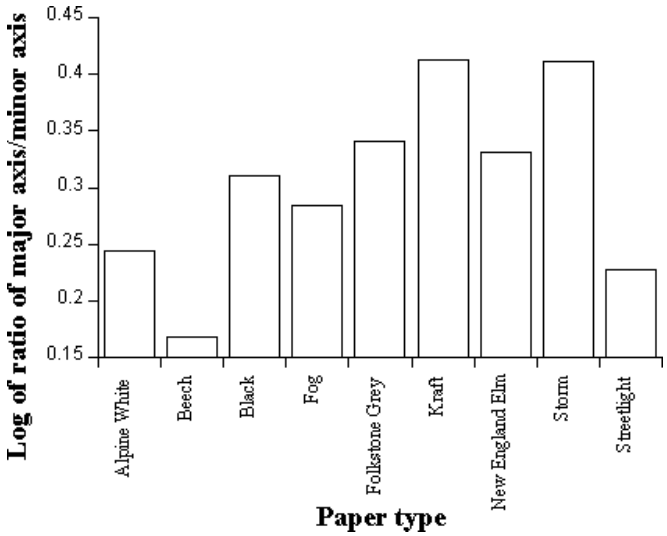

***Figure 3.15**: Effect of paper type on the ratio of the major to minor axis of unfilled pores.*

There was a significant effect *(p = 0.008)* of paper type on the log of the total area of unfilled pores. Beech and Folkstone Grey had significantly lower total areas of unfilled pores that the other papers (Figure 3.14).

There was also a significant effect *(p = 0.008)* of paper type on the ratio of the major to the minor axis of unfilled pores (Figure 3.15). Unfilled pores in Beech, Alpine White and Streetlight were significantly more symmetrical than pores in all other paper types. Unfilled pores in Kraft and Storm were significantly less symmetrical than pores in all other papers except for Folkstone Grey and New England Elm. From Table A.2 it appears that the symmetry of unfilled pores may be related to the ash content, *i.e.* amount of inorganic filler, of the different paper types. Those papers whose unfilled pores were more symmetrical tended to have more filler than those with less symmetrical unfilled pores (Table A.2). This suggestion is supported by the images of raw papers showing the shapes of unfilled pores in Beech (Figure 3.39) and Streetlight (Figure 3.40) compared to Black (Figure 3.41) and Kraft (Figure 3.42). These images also show the effect of the distribution of filler on pore symmetry of the larger open pores on the surface of paper.

There appeared to be a relationship between the depth of unfilled pores and the level of UF saturation. The number of un-resinated fibres visible in an unfilled pore was used as a qualitative indication of pore depth. For example, where four such fibres crossed in an unfilled pore, the depth of the unfilled pore was clearly greater than that of an unfilled pore containing only two un-resinated fibres. Increasing levels of UF saturation reduced the number of unfilled pores containing un-resinated fibres. This can be seen in the SEM images of Storm and Streetlight, (Figures 3.34, 3.35 & 3.36), which were not treated or had low levels of UF resin saturation. The images in Figure 3.28 are of Streetlight with a normal UF loading. There are large unfilled voids below the surface, which were covered by resin during treatment. However subsequently it appears that the resin covering the voids was dislodged. The bottom image also shows un-resinated fibres at a significant depth from the surface.

3.3.3.2 Subsurface

There was a weak effect *(p = 0.1)* of paper type on the total proportion of unfilled pores beneath the paper surface. Earlier it was hypothesised that with less than full saturation with UF resin, MF resin would migrate away from the paper surface filling the pores below the surface and creating voids in the resin coating on the surface. Raman microscopy, described below, confirmed this suggestion. However, Beech had the highest level of unfilled pores beneath the surface (Figure 3.37 almost twice the average number of unfilled pores) but had the lowest number of unfilled pores on the surface (Figures 3.13, 3.14 & 3.32). This was contrary to expectations in that there was less than complete saturation of this paper with UF resin but very effective surface coating with MF resin. This suggests that the UF resin formed

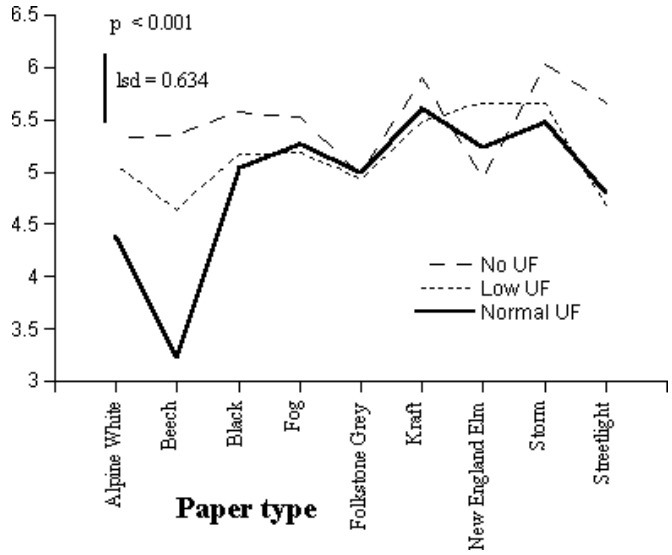

***Figure 3.16**: Effect of paper type and treatment on the average unfilled pore area after pressing.*

an impenetrable barrier just below the surface of the paper preventing MF resin from migrating away from the surface. The possible reasons for this are outlined in the Section 3.4.

3.3.4 Interactions of treatment & paper type on surface defects & subsurface pores

3.3.4.1 Surface defects

There was a significant two-way interaction *($p < 0.001$)* between paper type and treatment on average area of unfilled pores, where the effect of level of UF treatment on average area of unfilled pores varied with paper type (Figure 3.16). This occurred because the average area of unfilled surface pores in untreated New England Elm was significantly lower compared to the other papers receiving no UF resin treatment (Figure 3.22). It is possible that so much MF resin migrated from the surface of New England Elm that even the smallest pores were unfilled, thus reducing the average area of unfilled pores. One might have expected that with increasing levels of saturation the average area of unfilled pores would be reduced for each paper type, however, this was not always the case (Figure 3.16). In fact only Alpine White, Beech, and Streetlight showed a significant reduction in the average area of unfilled pores with increasing levels of UF treatment as illustrated in the images of treated Beech (Figure 3.32).

There was no significant interaction of treatment and paper type on the total area of unfilled pores. There was no significant difference in average pore size in Black, Fog, Folkstone Grey, Kraft and Storm with different levels of UF treatment.

In Folkstone Grey and Kraft there was no significant effect of UF treatment on average pore size. SEM images clearly show that in Kraft with no UF treatment there was a full range of

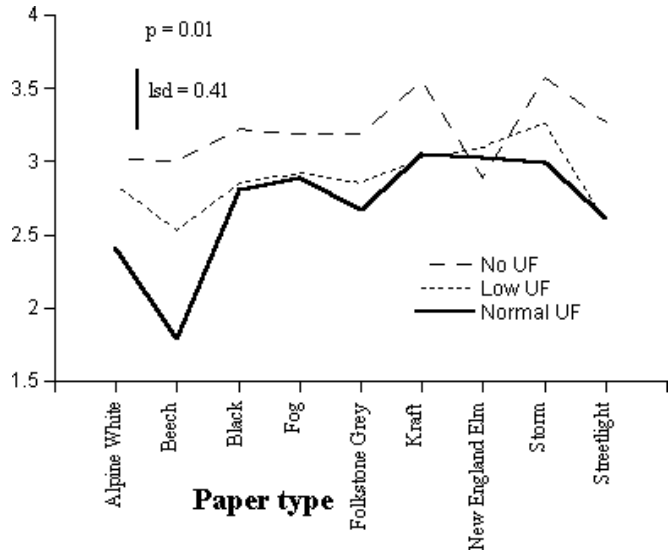

Figure 3.17: *Effect of paper type and treatment on the length of the major axis of unfilled voids after pressing.*

unfilled pores from ones which were very large (200 μm in the long direction) to ones less than 5 μm in length (Figure 3.30, top). In contrast in Folkstone Grey with no UF treatment (Figure 3.24, top) there appeared to be a much more even spread of average area of unfilled pores. Higher levels of saturation with UF resin resulted in less variation in pore size however, the average pore size was unaffected. This presumably occurred because fewer of the very large or very small unfilled pores were present compared to those in papers receiving low and higher levels of treatment. With papers such as Fog, the level of UF saturation did not significantly affect the average pore size, however the number of unfilled pores became smaller. This can be seen in the SEM images of Fog in Figure 3.33. Figure 3.16 shows that the areas of unfilled pores in Beech treated with normal UF saturation were significantly less than for all other paper types.

There was also a significant two-way interaction *($p = 0.01$)* between treatment and paper type on the length of the major axis of the unfilled pores (Figure 3.17). This was as a result of the response of New England Elm to resin treatment. In this paper the shortest pores were found in paper that had received no resin treatment whereas in the other papers the shortest pores were found in papers that had received low or normal UF treatment. The reason for this effect is explained more fully in Chapter 8 and is related to the type and distribution of filler used in the paper and resulting pore size distribution.

With Beech there was a significantly *($p = 0.01$)* greater reduction in the length of the major axis of the unfilled pores with each increasing level of UF saturation treatment. In the case of Black, Folkstone Grey, Kraft, Storm, and Streetlight there was also a significant difference in the length of the major axis of unfilled pores in samples subjected different UF saturation

levels. This is clearly shown in the SEM images of Storm, Figure 3.25. With Alpine White there was a significant difference in the length of the major axis of pores in samples subjected to low UF saturation and normal UF saturation. With New England Elm and Fog there was no significant effect of level of treatment on length of the major axis of the unfilled pores.

Figure 3.17 also shows that the unfilled pores of Beech were on average shorter than in all other paper types, and that with normal UF treatment the unfilled pores in Alpine White and Beech were significantly shorter than in all other paper types as seen in the first images in Figures 3.29 & 3.32.

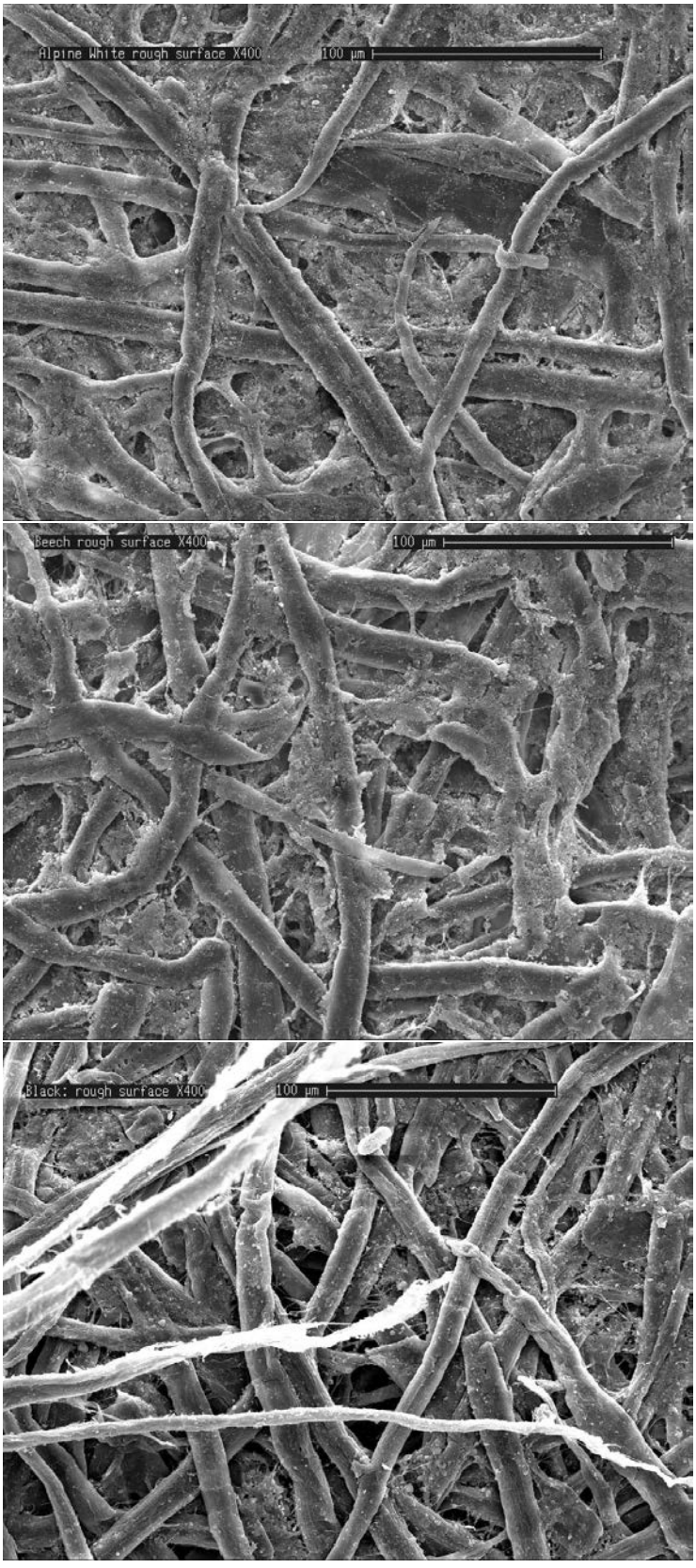

Figure 3.18: *SEM images of untreated decor papers, top: Alpine White, middle: Beech and bottom: Black.*

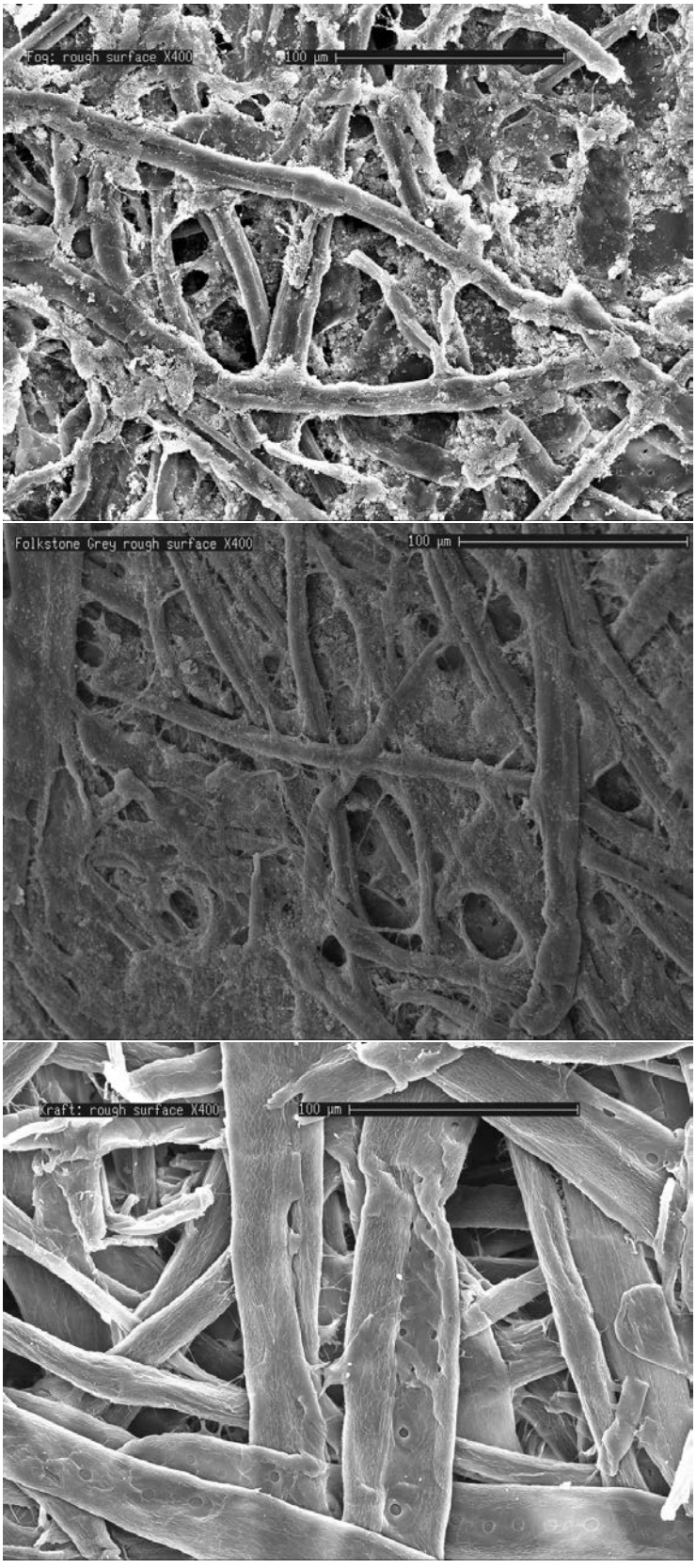

Figure 3.19: *SEM images of untreated decor papers, top: Fog, middle: Folkstone Grey and bottom: Kraft.*

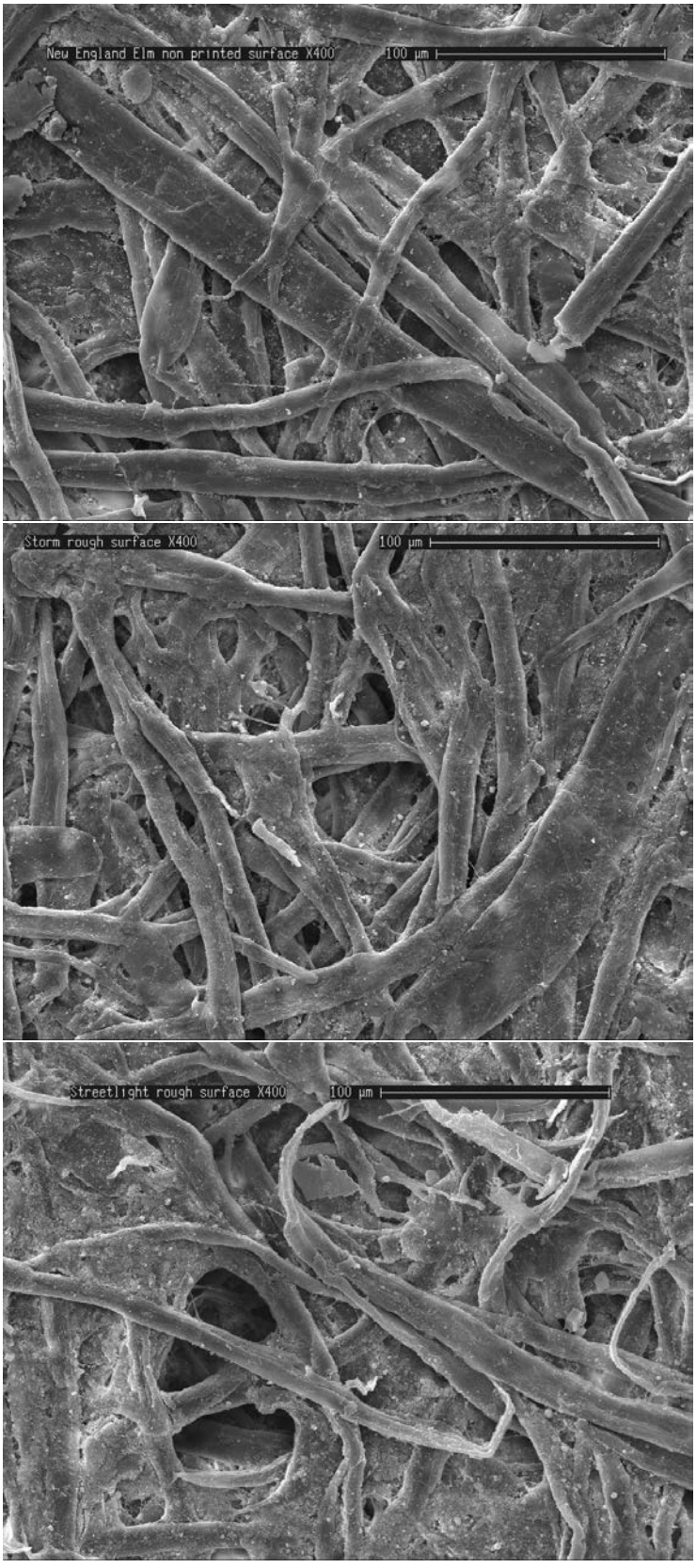

Figure 3.20: *SEM images of untreated decor papers, top: New England Elm, middle: Storm and bottom: Streetlight.*

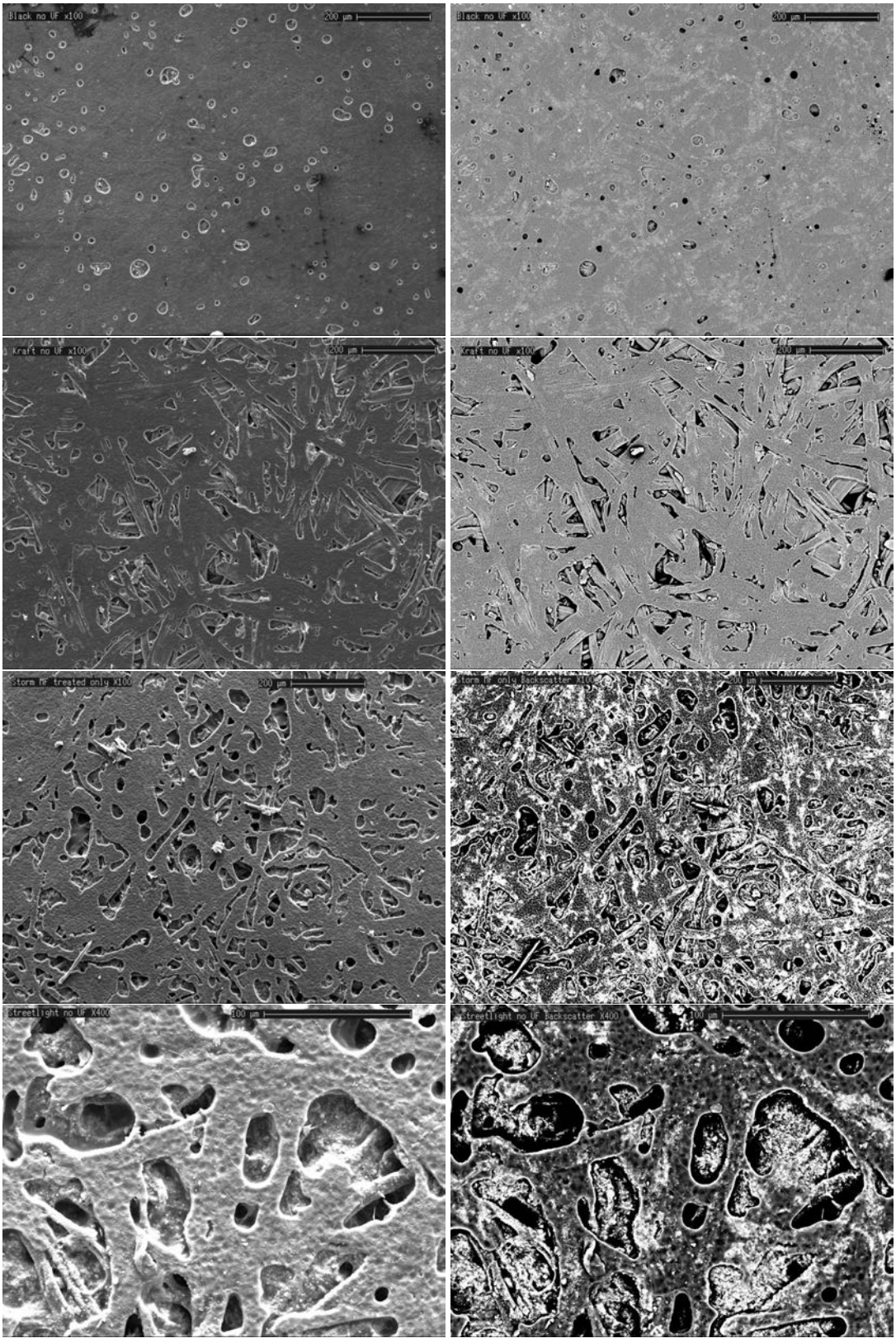

Figure 3.21: *Secondary electron (left) and backscattered (right) images of Black, Kraft, Storm and Streetlight with no UF resin treatment.*

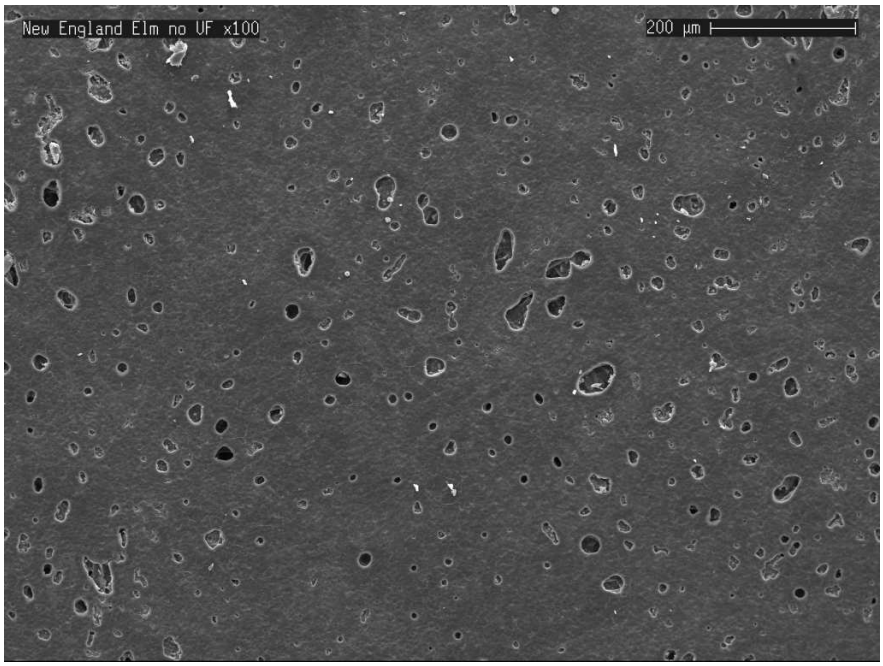

Figure 3.22: *SEM image of MF coating on New England Elm which was not subjected to preliminary UF treatment. Note the small size of the pores.*

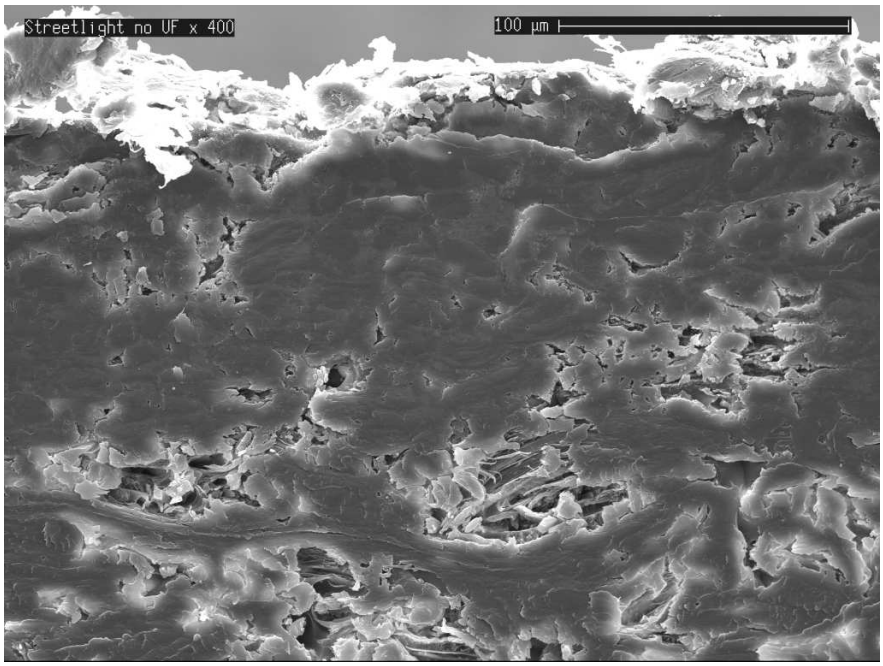

Figure 3.23: *SEM image of the edge of the treated decor paper Streetlight with no UF treatment showing large unfilled voids in the centre of the paper.*

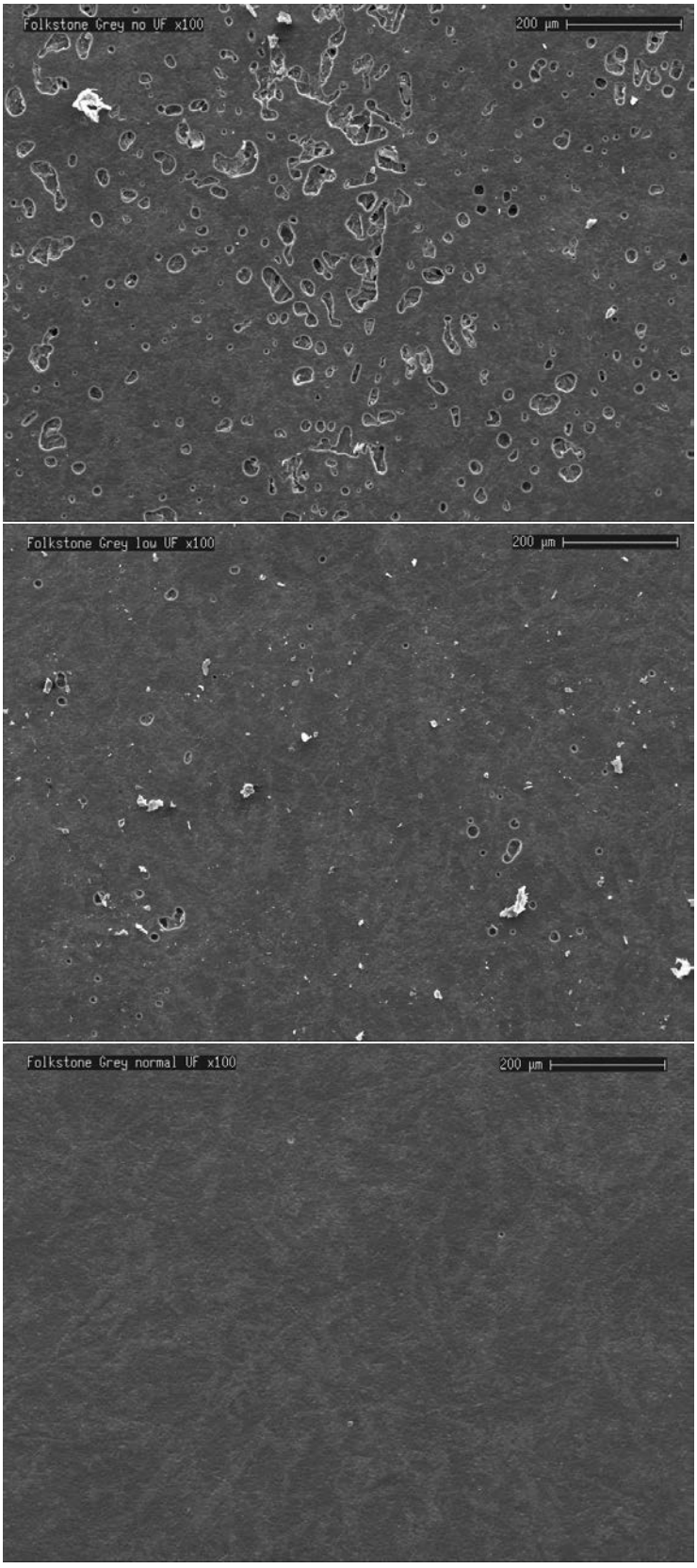

Figure 3.24: *SEM images of the MF coating on the surface of pressed Folkstone Grey showing the relationship between treatment level and numbers of unfilled pores, top to bottom; no UF resin, deliberately under resinated and normal resin treatments.*

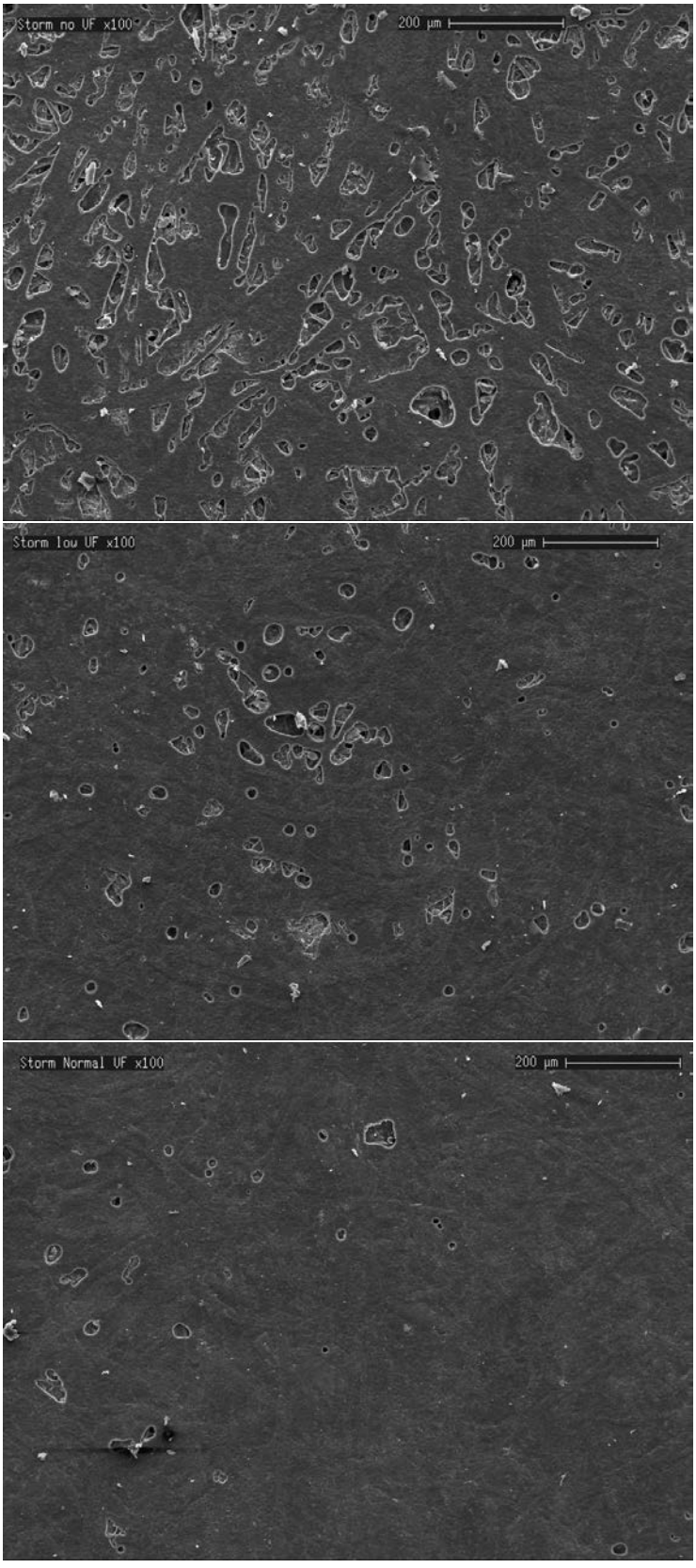

Figure 3.25: *SEM images of the MF coating on the surface of pressed Storm showing the relationship between treatment level and numbers of unfilled pores, top to bottom; no UF resin, deliberately under resinated and normal resin treatments.*

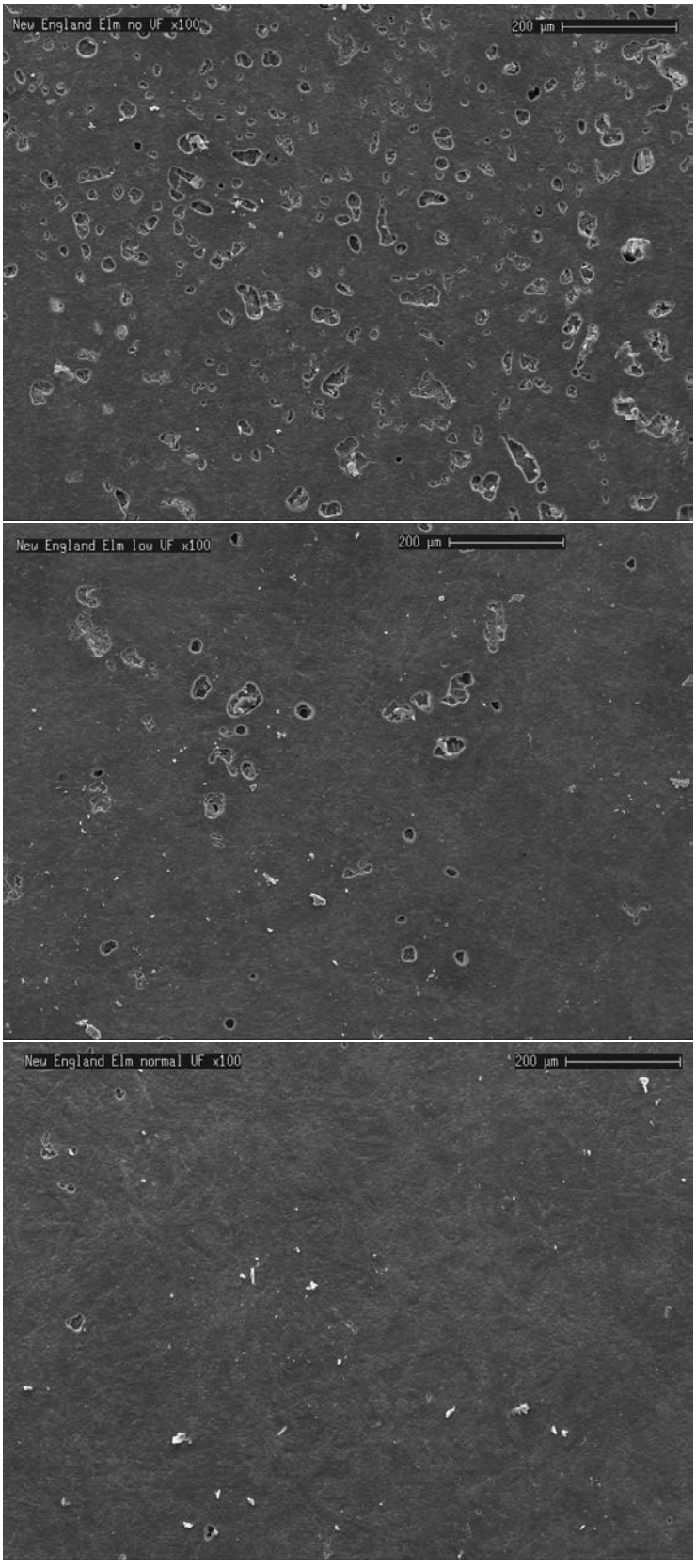

Figure 3.26: *SEM images of the MF coating on the surface of pressed New England Elm showing the relationship between treatment level and numbers of unfilled pores, top to bottom; no UF resin, deliberately under resinated and normal resin treatments.*

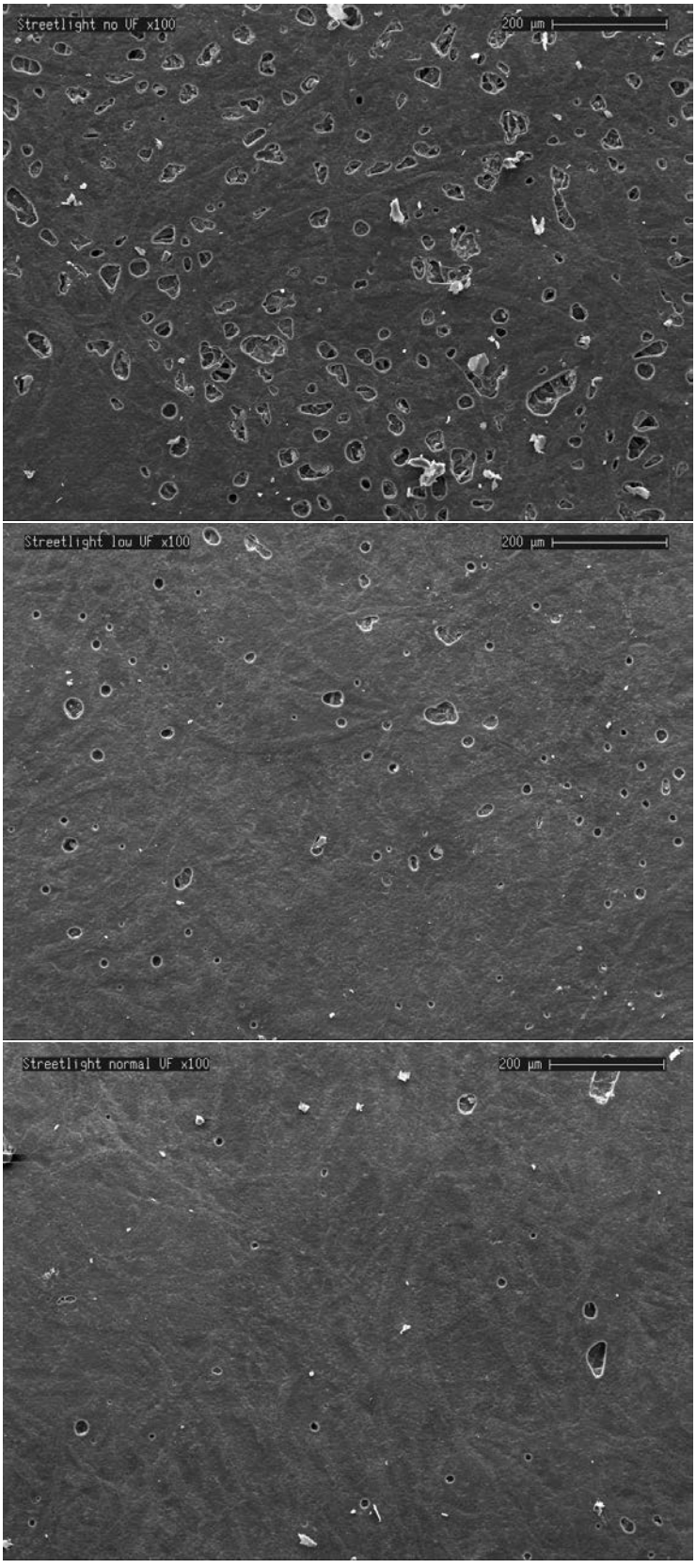

Figure 3.27: *SEM images of the MF coating on the surface of pressed Streetlight showing the relationship between treatment level and numbers of unfilled pores, top to bottom; no UF resin, deliberately under resinated and normal resin treatments.*

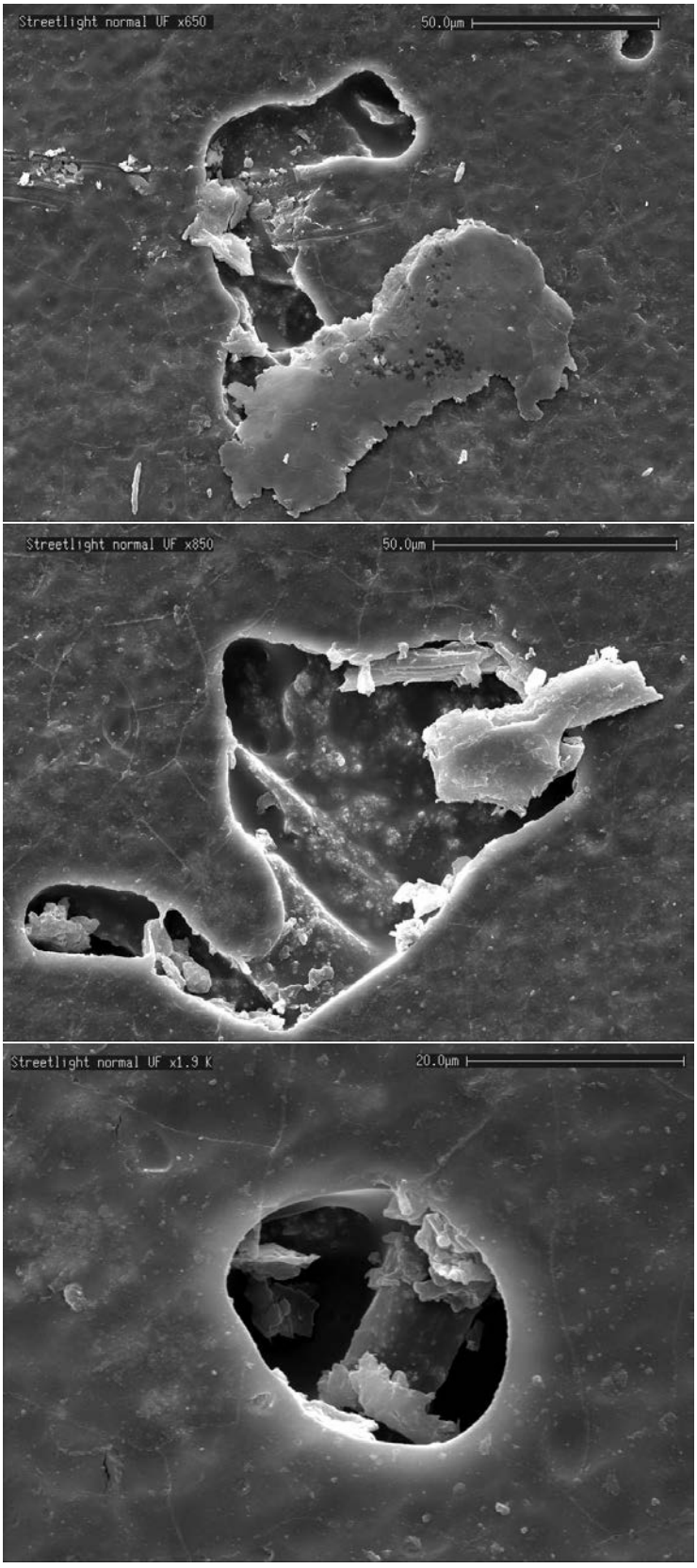

Figure 3.28: *Higher magnification SEM images of MF coating on Streetlight showing details of unfilled surface voids caused by migration of MF resin even though normally treated with UF resin. Note also the presence of MF "caps" dislodged from the unfilled surface voids during pressing.*

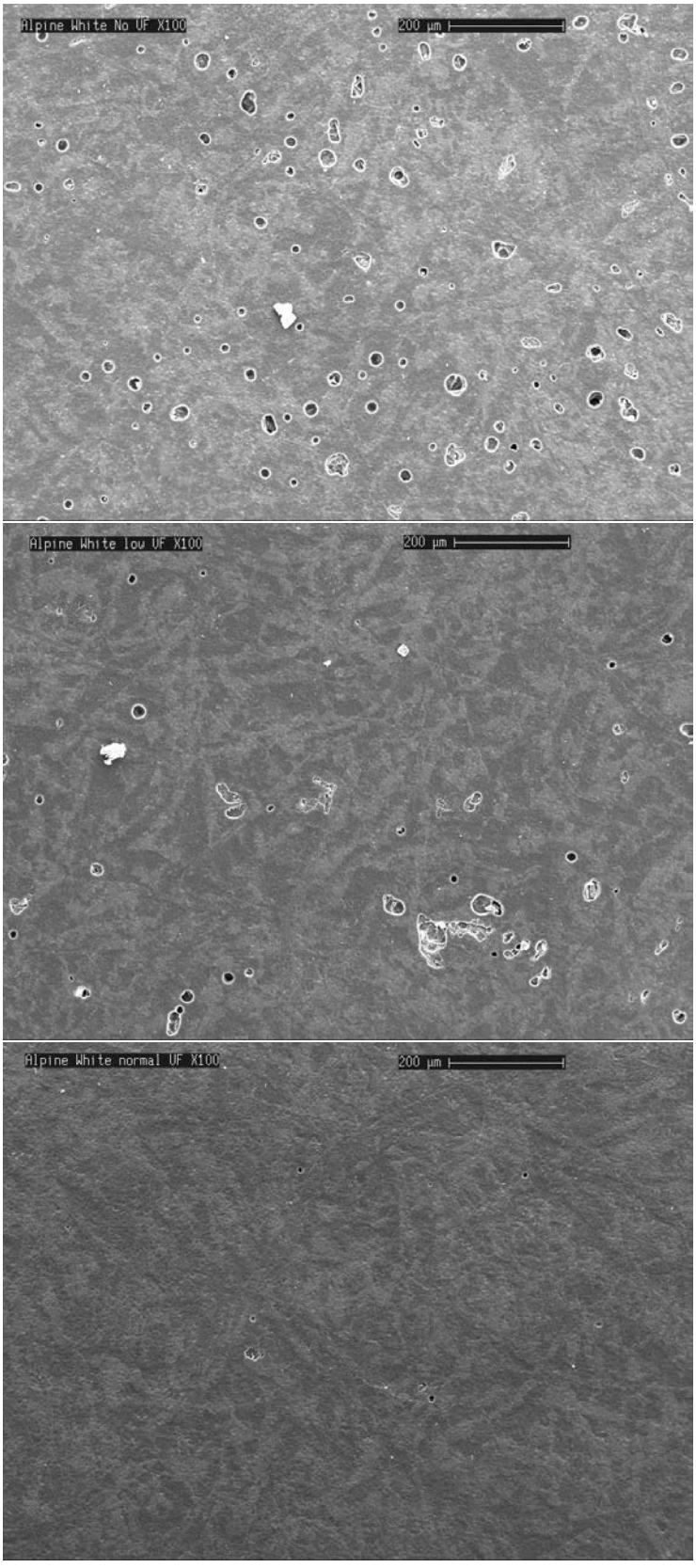

Figure 3.29: *SEM images of the MF coating on the surface of pressed Alpine White showing the relationship between treatment level and the number of unfilled voids on the surface, top to bottom; no UF resin, deliberately under resinated and normal resin treatments.*

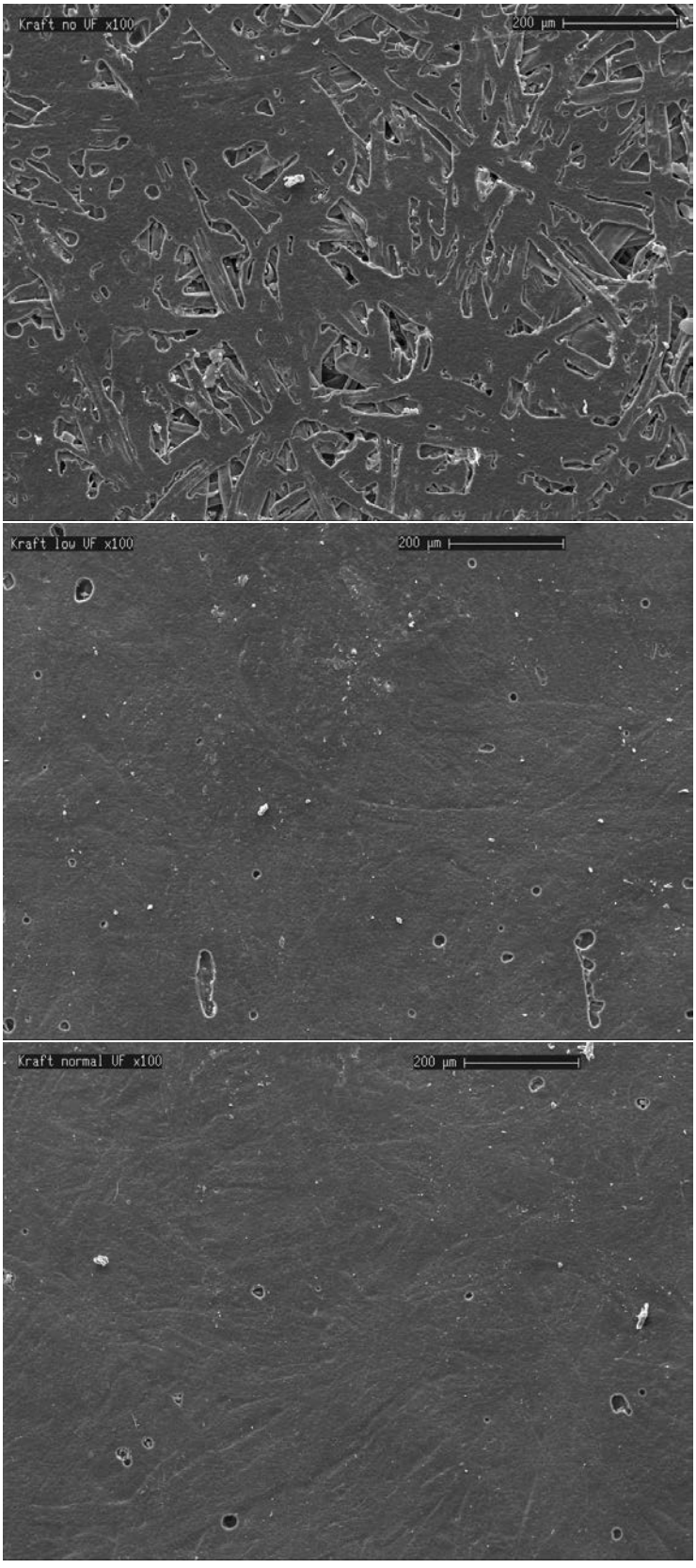

Figure 3.30: *SEM images of the MF coating on the surface of pressed Kraft showing the relationship between treatment level and the symmetry of unfilled voids on the surface, top to bottom; no UF resin, deliberately under resinated and normal resin treatments.*

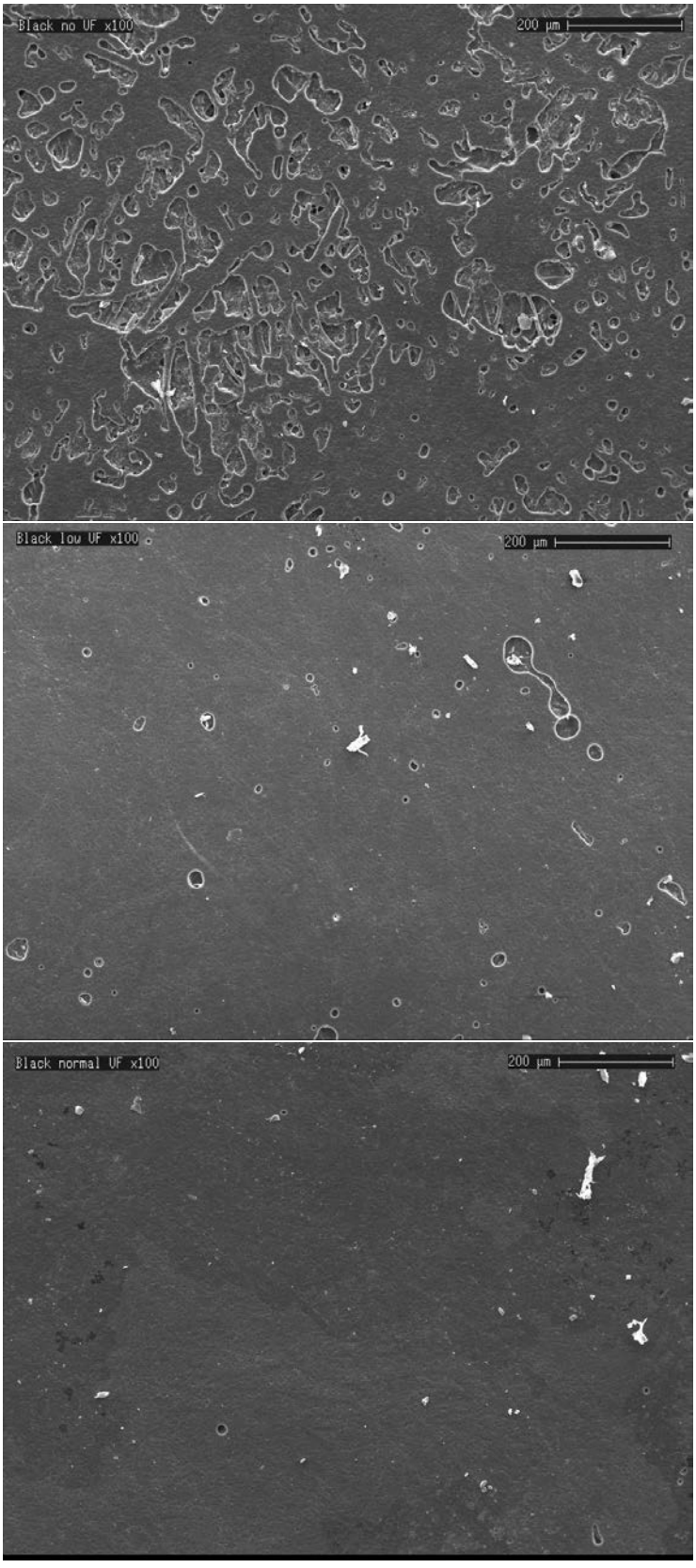

Figure 3.31: *SEM images of the MF coating on the surface of Black, from top to bottom; showing no, low and normal UF saturation respectively demonstrating the considerable variability in individual unfilled pore area.*

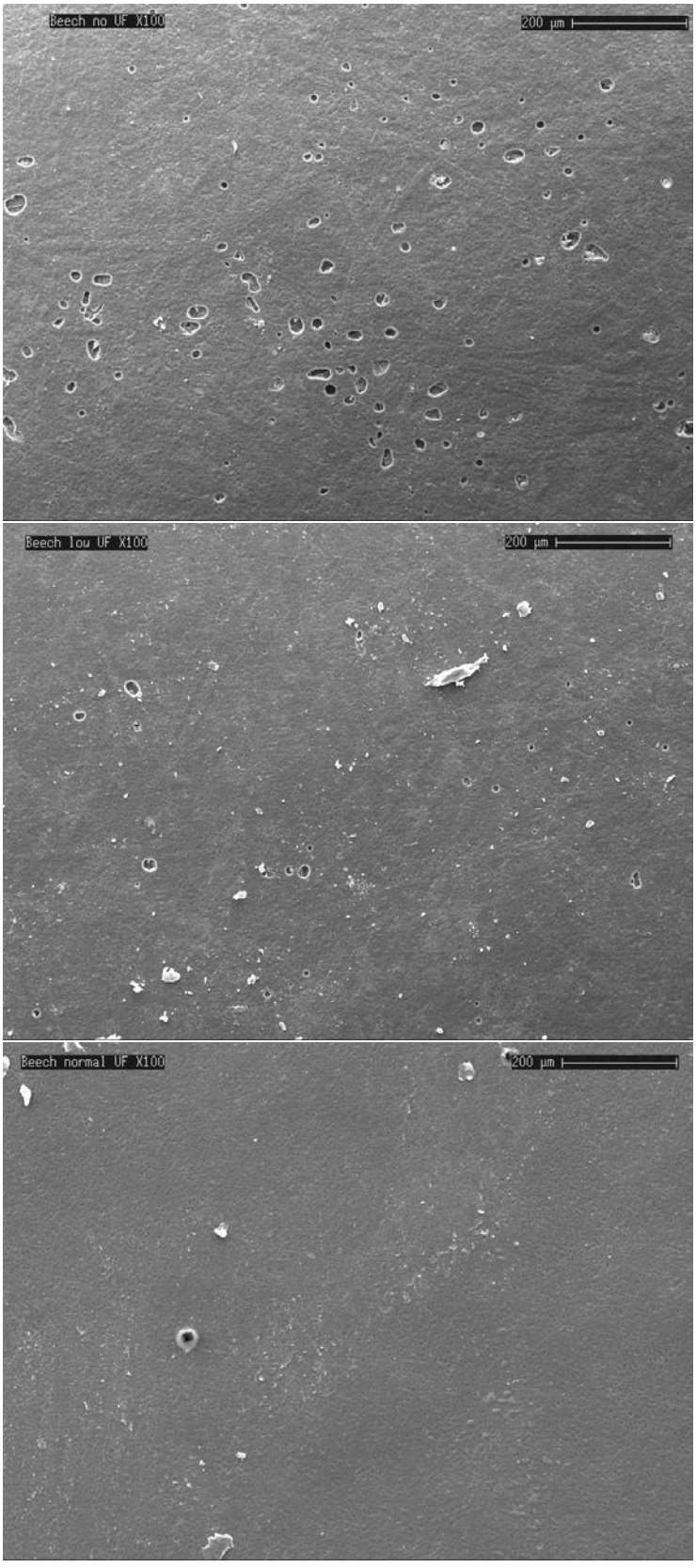

Figure 3.32: *SEM images of the MF coating on Beech showing a reduction in average unfilled pore area with no, low and normal UF saturation respectively.*

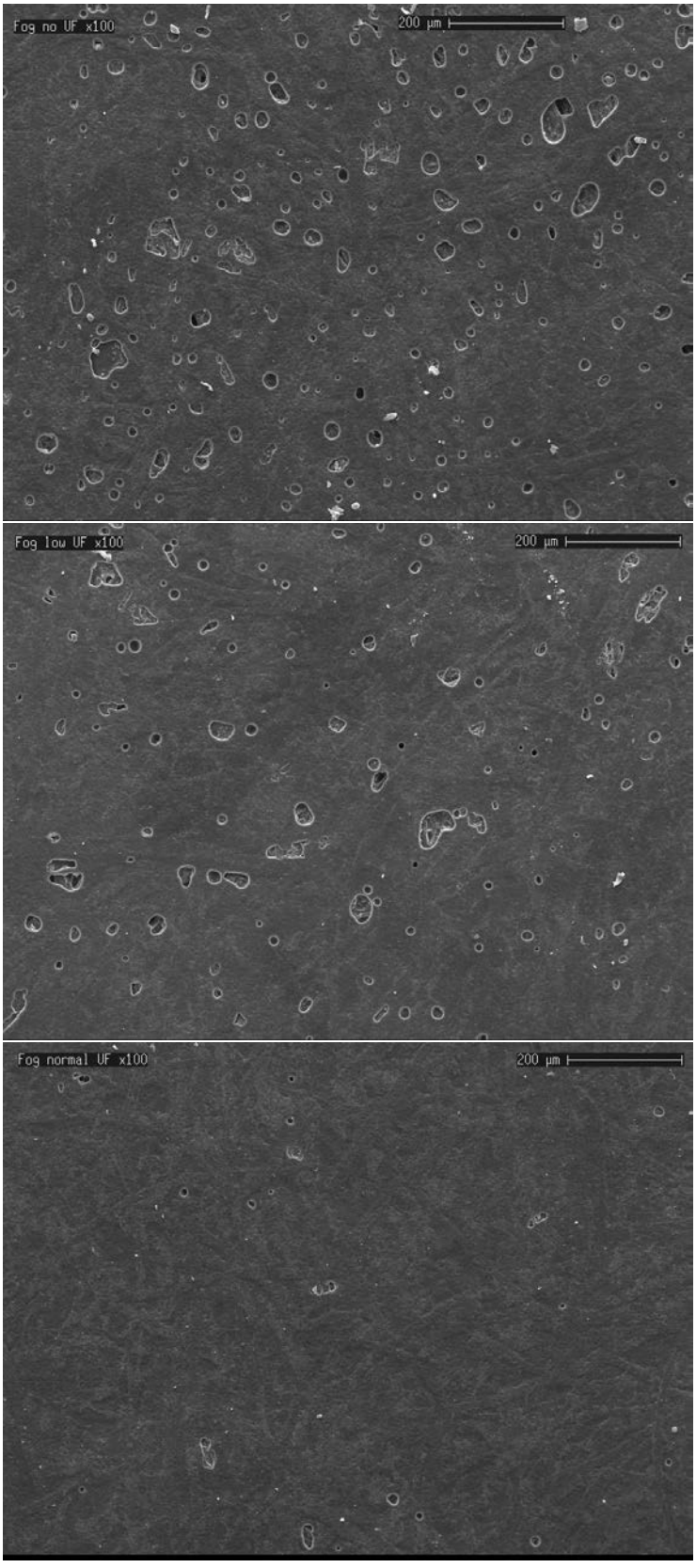

Figure 3.33: *SEM images of the MF coating on Fog showing average pore sizes in paper with top to bottom; no, low and normal UF saturation respectively.*

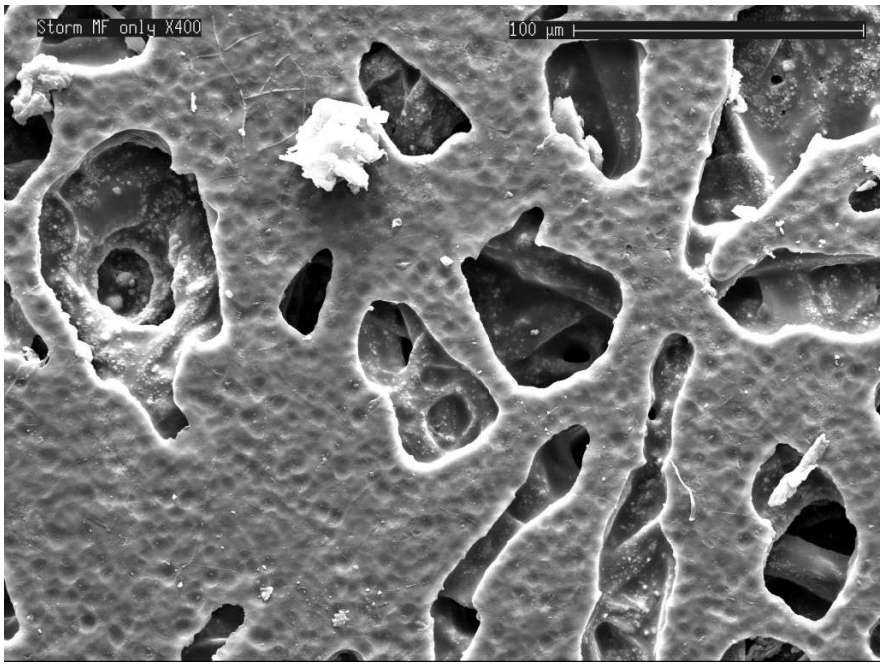

Figure 3.34: *The appearance of the decor paper Storm not treated with UF resin prior to MF resin application.*

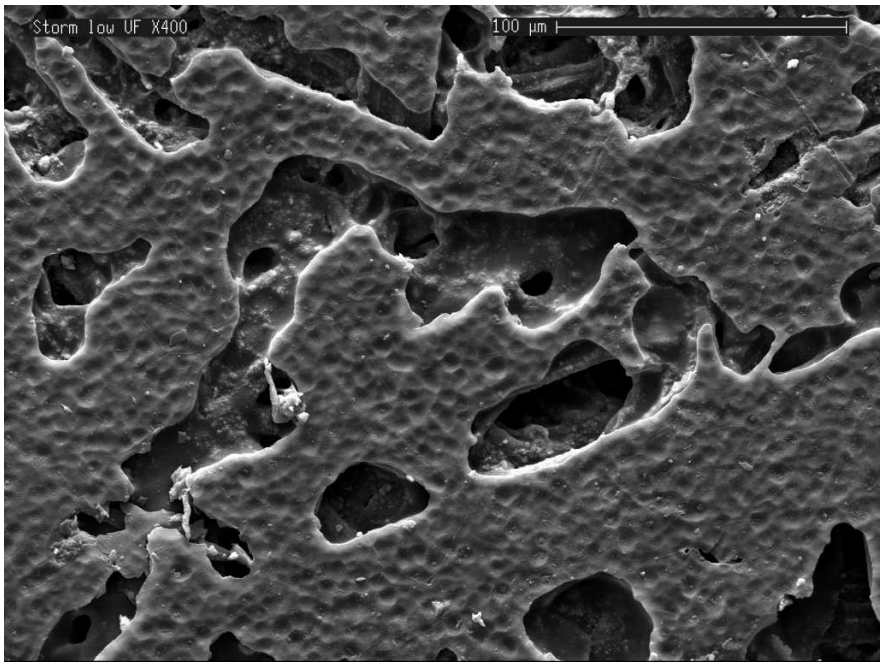

Figure 3.35: *The appearance of the decor paper Storm deliberately under treated with UF resin prior to MF resin application.*

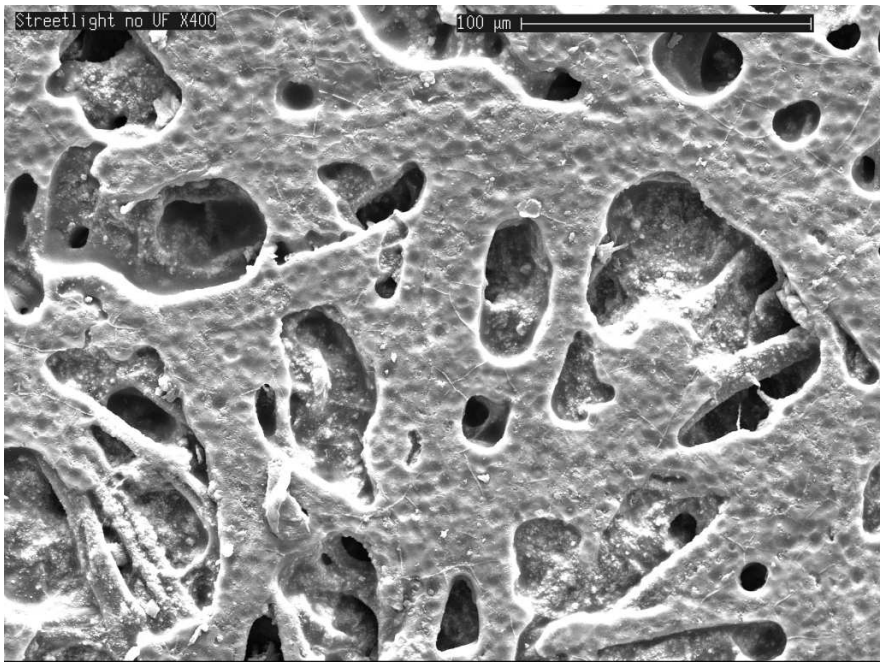

Figure 3.36: *The appearance of the decor paper Streetlight not treated with UF resin prior to MF resin application*

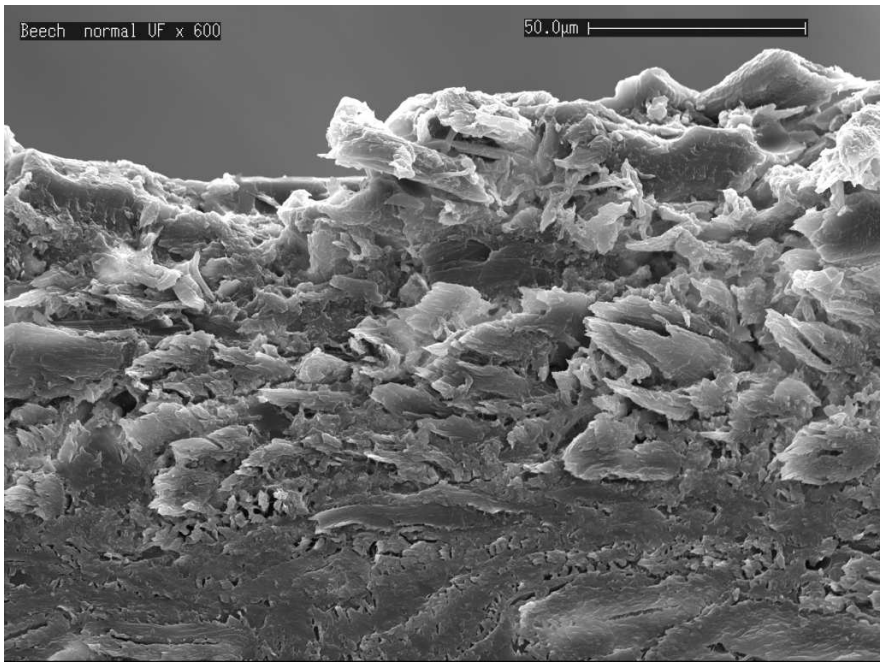

Figure 3.37: *Edge image of normally treated Beech after pressing showing a high level of unfilled voids below the surface*

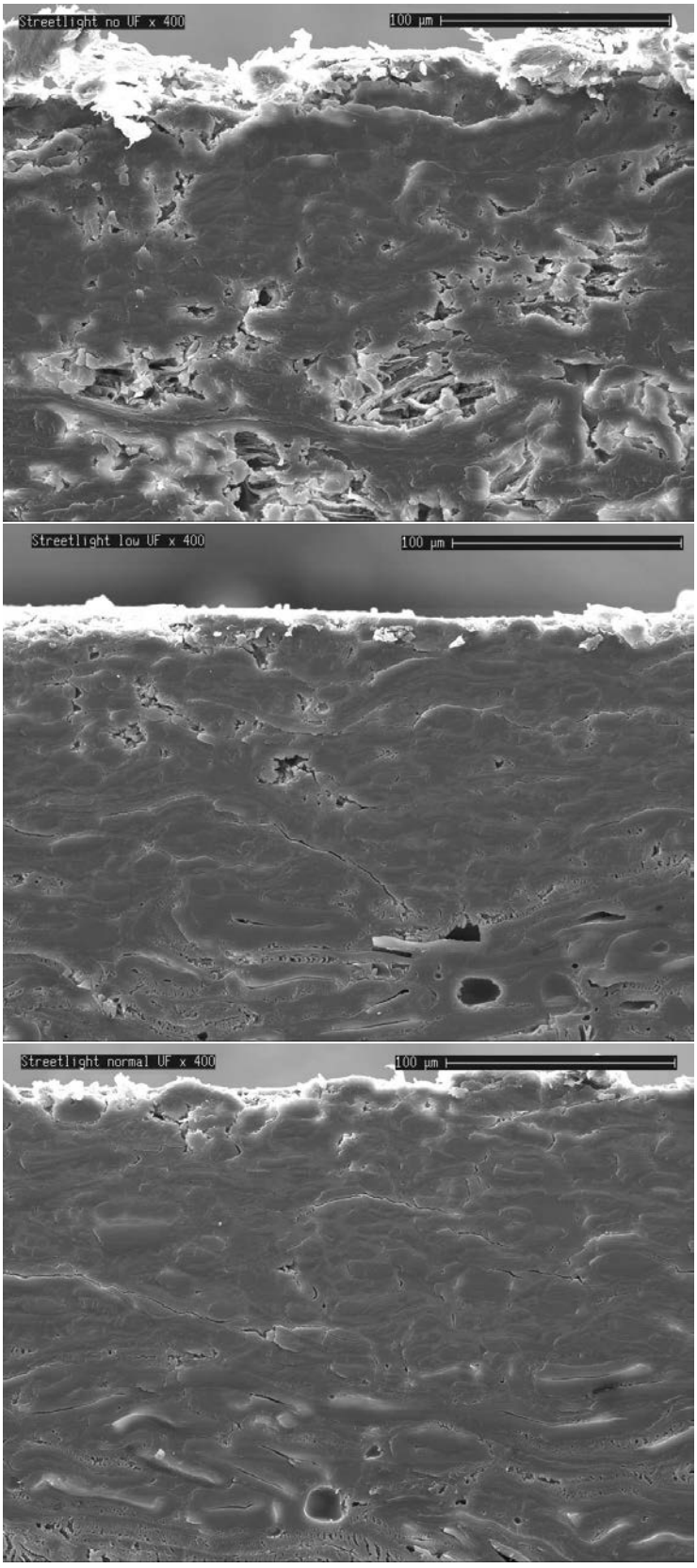

Figure 3.38: *SEM images of the edge of MF coated Streetlight showing the relationship between treatment level and the proportion of unfilled voids below the surface of pressed paper, showing top to bottom; no UF resin, deliberately under resinated and normal resin treatments.*

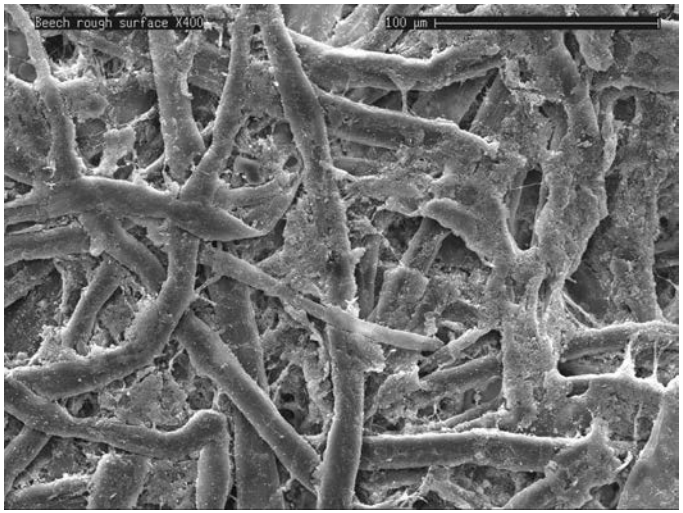

Figure 3.39: *SEM image of the rough side of the untreated decor paper Beech showing high filler content. The unfilled pores are more symmetrical after pressing (Figure 3.32).*

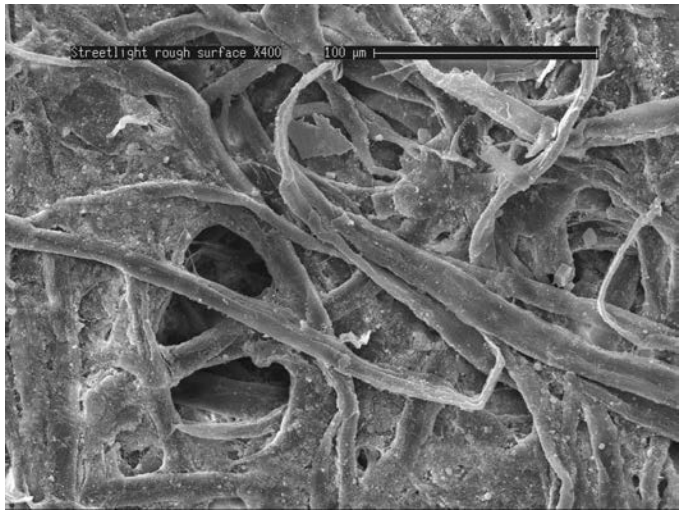

Figure 3.40: *SEM images of the rough side of the untreated decor paper Streetlight, showing high filler content. The unfilled pores are more symmetrical after pressing (Figure 3.28).*

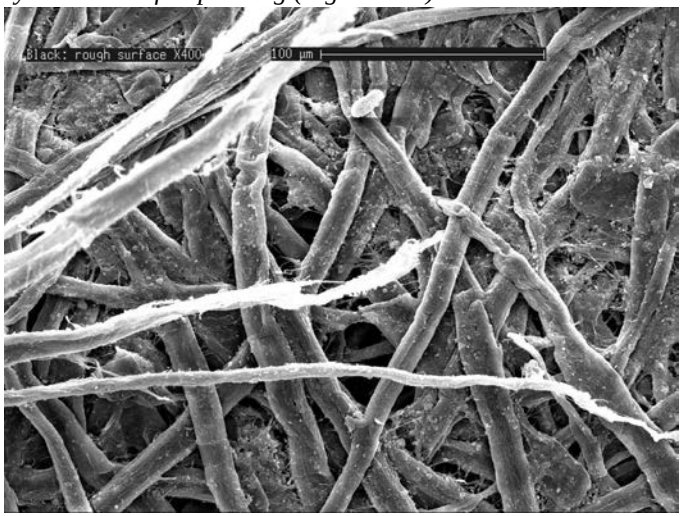

Figure 3.41: *SEM images of the rough side of the untreated decor paper Black, showing very low filler content. The unfilled pores are less symmetrical after pressing (Figure 3.31).*

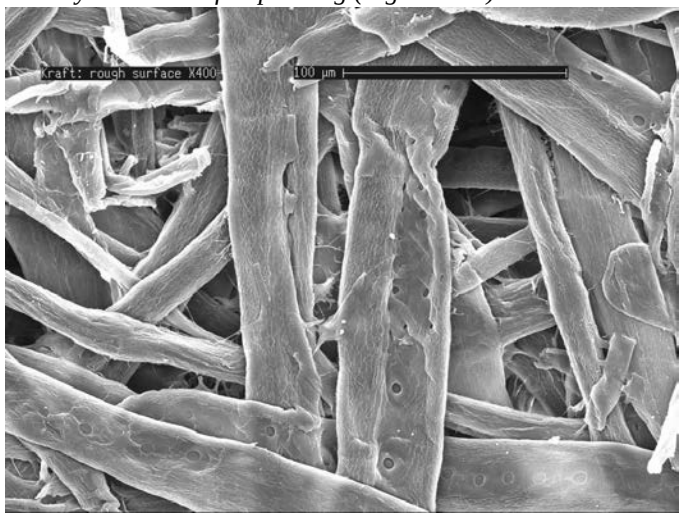

Figure 3.42: *SEM images of the rough side of the untreated decor paper Kraft, which has no filler. The unfilled pores are less symmetrical after pressing (Figure 3.30).*

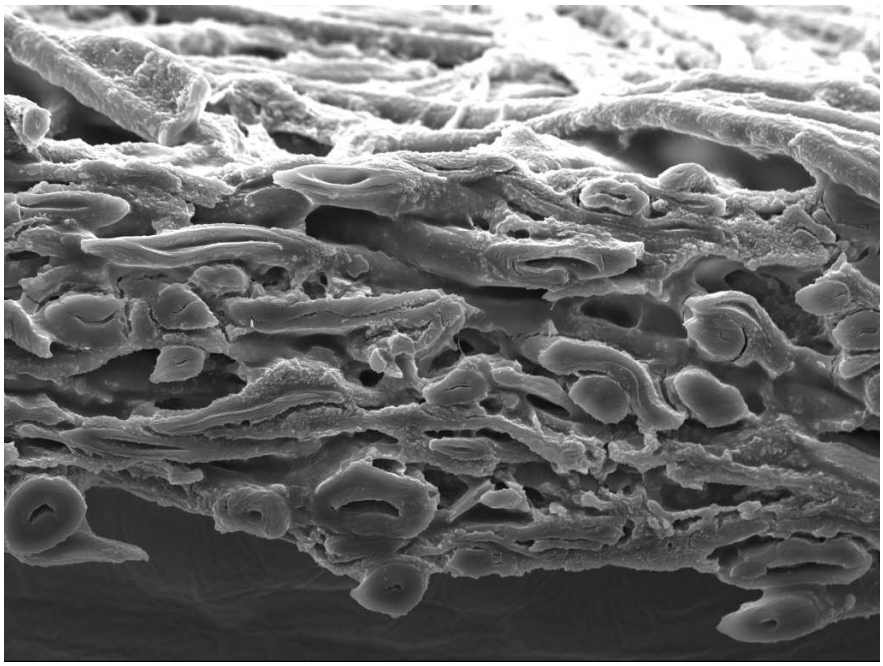

Figure 3.43: *SEM image of the edge of Beech raw paper showing a heterogeneous distribution of filler material resulting in a significant increase in pore sizes away from the surface of the paper.*

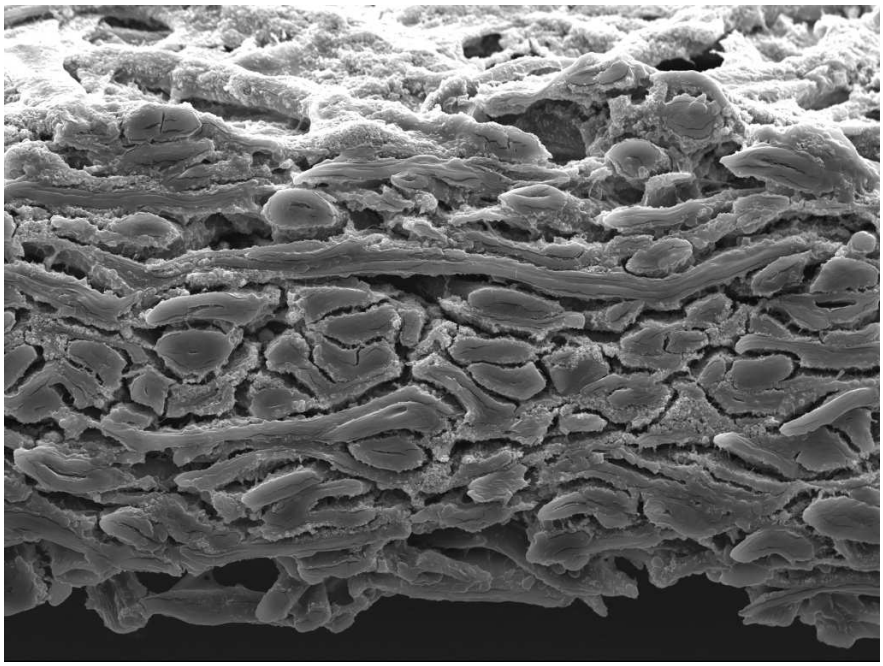

Figure 3.44: *SEM image of the edge of Folkstone Grey raw paper showing a homogeneous distribution of filler material resulting in a more even distribution in pore sizes below the surface of the paper.*

3.3.5 Melamine distribution

3.3.5.1 Preliminary studies of Raman spectra of resins

Examination of UF resin impregnated discs after pressing showed that there was no flow of UF resin once discs were cured in the oven before coating with MF resin. As expected cured and uncured MF resin had strong Raman peaks at around 975 cm^{-1} and at 676 cm^{-1} (Figures 3.46 & 3.47). Raman spectra for cured and uncured UF resin were also obtained and there were no peaks that coincided with the peaks at 975 or 675 cm^{-1} (Figures 3.46 & 3.47). This finding is in accord with those of Hill et al. (1984) who used Raman spectroscopy to characterize various UF resins and model compounds and found no peaks near 975 cm^{-1}. The MF peak at 975 cm^{-1} was also used by Schnieder (1997b) in her study of melamine distribution in industrial low pressure melamine impregnates. The results of her study are summarised in Section 3.2.9

In addition to characterising resins, three different raw papers, Storm, Streetlight and Black were analysed using Raman spectroscopy. Figure 3.48 is the Raman spectra for Streetlight, a very light coloured paper with very strong TiO_2 peaks at 447 and 610 cm^{-1}, and Storm a darker paper with strong carbon signals at 1328 and 1599 cm^{-1} as well as the strong TiO_2 peaks at 447 and 610 cm^{-1}. The TiO_2 peaks at 447 and 610 cm^{-1} swamp the melamine peak at 675 cm^{-1} but there is no TiO_2 peak at 975 cm^{-1}. Therefore the detection of melamine in treated pressed paper was based around the peak at 975 cm^{-1}.[11] Raman analysis of Black paper, showed no detectable TiO_2 peaks and therefore this paper was not used in subsequent experiments.

3.3.5.2 Melamine distribution in treated and pressed paper

There was a significant interaction *($p < 0.001$)* between position within the paper and level of UF resin treatment on concentration of melamine detected in paper by Raman microscopy (Figure 3.45). In papers with either no UF resin treatment or low levels of treatment there was no significant difference in the concentration of MF resin at the surface and in the core of the papers. In contrast, the concentration of melamine in the core of the papers was significantly lower when the papers were pre-treated with a normal level of UF resin (Figure 3.45). This suggests that MF resin flows away from the surface of the paper during pressing if the level of saturation of paper with UF resin is below normal.

Figure 3.49 shows the spectrum for unsaturated (*i.e.* no UF treatment) Fog at the surface, halfway to the centre and in the centre of the paper. Melamine was present throughout the paper and its concentration is particularly high in the centre of the paper. With Fog which had been pre-treated with a low level of UF resin, there was a reduction in the intensity of the melamine peak toward the centre of the paper, but melamine could still be detected (Figure 3.50). In the case of paper treated with a normal level of UF resin, melamine was virtually

[11] In one instance it was possible to identify on the shoulder of the TiO_2 peak at 610 cm^{-1} the melamine peak at 675 cm^{-1} (in Fog), however this peak was not used in any subsequent analyses.

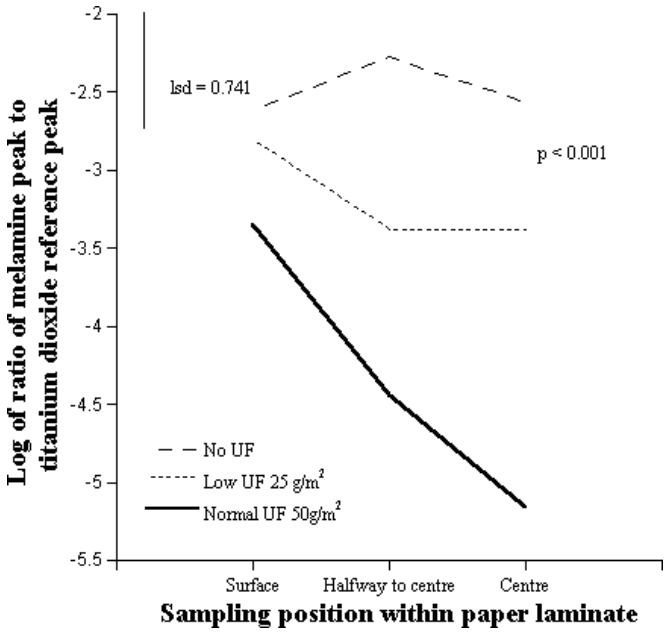

Figure 3.45: *Effect of treatment and position in the paper on the concentration of melamine in the treated pressed paper.*

undetectable away from the surface of the paper, *i.e.* it was only present on the surface (Figure 3.51). Similar trends were also observed for Streetlight (Figures 3.52, 3.53 & 3.54) and all other resin impregnated and pressed papers analysed.

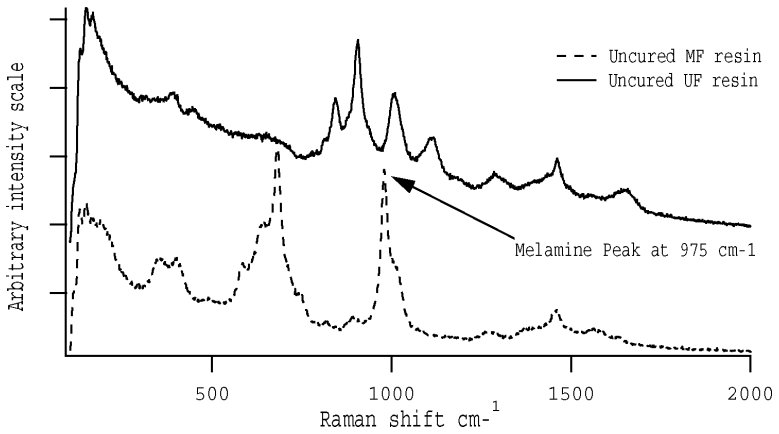

***Figure 3.46**: Raman spectra for uncured MF and UF resins.*

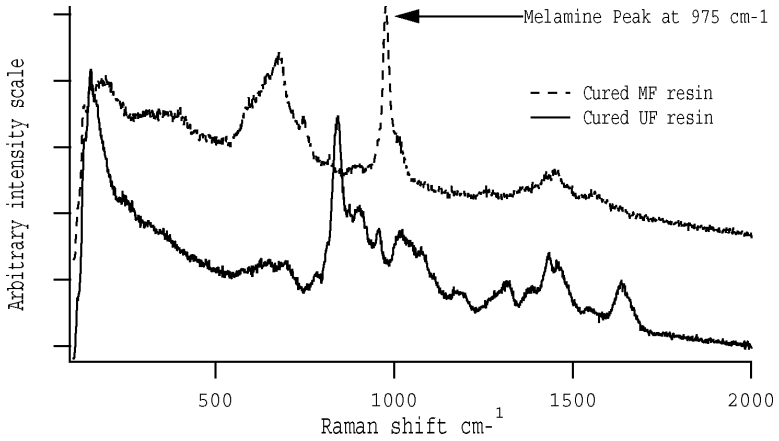

***Figure 3.47**: Raman spectra for cured MF and UF resins.*

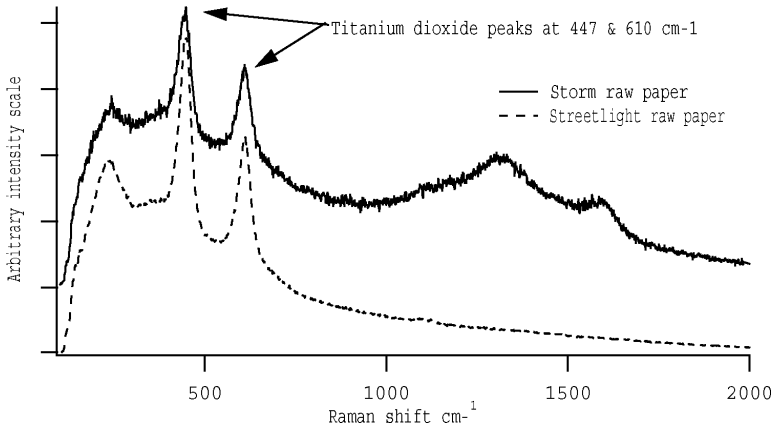

***Figure 3.48**: Raman spectra for untreated Storm & Streetlight raw paper*

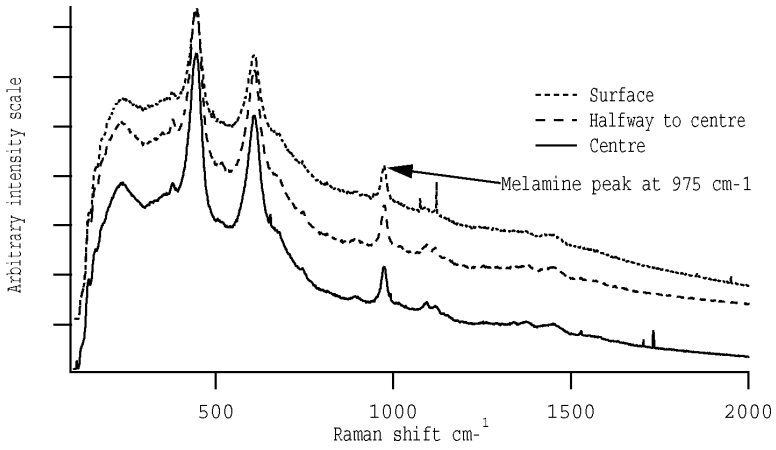

Figure 3.49: *Raman spectra for Fog paper samples treated with MF, but not subjected to a preliminary UF resin treatment showing a strong melamine peak in the centre of the paper.*

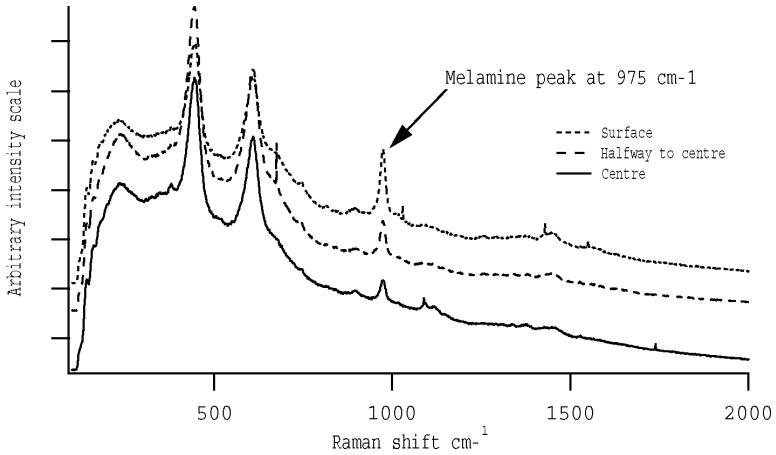

Figure 3.50: *Raman spectra for Fog paper samples treated with MF, and a low preliminary UF treatment showing detectable melamine in the centre of the paper.*

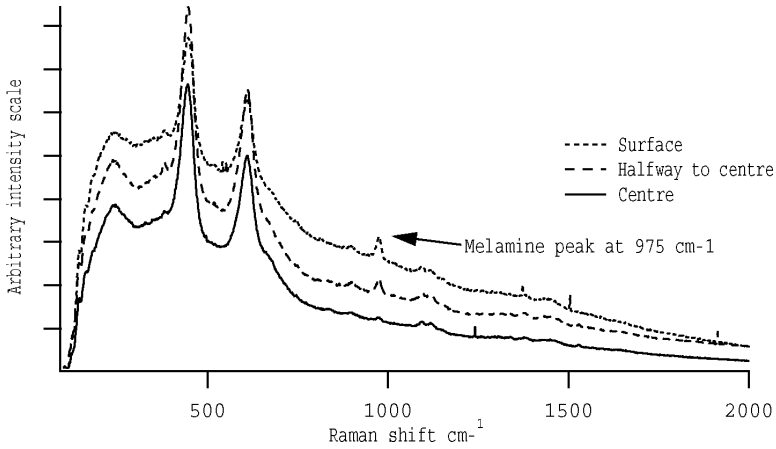

Figure 3.51: *Raman spectra for Fog paper samples treated with MF, and a normal preliminary UF treatment showing no detectable melamine in the centre of the paper.*

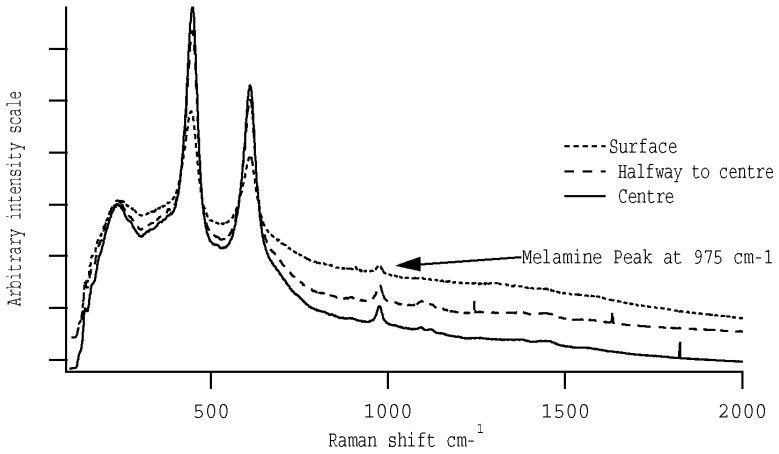

Figure 3.52: *Raman spectra for Streetlight paper samples treated with MF, but not subjected to a preliminary UF resin treatment. Melamine is detectable at all positions in the paper.*

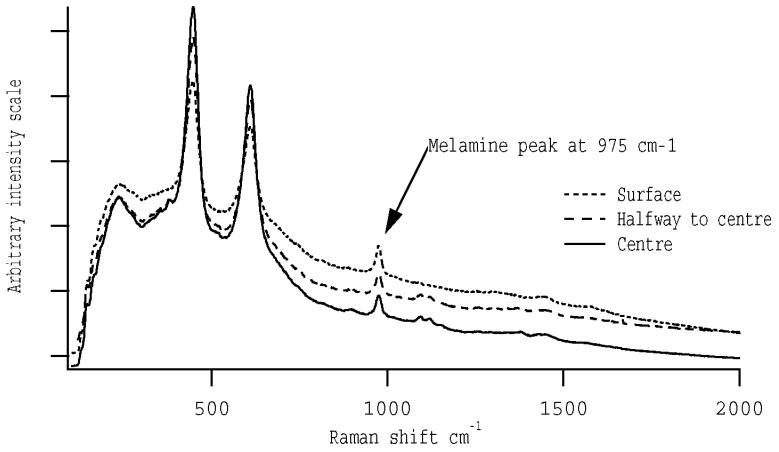

Figure 3.53: *Raman spectra for Streetlight paper samples treated with MF and a low UF preliminary UF resin treatment. Melamine is detectable at all positions within the paper.*

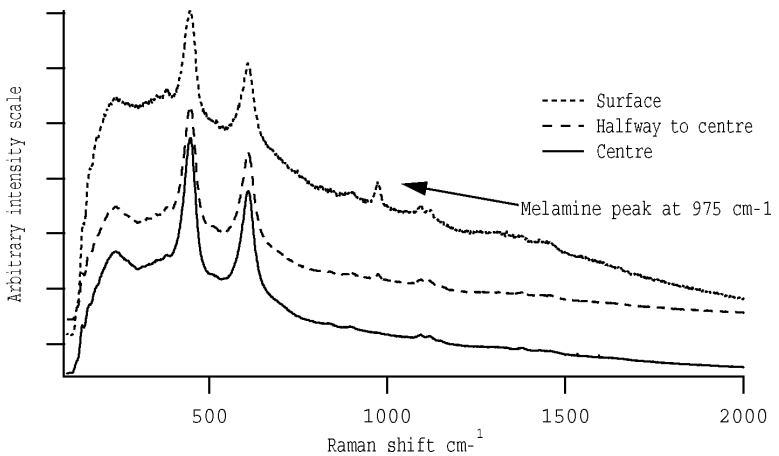

Figure 3.54: *Raman spectra for Streetlight paper samples treated with MF and a normal preliminary UF resin treatment. No melamine is detected away from the surface of the paper.*

3.4 Discussion

A strong relationship was established between level of UF resin treatment and the quality of the MF coating on pressed low pressure paper laminates. No UF saturation and less than complete UF saturation led to larger total numbers of unfilled pores (Figure 3.7) and a larger total area of unfilled pores on the surfaces of treated pressed papers (Figure 3.9). These microscopic voids were present on the surface of the paper after pressing. For these "defects" to be present on the surface of paper, the MF resin would have had to migrate away from the surface either by combining with the UF resin already present in the paper after the first stage of the treatment process or by flowing into pore spaces not saturated with UF resin. MF resins are formulated to flow during pressing prior to full cure in order to achieve the desired surface finish (governed by the texture of the caul plate) so that during pressing MF resins have the potential to migrate into voids (Pizzi, 1983a). In general it was also found that the amount of unfilled pores beneath the surface of the paper was related to the level of UF saturation (Figure 3.11). This clearly supported the first hypothesis in Section 3.1. There were exceptions to this, however, and in some cases most notably for Beech, defect free coatings were observed in papers that were not fully saturated with UF resin. This indicates that the structure of paper has a significant effect on the level of defects in MF coatings on LPM panels.

Accordingly paper type had a significant effect on the presence of surface defects and migration of MF resin in treated paper. Beech and Folkstone Grey had significantly lower total numbers of unfilled pores than all other paper types tested (Figure 3.13). This was also the case for the total area of unfilled pores (Figure 3.14). Folkstone Grey appeared to saturate and coat better than the other papers tested and it had the lowest amount of defects. Conversely Storm and Black had the highest level of defects and therefore it can be concluded that they did not saturate as well as the other papers. These paper types showed a high frequency of unfilled pores even with normal levels of UF saturation as shown in the third image in Figure 3.25.

Some papers that had lower levels of unfilled pores after pressing such as Alpine White and Beech also had the highest amount of filler or ash content (Table A.2) and papers that were more difficult to treat such as Storm, Black and Kraft had less filler. The papers with the highest defects such as Black, Kraft, New England Elm, Storm and Streetlight (Figures 3.18, 3.19 & 3.20) also had the largest surface pores. This will be examined further in Chapter 8.

One paper type, Beech, behaved differently to all of the other papers. It had the lowest number of unfilled pores (defects) on the surface (Figure 3.32 bottom) and had the highest level of unfilled pores beneath the surface when normally saturated with UF resin. There appeared to be less than complete saturation with UF resin but very effective surface coating with MF resin. Raman spectroscopy confirmed that there was no melamine in the centre of the normally UF saturated Beech. This suggested that the UF resin was able to prevent the migration of MF resin into the centre of the paper, despite the fact that the paper was not completely saturated

with UF resin and hence contained large numbers of voids in the centre of the paper. In all other papers where there were voids in the centre of paper there was detectable melamine in the core, and higher levels of unfilled pores on the surface, (this being related to lower levels of UF saturation).

This behaviour was contrary to expectations, as the behaviour of the majority of the decor papers was that they developed large numbers of defects only when there was less than complete saturation of the paper by UF resin. Hence there was at least one exception to the hypothesis proposed in the introduction to this Chapter. The SEM photomicrograph Figure 3.43 reveals that there is a heterogeneous distribution of pore sizes beneath the surface of Beech, with very small sub-surface pore spaces just below both surfaces and larger pores towards the centre of the paper. This appears to be caused by an uneven distribution of filler, which is concentrated immediately below the surface of the paper. It is proposed that this distribution of pore sizes may account for the anomalous behaviour of Beech during resin treatment. In comparison a paper such as Folkstone Grey had a more even distribution of filler and pore sizes throughout the paper (Figure 3.44) and also developed fewer defects, but had few if any unfilled voids below the surface at normal levels of UF saturation.

Kent and Lyne (1989a,b) stated that "the rate-determining factors for penetration of liquids into paper may be the distribution of divergence and convergence in pore wall geometry and the presence of discontinuities." Such a divergence occurs when a small pore connects with a larger pore as observed in Beech. In this case one could expect a reduction in the interfacial pressure as described by Kent and Lyne (1989a,b) resulting in a slowing of liquid flow without any externally applied pressure. The paper may therefore have behaved like a "hard sized" paper where normally hydrophobic additives are added to the surfaces of the paper at the dry end of a paper machine (Biermann, 1996) to reduce the size of surface pores. Kent and Lyne (1989a,b) explained that when water is introduced to the surface of a sized fine paper it fills the surface voids in less than a millisecond *i.e.* they believed that the pores on the surface would be predominantly convergent and would be filled rapidly. After filling the convergent surface pores in the paper, the progress into divergent capillaries in the bulk of the paper was halted. This aspect of fluid flow is dealt with in greater detail in Chapter 6.

The fact that the UF resin created an effective barrier in Beech to migration of MF resin was unexpected. This observation does not support the hypothesis proposed above, and could lead to an alternative hypothesis that in certain papers UF saturating resins create an impenetrable barrier preventing MF resin migration and associated production of defects. However, in all other papers there was a strong relationship between level of UF treatment and reduction in surface defects in the MF coating. Therefore subsequent work in this thesis assumes that it is necessary to achieve full saturation of paper with UF resin in order to prevent MF migration and reduce the level of defects in the MF coating. The effect of filler on pore size and paper structure on fluid flow is discussed in much more detail in Chapter 7.

Raman microscopy provided evidence contrary to the suggestion (Schnieder, 1997b) that MF resin combined with UF resin. Raman spectra of treated paper showed that with full UF saturation there was little (if any) MF resin located in the centre of treated papers (in two papers Fog & Streetlight there was no detectable melamine at all (Figures 3.51 & 3.54). With less than complete saturation, MF resin was detected in the centre of papers (Figures 3.49, 3.50, 3.52 & 3.53). If MF resin had combined with UF resin then melamine would have been detected in the centre of papers fully saturated with UF resin.

Raman microscopy was a useful technique to determine the final distribution of MF resin in paper however it was not possible to use it in confocal mode with thick paper samples due to the quenching of laser. Thus imaging using Raman microscopy had to be done on specially prepared edge sections involving a large amount of sample preparation including ultra-microtoming to ensure no contamination of the MF resin from the surface into the core of the paper occurred. Thus the technique is not suitable for use in an industrial situation. It may not be necessary however to examine the distribution of MF resin in order to measure the quality of treated paper. Direct determination of surface voids on paper would be more practical and could be done using an optical system with as little sample preparation as rubbing coloured wax over the surface of the laminate and wiping off the excess. The wax would remain in the unfilled voids on the surface giving a very good indication of the effectiveness of saturation with UF resin and the quality of the MF coating.

Schnieder (1997b) suggested that Raman microscopy offered new opportunities to further examine the distribution of MF resin in industrial paper laminates and this work confirms her suggestion. Raman microscopy revealed trends in the distribution of MF resin in laminates such as its presence or absence in the centre of paper, or changes in concentration from the centre to the surface of paper. Schnieder (1997b) stated that where impregnates showed evidence of melamine in the core, a mixing of UF and MF occurred during the impregnation process. Such distribution of the resins, it was argued, could not be related to the structure or porosity of the paper because melamine was found in the core of both compressed and open-structured papers. The interpretation by Schnieder (1997b) that MF resins combine with UF resin is rebutted as is her suggestion that the distribution of resins could not be related to the structure or porosity of the paper (a very strong paper effect on the production of defects was found in this chapter). The papers studied in this Chapter were both open-structured and compressed and while there was a paper effect which is examined in greater detail in Chapters 4, 7 & 8 it was clear that the presence of melamine in the core of the paper was primarily a function of the degree of saturation of UF resin during the first stage of treatment.

The results obtained here help to answer the following questions posed by Schnieder (1997b) a) “Are melamine and urea separate phases? Urea in the core and melamine on the edges; b) Do urea and melamine mix together during the second impregnation? and; c) Will the liquid melamine resin penetrate the already solidified urea?” In answer to the first question,

it was clear that, given effective saturation of paper by UF resin there was significantly less melamine in the centre of the paper than on the surface. For example, in the case of papers such as Beech and Fog, MF resin did not penetrate into the centre of the paper at all. This suggested that melamine and urea are separate phases, and melamine only penetrated into the paper when there was less than effective saturation with UF resin. Further evidence supporting the suggestion that both UF and MF resins remained as separate phases was provided by an experiment that showed that after UF resin was impregnated into samples of paper and subsequently pressed, (before coating with MF resin and after the first stage oven), there was no flow of the UF resin beyond the edge of the paper. Hence it can be concluded that if there is effective saturation of paper with UF resin, MF resin penetration into paper appears to be minimal, and the MF resin certainly does not combine with UF resin.

In answer to the second question posed by Schnieder (1997b), results also indicate that urea and melamine did not mix during the MF coating stage when the paper was fully saturated with UF resin. Findings here also answer the third question, as the presence of melamine away from the surface of the paper appeared to be related to the effectiveness of UF resin saturation *i.e.* if high levels of UF resin were applied to the paper there was no detectable melamine in the core. Therefore the presence of solid UF resin probably acted as a barrier to the migration of MF resin into the paper, the effectiveness of such a barrier being dependent on how effectively the UF resin imbibed into the paper and blocked flow paths into the centre of the paper. Thus it appears that MF resin could not penetrate cured UF resin.

The inadequate saturation of decor papers by UF resins and the redistribution of MF resin away from the surface during pressing both involve flow of fluids in paper, either too little flow in the case of the saturating UF resin, or too much flow in the case of the MF resin. Therefore a more complete study of the fluid imbibition characteristics of the papers studied in this chapter is described in the next chapter. In subsequent chapters the mechanisms of fluid flow in paper as well as the factors affecting fluid flow in paper are explored.

3.4.1 Conclusion

The hypothesis proposed in the introduction to this Chapter that defects in the surface of LPM panels after pressing are caused by inadequate saturation of papers by UF resin resulting in the flow of MF resin from the surface into the unfilled voids in the paper needs to be slightly modified. In the majority of cases effective saturation was necessary to significantly reduce the level of defects in MF coatings on decor paper. However it was demonstrated in one paper, Beech, that even though UF resin saturation was less than complete, it was sufficient to prevent significant migration of MF resin from the surface thereby reducing the level of surface defects. Thus an effective barrier of UF resin just below the surface could prevent MF migration, however, this might be difficult to achieve in practice. Thus complete saturation of

decor paper with UF resin is still required in the majority of cases to minimize surface defects in the MF coating on LPM panels and work in the rest of the thesis is based on this premise.

The hypothesis that the type of paper influences the quality of the MF coating can be supported by the results in this Chapter although in some cases there were interactions of level of resin treatment and paper type on defects in the MF coating.

Chapter 4

Relationship between the physical properties of decor papers and surface defects in LPM overlays

An effect of paper type on level of surface defects in resin impregnated paper on MDF was demonstrated in the previous chapter. The purpose of this chapter is to determine whether this effect can be related to any of the standard measures of paper properties and also to the imbibition performance of the papers.

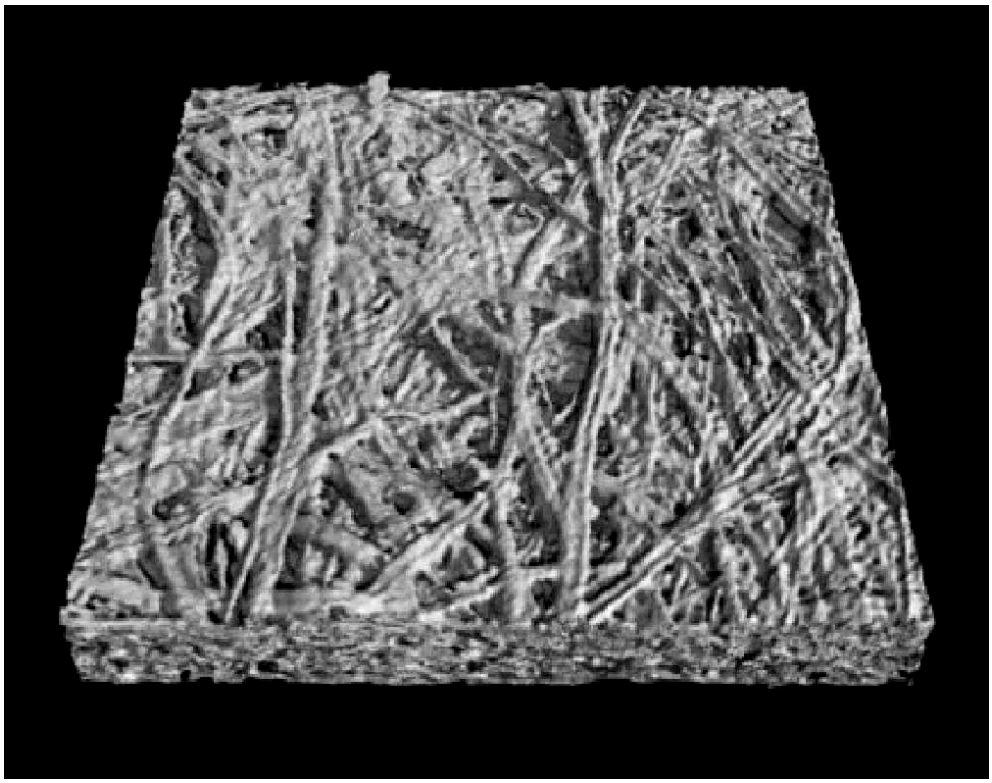

A reconstructed image of an unfilled laboratory paper obtained using x-ray micro-CT.

4.1 Introduction

One of the main aims of this thesis is to better understand the factors that affect the impregnation of thermosetting resins into decor papers in order to improve the treatment process and performance of the resin impregnated papers when they are pressed onto wood based composites.

A strong effect of paper type on the level of defects in MF coatings on decor paper was observed in Chapter 3. The generation of such defects may be related to certain physical characteristics of paper that influence the flow of resin into the paper. Accordingly the rate of liquid imbibition of different decor papers should be related to generation of defects and in turn the physical properties of decor papers.

There are many methods of measuring the physical and imbibition characteristics of decor paper. They can be described in terms of their Gurley porosity (measure of air permeability), Klemm wicking (rate of water movement in the machine and cross directions *i.e.* in plane), total resin uptake (g), bulk density (g/cm^3 which includes void volume, Mark et al. (2002)), paper weight (g/m^2) and thickness (μm).

There is very little information in the literature, however, about the effect of these characteristics on the performance of decor papers. Arledter (1957) showed how the capillary rise of a solution in a paper (Klemm test) might give supporting evidence for the treatability of an absorbent paper with aqueous solutions, and Verhoeff et al. (1963) used the Klemm test to measure the velocity of capillary rise in papers subjected to different levels of beating. Seiler (1957) looking at penetrability examined the saturation of kraft papers for resin impregnation and concluded that rate of penetration on its own does not define the overall impregnating and saturating qualities of paper. Neither he or others have looked at the relationship between the saturating of paper and the quality of the finished products, especially the relationship between resin saturation, subsequent resin flow and defects. Cussons (1997) stated that the Klemm test, although widely used did not relate well to resin penetration. A detailed review of work on measuring fluid flow into paper was given in Chapter 2.

It was therefore important to develop an accurate method of determining the uptake of liquid into decor papers. The majority of applications of paper *eg.* printing require liquid penetration resistance rather than enhanced penetration properties. Thus most tests of liquid penetration into paper have been developed to assess degree of sizing; or water resistance of paper (Biermann, 1996). As such these test methods are designed to measure penetration of liquids into paper over periods of many minutes rather than fractions of a second. However, resin penetration into decor paper occurs rapidly (< 2 s) (Cussons, 1997) and hence test methods described in the literature and reviewed in Chapter 2 may not accurately assess the suitability of decor paper for resin treatment. Arledter (1957) in his study of the penetration of resins and oils into absorbent papers stated “for most of their history the paper makers were concerned

with trials to reduce the unwanted natural absorbency of paper. The invention of blotting paper probably started the paper industry to devote time to improve the natural ability of cellulose fibers and the paper structure to absorb water or ink, and the industry is still working on this problem". The development of test methods for measuring resin uptake in decor papers has received little attention and better test methods are required to measure rates of liquid penetration into decor paper over short time scales.

The aim of the work described in this chapter is to determine whether standard properties measured by paper manufacturers to describe decor papers could be related to the level of defects that were found to occur in treated papers (Chapter 3). Secondly, to develop a new method for quantifying liquid imbibition into decor papers and determine whether it would be a better guide to the performance of decor papers than those currently used.

4.2 Materials and methods

4.2.1 Sampling

During examination of the physical characteristics of the different decor papers, it was essential to correctly identify them by replicate number and location with each large sheet. A representative number of samples were required to comprehensively sample all of the papers tested. The order of sampling and experimentation was randomised. All samples were obtained just prior to experimentation from paper rolls stored in a conditioning room at $20 \pm 1^{\circ}$C and $50 \pm 5\%$ r.h. Samples were transferred in zip-lock bags and handled with cotton gloves or tweezers to eliminate contamination of samples with skin oils.

As paper is very heterogeneous, due to variation in fibre and filler properties, (Biermann, 1996) and structure (Bristow, 1986a; Cutshall, 1990) it was essential that representative samples were obtained. Before sampling, three full rounds (approximately 8 m^2) was unwound from each roll of the different decor papers and discarded to ensure that uncontaminated paper was used for experimentation. For each decor paper there were two replicates, each obtained from a separate roll of paper. 10 samples were obtained from each of the rolls. In the case of one of the paper types (Black), which was supplied as a 1200 mm wide roll, two groups of 5 samples were obtained 240 mm apart along each row and 600 mm between each row. The remaining papers were supplied as 1800 mm wide rolls. The distance between samples within a row for these paper types was 365 mm, and the distance between each row was 600 mm. Samples were selected from each replicate using a random number generator, the number referring to the type of paper that was selected. All samples were identified using replicate (roll no.) and a number denoting their sampling position and paper type. The sampling scheme that was used is shown in Figure 4.1. The size of the test sample depended on the type of test, and is fully described in the relevant sections below. Where a published test method was used,

however, the sample size was in accordance with the test method.

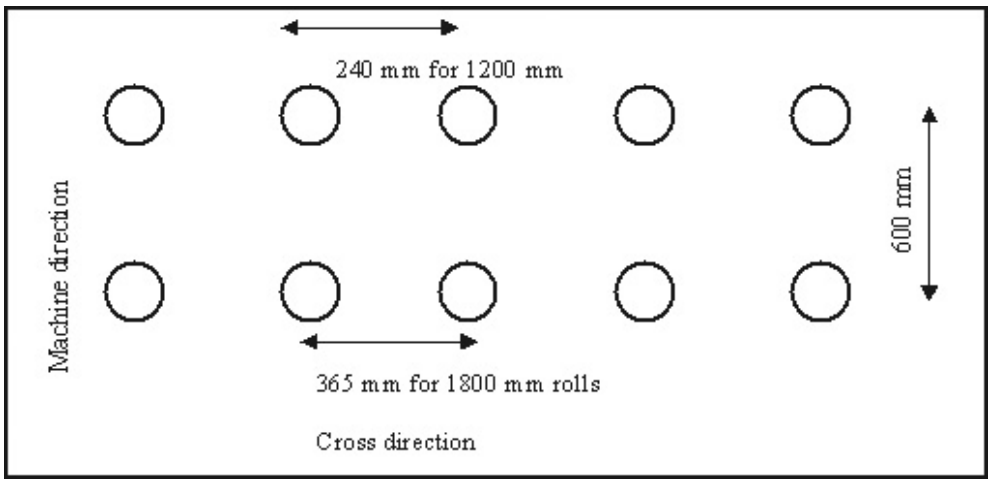

***Figure 4.1**: Sampling diagram for all paper tests including the imbibition test.*

4.2.2 Standard paper testing

The following basic paper tests were carried out; Klemm liquid wicking in the machine direction, Klemm liquid wicking in the cross-direction, resin demand as used by industry to predict total resin pickup, Gurley porosity, thickness and density.

4.2.2.1 Klemm testing

This test was based on TAPPI T441 om-90 and measures the distance a liquid (usually water) wicks up a strip of paper in 10 minutes. It is a test of liquid imbibition of paper that is still commonly used by both paper makers and end users. The sample size for the Klemm test method was 200 mm x 15 mm (TAPPI T402 om-88). Samples were placed in a beaker of water as shown in Figure 4.2. They were left in the test solution for 10 minutes, removed and the distance the water had moved up the strip of paper was measured in millimetres (mm).

***Figure 4.2**: Klemm testing apparatus*

Klemm tests were repeated (as above) for each paper using diethylene glycol, (which has a similar viscosity to UF resins, as tested by a No. 4 Flow cup) as the test liquid.

4.2.2.2 Resin demand

This is a test method commonly used by manufacturers of decor papers (and modified by industry) to estimate the total amount of UF and MF resin a new decor paper will absorb. It estimates resin uptake from the water absorbency of a paper. 100 cm^2 samples (circles) of paper were obtained using an AP Lever 3M paper circle cutter and weighed to the nearest 0.001 g. The sample was dipped in clean tap water at $25 \pm 1°C$ for 30 seconds. Each disc was carefully removed from the water using tongs and excess water was wiped off using two glass rods acting as squeeze rollers. The disc was re-weighed and uptake of water calculated. Resin demand was calculated as follows (Equn. 4.2):

$$UF = ((ww - dw) * 1.2sg * 0.8(se)) * sc - ((ww - dw) * 0.8(se) * 0.38(d)) \qquad (4.1)$$

UF = UF resin demand, ww = wet weight, dw = dry weight, sg = specific gravity of resin, se = scraping efficiency of the glass rods, sc = solids content of the resin, d = the effect of drying

4.2.2.3 Gurley porosity

The Gurley porosity test was carried out according to TAPPI test method T-460. The Gurley porosity test measures the time taken to the nearest 0.1 s for 100 mL of air to pass through a paper sample, 6.45 cm^2 (1 in^2) in area. The Gurley test is widely used in the paper industry for determining the porosity (air permeability) of paper, and it is also used as an indirect indicator of the ease of penetration of paper by liquids.

4.2.2.4 Thickness and density

Thickness of paper samples was measured on the same samples used for testing Gurley porosity. A sample measuring 50 mm x 62 mm was cut from the paper using a small guillotine. A British Indicators micrometer (a standard paper testing tool) was used to measure the thickness of each corner of the sample to the nearest micron, and the weight of the samples was determined using a digital laboratory balance accurate to 0.001 g. Density was calculated as (air dry mass (g))/(air dry vol. cm^3).

4.2.3 Measuring rate of saturation

4.2.3.1 Inverted Bottle Test

The inverted bottle method used in this thesis to measure rate of saturation of paper was similar to that developed by Cussons (1997). 125 mL of diethylene glycol at 25°C is placed into a 250 mL test bottle. Liquid Turquoise dye (Oxford Chemicals) was added to the diethylene glycol (DEG) at a concentration of 0.3% w/w to assist in the visual determination of the endpoint, as this proved to be difficult to assess when using undyed DEG particularly with the lighter coloured papers. To minimise the effect of variation in temperature and viscosity on liquid uptake, test bottles and the test liquid were stored in a water bath at 25°C prior to use. The rough sides of the paper were orientated toward the liquid in accord with the orientation of paper in a commercial treater (Figures 1.1 & 1.2). All experiments and visualisations on paper in this thesis were carried out using the rough (wire) side of the paper. The rough side of the paper was identified by observing the fibre raise on the paper surface using a Nikon 8x hand lens. Saturation time was determined by stopwatch and started when the bottle was inverted, and finished when the endpoint, *i.e.* total saturation, was reached. This was estimated visually as being the point when the whole disc area was saturated.

4.2.4 Relative reflectance method

As UF resin penetrates decor paper from one side to the other during treatment in an industrial paper treater in a process that lasts only a few seconds, a new method was developed to simulate the initial penetration of resin at the pre-wetting roller of a treater. The test method also had

to avoid the weakness of the ambiguity of end point determination inherent in visual based methods. The principle behind the method developed, the "relative reflectance technique" was that the amount of light reflected off the top surface of paper changes as liquid was imbibed through and from the bottom surface of the paper sample. Changing light reflectivity was measured against a constant to ensure that even the most subtle changes in reflection resulting from liquid penetration over very short time intervals were detected and measured. Materials such as squares of Teflon, thin shimming steel as well as paper correcting fluid were tried as the constant standard, however, an 8 mm stainless steel washer that had been sanded perfectly flat and sand blasted to provide even and constant reflection of light proved to be the most suitable material to use as a reflectance constant (Figure 4.4). The use of a stainless steel washer as a reflectance constant resulted in a much more accurate determination of the start and the end point, (when saturation was deemed to be complete). The former was important in determining whether or not a "wetting delay" (Bristow, 1967) existed for decor papers. A detailed review of optical methods for determining rate of liquid imbibition was presented in Chapter 2. Most of the methods developed were used to determine sizing efficiency and therefore only measure rates of liquid uptake by paper over longer time scales.

The paper sample with the washer in the middle held with tweezers was placed into a Petrie dish containing DEG. The video recorder and video timer were started and not stopped until at least 10 seconds after it appeared that saturation had been completed. This was necessary because full saturation could not be determined by eye alone.

Between 20 and 50 images were obtained for each sample depending on their rate of liquid uptake. Reflectance values were saved as an ASCII delimited text file which was then converted into a graph of reflectance ratios versus time. Data measured in seconds were transformed into natural logarithms. The end point had to be determined first by plotting an asymptote and smoothing data points after full saturation had been achieved. This enabled time from first contact of the paper with the saturating liquid to the endpoint to be calculated. The x axis on the graph (Figure B.1 in Appendix B) was corrected back to zero by subtracting the time in seconds from when the sample was placed on the DEG. The saturation ratio was normalised by first offsetting the point of full saturation to zero by subtracting the y value of each data point from the final reflectance y value when complete saturation was achieved. This final reflectance value at full saturation was calculated by averaging out the last few y values in Figure B.1. The data then was divided by the difference of the value of the reflectance ratio of dry paper by the offset. This resulted in reflectance values from 1 for dry paper to 0 when the paper was completely saturated. This can be seen by comparing the axes in the graphs (Figures B.1 & B.2), which were obtained from the same samples. The data analysed were the rate to 50% saturation and rate to 95% saturation (calculated by dividing the time in seconds by 100 times the thickness in microns). These parameters were calculated as 50% and 95% of the total change in reflectivity from dry paper to totally saturated paper (the time when the reflectance

value on the y axis in Figure B.2 was 0.5 and 0.05, respectively). This approach minimised the effects of potential error in end point determination on measured values, *i.e.* small differences in saturation near the end point occurred over longer time intervals. Full details of the development and use of the relative reflectance method are attached as Appendix B.

***Figure 4.3**: Experimental set-up for relative reflectance measurements*

***Figure 4.4:** Images showing position of CCD camera in relation to paper samples in the relative reflectance measurement apparatus and closeup of paper sample in temperature controlled bath showing "standard" washer.*

4.2.5 Statistical analysis of data

Statistical analysis of data was undertaken to determine the effect of paper type on density, ash content, thickness, Gurley porosity, Klemm test (both in machine and cross direction), resin demand, inverted bottle saturation test, and rates to both 50% and 95% saturation. The number of runs in each experiment was 10 samples within a replicate. There were two replicates with 9 different paper types, *i.e* each experiment had 180 different observations.

The design of all of the experiments involved factorial principles where the aim was to examine the effect of the fixed factors (paper type), on the response variables listed above. Random effects that were identified included; between roll variation, between row variation (machine direction effects), between column variation (cross direction effects) and the sampling position within the paper sheet *i.e.* row; column effect.

Analysis of variance (ANOVA) for a randomised block design was used to analyse data as the units were divided into homogeneous blocks (replicates) and the treatments were allocated at random within the blocks. Some data were transformed into natural logarithms to ensure that they complied with the assumptions of ANOVA, *i.e.* normality with constant variance. Statistical computation was carried out using Genstat 5 (Lawes Agricultural Trust).

The factorial design of the experiment allowed data to be averaged across non-significant *($p > 0.05$)* effects thereby giving the experiment greater precision. Significant results are presented graphically and individual means can be compared using least significant differences *($p < 0.05$)*. In addition significant effects are tabulated.

To determine how effectively the standard paper or the saturation tests predicted the tendency of decor papers to develop defects during LPM pressing, linear regression analyses were carried out on paper properties and measures of imbibition (explanatory variables) and defects in decor papers (response variables), measured in Chapter 3. Regression analyses were carried out using Genstat 5 (Table 4.1). Where regression analyses were used, the probability (*p* value) is given along with a percentage variance accounted for by the regression equation 4.2 where *rms* = residual mean square and *tms* = total mean square.

$$100(1-(rms)/(tms)) \tag{4.2}$$

When expressed as a proportion rather than a percentage, this statistic is called the adjusted R^2; and has the advantage over the statistic R^2 (the squared coefficient of correlation, often used in regression) in that it takes account of the number of parameters that have been fitted in the model. The regression equations are also annotated onto each of the graphs.

4.3 Results

Results are presented in 3 sections; a) heterogeneity of paper and the relationship between the physical characteristics of paper and suitability of decor papers for LPM, b) heterogeneity of paper and the relationship between rates of imbibition of decor papers and their suitability for use in LPM panels and c) relationship between physical characteristics of paper and imbibition of liquids. Table 4.1 summarises the significant relationships between all experimental factors and response variables including liquid imbibition and pressing performance.

Table 4.1: *Significant effects of, and interactions between the physical characteristics of papers, the level of defects and the imbibition characteristics of decor papers.*

Experimental factors	**Response variables**							
	Klemm MD	Klemm MD DEG	Resin demand test	Saturation rate Inverted bottle method	50% saturation rate	Total area of unfilled pores	Total no. of of unfilled pores	Average unfilled pore area
Density	***	**	*	***	*	***	*	*
Gurley	**	*	**	***	NS	NS	NS	*
Klemm MD	x	x	***	***	NS	*	*	NS
Klemm DEG MD	***	x	***	*	NS	NS	NS	NS
Resin demand	x	x	x	NS	NS	*	***	NS
Inverted bottle test	x	x	x	x	NS	NS	NS	NS
50% saturation (reflectance)	x	x	x	x	x	*	*	NS
95%	x	x	x	x	NS	NS	NS	NS

(* = $p < 0.05$, ** = $p < 0.01$, *** = $p < 0.001$, NS = not significant $p > 0.05$)

Areas marked x indicate tests not carried out due to similarity i.e. *the reversal of response and experimental factors and due to the very close relationship between Klemm in the machine and cross directions with both water and DEG.*

4.3.1 Heterogeneity of paper and the relationship between the physical characteristics of paper and suitability of decor papers for LPM

4.3.1.1 Density

There were significant differences *($p < 0.001$)* in the densities of the decor papers tested (Figure 4.5). The densities of the papers varied from 1.04 g/cm^3 for Alpine White to 0.71 g/cm^3 for Kraft. There was a significant relationship between density and ash content *($p < 0.001$)* of the papers and the regression equation explained 73.6% of the variance (Figure 4.6). The density of the papers increased with increasing ash content. Figure 4.7 shows a significant inverse relationship between density and thickness (p = 0.003) with the regression equation explaining

40.2% of the variance. Clearly ash content is a better explanatory variable for density than thickness (Figure 4.6).

There was a significant inverse relationship *($p < 0.001$)* between total area of unfilled pores in pressed treated LPM decor paper and the density of the papers (Figure 4.8). The regression equation explained 48.1% of the variance. There was a significant relationship *($p = 0.03$)* between the number of unfilled pores and the density of the decor papers, but the regression equation only accounted for 21.5% of the variance (Figure 4.9). Increasing paper density resulted in a decrease in the total number of unfilled pores in the decor papers after pressing. There was a significant relationship *($p = 0.003$)* between density and the average area of unfilled pores (Figure 4.10), with the regression equation explaining 40.9% of the variance. In accord with the results for total area of unfilled pores and numbers of pores, there was a reduction in average pore area with increasing paper density.

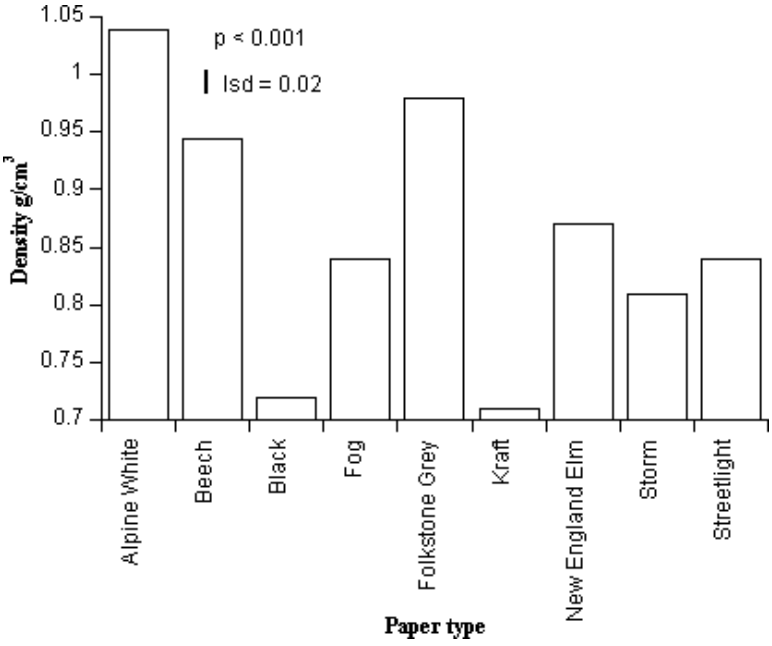

Figure 4.5: *Densities of the papers tested, the error bar (LSD) represents the least significant difference ($p < 0.05$).*

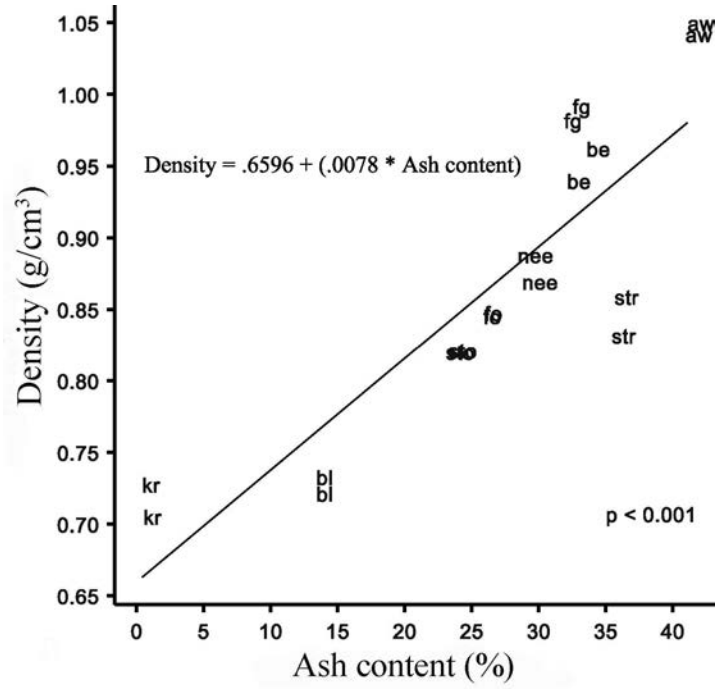

***Figure 4.6**: Relationship between density and ash content.*

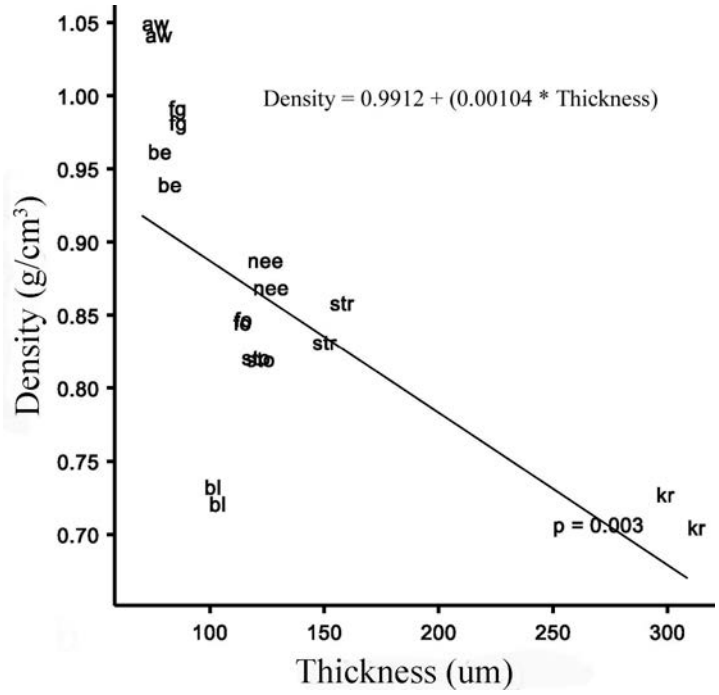

***Figure 4.7**: Relationship between density and thickness.*

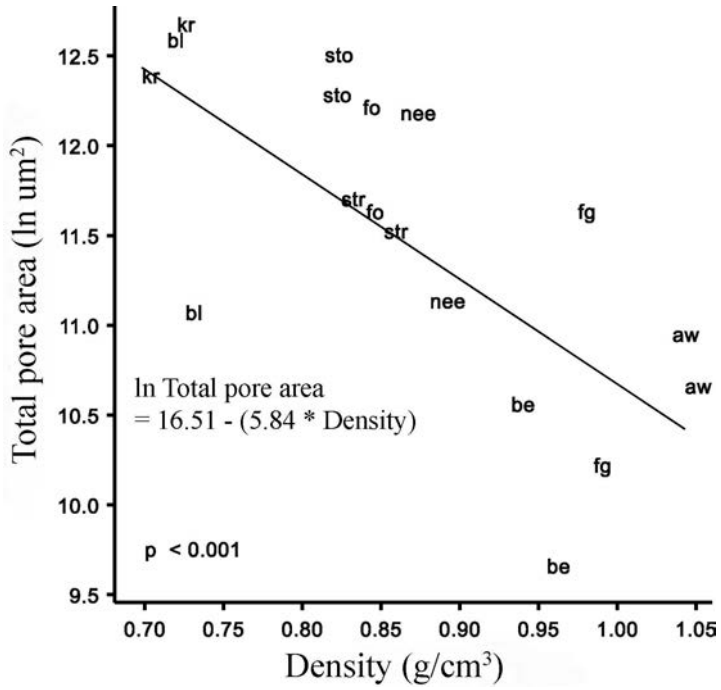

***Figure 4.8**: Relationship between paper density and total pore area.*

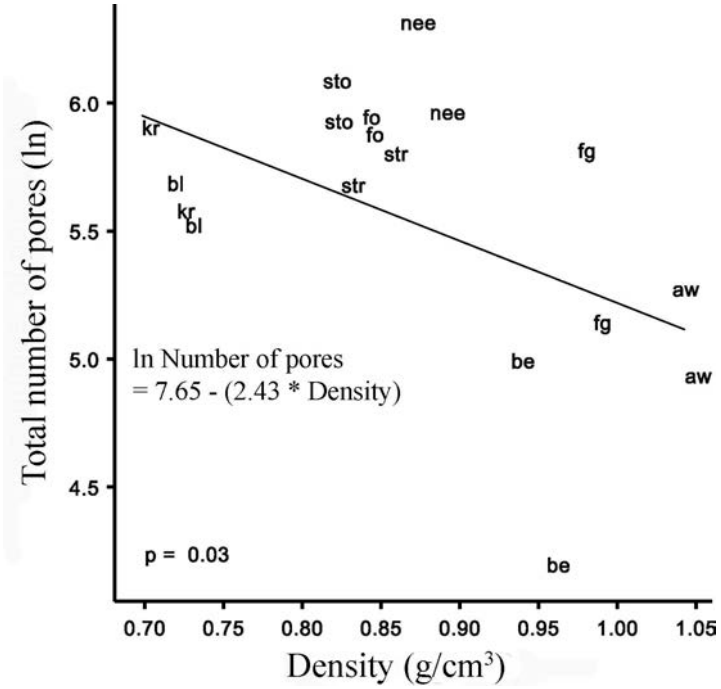

***Figure 4.9**: Relationship between paper density and total number of unfilled pores.*

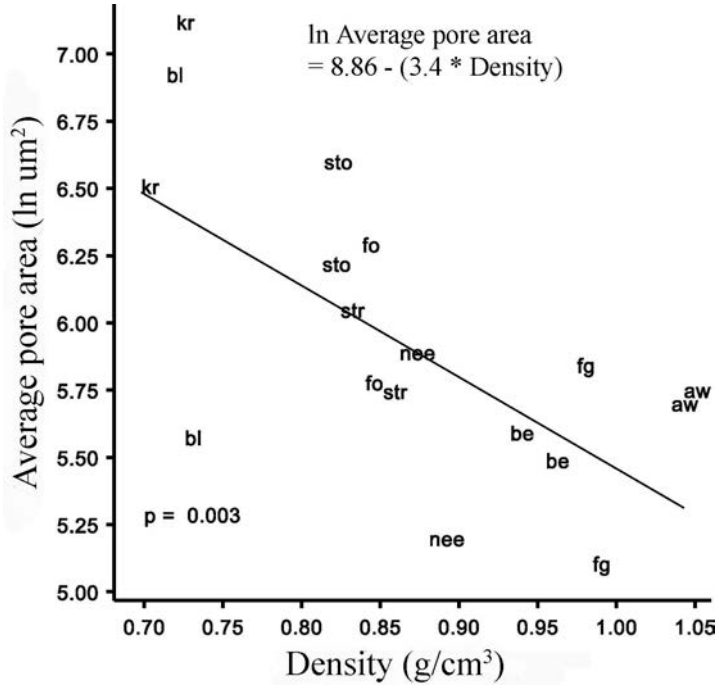

***Figure 4.10**: Relationship between paper density and the average area of unfilled pores.*

4.3.1.2 Paper thickness

There were significant differences *($p < 0.001$)* in the thickness of the decor papers tested (Figure 4.11). The thickness of the papers varied from 70 μm for Alpine White and Beech to 300 μm for Kraft. There was a significant relationship between the total area of unfilled pores and paper thickness (*$p = 0.003$)*, the relevant regression equation explaining 39.8% of the variance (Figure 4.12). There was a significant relationship *($p = 0.001$)* between the number of unfilled pores and paper thickness, the regression equation explaining 50.5% of the variance (Figure 4.13). If this analysis had included Kraft the relationship would have been much weaker *($p = 0.04$)* with the explained variance reduced to 18.5%. There was no significant relationship between the average unfilled pore area and the thickness of paper.

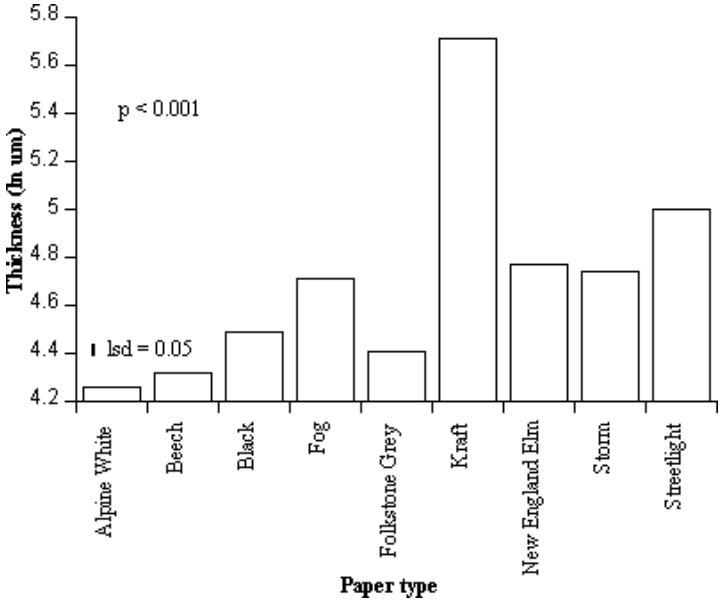

***Figure 4.11**: Thickness of the papers tested measured on a log scale.*

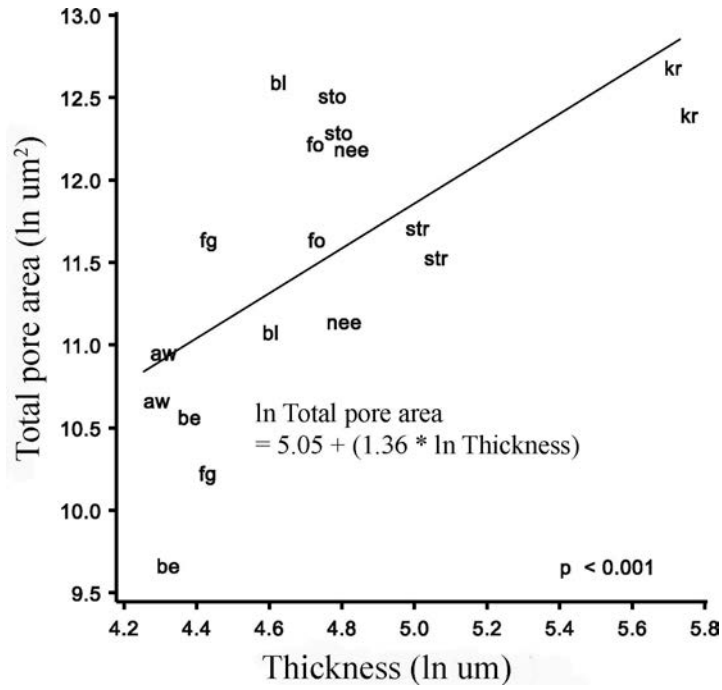

***Figure 4.12**: Relationship between paper thickness and total area unfilled pores (on a log scale).*

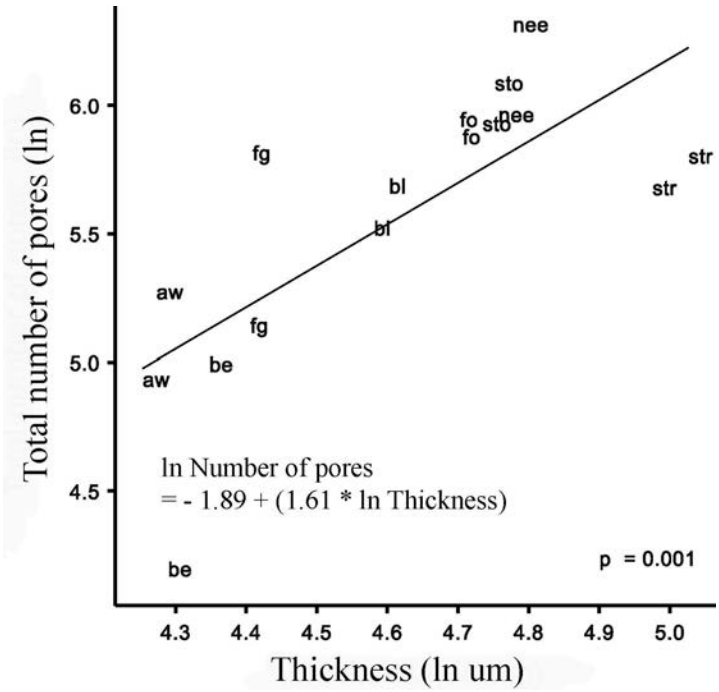

Figure 4.13: *Relationship between thickness of paper and total number of unfilled pores (measured on a log scale).*

4.3.1.3 Gurley porosity

There was a significant effect of paper type *($p < 0.001$)* on Gurley porosity (Figure 4.14). There was a very strong relationship between paper density and Gurley porosity *($p < 0.001$)*. The regression equation developed explained 84.2% of the variance (Figure 4.15) and showed that with increasing density the air permeability of decor papers decreased. There was also a significant relationship *($p < 0.001$)* between Gurley porosity and ash content (Figure 4.16). Regression analysis indicated that 56.7% of the variability in Gurley value was explained by variation in ash content. There was a negative correlation between ash content and the air permeability of the decor papers.

There was a significant relationship *($p = 0.004$)* between the average area of unfilled pores in papers after pressing and the Gurley porosity of the papers (Figure 4.17) with the relevant regression equation explaining 38.4% of the variance. The average area of unfilled pores decreased as the Gurley porosity value increased (air permeability decreased). There was no significant relationship between total number of unfilled pores or the log of total unfilled pore area and Gurley porosity.

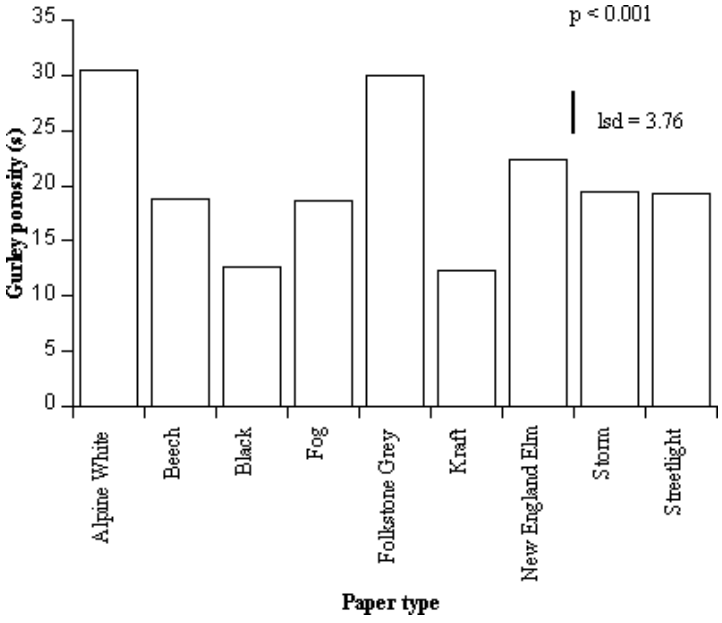

***Figure 4.14**: Effect of paper type on Gurley porosity.*

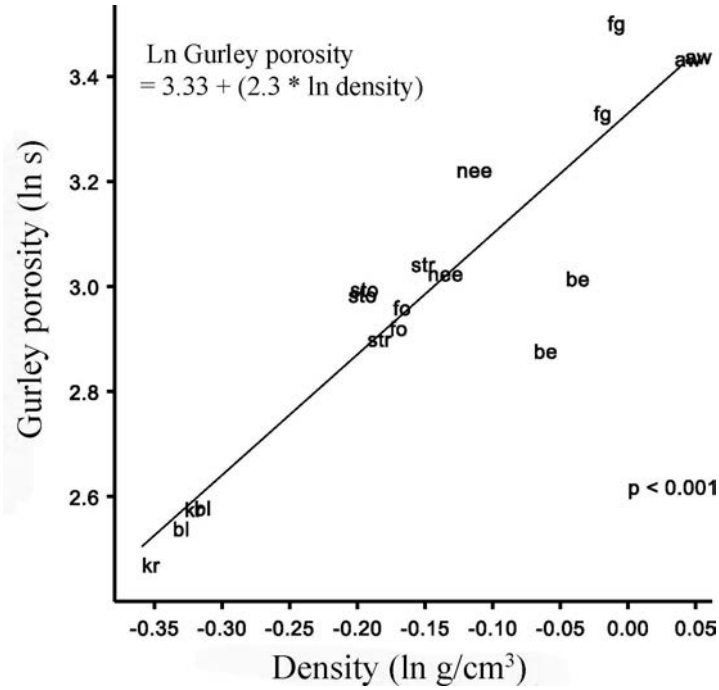

***Figure 4.15**: Effect of density on Gurley porosity.*

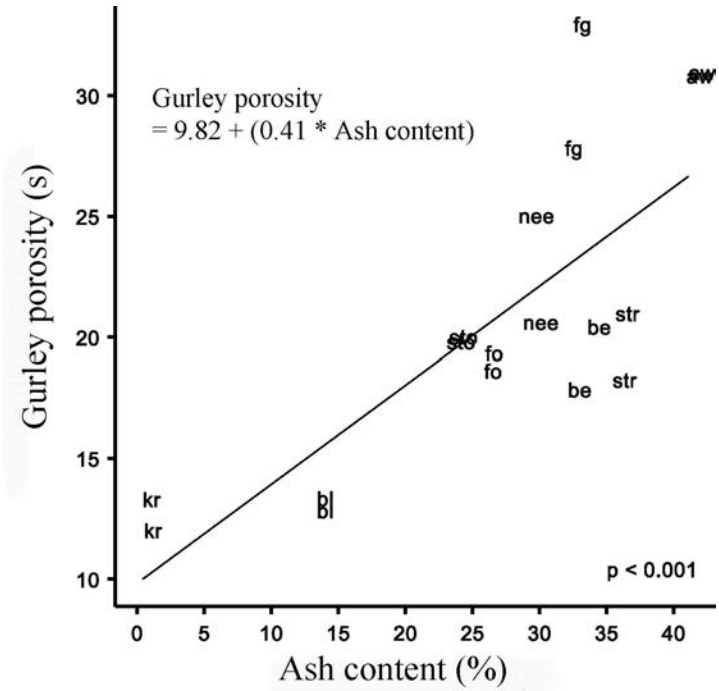

***Figure 4.16**: Effect of ash content on Gurley porosity.*

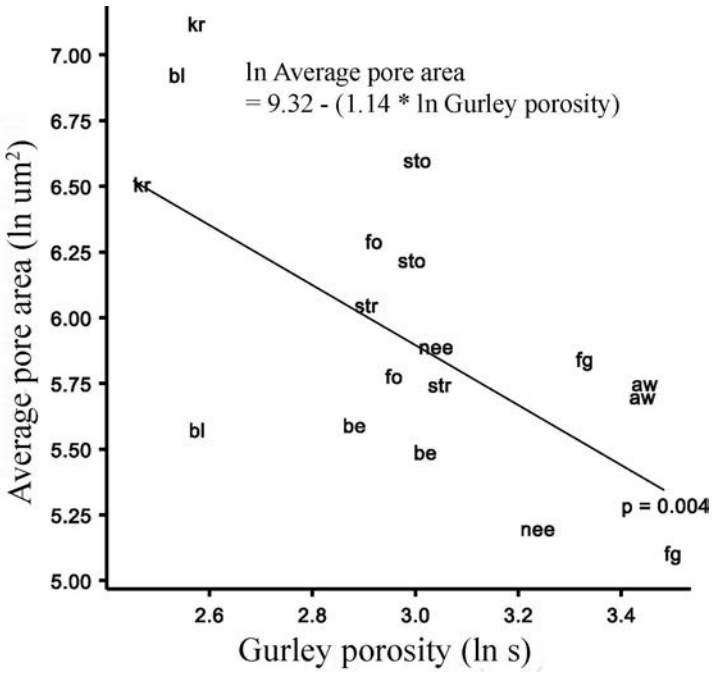

***Figure 4.17**: Relationship between Gurley porosity and average area of unfilled pores.*

4.3.2 Heterogeneity of paper and the relationship between fluid imbibition and suitability of decor papers for LPM

4.3.2.1 Klemm test

When the Klemm test was conducted with water there was a significant difference *($p < 0.001$)* in the wicking of water between paper types (Figure 4.18). Higher density, high ash, papers such as Alpine White, Beech and Folkstone Grey wicked up the smallest amount of water followed by New England Elm, Storm, Streetlight, Fog, Black and Kraft. Black and Kraft are the lowest density papers. In accord with the results for water wicking there was a significant difference *($p < 0.001$)* in the amount of DEG taken up by different paper types (Figure 4.19), but less DEG was taken up, irrespective of paper type (compare Figures 4.18 and 4.19). There was also less variation in the wicking of DEG compared to the wicking of water. The Klemm test was performed over a period of 10 minutes which might be insufficient for differences in the wicking of DEG by papers to develop.

There was a very strong relationship *($p < 0.001$)* between the results of the Klemm test carried out in the machine (MD) and cross-directions (CD) when water was used as the test liquid. The regression equation developed explained 99% of the variance (Figure 4.21). The relationship was not as strong *($p < 0.001$)* when DEG was used (Figure 4.22), the regression equation only explaining 63.7% of the variance. MD permeability was 0.73 x CD permeability,

i.e. the degree of anisotropy was greater with DEG. The relationship was considered strong enough, however, to use results of Klemm tests in the machine direction for further analyses.

There was a significant relationship *($p < 0.001$)* between the wicking of water and DEG between the different papers (Figure 4.20) with the variance explained by the regression equations being 72.4%.

There was a significant positive relationship *($p = 0.01$)* between the wicking of water in the machine direction measured using the Klemm test (Figure 4.23) and the total area of unfilled pores. The regression equation explained 30.6% of the variance. There was also a significant positive relationship *($p = 0.03$)* between the wicking of water in the machine direction and the number of unfilled pores (Figure 4.24). The regression equation explained 24.1% of the variance. With the inclusion of Kraft paper there was no significant relationship between the two variables. There was no significant relationship between the wicking of DEG in the machine direction measured using the Klemm test and the total area of unfilled pores, the total number of unfilled pores or the average unfilled pore area.

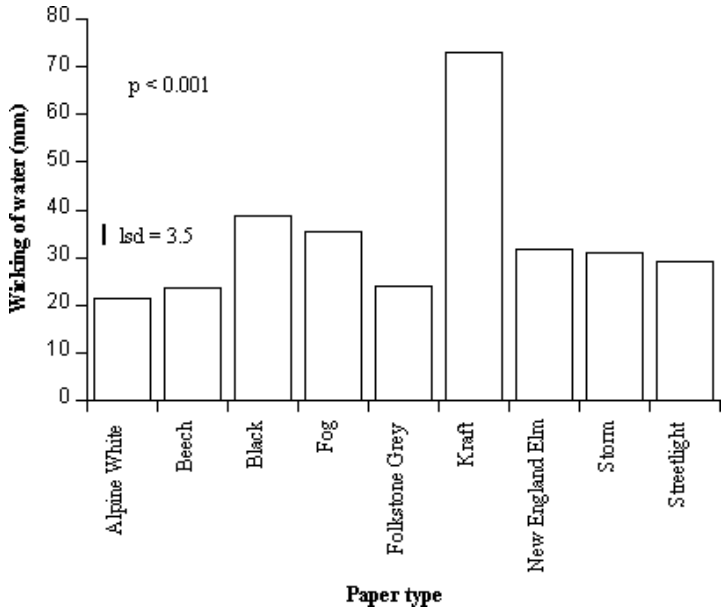

Figure 4.18: *Effect of paper type on the wicking of water in the machine direction as measured by the Klemm method*

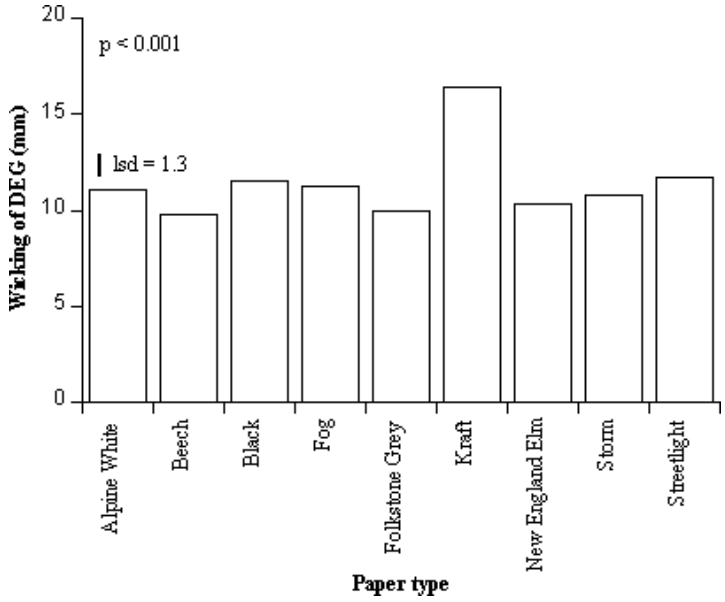

Figure 4.19: *Effect of paper type on the wicking of diethylene glycol in the machine direction as measured by the Klemm method*

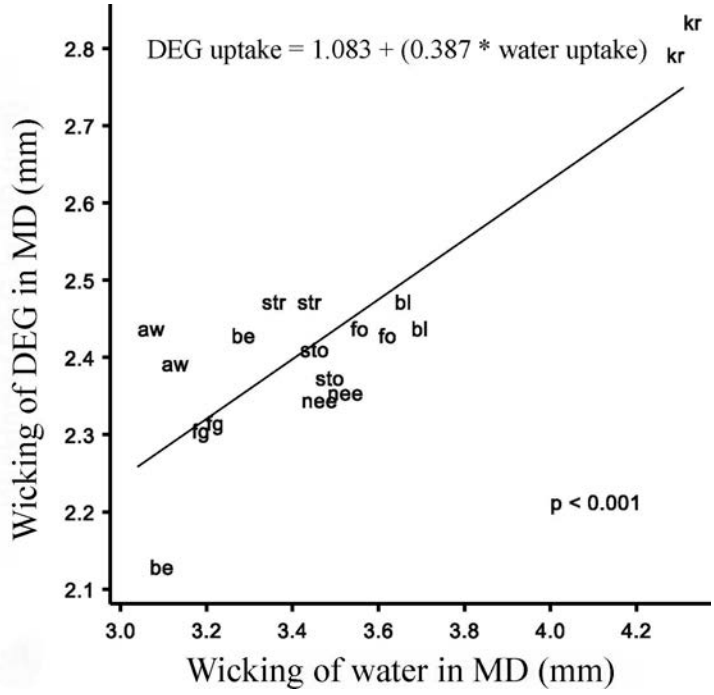

Figure 4.20: *Relationship between Klemm with diethylene glycol and the standard Klemm test in the machine direction.*

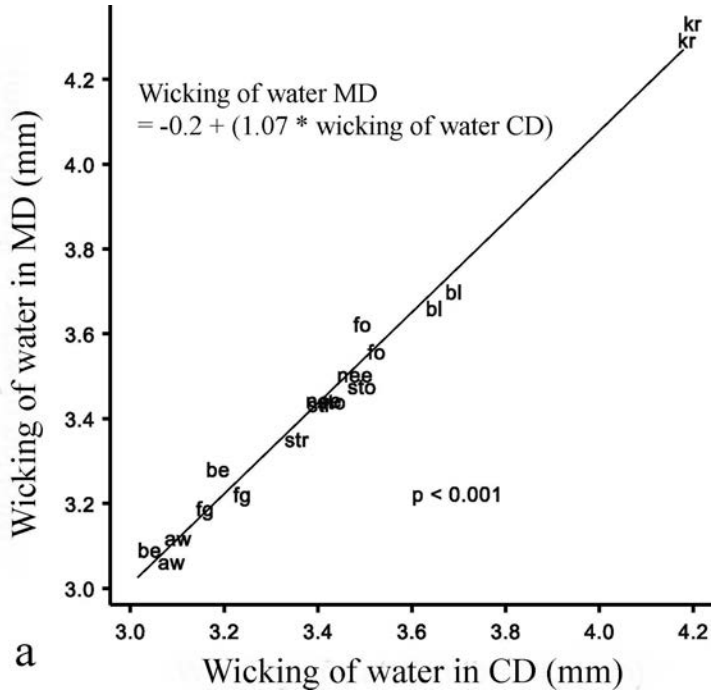

Figure 4.21: *Relationship between Klemm tests carried out with water in the machine and cross directions.*

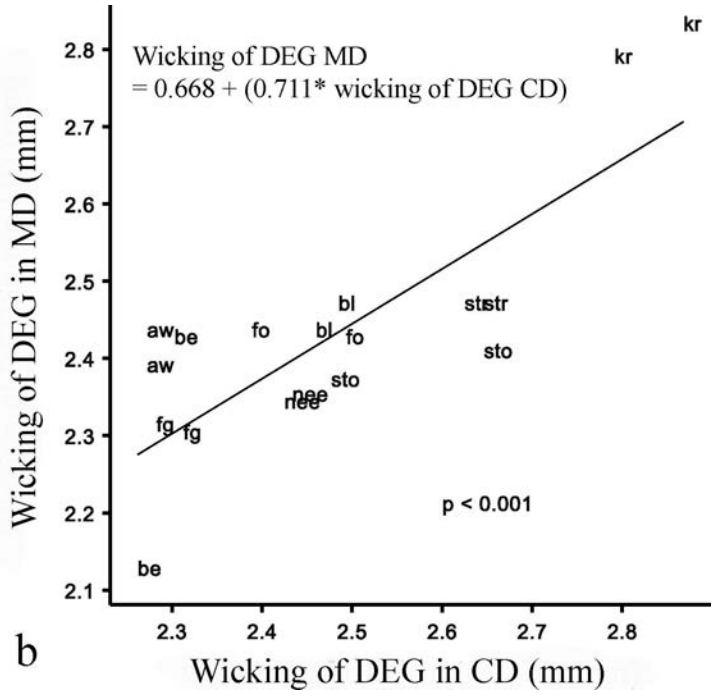

Figure 4.22: *The relationship with Klemm tests carried out in the machine and cross directions with diethylene glycol.*

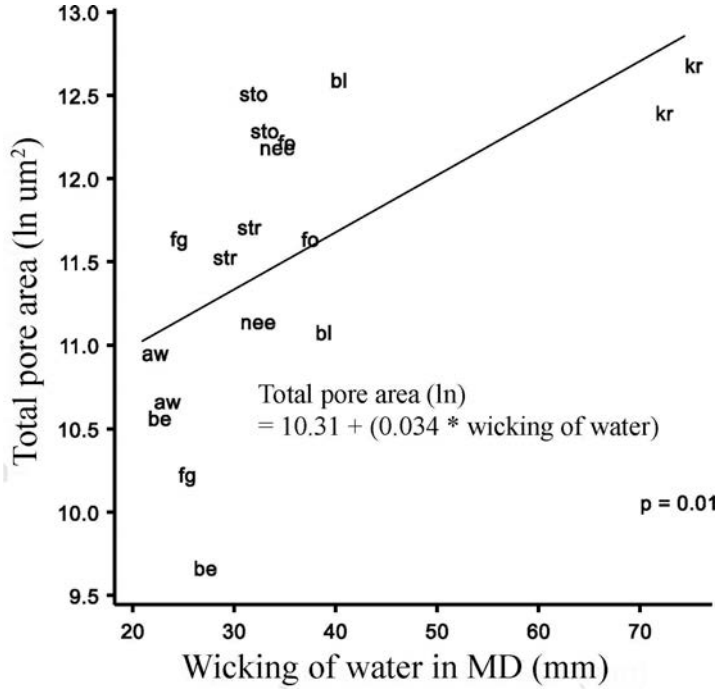

***Figure 4.23**: Relationship between Klemm MD and total area of unfilled pores.*

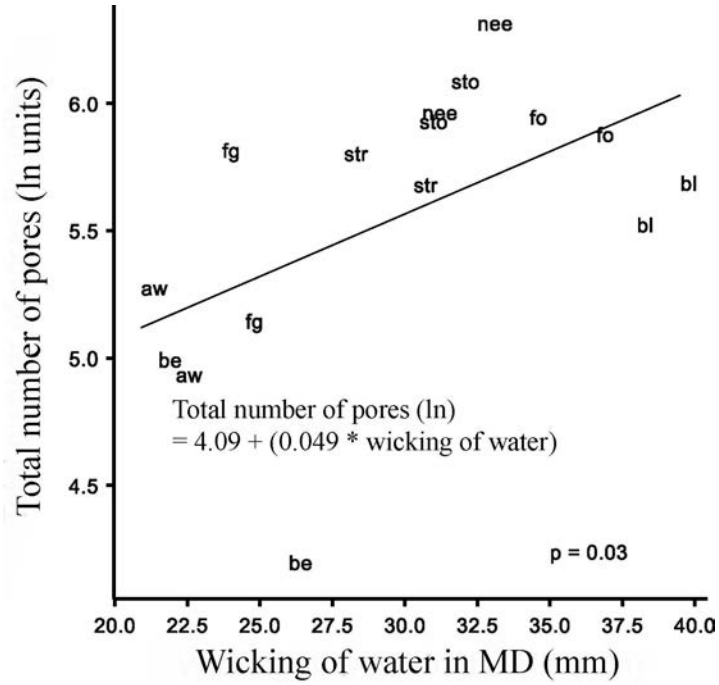

***Figure 4.24**: Relationship between Klemm MD and number of unfilled pores.*

4.3.2.2 Resin demand

There were significant differences in resin demand ($p < 0.001$) between the different paper types (Figure 4.25). There was a significant relationship ($p = 0.01$) between resin demand and total unfilled pore area with the regression equation explaining 28.7% of the variance (Figure 4.26). Papers with increased resin demand tended to have a greater total area of unfilled pores after pressing. There was a significant relationship ($p < 0.001$) between the resin demand of papers and total number of unfilled pores (Figure 4.27) The regression equation between the two variables explained 52.9% of the variance. Papers with a higher resin demand tended to have more unfilled pores after pressing, in accord with results shown in Figure 4.26. There was no significant relationship between the resin demand of paper and the average unfilled pore area after pressing.

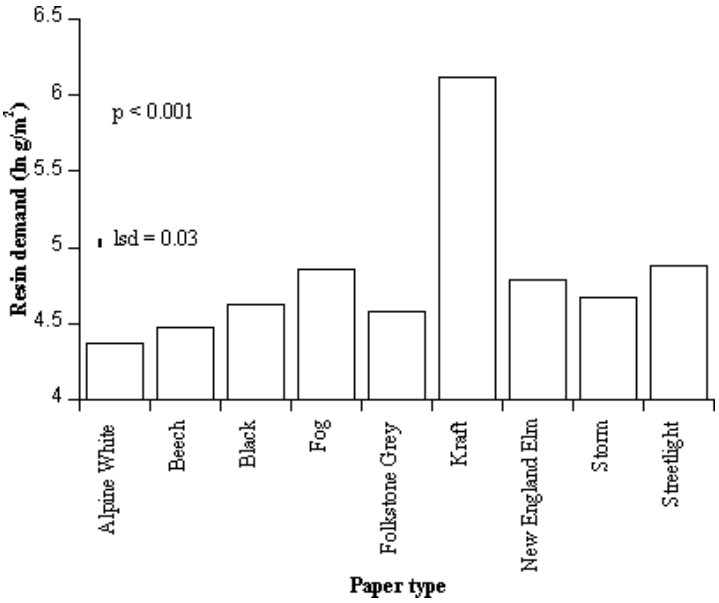

***Figure 4.25**: Effect of paper type on resin demand.*

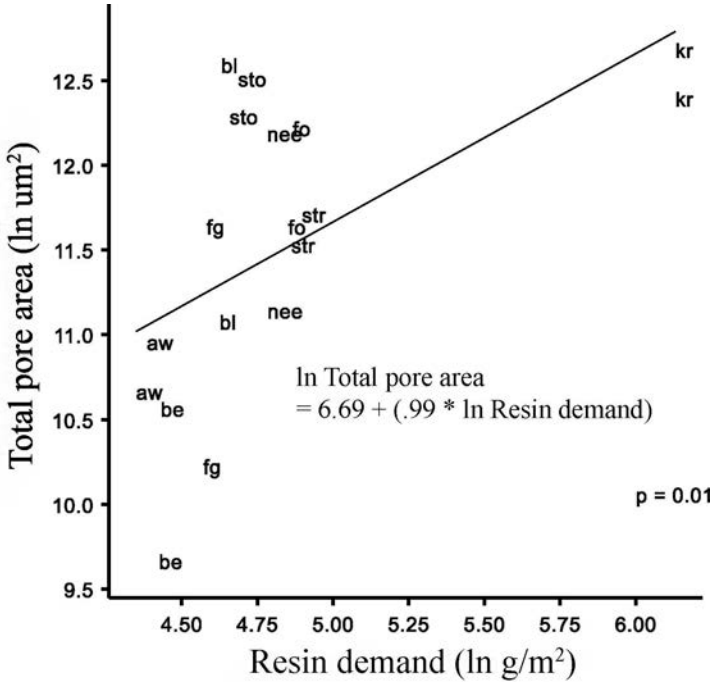

***Figure 4.26**: Relationship between resin demand and total area of unfilled pores.*

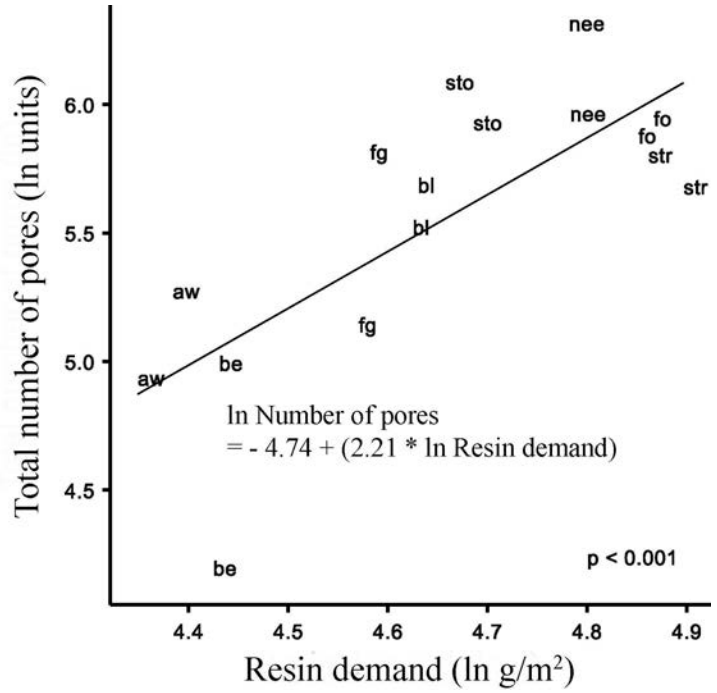

***Figure 4.27**: Relationship between resin demand and total number of unfilled pores.*

4.3.2.3 Inverted bottle test

There was a significant difference *($p < 0.001$)* between paper types with the saturation times of different paper types as determined by the inverted bottle test (Figure 4.28). Beech and Black saturated fastest followed by Alpine White, Fog, Folkstone Grey, New England Elm and Storm, Kraft and Streetlight. The data is untransformed and expressed in seconds. When results are corrected for paper thickness (s/100μm) the ranking of papers completely changed, however the effect was still significant *($p < 0.001$)* (Figure 4.29).

When uncorrected saturation data was plotted there was no difference between papers such as Fog and Folkstone Grey. Correcting data for thickness resulted in a significant and substantial decrease in saturation time for Folkstone Grey compared to Fog. Furthermore, differences between Alpine White and Beech and Black became more pronounced when corrected data was used for the comparison. Alpine White, Folkstone Grey and Streetlight saturated slowly. Saturation values for Black and Beech when uncorrected for thickness were similar, but when data was corrected for thickness the rate of saturation of Beech was significantly and substantially lower than that of Black. Kraft saturated slowest on the basis of uncorrected data, but when corrected for thickness it saturated fastest. All subsequent imbibition data in the z direction is corrected for thickness and is presented as seconds per 100 microns (s/100 μm), which is close to the average thickness of decor papers.

There was no significant relationship between the rate of saturation determined by the inverted bottle test and the number of unfilled pores, total unfilled pore area and average area of unfilled pores.

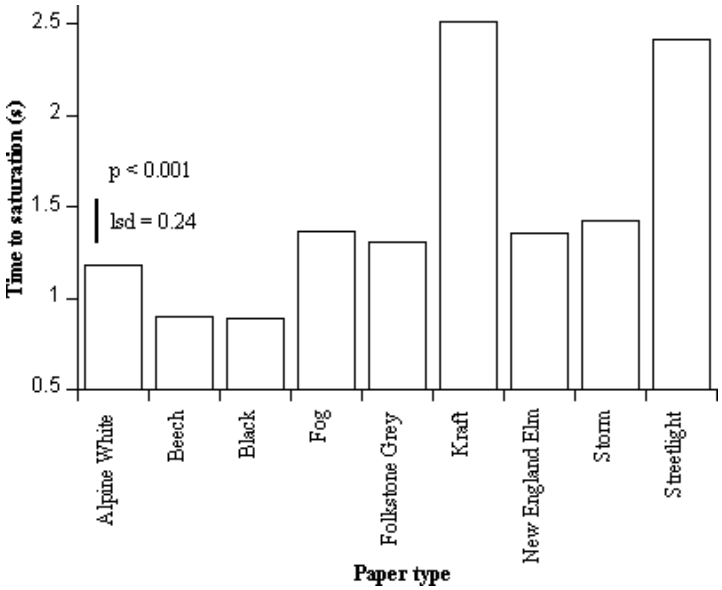

Figure 4.28: *Effect of paper type on the rate of saturation of DEG using the inverted bottle test, uncorrected for thickness (s).*

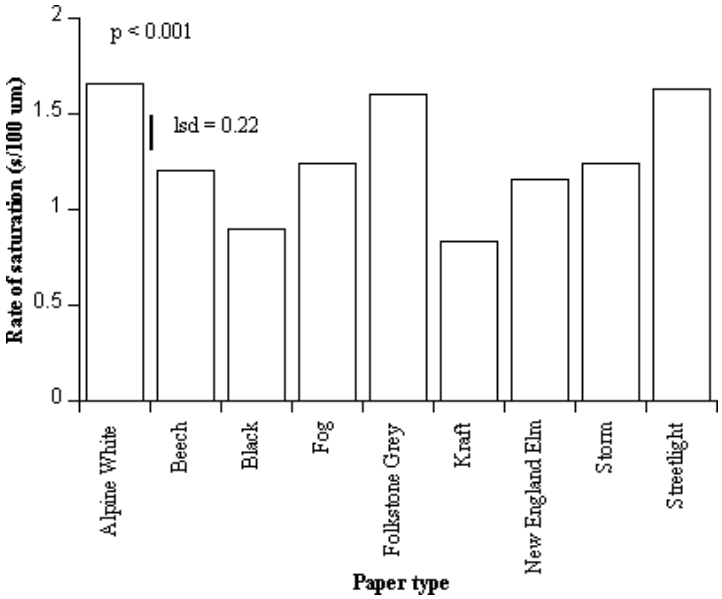

Figure 4.29: *Effect of paper type on the rate of saturation of DEG using the inverted bottle test, corrected for thickness (s/100 µm).*

4.3.2.4 Rate of saturation to 50% & 95% using relative reflectance method

There was a significant effect of paper type on rate of imbibition to 50% *(p = 0.02*, Figure 4.30) and rate of imbibition to 95% *(p = 0.03,* Figure 4.31) when results were corrected for thickness. There was no relationship however between these two measures of saturation. Fog, Kraft and Storm were significantly slower than other papers to saturate to 50%. Beech, Black, New England Elm and Storm were significantly slower than the other papers to saturate to 95%. Interestingly Beech was one of the fastest papers to saturate to 50% and the slowest to saturate to 95%.

There was a significant relationship *(p = 0.033)* between the rate of imbibition to 50% saturation and total area of unfilled pores (Figure 4.32). The regression equation explained 20.7% of the variance. As the rate of saturation (50%) decreased, the total area of unfilled pores increased after pressing. There was a significant relationship between total number of unfilled pores and rate of imbibition to 50% saturation *(p = 0.011)*. The regression equation explained 29.7% of the variance (Figure 4.33). As the rate of saturation to 50% decreased, the total number of unfilled pores increased after pressing. There was no relationship between the rate of saturation to 50% and average pore area. There was no relationship between the rate of saturation to 95% and any of the measures of defects in resinated pressed paper, total pore area, total number of pores, or average pore area.

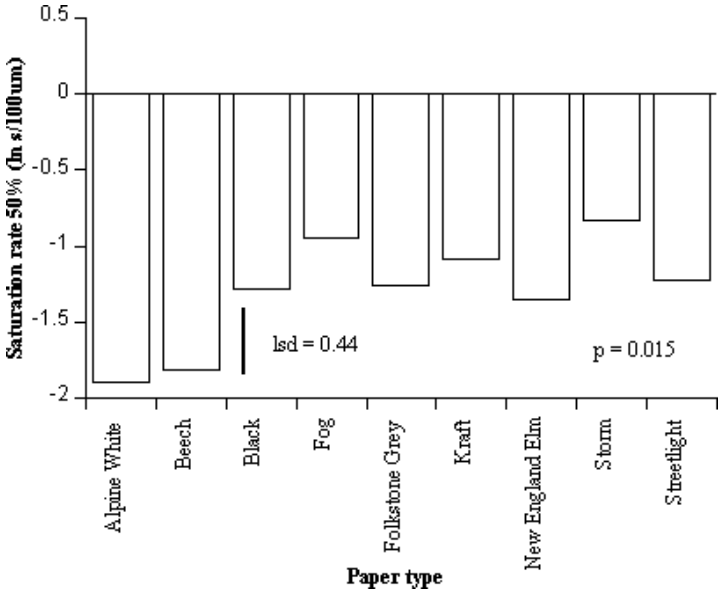

Figure 4.30: *Effect of paper type on time taken to saturate to 50% of the decor paper sample as determined by the relative reflectance method corrected for thickness. Measure is seconds/100µm measured on a log scale.*

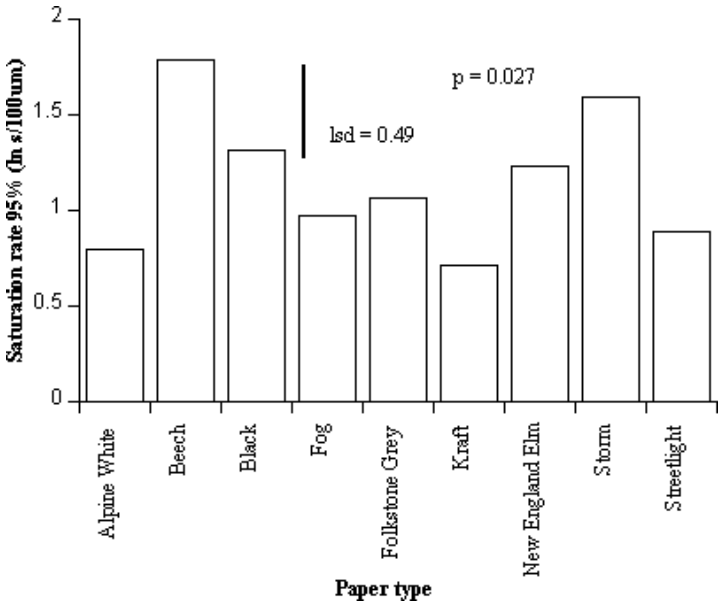

Figure 4.31: *Effect of paper type on time taken to saturate to 95% of the decor paper sample as determined by the relative reflectance method corrected for thickness. Measure is seconds/100µm measured on a log scale.*

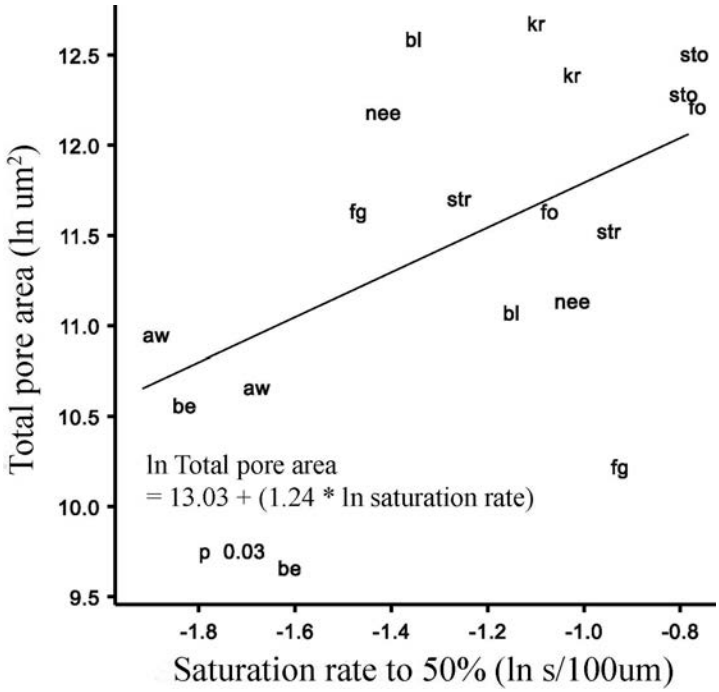

Figure 4.32: *Relationship between the rate of imbibition to 50% saturation and the log of total number of pores.*

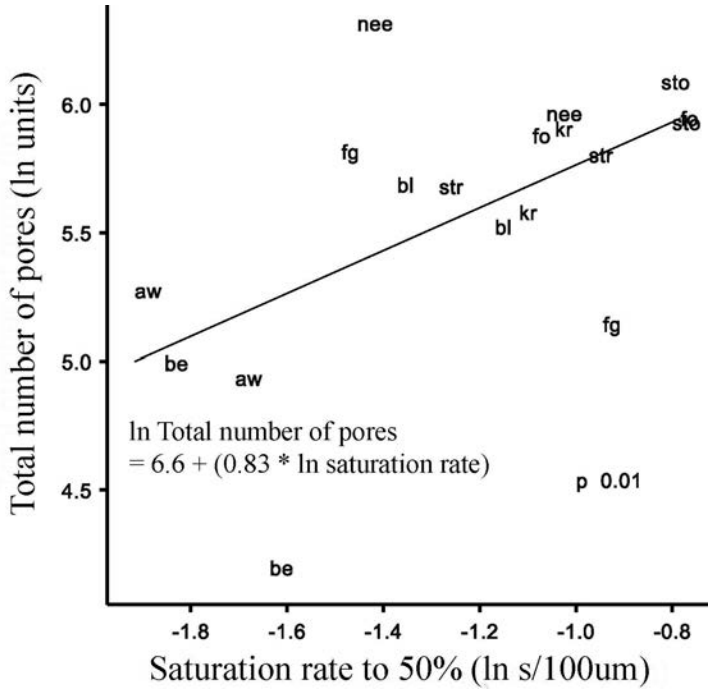

Figure 4.33: *Relationship between the rate of imbibition to 50% saturation and the log of total number of pores.*

4.3.3 Relationship between the imbibition of liquids into decor papers and their physical characteristics

4.3.3.1 Klemm tests

There was a significant relationship *($p < 0.001$)* between Klemm MD using water and density (Figure 4.34), the regression equation explained 73.5% of the variance. Clearly, reducing paper density resulted in increasing levels of wicking of water. There was a relationship between wicking of DEG (Klemm) MD and density *($p = 0.005$)* (Figure 4.35) however it was not strong with the regression equation only explaining 36.1% of the variance, but again the trend was similar to that observed with water.

There was a significant relationship *($p = 0.002$)* between water wicking in the machine direction measured using the Klemm test and Gurley porosity. The regression equation explained 42.1% of the variance. These findings suggest, as might be expected, an inverse relationship between the Gurley value and the wicking of water, *i.e*, the greater the air permeability the larger the wicking of water (Figure 4.36). There was a significant relationship (p = 0.03) between wicking of DEG (Klemm) in the machine direction and Gurley porosity with the regression equation explaining 21.7% of the variance (Figure 4.37). This relationship was similar to that observed for the water-based Klemm tests.

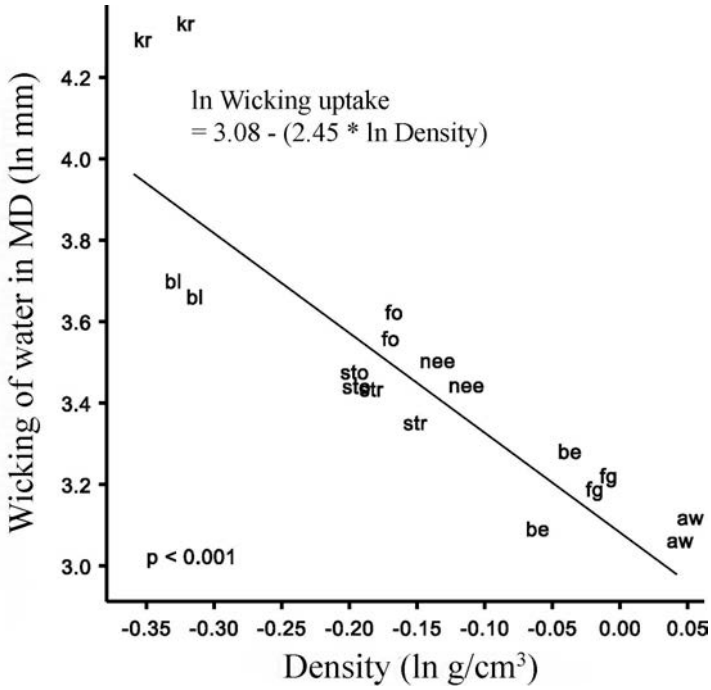

Figure 4.34: *Relationship between the Klemm test with water in the machine direction and density, the higher the density the lower the Klemm wicking of either water or DEG.*

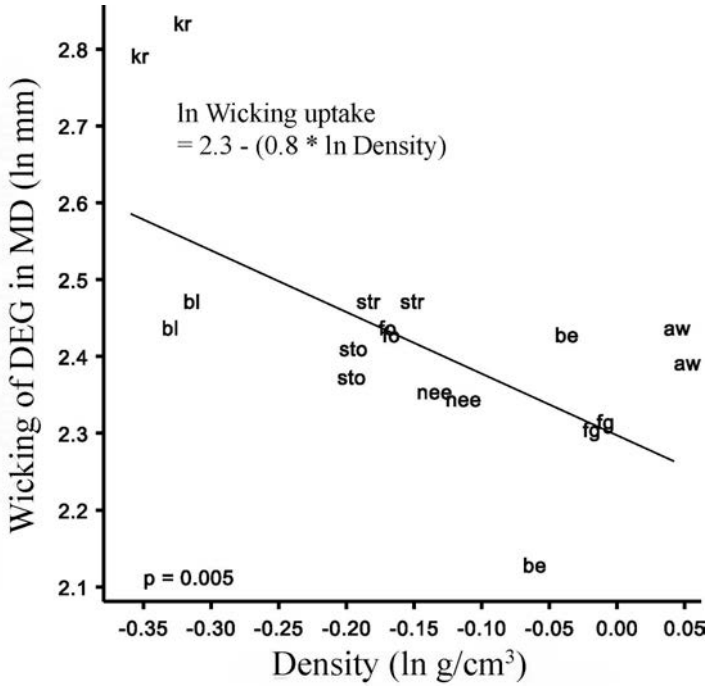

Figure 4.35: *Relationship between the Klemm test with DEG in the machine direction and density, the higher the density the lower the Klemm wicking of either water or DEG.*

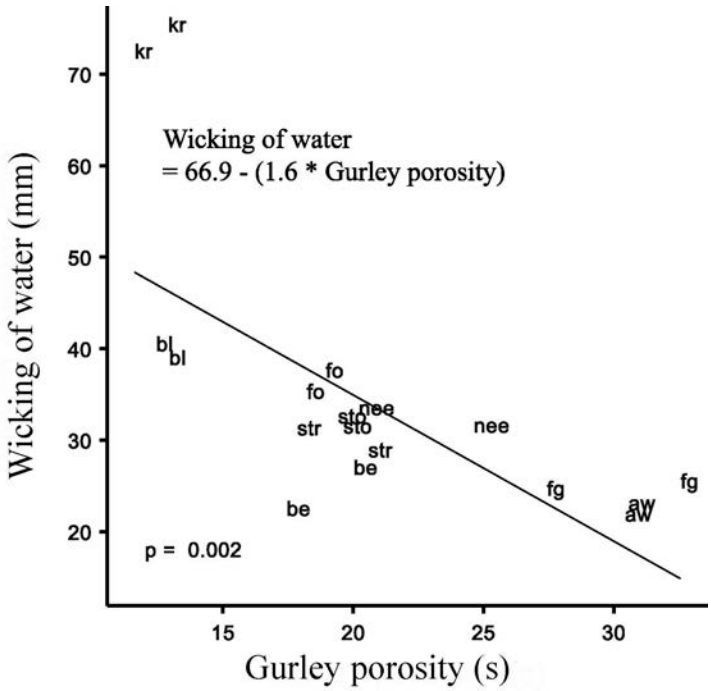

Figure 4.36: *Relationship between Klemm MD and Gurley porosity, without Kraft showing that increasing air permeability increases Klemm wicking.*

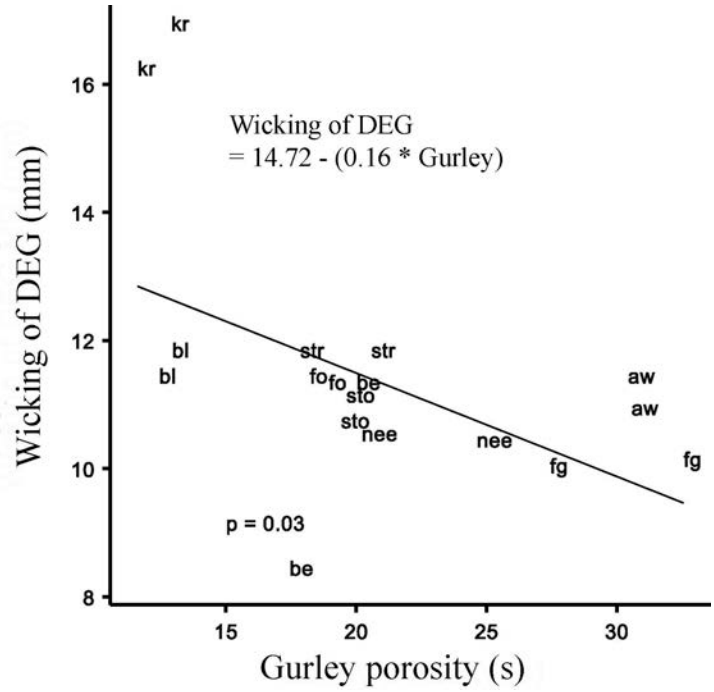

Figure 4.37: *Relationship between Klemm MD with DEG and Gurley porosity showing a similar trend to that of water where with increasing air permeability the Klemm wicking increases.*

4.3.3.2 Resin demand

There was an inverse relationship *($p = 0.01$)* between density and resin demand (Figure 4.38). The regression equation explained 30% of the variance. There was a statistically significant but not very strong relationship *($p = 0.007$)* between resin demand and Gurley porosity with the regression equation explaining 33.2% of the variance (Figure 4.39). Resin demand decreased as the Gurley values of the paper increased.

There was a significant relationship *($p < 0.001$)* between resin demand and Klemm wicking of water in the machine direction, the regression equation explaining 82.9% of the variance (Figure 4.40). Increasing Klemm wicking resulted in increasing resin demand.

There was a significant relationship *($p < 0.001$)* between resin demand and Klemm wicking of DEG in the machine direction with the regression equation explaining 74.4% of the variance Figure 4.41 shows the same trend as for the uptake of water. If Kraft was removed from the analysis, however, there was no relationship between the two variables.

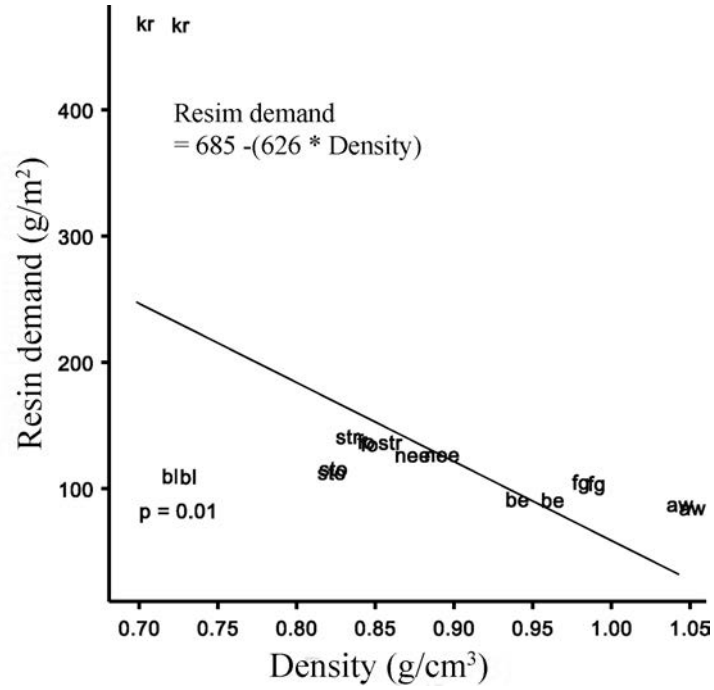

***Figure 4.38**: Relationship between resin demand and density.*

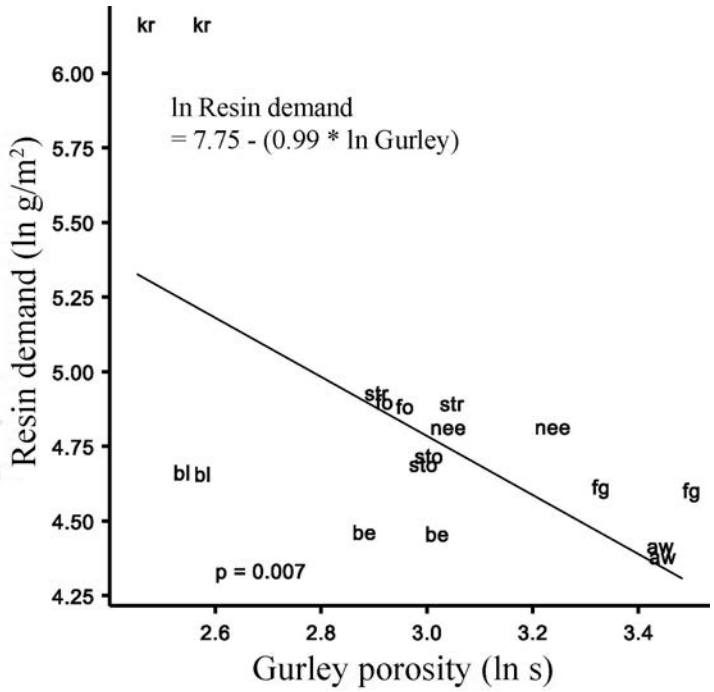

***Figure 4.39**: Relationship between resin demand and Gurley porosity.*

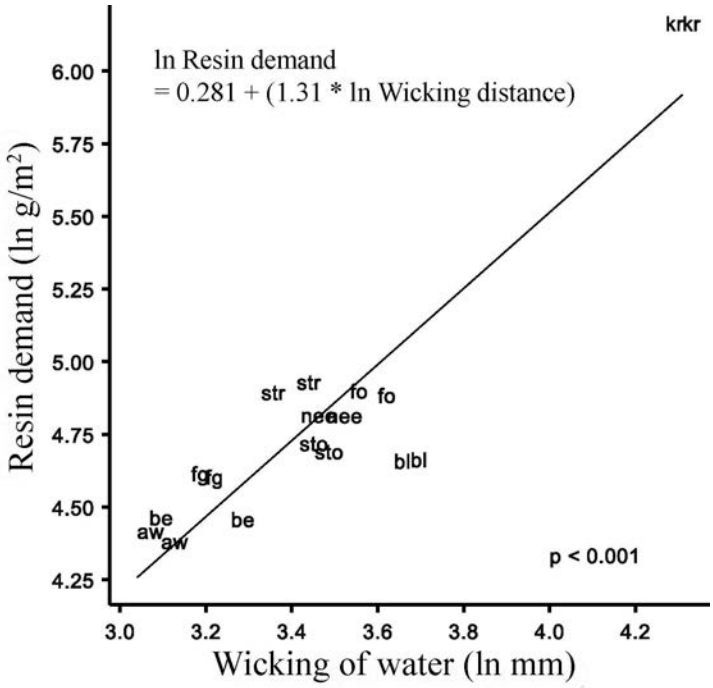

Figure 4.40: *Relationship between resin demand and wicking of water in the machine direction using the Klemm test.*

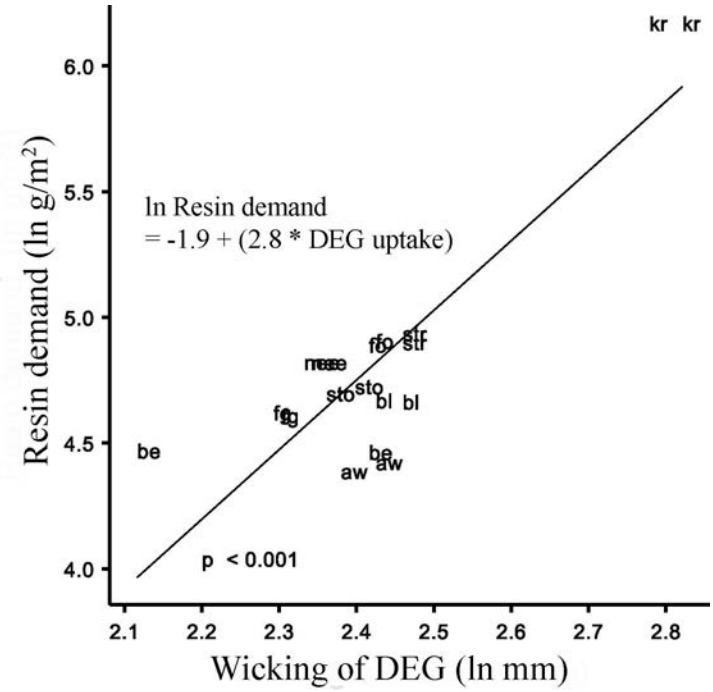

Figure 4.41: *Relationship between resin demand and wicking of DEG in the machine direction using the Klemm test.*

4.3.3.3 Rate of saturation to 50% using relative reflectance method

There was a significant relationship between rate to 50% saturation and paper density *(p = 0.017)* the regression equation explaining 26.6% of the variance (Figure 4.42). Increasing density increased the imbibition rate to 50% saturation. There was no relationships between a) the rate to 50% saturation and the Klemm wicking of water or DEG in the machine direction, b) between the rate to 50% saturation and the rate of saturation as determined by the inverted bottle test, c) between the rate to 50% saturation and resin demand of the papers and d) between air permeability as measured by the Gurley method and rate of imbibition to 50%.

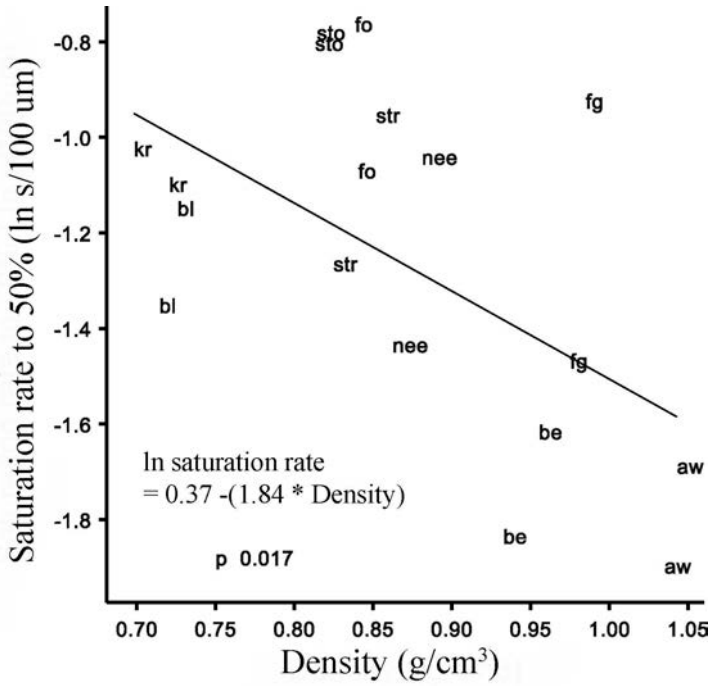

Figure 4.42: *Relationship between log of the rate to 50% saturation as measured on a log scale with density.*

4.4 Discussion

4.4.1 Relating measures to defect levels

It was shown in this Chapter, as expected, that there was considerable heterogeneity in the physical characteristics of decor papers. Measures of these physical characteristics are used commonly by both manufacturers and end users of decor papers to predict the suitability of the papers for resin treatment and pressing. These characteristics were found here to be weakly related to the pressing performance of the decor papers. There were relationships between density, thickness and Gurley porosity and the presence of defects in decor paper but the strength

of the relationships are not sufficient to accurately predict performance of decor paper in an industrial situation.

It was demonstrated in Chapter 3 that defects in LPM panels were caused by two fluid flow problems; firstly flow of MF resins into unfilled voids in the resinated decor papers during pressing and secondly by insufficient flow of UF resins into the paper during the impregnation process. It was shown here that there was considerable heterogeneity in the imbibition characteristics of the different decor papers. The pressing performance of decor papers was found to be related, by varying degrees to the physical and imbibition characteristics of the paper.

The presence of defects in resinated pressed decor papers was related to their density. Higher density papers showed fewer defects than lower density papers. Density was the only factor commonly used by manufacturers and end users which was related to all three measures of surface defects in MF coatings, *i.e.* total unfilled pore area, total number of unfilled pores and average unfilled pore area. Density of paper is a function of the proportion of inter-fibre and intra-fibre void space present after manufacture (Biermann, 1996; Mark et al., 2002). Higher density papers would have a lower proportion of void space than lower density papers. From this one could infer that papers with less void space *i.e.* smaller pores would generate less defects. However, density and hence the proportion of void space in a paper is primarily a function of two characteristics, firstly how much inorganic filler has been added to the papers and secondly how effectively are the fibres crushed in the paper making process. The addition of filler would increase density by replacing air in void spaces and so reducing the volumes of the void spaces in the paper structure available to imbibing resins. Thinner or calendared papers would also be expected to have smaller void spaces than thicker and uncalendared papers. However from the data in this chapter it is not possible to determine what characteristic of density *i.e.* the addition of filler or how much a paper is pressed affected the generation of defects because the highest density papers such as Alpine White, Fog and Beech not only had high ash contents, but were also calendared. The effect of the addition of filler on paper structure is dealt with at length in Chapter 7 and in particular the effect of fillers on decor papers is detailed in Chapter 8.

One of the most widely used measures of the efficacy of decor papers is Gurley porosity (air permeability). It is a measure of air resistance of paper and can be used as an indirect measure of absorbency by liquids such as oils and water, but is most useful as a control test for machine production (TAPPI, 1992). The air permeability measured by Gurley was found here to be closely related to density and ash content however it was only weakly related to the generation of defects in pressed LPM panels. Specifically Gurley porosity was found to be inversely related to average unfilled pore area. This is still consistent with the relationship of density to defects.

Another widely used method to determine the efficacy of decor papers is the Klemm test which measures fluid flow (water) in the x & y directions (notwithstanding the fact that im-

pregnation of resins occurs in the *z* direction). There was a consistent relationship between the wicking of water and DEG in the machine direction and it was shown that papers with increased rates of fluid flow in the *x & y* directions showed greater total area and greater numbers of unfilled pores in decor papers after pressing. Imbibition rates in the *x & y* directions measured using the Klemm test were also shown to be related to density. Higher density papers wicked up less water and DEG and tended to be the ones with the fewest unfilled pores.

Eklund and Salminen (1987) related air permeability to fluid flow and introduced the concept of the counter pressure of air on fluid uptake by paper. They suggested that air trapped in the pore system of paper could cause a high counter pressure that would restrict penetration of liquids into paper over short time scales. Furthermore they suggested that the counter pressure was so high that water penetration at low pressures must take place as a result of other mechanisms other than that caused by surface tension forces. The Gurley value is a measure of specific air resistance and therefore at higher Gurley values (lower air permeability) one would expect reduced rates of fluid imbibition. This was the case here. The wicking of both water and DEG measured with the Klemm method with the results followed the same trend. Higher density papers had lower wicking distances which appears to accord with the findings of Eklund and Salminen (1987). However when looking at flow in the *z* direction with saturation to 50%, increasing density resulted in an *increased* rate of imbibition. This finding puts into question the validity of using fluid imbibition measures in the *x & y* dimensions for predicting flow in the *z* dimension which is the dimension for the flow of resin during decor paper treatment. In addition there was no relationship between the Gurley value and the rate of saturation to 50%. This raises significant doubts about the value of using air permeability to predict fluid flow in the *z* direction.

Similar trends were observed for the overall resin demand of a paper *i.e.* the total capacity of decor papers to absorb a liquid. Papers that absorbed more liquid were the ones that developed higher levels of unfilled pores after pressing and also were the ones that had lower densities.

When rate-based measures of fluid flow in the *z* direction were investigated the relationship between presence of defects in treated paper and rate of fluid flow was not so clear. There were significant differences in rates of saturation as determined by the inverted bottle test when corrected for thickness, however the presence of defects was not related to rate of saturation. This was related in part to the shortcomings of this visually based method and specifically to problems in accurately determining the end point of saturation.

There was, however a clear relationship between imbibition rate to 50% saturation measured by relative reflectance and the amount of defects present in pressed resinated paper. This is one of the most significant findings of this chapter. Interestingly there was no relationship between level of defects and imbibition rate to 95% saturation. This is illustrated by Beech which saturated very rapidly to 50% and then very slowly to 95%. It had a heterogeneous

distribution of filler as shown in Chapter 3 (Figure 3.43), resulting in very small pores on and just below the surface and much larger pores toward the centre of the paper. According to Kent and Lyne (1989a,b) who discussed in detail the effects of divergent pores on fluid flow, pores close to the surface would saturate rapidly and the larger pores in the centre of the paper would saturate more slowly. Other papers that were slow to saturate to 95%, Black, New England Elm and Storm also had the largest surface and subsurface pores as can be seen in the relevant SEM images of the raw papers (Figures 3.18 & 3.19). The papers that saturated fastest to both 50% and 95% appear to have a much narrower distribution of pore sizes and in particular had smaller pores on and below the surface. This suggests that the structure of paper influences the performance of decor papers and in particular the nature of the sub-surface void space. This is examined in more detail in Chapters 7 & 8. Yamazaki and Munakata (1993) also examined the effect of paper structure on liquid absorption. They developed a liquid absorption model which included tortuosity and mean pore radius, and found that a reduction of pore volume brought about by calendering decreased the porosity and the mean pore radius (on the surface of paper), but increased the tortuosity resulting in a slowing of imbibition. This contradicts Kent and Lyne (1989a,b) and results here which showed that higher density papers, with smaller void volumes saturated faster.

There was no relationship between the rate to 50% saturation and the Klemm wicking of water or DEG in the machine direction. This is in contrast to Winspear (1979) who found a moderate correlation between capillary rise using the Klemm test and transverse penetration rate for unsized papers. As mentioned above this puts into question the use of imbibition measures in the *x & y* dimensions predicting flow in the *z* dimension. This finding is noteworthy as the Klemm test is probably the most commonly used method of determining the efficacy of decor papers.

Ketoja et al. (2001) also found that density affected the rate of fluid flow. They measured the variation in light transmittance values of saturating paper using a high speed CCD in order to determine the rate of imbibition of liquids from the inter-fibre pore space into fibres. They found that as density and total fibre surface area increased, the rate of fibre sorption increased. The amount of water in the inter-fiber pores was sorbed faster if paper density was high. They concluded that it takes only a few microseconds for water to fill the topmost pores of an uncoated paper. This was followed by much slower water sorption into fibers, which lasted over a few seconds. The importance of fluid flow into fibres at short time scales is discussed in Chapter 6.

An interesting outcome of the development and use of the relative reflectance method was that both Black and Kraft were the only papers to exhibit a wetting delay, both taking 0.1 s & 0.3 s respectively to register changes in reflectance on the top surface of the paper (Figures B.1a & c & B.2a & c). The concept of a wetting delay was introduced by Bristow (1967) and subsequently referred to by others (Hoyland, 1977; Pan et al., 1988; Kent and Lyne, 1989a,b;

Lepoutre, 1990). They thought that the wetting delay was caused by the time taken for large open pores on the surface of paper to fill up with liquid. Both Black and Kraft had very low inorganic ash contents and had very open pore structures, however the delay for Black and Kraft is believed to be an artifact of the reflectance test method. Even though wetting may have taken place immediately upon contact of liquid with the paper, it took a short period of time before any changes in reflectance could be measured on the other side of the papers. Black has a high carbon black content and Kraft is a thick unbleached paper resulting in both papers being strongly opaque. Thus the initial wetting on the bottom of the paper would not have resulted in any change in reflectance on the top surface of those papers. This supports Eklund and Salminen (1987) who refuted the idea of a wetting delay.

4.5 Conclusion

There are three main findings from this Chapter. The first is that of all the measurements used by paper makers to determine the suitability of decor papers for the production of LPM only density was found to be related to the level of defects produced as a result of inadequate treatment. Therefore it seems reasonable to conclude that the "paper effect" in fact is related to the density of the decor papers. From this Chapter it was not possible to determine exactly whether the density effect was related to fibre density or whether papers had been calendared or not, or the amount of filler. However as the correlation between ash (filler) content and density was so strong it seems reasonable to conclude that the density effect was probably related to the amount of filler in a paper. This will be looked at in much more detail in Chapters 7 & 8.

Secondly, measures of air permeability, and fluid flow in the x y dimensions were unable to predict fluid flow in the z dimension which casts doubt on whether they are useful for predicting the performance of decor paper, yet they are commonly used.

Thirdly there was a reasonable relationship between the rate of imbibition to 50% saturation and the production of defects. Given this relationship and the fact that it was shown that defects in LPM panels were caused by two fluid flow problems, the remainder of this thesis will deal with the issue of the kinetics of fluid flow in paper.

Finally, the relative reflectance method developed here is an improvement over existing test methods in giving an indication of the performance of decor papers.

Chapter 5

Mechanisms of Liquid Imbibition

The proposed mechanisms of liquid imbibition in porous media are presented in this chapter. In particular the role of surface tension and pore morphologies on imbibition in idealised systems will be presented. Although simplified as two-dimensional porous systems all the relevant mechanisms are demonstrated without the confounding effect of the structural complexities of paper.

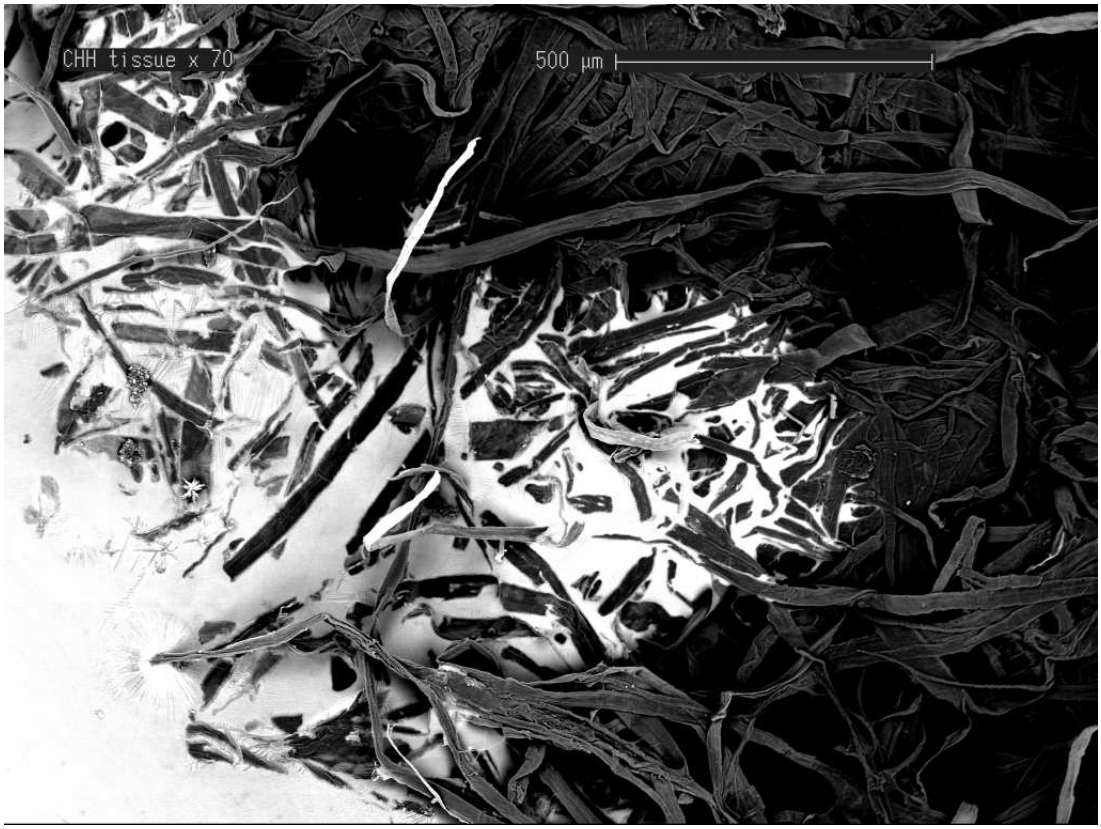

Cryo-SEM image of fluid imbibing into tissue paper.

5.1 Introduction

In Chapter 4 relationships between the physical characteristics of decor papers and their performance during liquid impregnation were examined. These were also related to the pressing performance of the decor papers detailed in Chapter 3. It was shown that different decor papers imbibed resin like liquids at different rates. Additionally, the physical characteristics of decor papers commonly used by industry did not bear any real relationship to either the imbibition performance of papers or their performance in the actual short cycle laminating pressing operation.

Qualification of the effect of different liquids on the rate of liquid imbibition into model porous media has been studied without the complexity of real paper structure (Rye et al., 1966; Dong and Chatzis, 1995; Senden et al., 2000). The purpose of the models used was to observe droplet penetration and rate of imbibition into a porous structure that had a generalised topology. There was no direct geometric similarity with paper as it was an attempt to understand phenomena associated with droplet penetration into well defined systems. Overall liquid penetration rate, surface and sub-surface spreading rates could be determined from the use of these micromodels. This approach allowed the direct study of the liquid-type effect without the complications of using real paper.

Therefore the aims of the work described in this chapter were to determine the effect surface tension and contact angle have on the rate of penetration, and spread in simple isotropic porous networks by looking at different classes of liquids ranging from simple liquids to a variety of surfactant solutions using simple micromodels. The purpose of the physical models was to observe droplet penetration and rate of imbibition into a porous structure that had a generalised topology. More specifically the microscopic detail of fluid advance could be studied at the pore-scale.

Theoretical models of imbibition could be tested experimentally. The Lucas-Washburn equation (Lucas, 1918; Washburn, 1921) is still the most widely used model to describe fluid flow in paper (equation 5.1), where γ is the surface tension, r is the pore radius, t is time, μ the kinematic viscosity and l is the distance penetrated. It is a purpose built equation that has been used for decades to describe fluid flow in paper. It assumes capillaries of cylindrical cross-section, where surface tension drives flow, and that surface energy is measured on flat surfaces. Most importantly however, it ignores capillary morphology and connectivity. It is therefore proposed that it is inadequate in fully describing fluid penetration even in simple model systems.

$$l^2 = \frac{\gamma r t \cos\theta}{\mu} \tag{5.1}$$

Rye et al. (1966) in the study of wetting kinetics on rough surfaces stated that a rough surface can be thought of as a three-dimensional network of connected, open capillaries and can

be viewed as a network of contiguous valleys through which liquid is drawn by capillary forces. They constructed a network of systematically varying straight V-shaped grooves machined into copper sheet. They showed experimentally for a wide range of surface tension to viscosity ratios, groove angles and depths that the spreading length of liquids in open surface V-grooves follows a square root of time dependence with the same basic form as for closed cylindrical capillaries. They concluded that the basic Washburn approach was fully capable of capturing the essential interdependence on surface chemistry involved in capillary flow in open triangular grooves.

Lenormand et al. (1983); Lenormand and Zarcone (1984) presented results for the time scales of the mechanisms of flow through the roughness of surfaces, along the edges of ducts, or in the bulk of the capillaries during the displacement of one fluid by another in a two dimensional etched network. They presented four mechanisms of meniscus displacement (Figure 5.1); A. piston flow, B. snap-off, and two types of imbibition C & D. They described "piston-type" motion where the frontal meniscus completely occludes the capillary and the wetting fluid (typically water) displaces the non-wetting phase (typically air) when the pressure becomes smaller than the capillary pressure of the capillary. "Snap-off" is where initially the frontal meniscus does not completely occlude the capillary, and the interface moves along the edges as long as its configuration remains stable. This wetting fluid continues to move along the capillary as films which eventually completely line the capillary wall, separating the air from the wall. The result is the creation of an unstable filament of the air. This spontaneously thins and "snaps-off", disconnecting the air, as is shown in Figure 5.1. The first imbibition mechanism, I_1, is where the air is only in one capillary and when the meniscus from the three adjacent filled ducts no longer contacts the walls of the capillary an instability appears and the air is rapidly displaced. The second type of imbibition, I_2, is where the air is in two adjacent capillaries and once the meniscus reaches the corner of the two adjacent capillaries containing the air, it collapses and the wetting fluid rapidly displaces the air in the two capillaries.

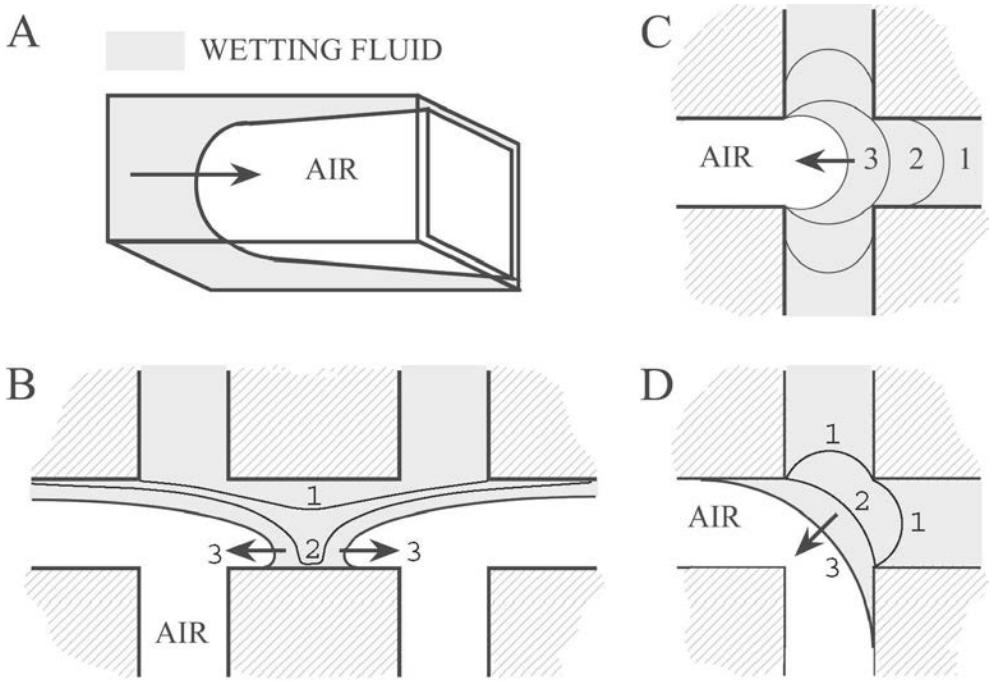

Figure 5.1: *Different imbibition mechanisms as described by Lenormand et al. (1983) A) piston displacement, B) snap-off, C) I_1 imbibition and D) I_2 imbibition. The most important of which in the micromodels used in this study being piston flow and snap-off as depicted in A & B.*

5.2 Materials and methods

5.2.1 Experimental design

Micromodels used were similar to those in Senden et al. (2000). The micromodels were smooth and of uniform surface energy. The choice of a compressible material of the model was important as a glass plate was placed over the model and compressed onto the model to ensure no leakage of the wetting fluid into adjacent pores. Prospective liquids had to be suitable for video microscopy and the use of dyes to aid contrast in visualisation was favoured. Once chosen their surface tension was measured and their macroscopic contact angle on a flat sample of the micromodel material determined.

Isopropanol/water combinations were used as surface tensions and contact angles could be manipulated by changing their relative concentrations and it was possible to get similar contact angles to the liquids with surface active solutions for direct comparison. The micromodels were a 2D representation of a simple porous system where a drop was represented by a disc of liquid, a surface a simple linear boundary and the porous network by a flat mono-continuous maze. The purpose of this experiment was to determine the effect of different liquids on penetration into simple micromodels and thus simulate the action of a freely falling liquid drop impacting on a porous substrate.

5.2.2 Determination of contact angle

The determination of contact angle of all the liquids used was done by recording fluorescence enhanced video microscopy of a droplet of the test liquid on a flat surface of the same material as used to make the micromodels. Sodium fluorescein (Sigma-Aldrich), was added to all liquids to improve contrast between the liquid and micromodel. This had no discernable effect on contact angle (see Table 5.1). Under UV light in a darkroom, profiles of the drop were recorded using a CCD camera (Cohu model 5152) and an image enhancer (Model 305 Colorado Video Inc).

Table 5.1*: Static advancing contact angles and their corresponding air-liquid surface energy.*

Liquid type in aqueous solution	**Contact angle** θ_a	**Air liquid surface energy** mJ/m^2
31.5% isopropanol	52	24.7
67% isopropanol	45	21.8
84% isopropanol	35	21.4
89% isopropanol	30	20.1
94% isopropanol	25	19.8
100% isopropanol	15	21.6
Teric* N1 & N9 @ 0.08%	52	27
Zonyl** @ 0.1%	30	18.3
Zonyl @ 0.2%	30	18.1

5.2.3 Determination of surface tension

The surface tension was measured using the Wilhelmy Plate method (Wilhelmy, 1863; Adamson, 1960). It is one of the most popular techniques to measure surface tension and is the force required to detach an object of known cross-section from the surface of a liquid. In this case paper was suspended from a balance in a Langmuir Minitrough (Loebl, 1985) into a liquid. As the liquid level is lowered and the maximum weight on the balance is recorded, noting the breadth of the slide (b) and the liquid surface tension (γ). Adamson (1960) states this measurement to be accurate to around 0.1% (Equation 5.2).

$$W_{tot} = W_{slide} + 2b\gamma \tag{5.2}$$

A contact angle of zero was assumed, as was the absence of fibre swelling in the paper. Samples 30 x 10 mm of Whatman No. 1 Filter paper were used, with about 20 ml of the test liquid placed in a Petri dish beneath the paper strip. Table 5.1 lists the surface tensions of all the liquids tested. Isopropanol was chosen over ethanol as the Marangoni effect was negligible, particularly in the confined space of the micromodel where the vapour pressure was high.

5.2.4 Use of micromodels

The fabrication of the micromodels used was described in Senden et al. (2000). The three isotropic model types used were one dimensional square section parallel capillaries about 0.5 mm per side, two dimensional crossed capillary network with the same vertical capillaries as the 1D model (*i.e* orthogonal to the inlet) and with capillaries parallel with the inlet about 7 mm apart and two dimensional crossed capillary network rotated 45° to the inlet (Figure 5.3). No attempt was made either to introduce any heterogeneity into the models, or in any way to represent the structure of paper. The micromodels were inclined at 35° to encourage all fluids to flow into the capillary network especially for liquids with higher surface tension to penetrate the models. The surface of the micromodels themselves were smooth and of uniform surface energy. The choice of a compressible material of the model was important as a glass plate was placed over the model and compressed onto the model to ensure no leakage of the wetting fluid into adjacent pores. .

The silicone moulding material was hydrophobic. The simple wetting fluids were solutions of isopropanol (Aldrich), which had a contact angle of about 15°, which could be altered by the addition of water (see Table 5.1). It also had low volatility and readily dissolved the sodium fluorescein. The surfactant based solutions were Teric N1 & N9 (Orica Pty Ltd.) both nonionic surfactants nonylphenol ethoxylates $(C_9H_{19}C_6H_4(OCH_2CH_2)_nOH)$ and Zonyl FSO-100 a Dow Chemicals nonionic fluorosurfactant $(R_fCH_2CH_2O(CH_2CH_2O)_xH)$. The concentration of the Teric based surfactants was similar to that used in the UF resin mix in Chapter 3 and in an industrial treater and the concentrations of Zonyl were 0.1% & 0.2%.

A 0.05 ml volume of fluorescent liquid was injected with a 1.0ml syringe into the space above the network. Removing the syringe caused the liquid disk to migrate towards the network. The process was recorded in a dark room under UV light. The high contrast afforded by the fluorescence meant that with simple thresholding of the video image the map of liquid distribution could be obtained as a function of time down to 40 ms resolution. Each frame was time stamped to 1 ms. All video data was digitised through a PCMIA card at 30 fps. Figure 5.2 shows the complete experimental setup. The image dimensions were 240 x 180 pixels and the image format was 8-bit monochrome. Using Igor Pro v. 3.1.4 (Wavemetrics Inc.) the digital video was thresholded and the pattern of liquid distribution was mapped automatically frame by frame. The algorithm recorded the evolution with time of the apparent contact angle, lateral spread of the drop along the surface, below the surface and overall depth of penetration in the network. Finally a graph containing information on penetration rate, surface spreading and apparent contact angle, subsurface spreading and the resultant distribution of the penetrating liquid (see Figure 5.5) as a function of time was obtained. The graph details actual t on the lower axis, normalised t on the upper axis to enable comparisons between models, and the penetration rate on the graphs is in reduced units of droplet volume at t/initial droplet volume

(see Figure 5.4). Rate of imbibition was the depth of penetration into the micromodel divided the time taken.

5.2.5 Experimentation

The experimental design was based on two replicates for each liquid type in each micromodel. The order of models used in both replicates was, simple capillary, then cross capillary and finally diagonal cross capillary. The order of liquids used was randomly determined for each experiment (replicate *x* micromodel *x* liquid). The starting contact angle of 52° was selected as the highest angle as liquids with higher contact angles did not move through the micromodel at the angle of incline selected. Some treatments were terminated after 30 minutes if it became apparent that penetration was not proceeding. The properties studied in this experiment were time and rate of imbibition of different types of liquids into three different isotropic micromodels described above.

Figure 5.2: *Complete setup of micromodelling experiments showing A: timer, B: video enhancer, C: video recorder, D: inclined platform, E: UV light source, F: micromodel and G: CCD camera.*

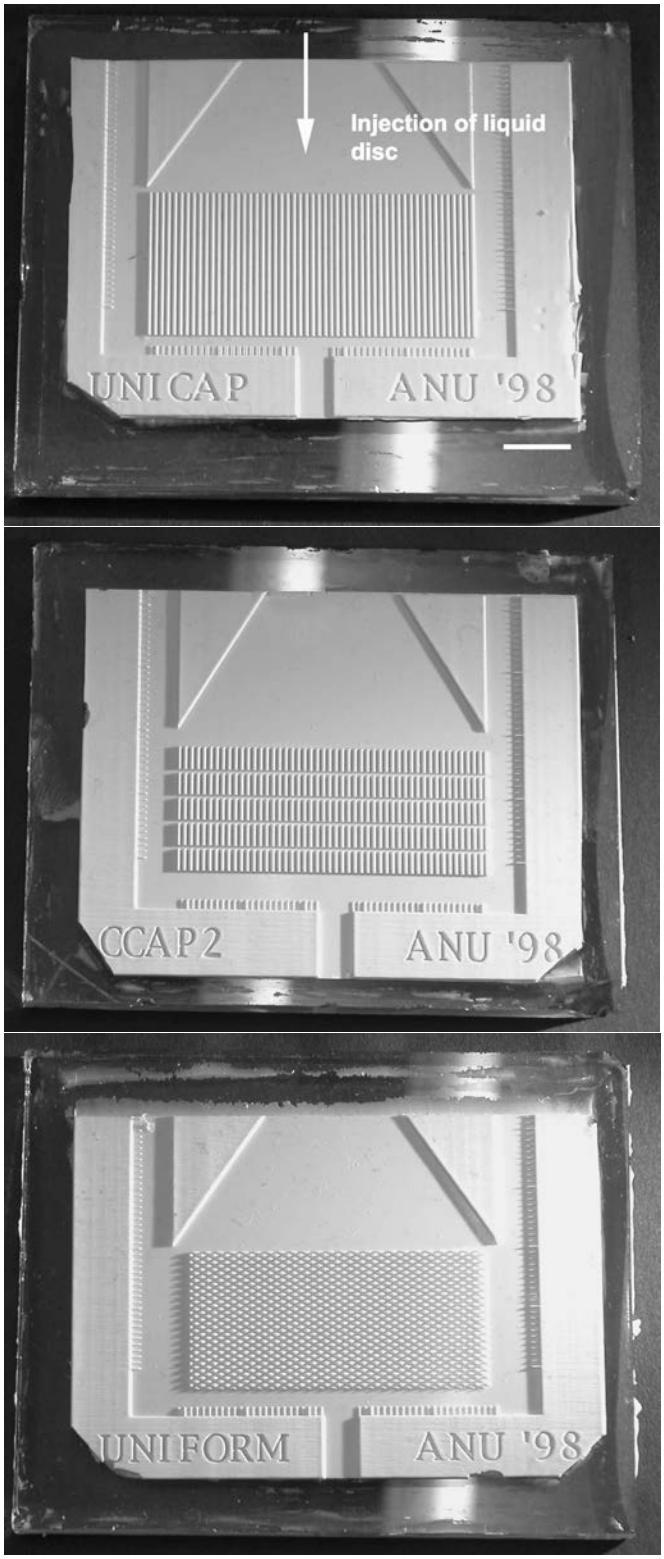

Figure 5.3: *Photographs of the actual models used; Top: Capillary micromodel, Middle: Cross capillary micromodel, Bottom: Diagonal micromodel. Scale bar represents 10 mm.*

5.2.6 Statistical analysis of data

The design of the experiment involved factorial principles where the aim was to examine the fixed effects of liquid type including contact angle and surface tension and type of micromodel on the response variables of droplet spread on the surface and subsurface, and penetration rate. Some data were transformed to a natural logarithm form to ensure that it complied with the assumptions of ANOVA, *i.e.* normality with constant variance. Statistical computation was carried out using Genstat 5[1]. Random effects identified were variation within micromodels (position of droplet placement on the micromodel) and replicate (micromodel to micromodel variation). The design of experiment led to maximum precision for treatment effect (type of liquid) within each model. All data were analysed using REML (residual maximum likelihood) Variance Components Analysis because the treatments were not fully orthogonal. A General Linear Mixed Model Analysis was conducted to determine the degree to which contact angle and surface tension alone could explain variation in imbibition rates. In addition, all video images were subjectively analysed for liquid behaviour.

5.3 Results

5.3.1 One-dimensional model

Results for a typical experiment for the one-dimensional model is shown in Figure 5.5 and all results summarised in Figure 5.4. The penetration rates were scaled approximately as $t^{1/2}$. Solving for t using the Lucas-Washburn equation (Eqn 5.3) showed very similar results to what was observed experimentally for simple wetting fluids except those with higher contact angles where the predicted rates were slightly higher than those experimentally derived.

$$t = \frac{l^2 \mu}{\gamma r \cos\theta} \tag{5.3}$$

With isopropanol based wetting fluids, the rate varied with the amount of water in the solution, the higher the water content the lower the rate of imbibition, relating to contact angle and surface tension as will be shown later with the mixed linear model analysis. Spreading of the drop on the surface of the model was minimal and subsurface spreading coincided with surface spreading. The rate of imbibition was constant for the simple wetting fluids.

The general observation of sub-surface penetration was that imbibition occurred more quickly at the centre of the droplet as evidenced by Figure 5.5. Also noticeable with the imbibition of simple wetting fluids was the advancing of the bulk liquid by flow in typically one or two corners of the capillary. This advanced film flow was very small in magnitude but was affected by the concentration of water in the isopropanol such that the higher the concentration

[1] Lawes Agricultural Trust

of water, the less the flow in the corners in advance of bulk flow.

The pattern of imbibition of a surfactant based fluid was completely different from that of the simple isopropanol based wetting fluids even with similar contact angles. Firstly, the rates of imbibition were much slower and were defined by a stick/slip advancement of the piston displacement down the pore as can be clearly seen in Figure 5.6 and briefly referred to by Senden et al. (2000). Also the partial wetting of the pores in the corners was much more pronounced than with the simple wetting fluids. This partial wetting was much faster than the piston flow and can be observed in the insert of Figure 5.6. The penetration rate for surfactant based fluids was one order of magnitude lower than that predicted by the Lucas-Washburn equation.

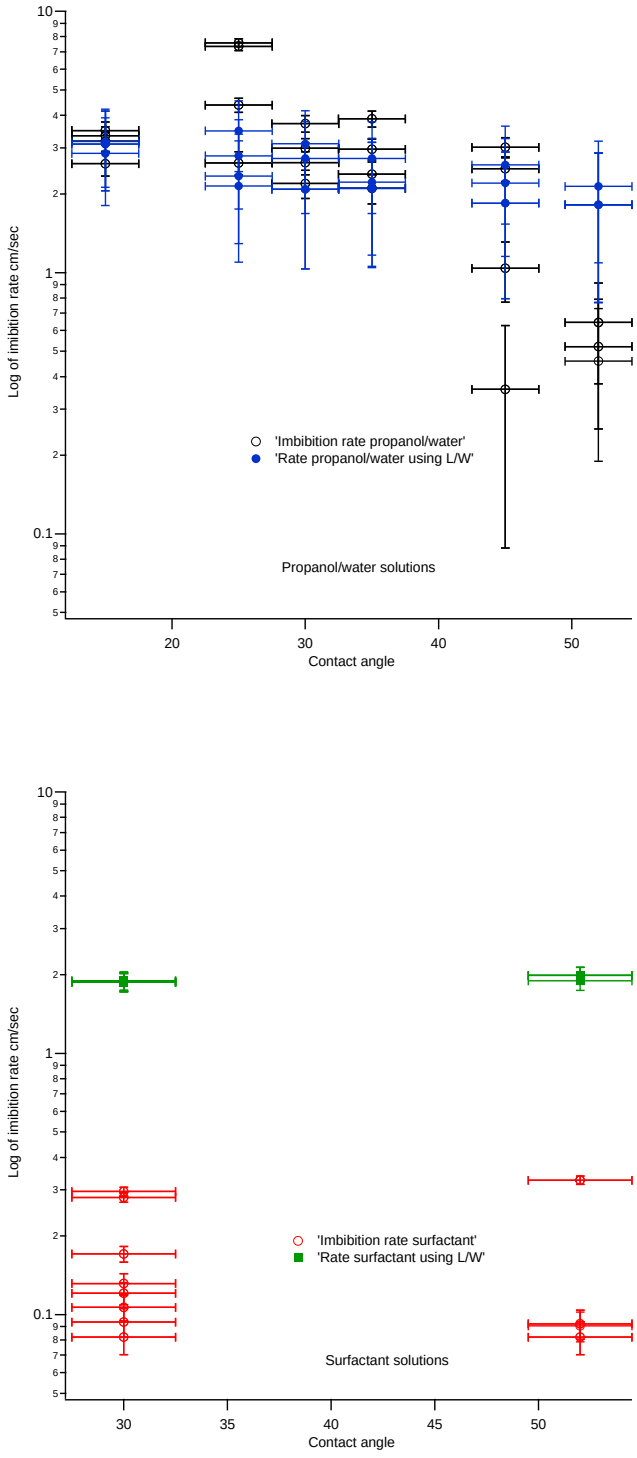

Figure 5.4: *Differences in imbibition rate between: top: simple wetting fluids and bottom: surfactant based wetting fluids for one-dimensional capillary micromodels observed experimentally and using the Lucas-Washburn equation. Error bars lsd, p = 0.05*

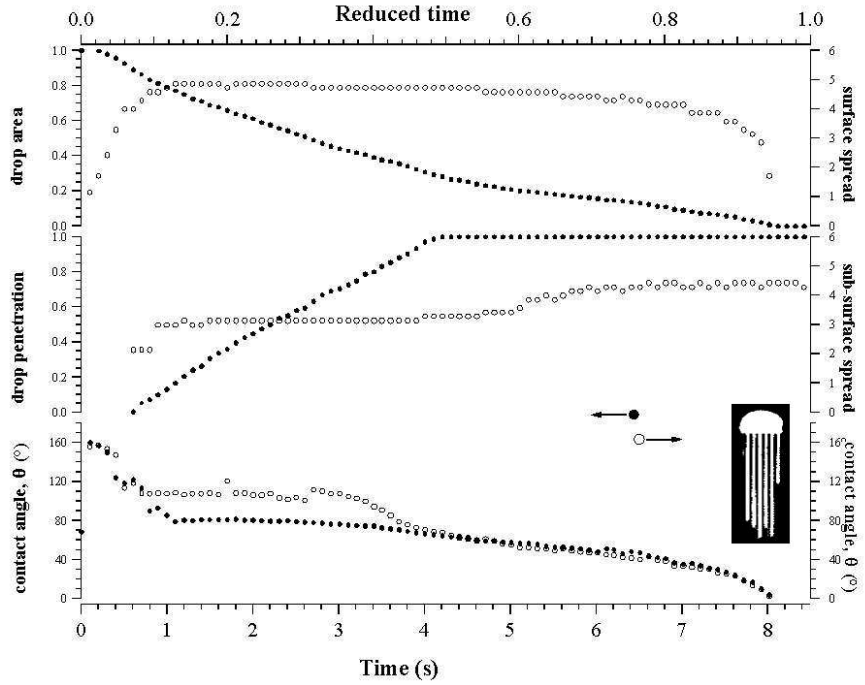

Figure 5.5: *Measurement of imbibition into a one dimensional capillary network with 31.5% iso-propanol θ = 52°. Inset is a thresholded image of the solution immediately as the drop impacts and the final fluid distribution with the model. Surface and sub-surface spread is in mm and drop area and spread have a normalised scale of 0-1 where 0 is the minimum value and 1 the maximum.*

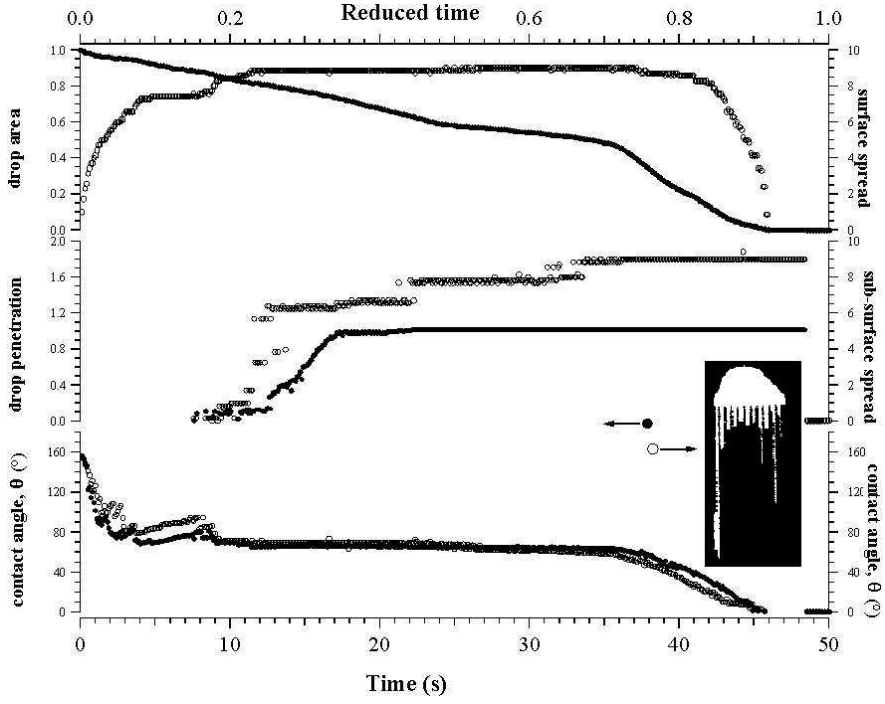

Figure 5.6: *Measurements of a one dimensional capillary network with the surfactant Zonyl at 0.1% θ = 30° including actual thresholded image of the solution in the micromodel showing preferential imbibition down the pores at the edge of the droplet as well as partial pore filling in advance of piston flow. Also shown is snap-off occurring at the bottom of the left hand capillary which would fill to the surface and cause the droplet to spread on the surface.*

5.3.2 Two-dimensional models: capillaries aligned with inlet

Results for simple isopropanol based fluids imbibing into the two-dimensional models with capillaries aligned with inlet (cross capillary model) are summarised in Figure 5.7. The main result is that imbibition rates are slightly slower than predicted by the Lucas-Washburn equation, especially for fluids with higher contact angles. The difference was due to the time taken for the fluid to pass all the discontinuities ("snap-off"). This compared with the close approximation found with the predicted values for the one-dimensional capillaries when using the Lucas-Washburn equation. With lower contact angle fluids, the penetration rates scaled approximately as $t^{1/2}$, however, with decreasing isopropanol content, the predicted rate overestimated actual rates, the difference being the time taken for the fluid to pass a discontinuity. For a liquid to pass a discontinuity snap-off had to occur which was then followed by an I_2 imbibition event (Figure 5.1) as the liquid imbibed across the lateral capillaries. This is seen in Figure 5.8 (inset). As a result penetration intermittently stopped at these discontinuities which can be clearly seen in Figure 5.9. The Lucas-Washburn equation could not have predicted this. Figure 5.8 shows a typical plot of a simple liquid (containing isopropanol) penetrating the two-dimensional cross capillary micromodel. From Figure 5.7 it can be seen that the contact angle effect was more substantial than with the one dimensional micromodel. There was also a greater rate of reduction of imbibition with higher contact angles and a greater difference between the calculated and actual penetration rates.

Results for surfactants in the imbibing fluid can be seen in Figures 5.10 & 5.11 where the longer penetration times for surfactant based liquids were evident even with similar contact angles to those of the simple fluid combinations. Note again the thresholded image of the imbibing surfactant showing preferential imbibition at the edges of the droplet as compared with the simple wetting fluid where clearly the penetration was more pronounced from the centre of the droplet. As occurred in the 1D micromodels film flow with the simple wetting fluids was much less pronounced than with the surfactants and was not at all evident at higher concentrations of isopropanol.

With simple wetting fluids snap-off occurred in discrete sections less than the full width of the penetrating drop and always near the centre (Figure 5.8). With surfactant based fluids snap-off occurred over the full width of the droplet starting at the edges of the lateral pore and moved towards the centre very rapidly, with penetration starting at the edge of the lateral pores directly underneath the edge of the droplet (Figure 5.11). Film flow which was very apparent with surfactant based fluids could go back up an unfilled pore after snap off had occurred filling a lateral pore resulting in piston flow up through the same pore. There was no sub-surface spreading with the simple wetting fluids, however with the surfactant based fluids there was slight sub-surface spreading due to the mechanism just described.

There was a clear trend both with type of surfactant and concentration of the Zonyl surfac-

tant in the two-dimensional models capillaries aligned with inlet. At the same concentration, the rate of imbibition with Zonyl was at least three times that of the Teric surfactants and at the higher concentration, there was an order of magnitude difference in the rate of penetration, compared to the Teric based surfactants.

5.3.3 Two-dimensional models: capillaries not aligned with inlet

Results for the two-dimensional model: capillaries not aligned with inlet (diagonal capillary model) with pore inlets at 45° to the surface of the model are summarised in Figure 5.12. Figure 5.13 shows a typical plot of a simple wetting fluid containing isopropanol penetrating the two-dimensional diagonal micromodel. Similar to the two dimensional models where the capillaries were aligned with the inlet, the Lucas-Washburn equation gave a reasonable approximation of the rate of flow of isopropanol/water solutions at lower contact angles however at higher contact angles it significantly overestimated flow rates (Figure 5.12). With surfactant solutions it predicted rates nearly three orders of magnitude greater than that observed experimentally showing that the equation was not able to take into consideration any complexity in the models used, especially with surfactant based fluids. The large error bars observed in the prediction of rate using Lucas-Washburn for surfactant based solutions were based on a variation in the actual length of imbibition within some surfactant treatments and that some liquids only penetrated a small distance into the diagonal micromodel. This caused a significant variation in the value of *"l"* when using the Lucas-Washburn equation.

From Figure 5.12 it can be seen that the effect of increasing contact angle with the iso-isopropanol based solutions was far greater for the diagonal micromodel than for the other two micromodels in that there was a greater reduction of rate of imbibition with increasing contact angle.

The pattern of penetration into the micromodel was only symmetrical with pure isopropanol (Figure 5.13). As the concentration of isopropanol was reduced and with all surfactant based solutions there was a marked skew in the distribution of the penetrating liquid (Figure 5.14) which showed more rapid penetration on the side of the droplet where the contact angle was lowest. Where skewed penetration occurred, snap-off occurred at the bottom of the penetration area irrespective of liquid type. With the diagonal micromodels there was very little evidence of any film flow ahead of the bulk piston type flow with any of the penetrating fluids. The effect of surfactant type and concentration was greatest with the diagonal micromodel. Only one of the Teric based solutions actually penetrated the model and it was substantially slower than the fluid made from an equivalent concentration of Zonyl. There was a large increase in rate of imbibition with an increase in the concentration of Zonyl to 0.2%.

For this model as with the other 2D model the overall imbibition rate was primarily determined by the slowest or rate limiting mechanisms which was snap-off. However unlike the

other 2D model there was no evidence of I_1 or I_2 imbibition mechanisms (Lenormand et al., 1983) in the diagonal 2D model either with the simple wetting fluids or with surfactant-based imbibition liquids.

The significant reduction in rates of imbibition of the non-aligned compared with the aligned models is due to the fact that with the aligned models the films can spread much further (up to 7 mm) before reaching a vertical discontinuity enabling film thickening to occur. This as has been described is followed by snap-off then piston flow rapidly filling that section of the capillary. However with the non-aligned model the film can only spread about 1 mm before reaching a discontinuity not allowing much film thickening to occur. This of course would limit the probability of snap-off.

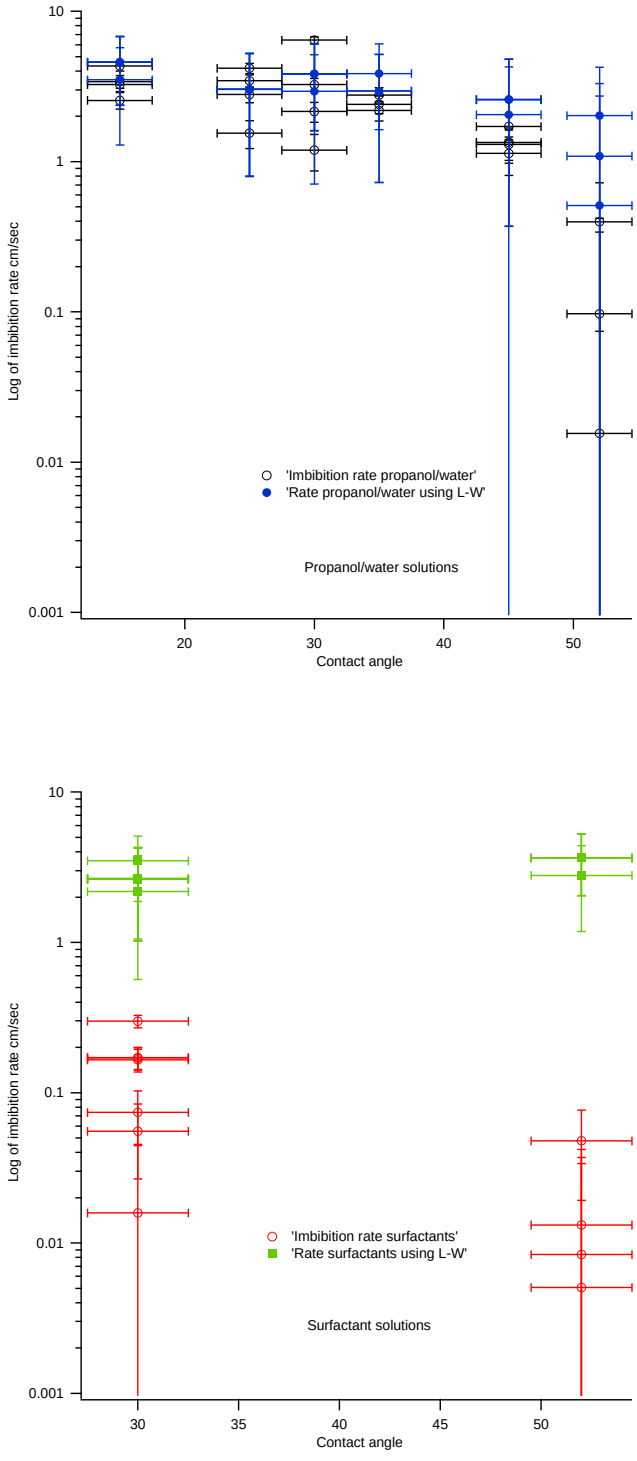

Figure 5.7: *Showing the difference in imbibition rate between top: simple wetting fluids and bottom: surfactant based wetting fluids for two-dimensional cross-capillary micromodels observed experimentally and using the Lucas-Washburn equation, error bars lsd p = 0.05.*

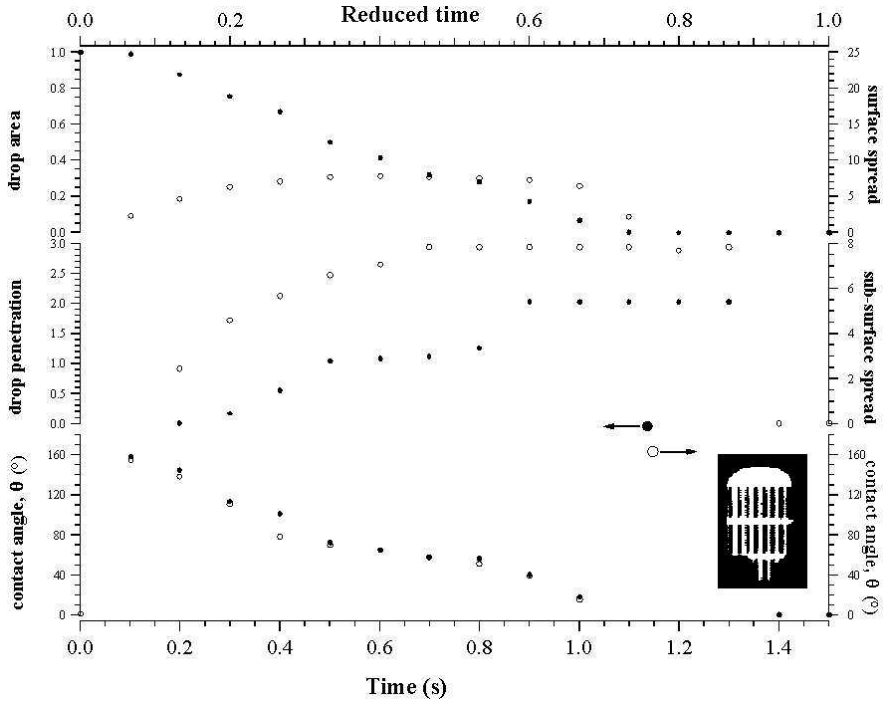

Figure 5.8: *Measurements of a two-dimensional cross-capillary micromodel using 100% isopropanol ($\theta \simeq 15°$). Inset is a thresholded image of the solution illustrating the pattern of fluid movement.*

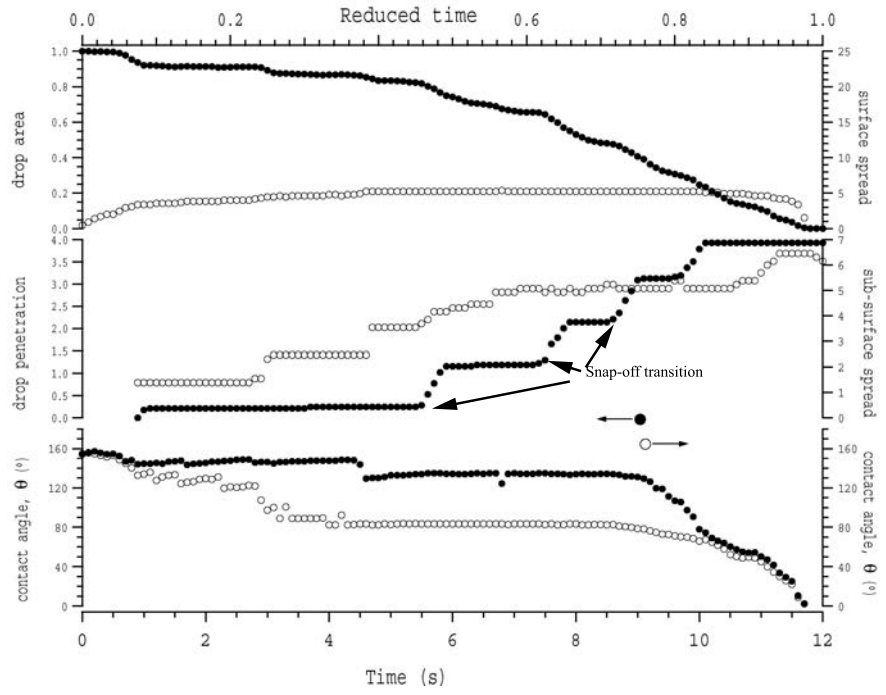

Figure 5.9: *Measurements of a two-dimensional cross-capillary micromodel using 31.5% isopropanol ($\theta \simeq 52°$) showing the times where penetration rate is actually zero while films spread and thicken prior to snap-off when the liquid front jumps the discontinuity.*

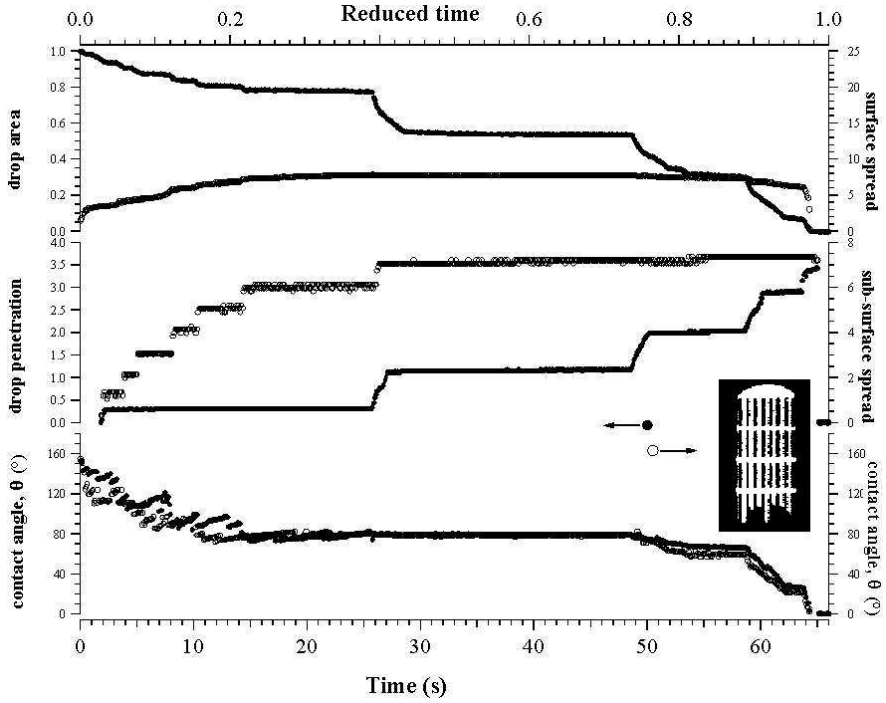

Figure 5.10: *Measurements of a two-dimensional cross-capillary micromodel using 0.1% Zonyl ($\theta \simeq 30°$) showing image of imbibing liquid.*

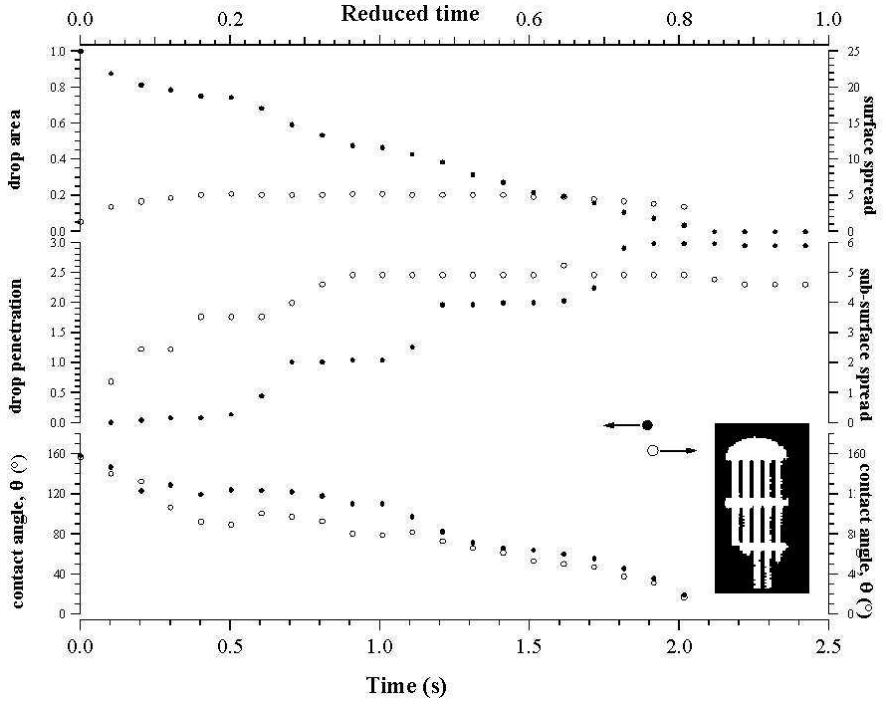

Figure 5.11: *Measurements of a two-dimensional cross-capillary micromodel using 84% isopropanol ($\theta \simeq 35°$) showing image of imbibing liquid.*

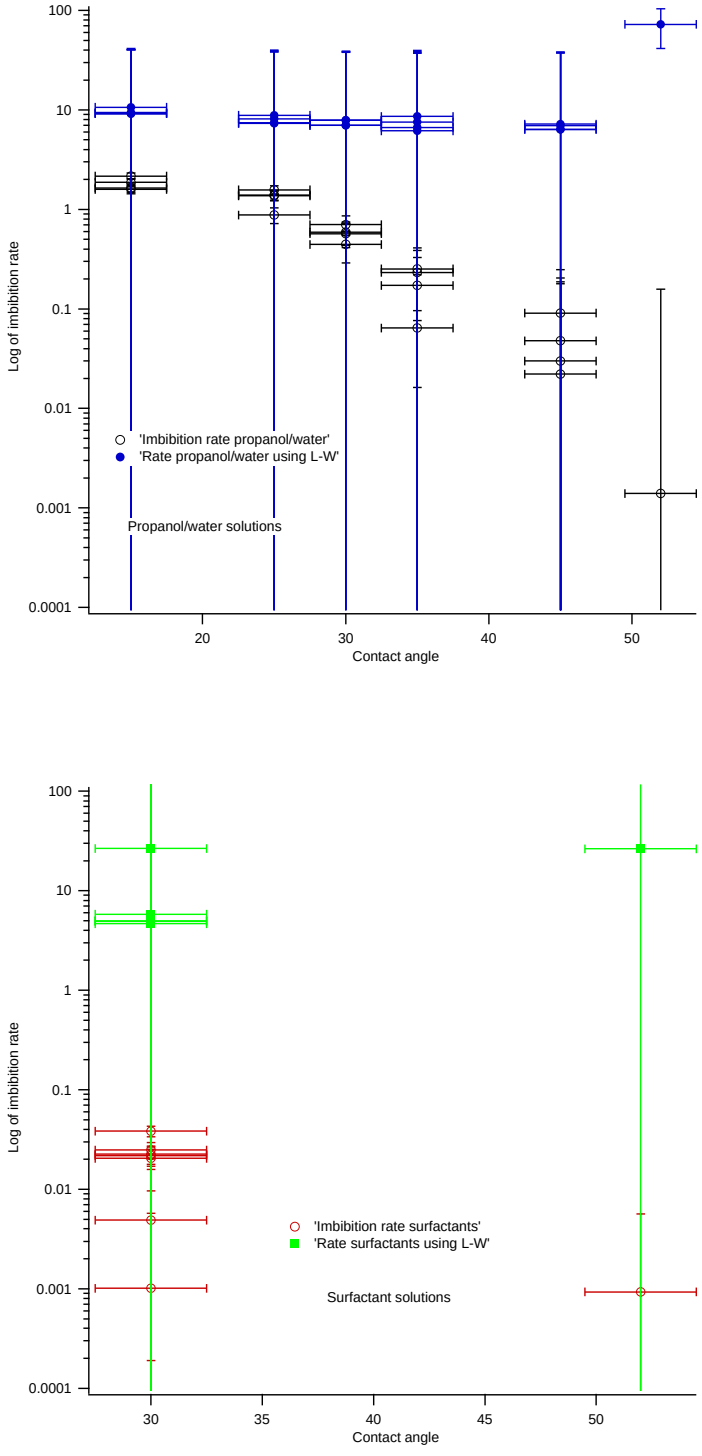

Figure 5.12: *Showing the difference in imbibition rate between top: simple wetting fluids and bottom: surfactant based wetting fluids for two-dimensional diagonal micromodels observed experimentally and using the Lucas-Washburn equation, error bars lsd p = 0.05.*

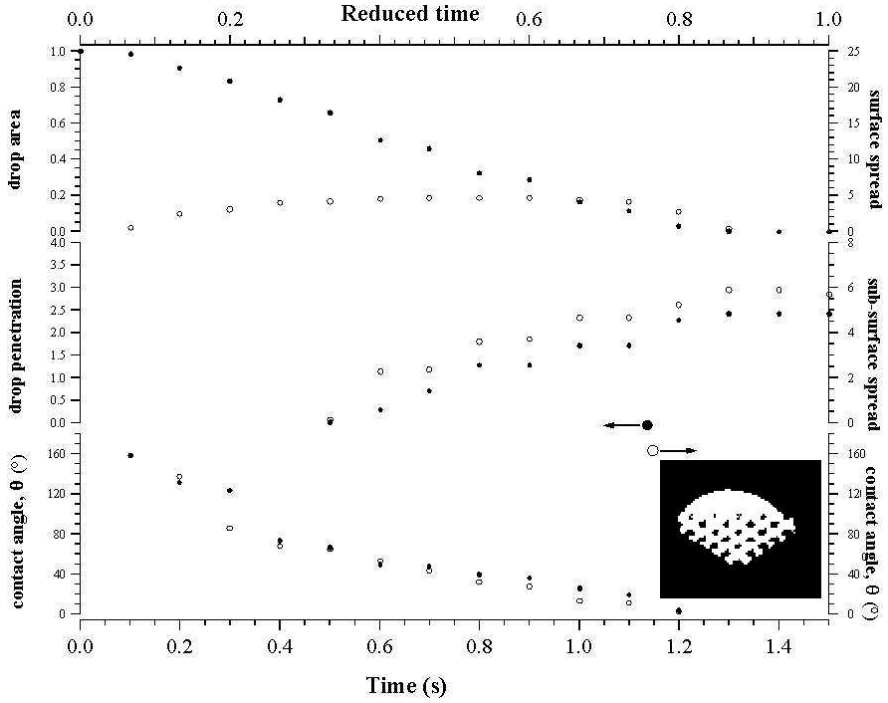

Figure 5.13: *Measurements of a two-dimensional diagonal micromodel using 100% isopropanol ($\theta \simeq 15°$) showing image of penetrating liquid and it's symmetrical distribution.*

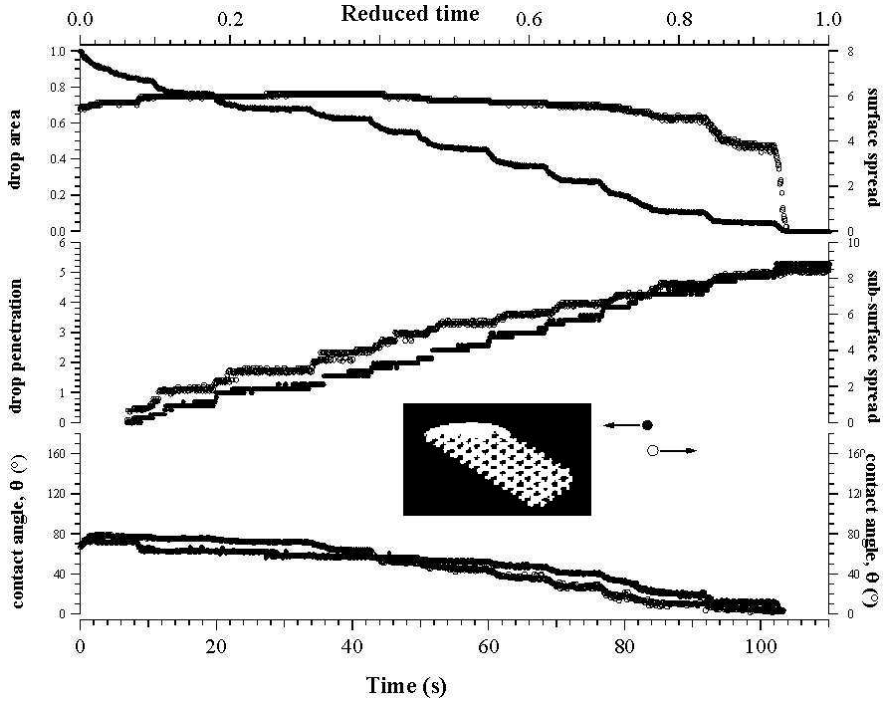

Figure 5.14: *Measurements of a two-dimensional diagonal micromodel using 0.2% Zonyl ($\theta \simeq 30°$) showing image of penetrating liquid and it's asymmetrical distribution1.*

5.3.4 Explaining rates of fluid imbibition into micromodels

Using a Restricted Maximum Likelihood (REML) Variance Components Analysis, time as a function of length of imbibition was analysed. There was a significant interaction between micromodel and treatment ($p < 0.001$) (Figures 5.15 & 5.16). These graphs show that with increasing isopropanol content the imbibition rate increased. However, the use of surfactant based fluids with similar contact angles significantly reduced the imbibition rates as had been previously shown. The chart shows that at the lowest concentration of isopropanol (at a contact angle of 52°) there was a significant difference between the imbibition rates for the one-dimensional capillary micromodel and both of the two-dimensional micromodels, there being no difference between the two-dimensional micro-models. For the remaining isopropanol solutions there was no significant difference between the one-dimensional capillary and two-dimensional cross capillary micromodels. Overall penetration rates were significantly slower ($p < 0.001$) with the diagonal micromodel with the largest differences in the mid range concentrations of iso-isopropanol. At 100% isopropanol there was no difference in imbibition rates between any of the models. When surfactants were used however, substantially different responses occurred. With the one-dimensional capillary micromodel there was no difference with type of surfactants used only their concentration. However with the two-dimensional cross capillary and diagonal micromodels there was a significant effect caused by both the type and concentration of the fluorosurfactant Zonyl. Interestingly at the higher concentration of 0.2% there was no difference between the one-dimensional and two-dimensional cross capillary micromodels, however there was a substantial difference with the two-dimensional diagonal micromodel.

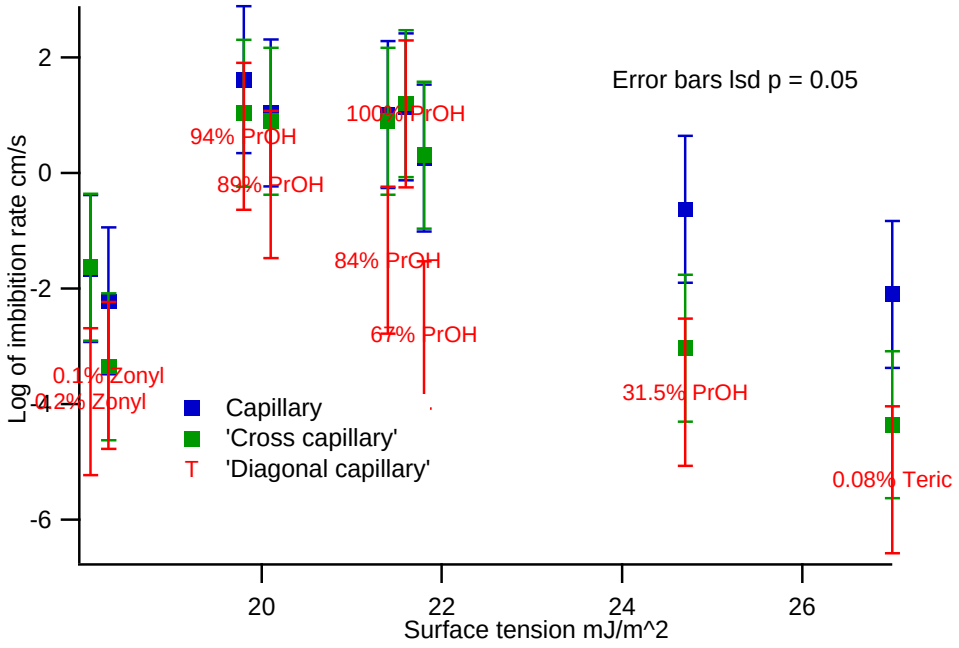

Figure 5.15: *Plot showing effect of liquid type and associated surface tension with imbibition rate for all micromodels.*

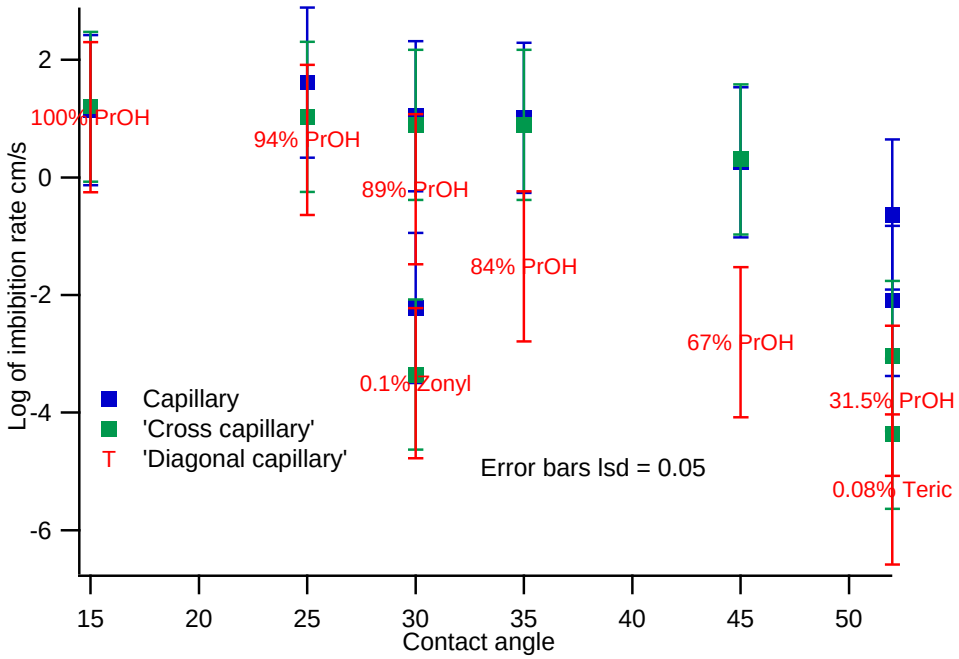

Figure 5.16: *Plot showing effect of liquid type and associated contact angles with imbibition rate for all micromodels.*

A general linear mixed model analysis was carried out to try to determine the degree to which contact angle and surface tension could explain the variation in imbibition rates over all micromodels. While contact angle ($p < 0.001$) and surface tension ($p < 0.001$) explained a considerable amount of the variation in imbibition rates there was still unexplained factors affecting rates of imbibition as explained by the magnitude of the remaining between treatment variation after removing the linear effects of contact angle and surface tension. This was most clearly demonstrated by the difference in imbibition rates between surfactant based and simple wetting solutions of similar contact angles. From the model, contact angle was better in explaining variation in imbibition rates than did surface tension. As contact angle and surface tension are normally very closely related, this effect could have been due to the fact that the data was pooled over all models for analysis. In addition the complexities of the surfactant based solution with the more complex models could also have added to this result.

5.4 Discussion

In using isotropic micromodels the complexity of the structure of paper was removed, and this simplified the identification of the effect of liquid contact angle and surface tension on imbibition. In addition, the examination of the mechanisms of fluid flow as a function of channel morphology was undertaken. Using the linear mixed model analysis it was shown that as the Lucas-Washburn equation predicted, both surface tension and contact angle were highly significant in determining the rates of imbibition into porous networks. There was, however, a considerable amount of variation in imbibition rates that could not be explained by either surface tension or contact angle (given that viscosity of all the treatment liquids was almost the same). This unexplained variation in imbibition rates could be explained in part by the effect of fluid flow at discontinuities which was dealt with at length by Lenormand et al. (1983); Kent and Lyne (1989a). In addition, the presence of surfactants affected imbibition rate as will be discussed below. Note that the discontinuities present in the model system are considerably less complex than those found in actual paper, which only further demonstrates the weakness of using the Lucas-Washburn equation in this system.

The results clearly showed that in some cases the Lucas-Washburn equation gave a *reasonable* approximation of flow rates with the $t^{1/2}$ relationship, particularly with simple wetting fluids. It is reasonable only to the extent that the small size of the networks precluded measurements of very large areas. This was particularly the case with the one-dimensional model and with strongly wetting fluids in the regular two-dimensional model. For poorly wetting liquids and where there was an element of complexity in the porous systems, the Lucas-Washburn equation overestimated flow rates. This was due to the fact that in more complex systems, the rate of flow down a capillary was much faster than where a discontinuity was encountered. This was because the rate of film spreading and thickening prior to snap-off was much slower

than the piston flow down a capillary.

Also demonstrated was that imbibition mechanisms even in simple porous networks were not always in the form of piston or bulk meniscus flow (Lenormand et al., 1983). This was also well demonstrated with the imbibition of surfactant based fluids. This was due to the fact that the rate of flow of these surfactant solutions was not constant, being limited by the diffusion of the surfactant to the wall of the capillary. This depletes the surfactant molecules at the surface, and results in penetration slowing down until more surfactant molecules diffuse to the surface. This was described by Elftonson and Strom (1995); Tiberg et al. (2000); Ridgway and Gane (2002) who showed that the rate of imbibition is limited by the rate of replenishment of surfactant molecules at the liquid/vapour interface and results in a stick/slip imbibition behaviour. This was in contrast to simple wetting fluids where vapour phase adsorption occurs prior to the formation of precursor wetting films and results in a more constant rate of fluid flow.

With two-dimensional models the differences between imbibition rates of simple and surface active liquids were much more marked and the differences between actual flow rates and those predicted by Lucas-Washburn were even greater. With surfactant based solutions the penetration of the droplet occurred from the edge of the droplet and with the simple fluids from the middle. This could be explained by the fact that displacement down pores at the edge of the droplet was far greater than in the middle of the droplet as these pores were only partially occluded and the initial flow was by partial wetting through films. Additionally the greater surface area meant more surfactant was available to diffuse to the 3-phase line. These films occurred in the corners of the capillary pores and this film flow was much faster than any piston flow observed. In some instances, partial wetting went down the full length of the pore, sometimes down all four corners then into a corner of an adjacent pore and up to the surface of the pore (Figure 5.6). This then would cause the droplet on the surface of the network to spread to that pore. The films would then thicken and snap-off filling the capillary. The difference between the predicted rate using Lucas-Washburn and the observed experimental data for surfactant-based liquids was very significant, the calculated imbibition rate averaging one order of magnitude faster than that observed experimentally. The only clear trend was that at the higher concentration of 0.2%, Zonyl based solutions had the fastest penetration rates, there being no significant differences between the Teric and Zonyl surfactants at the same concentration.

There was no wetting delay (Kent and Lyne, 1989a; Bristow, 1986b; Lyne and Aspler, 1982) observed with any liquid in any of the micromodels. Therefore, the results concur with Eklund and Salminen (1987) who rejected the concept of a wetting delay as penetration down capillaries with all solutions occurred as soon as the disc of liquid contacted the capillaries. This is shown in Figure 5.5 where it can be seen that surface contact angle immediately reduced after time zero when the liquid contacted the capillaries. In addition, it can also be seen that spread below the surface began immediately, obviously simultaneously with drop penetration.

5.5 Conclusion

Although the $t^{1/2}$ dependency of rate seems universal, it has been demonstrated that even in simple pore networks the main parameters of the Lucas-Washburn model do not satisfactorily explain fluid imbibition rates overall. Therefore, in more complex random porous media such as paper the Lucas-Washburn approach seems poorly predictive. Thus armed with an understanding of pore-scale imbibition mechanisms, the following chapter is devoted to the exploration of the kinetics of fluid flow in paper.

Chapter 6

Mechanisms of Fluid Flow in Paper

Cryo-SEM was used to visualise the penetration of a wetting fluid into various bleached softwood kraft papers. The results indicated that the fluid movement was primarily due to the advance of the wetting fluid in the form of bulk liquid films along channels formed by fibre overlaps. This was in contrast to the common description of fluid penetration where the primary flow mechanism was based on the bulk filling of pores.

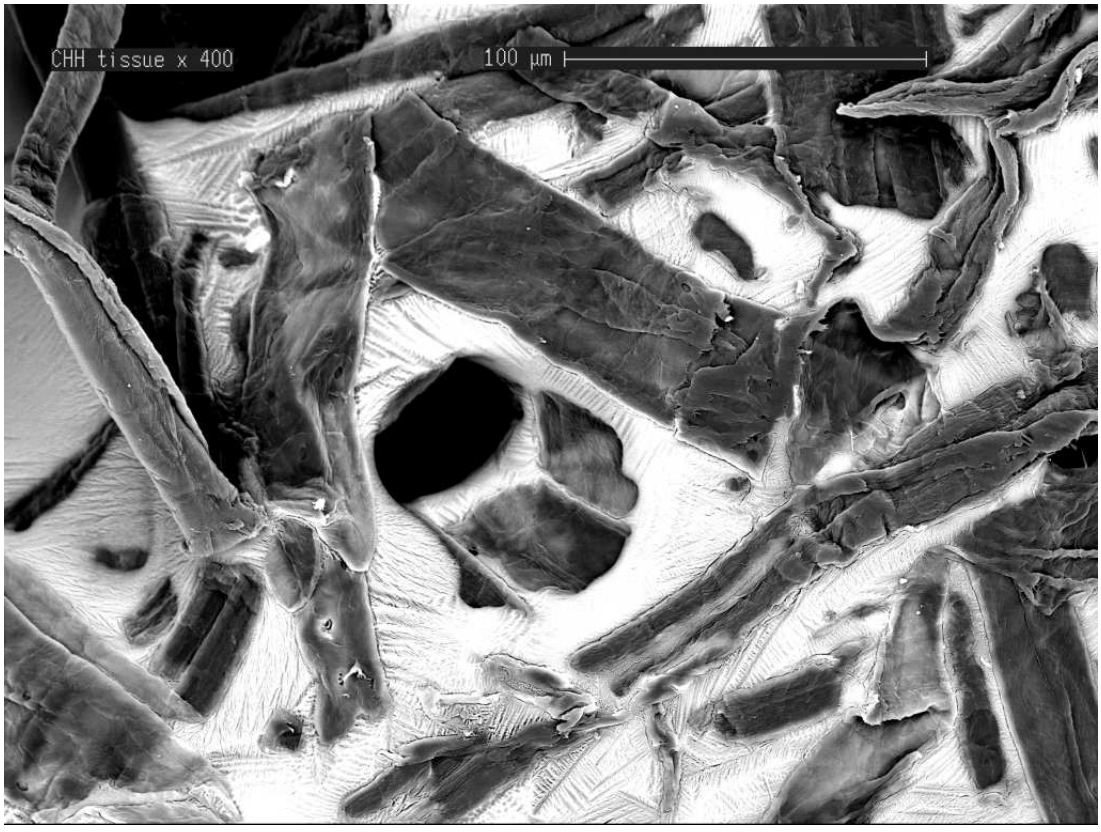

High magnification cryo-SEM image of film thickening around a large pore in tissue paper.

6.1 Introduction

6.1.1 Background

The kinetics of capillary penetration of wetting liquids into porous media is of particular interest due to its applications in the paper and textile industries and in printing technologies. An understanding of fluid penetration processes is necessary in understanding all converting processes where contact between paper and fluid plays a role. The potential mechanisms of these processes were presented in Chapter 5.

Lucas-Washburn theory (Lucas, 1918; Washburn, 1921) is commonly used to model the penetration of liquids into porous materials where the rate of penetration is a function of the balance between surface tension forces and viscous drag. Interfacial contact angle is assumed to be constant and the pore morphology is reduced to an equivalent cylindrical pore. It has long been recognized that this was a gross over simplification of the true morphology of paper, which, in reality is a material made up of a cellulose fiber matrix in many cases coated with a consolidated mass of pigment and binder. It has been noted before that important differences exist between penetration of a liquid into a capillary and penetration into a more complex porous medium (Kent and Lyne, 1989a; Marmur, 1988). The development of tools to more realistically describe the pore morphology of real porous materials is an emerging discipline of recent interest (Larson et al., 1977; Lindquist et al., 1996, 2000; Sok et al., 2002; Goel et al., 2001).

To gain a better understanding of fluid penetration into paper one must not only effectively characterise the morphology of the pores within the fibre web. One must also obtain a fundamental understanding of the physical processes which affect fluid movement and fluid-solid interactions during fluid penetration. Penetration models, including the classical Lucas-Washburn equation, assume that the major mechanism for fluid penetration into paper was via capillary transport within pores. Eklund and Salminen (1987) considered a number of water transport mechanisms including liquid capillary transport through pores, diffusion of vapour, surface diffusion in pores and intra-fibre flow; they observe that bulk capillary transport in pores remains the most important mechanism. Recent work Schoelkopf et al. (2000a) has included the study of inertial effects on fluid penetration. In all descriptions of fluid penetration, pores are considered to be occupied by a single fluid and the pore filling mechanism was by meniscus movement down the pore center.

In this chapter cryo-SEM was used to visualise the fluid phase as it penetrated into a range of paper types. Paper types studied include fully bleached softwood kraft paper and a number of saturating kraft papers used as low pressure melamine laminates. It was observed that the fluid flow cannot be characterised by an advancing wetting front moving along the bulk of the pores. One observes a large and diffuse zone, where fluid occupies only the edges of pores and forms films along channels formed by fibre overlaps. The results indicated that the fluid

movement was primarily due to the advance of the wetting fluid in the form of bulk liquid films along these channels.

To understand the observed behaviour the 3D structure of a paper web was considered. One observes that a number of potential flow paths for the wetting fluid exist within the fibre network at different length scales; these include flow within the pores, flow along channels formed by fibre overlap, flow along the fibre indentations caused by fibre collapse during pressing and fibre roughness, and intra-fibre flow. The relevant length scale associated with each flow path is defined and the continuity and representative morphology of the pathways is discussed. A description of pore-scale mechanisms for fluid penetration is given for the pore morphologies associated with each potential flow path. It was found that the continuous displacement of a meniscus along bulk pores was highly unlikely due to the presence of discontinuities in the pore morphology. The preferential displacement mechanism was via film flow along the channels formed by fibre overlaps. These channels form a highly interconnected and dense network of flow paths which efficiently transport the wetting fluid. The flow rates associated with penetration along each transport pathway are calculated; the experimentally observed penetration rate was consistent with a film flow process through channels and significantly slower than a penetration process dominated by meniscus driven flow through pores.

6.2 Materials and methods

6.2.1 Introduction

The experimental method had to ensure that 1) droplets were maintained in a frozen state for long periods, 2) samples had to be frozen quickly and 3) a high contrast liquid had to be used to ensure differentiation with fibres. Cryo-SEM was chosen as it would satisfy all of these requirements. Cryo-SEM is the use of scanning electron microscopy under freezing conditions, normally below -130°C. Cryo-SEM had two advantages over optical microscopy, firstly one cannot keep samples frozen using optical microscopy and secondly it is easier to differentiate between the paper fibres and the imbibing liquid. A brief review of work done using SEM on fluid interactions with paper was presented in Section 2.2.1, Chapter 2. The Cambridge Instruments S360 Stereoscan SEM described in Chapter 3 fitted with an Oxford CT1500B Cryotrans coldstage/coating unit was used for the imbibition experiments. Secondary electron and backscattered electron images were obtained. The latter enabled high contrast images to be obtained which clearly identified the presence of the penetrating liquid due to the use of an 2M aqueous solution of caesium iodide (CsI) as a tracer.

SEM enabled visualisation only on the surface of paper. It was essential to confirm imbibition mechanisms throughout the paper structure. Therefore another method was developed to image liquid flow below the paper surface and underneath the fluid droplet. The success

of cryo-SEM encouraged the parallel development of another cryogenic application, this time using laser confocal laser scanning microscopy (CLSM) which provides comparable spatial resolution to SEM.

A novel cell was designed, and in concept duplicated the cryogenic facility of the SEM. Samples were prepared in an identical fashion except that CsI was replaced with a fluorescent dye, Rhodamine B. This dye showed no chromatographic separation and did not adsorb onto the paper fibres. The paper sample was maintained in a frozen state by circulating chilled N_2 gas through a porous sample mount.

Even though the thesis concentrates on fluid imbibition into unsized papers the techniques used to identify mechanisms of fluid flow in unsized papers were also used to identify the mechanisms of fluid flow in sized papers.

6.2.2 Paper samples

Samples of paper approximately 15 x 5 mm for use with SEM and 19.5 mm discs for CLSM were selected from the following paper types:

1. Bleached unfilled & unsized pure cellulose paper type BL control 5, 75 gsm, 70% hardwood pulp and 30% softwood pulp pressed at 0.5 Bar, then 1 Bar and dried at 114 degrees C for 5 minutes, (International Paper)

2. Bleached unfilled pure cellulose paper BL 8-2 , same as BL 5 however sized with 1.6kg/tonne of alkyl ketene dimer (AKD) (International Paper).

3. Corporate Express Exp 2000 Laser/Copy paper, 80 gsm sized with 1kg/tonne AKD (Australian Paper No. 3 paper machine, Maryvale Mill)

4. All the decor papers described in Chapters 3 & 4

6.2.3 Cryo-SEM imaging

6.2.3.1 Sample preparation for SEM

The samples of paper were fixed to a CR101 standard specimen holder used in the Oxford CT1500B Cryotrans coldstage/coating unit using the tissue freezing medium made up of equal proportions of G. 303 Colloidal Graphite (Aquadag) (Agar Aids) and Tissue-Tek OCT Compound 4583 embedding medium (Miles Scientific). Aqueous solutions of different heavy metal ions of approximately 2 μl were placed onto the rough side of paper samples by glass pipette. Rapid sample freezing was achieved by placing the drop of the penetrating liquid onto the paper which was then immediately plunged into nitrogen slush at -230°C. Freezing was achieved in less than half a second after droplet placement. The use of nitrogen slush (SN_2) rather than liquid nitrogen (LN_2) ensured liquid rather than gas to sample contact (Robards and Sleytr,

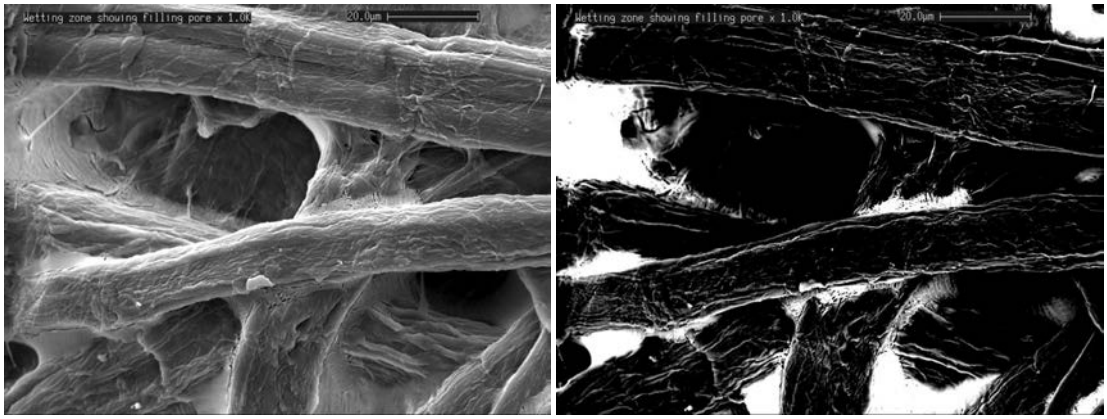

Figure 6.1: *An example of an SEM image of fluid penetration into kraft paper in (a) secondary electron mode and (b) backscattered mode.*

1985; Echlin, 1992; Duchesne and Daniel, 1999) ensuring the reduction of artifacts and the avoidance of crystallisation.

Three aqueous solutions of metal ions were tried in order to enhance the detection of the wetting fluid with the backscattered electrons in the SEM; uranyl acetate $U(CH_3COO)_3$ (6% & 50% w/w), sodium chloride NaCl (1.85M) and caesium iodide CsI (2M, 1.85 atom%). The caesium iodide solution gave good images with the SEM both with secondary and backscattered electrons (Figure 6.1). Uranyl acetate solution appeared to chromatographically separate and was discarded. Diethylene glycol was used as an imbibing liquid on one paper type and proved too viscous and was also discarded.

The stub with the attached sample was then inserted into the preparation chamber of an Oxford CT1500B Cryotrans coldstage/coating unit and into the SEM chamber and slowly warmed to - 80°C in order to remove the small amount of ice crystals that formed on the surface of the sample due to condensation. The progress of this was followed by observing the specimen on the SEM screen (at a low 5 kv accelerating voltage).

The frozen sample was then transferred from the SEM chamber back to the Oxford CT1500B Cryotrans coldstage/coating unit (Figure 6.2), sputter coated with a 10nm layer of gold and then transferred back to the SEM chamber which was then cooled to about -130°C using the cold sample stage inside the SEM chamber. The sample stage was cooled by dry nitrogen gas which was itself pre-cooled through a heat exchanger immersed in liquid nitrogen. The gas was conducted to and from the stage by flexible Teflon tubes thus permitting free movement in the *x*, *y* and *z*-axes. Stage temperature was monitored by a built-in thermocouple with temperature regulation obtained by an internal heater permitting temperature regulation from - 80°C during ice crystal ablation before gold coating, to -130°C for imaging.

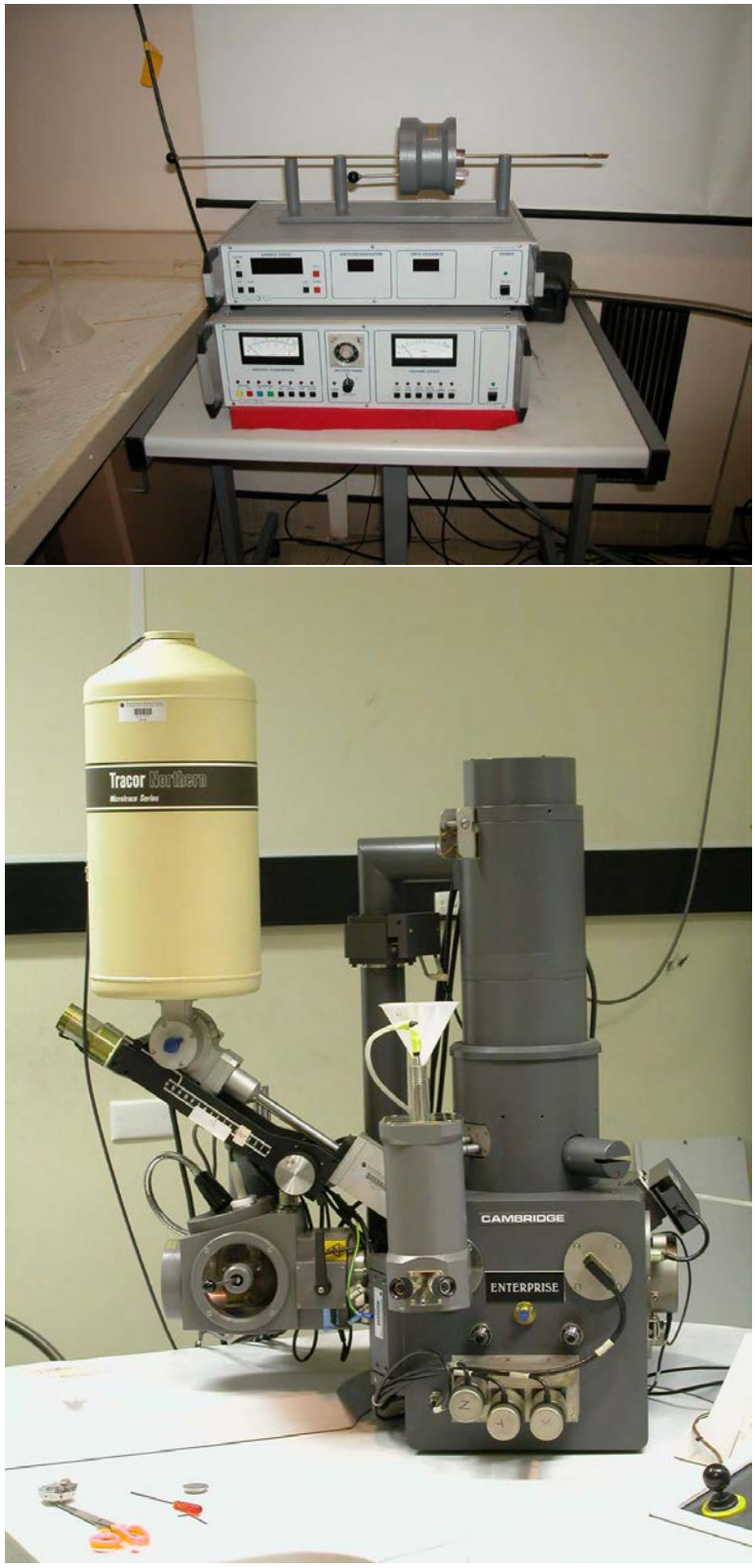

Figure 6.2: *Left; controller for Oxford CT1500B Cryotrans coldstage/coating unit for use with the Cambridge Instruments S360 SEM, Right image of the SEM showing cryo chamber which was on the left of the beam tower which was in use as seen by the funnel used for placement of liquid nitrogen into the heat exchanger for the cold stage.*

Sample preparation for sized papers was exactly as for saturating papers except the time allowed between droplet placement and freezing was extended to as much as 30 minutes.

The SEM was used to examine the specimen and for the production of micrographs both in secondary electron and backscattered mode. The electron optics system of the SEM was optimised for high resolution, ensuring sufficient depth-of-field to enable the entire selected field of view to be in focus. This involved the use of a 30 mm diameter final aperture, a working distance of approximately 23 mm, electron beam current of 1.94 na, a probe current of 1.05na and an accelerating voltage of 20 kV.

6.2.4 Imaging using cryo-two-photon confocal laser confocal microscopy

While cryo-SEM allowed one to visualize liquid flow on the surface of the papers at the edge of the droplet, one could not image below the surface or below the bulk liquid droplet. A cryo-two-photon confocal microscopic technique was introduced which enables one to obtain quantitative 3D images of the fluid penetration into paper at arbitrary depth within the sheet and to visualise penetration below the droplet.

A review of the principles and use of two-photon confocal laser confocal microscopy is in Section 2.2.2 in Chapter 2.

6.2.4.1 Development of cryo-cell for CLSM

As with cryo-SEM, the experimental method had to ensure that 1) droplets were maintained in a frozen state for long periods, 2) samples had to be frozen quickly and 3) a fluorescent liquid had to be used to ensure differentiation from fibres.

A cryo stage was developed for a 2-photon confocal laser scanning microscope enabling very cold dry nitrogen to be passed in close proximity to the frozen sample for long periods of time. Image capture could take up to 45 minutes, each image taking about 5 minutes *i.e.* 15 seconds per slice two acquisitions per slice (to improve signal to noise ratio) and up to 40 slices for each completed acquisition. Up to six separate acquisitions were obtained from each sample to ensure the imaging of the full dynamics of wetting. Temperature stability was therefore essential to minimise thermal expansion and contraction of the frozen sample. If temperatures varied by more than $\pm\ 5^{\circ}C$ during each individual image acquisition, distortion would occur between consecutive image sections ruining the acquisition sequence.

Full details of the design, construction and use of the cryo-cell used with the CLSM are attached in Appendix C.

6.2.4.2 Sample preparation for CLSM

Samples of 19.5 mm diameter were produced so they could be placed rapidly into the cryo-cell after liquid placement and freezing. The sample preparation method was identical to that

carried out for cryo SEM (Section 6.2.3.1). However the SEM had a purpose built unit that created (SN_2) enabling sample freezing and placement onto the SEM. For the cryo 2-photon confocal experiments, a vacuum sample preparation chamber had to be constructed to create the (SN_2) needed for sample preparation (Figure 6.3).

The cryo-cell consisted of a *Kel-F* cryo-cell insert containing a sintered bronze ring onto which the frozen sample was placed (see Appendix C). The insert was placed inside a *Delrin* base plate which was fixed to the microscope slide. The insert was removed from the base plate and the bottom window and rubber spacing washer removed from the insert. The dewar containing the copper cooling coil was filled with liquid nitrogen. A regulated supply of gas was passed through the double copper coil to the base plate of the cryo-cell. The sample of paper to be imaged plus a piece of 0.05mm thick *Teflon* sheet punched to the same size was placed in a surgical arterial clamp. The *Teflon* stopped any potential hydraulic interference between the liquid nitrogen and the liquid in the paper sample. A Styrofoam cup full of liquid nitrogen was placed into the chamber connected to a vacuum pump, the acrylic lid (seen in the top left hand side of Figure 6.3) was then placed onto the chamber and a vacuum applied. When the liquid nitrogen solidified the chamber was opened and the slush stirred. The cryo-cell insert was partially placed into a container of liquid nitrogen in order to maintain the sample in a frozen state after placement for the few seconds it took for the cryo-cell to be inserted into the base plate through which cold gas was being passed.

Using a Gilson P200 Pipetman micro pipette in the left hand and holding the sample in the right just above the nitrogen slush, a 5 μl aliquot of the fluorophore solution was placed on the rough surface of the paper sample. Immediately after droplet placement the sample was plunged into the SN_2 Teflon side down (Figure 6.3). Freezing was achieved in less than half a second after droplet placement.

Figure 6.3: *Vacuum chamber for preparation of (SLN_2) and placement of droplet onto paper sample immediately prior to freezing in the chamber. This technique was exactly the same as that used for cryo-SEM except with the purpose built Oxford cryo chamber.*

After removal from the SN_2, the sample was separated from the *Teflon* disc and placed onto the bronze sinter in the cryo-cell which had been cooled with LN_2. The rubber spacing washer was placed onto the sample and the assembly completed by fitting the stainless steel disc with the viewing window onto the bottom of the cryo-cell (Figure C.1a, Appendix C). The cryo-cell was immediately placed into the baseplate attached to the microscope stage, enabling the cold gas to immediately flow through the cryo-cell and around the sample. A lug in the baseplate corresponding to a notch in the cryo-cell ensured the gas ports were perfectly aligned (Figure C.1b, Appendix C). The thermocouple wire was placed into one of the exhaust ports and the flow of gas regulated to ensure the desired temperature of between - 60°C and - 70°C at the sample.

Given the very cold temperatures, the rapid build up of condensation and ice on the cell assembly had to be prevented in order to enable imaging over long periods. This was achieved by passing dry nitrogen gas at room temperature onto the viewing window of the cryo-cell using a length of 6mm copper pipe, the end of which was flattened to a fan shape, increasing the velocity and spread (see Figure 6.4). The top window was kept ice free using ethanol to enable positioning and focussing of the laser.

***Figure 6.4**: Nitrogen gas nozzle used to remove condensation from bottom window of cryo-cell*

6.2.4.3 Obtaining images

Images were obtained using a Leica DM IRB/E inverted microscope[1], fitted with a Leica N PLAN L 40 x objective lens with a long working distance (2.0 mm) and a numerical aperture (NA) of 0.55. The long working distance was essential as the distance between the sample and the objective was over 1.0 mm due to the position of the bottom viewing window. A Coherent Mira 900 Titanium sapphire infra red laser with a wavelength of 800 nm was used. It had a path width of 15 nm, a pulse rate of 150 femto seconds, a peak power of 100 kW, pulse width of < 2 psec, a repetition rate of 76 mHz and a beam diameter of 0.8 mm (see Figure 6.5).

[1]The controlling software used was Leica Confocal Software Version 2.00 Build 0858 1997 - 2001 from Leica Microsystems Heidelberg GMBH.

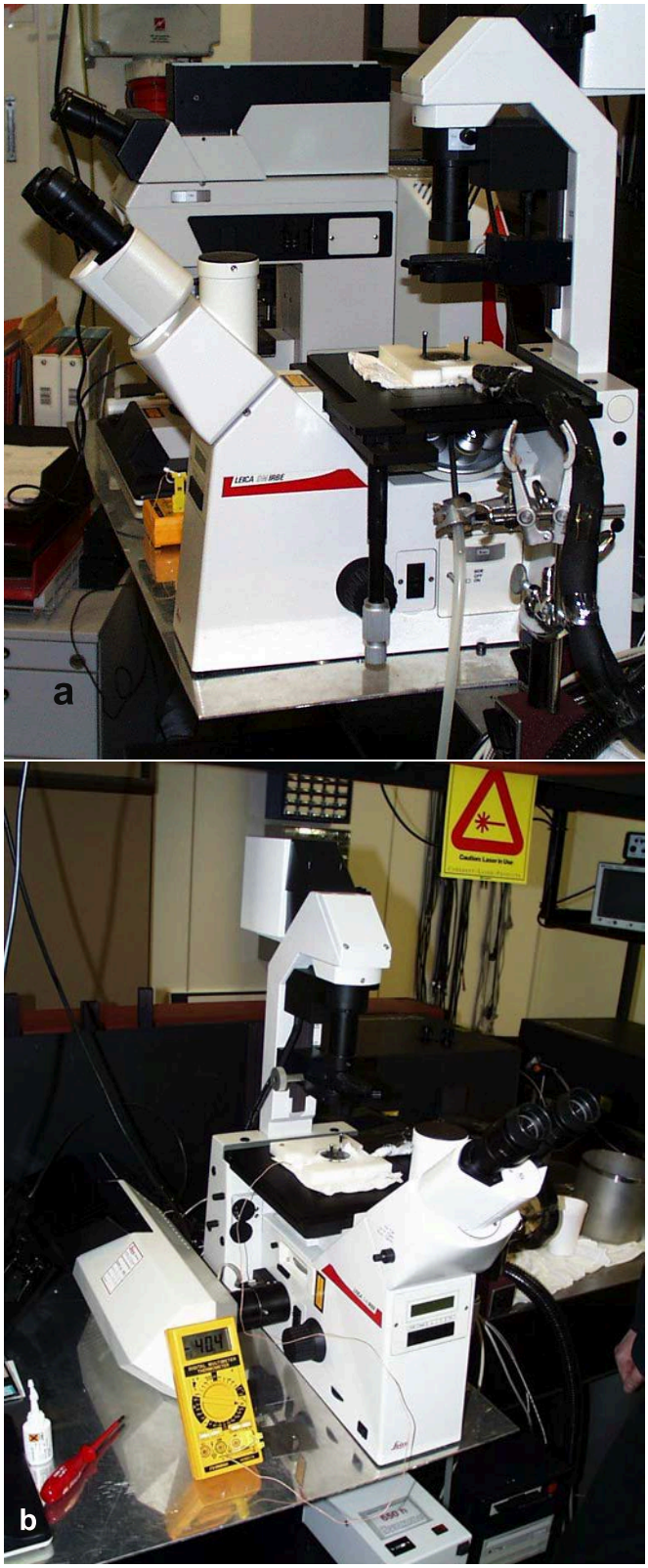

Figure 6.5: *Leica inverted 2-photon confocal laser scanning microscope used to obtain all images. Note the thermocouple temperature in image b: showing a temperature of -40.4°C, showing that this was during the cooling phase before imaging as the temperature was not stable below - 50°C. Note the cryo cell positioned on the microscope stage.*

The power of the laser could only be altered by the use of neutral density filters. However due to the extremely low temperatures at which images were obtained there was no photo-bleaching of the chosen fluorophore even when neutral density filters were not used (whereas at room temperatures photo-bleaching occurred rapidly).

Three fluorophores were tried; Cascade Blue hydrazide C-3239, a trilithium salt from Molecular Probes, Inc., sodium fluoroscein and Rhodamine B each at various concentrations. They were tested by placing a droplet of the fluorophore solution onto a microscope slide to determine the strength of the fluorescence under similar excitation conditions and also to determine the optimum solution strength, given quenching could occur with higher solution strengths. The fluorophores were also absorbed into paper and imaged to determine how strongly the fluorophore adsorbed onto the paper fibres. As the aim was to highlight the fluid (ice) phase not the fibrous material within the papers, it was essential that the fluorophore did not adsorb onto the fibres at all. The fluorophore selected as giving the best definition was 0.01% w/v Rhodamine B, $C_{28}H_{31}N_2O_3Cl$, 2-[6-(Diethyl amino)-3-(diethyl amino)-3H-xanthen-9-yl] benzoic acid. It did not adsorb onto the fibres at all.

To test for background fluorescence of dry fibres, a dry piece of paper was imaged. It was found that only very slight fluorescence was achieved at the maximum photo multiplier setting. At the photo-multiplier settings used during imaging of liquid imbibition, there was no background fluorescence of the fibres at all. Therefore if fluorescence occurred it indicated the presence of the fluorophore and hence the liquid.

Once the sample was in place and the temperature stabilized at - 60°C and - 70°C $\pm$ 2°C (which usually took about 2 minutes), the laser was turned on and the photo-multiplier was set to maximum and the offset to minimum. The laser and lens were coarse focused by observing the clarity of the beam passing through the sample and then fine focused by looking at the projected image on the computer screen (see Figure 6.6). After focussing, the photo-multiplier gain and offset were adjusted for each image with the aim of getting a slight level of photo-bleaching at the high end of fluorescence to ensure sufficient detail through the image. The image size was 250 x 250 μm (1024 x 1024 pixels) and the voxel size was 0.02 x 0.02 μm *(x, y)* x 2.5 μm *(z)*.

Figure 6.6: *Computer station controlling two-photon microscope showing image acquisition on right screen and microscope and laser configurations on the left screen.*

Samples were imaged droplet side up, or down, depending on the nature of the experiment, however the droplet was always applied onto the rough (wire) side of the papers imaged. The maximum depth of imaging through the paper was about 70-80 μm as attenuation of the detected fluorescence signal usually occurred beyond this depth. Two scans per section and scanning at a low speed were used to improve the signal to noise ratio of the image (Tsien and Waggoner, 1995; Xu and Parker, 1999).

To ensure accurate identification of the position of the region of interest being imaged, it was necessary to locate the drop surface with the high magnification lens. Changing the objective lens in order to locate the region of interest was not possible given the positioning of the gas nozzle required to remove condensation from the bottom of the cryo-cell (Figure 6.4). Positioning was achieved by reducing the photo-multiplier gain so the focus was on a narrow ring of fluorescence on the droplet. By slightly moving the focus, the side of the droplet being imaged could be determined, by then focusing towards the sample and continually shifting the sample, the interface of the droplet and the saturated zone on the paper was found.

6.2.5 EDXA analysis of sized papers

Energy Dispersive X-ray Analysis (EDXA) (Echlin, 1992) was used to identify the distribution of caesium iodide (CsI) using the Cambridge S600 scanning electron microscope. X-ray spectra were generated by focusing onto a pre-selected area of a specimen. Sampling volumes were around 10 μm^3 and clearly distinguished between fibre walls and fibre lumen. Where it appeared that CsI was present using backscattered electrons, EDXA was used as confirmation for the presence of CsI[2]. Even in normal imaging mode, using secondary electrons, the CsI rich zones showed enhanced contrast.[3]

***Figure 6.7**: Reichert Jung FC4 Ultracut cryo-microtome.*

Sample preparation for EDXA analysis was the same as for cryo-SEM analysis however the samples were cryo-microtomed (Duchesne and Daniel, 1999) using a Reichert Jung FC4 Ultracut cryo-microtome (Figure 6.7) at -90°C). Apart from the use of the cryo-microtome the microtoming technique including preparation of glass knives was identical to that described in Chapter 3.

[2]Normally when using EDXA one coats the sample with carbon, however as the samples were being imaged as well, gold coating was used hence the strong peaks for gold in the EDXA spectra in Figures 6.37 & 6.39. However the Cs peaks were clearly discernable.

[3]X-ray spectra were analysed using Moran Scientific Energy Dispersive Analysis System V 9.3.

6.3 Results

6.3.1 Unsized & unfilled bleached kraft papers

Figure 6.8 shows a low magnification image which illustrates the typical penetrating fluid configuration at the paper surface emanating from near the drop edge (upper left corner) radially outwards. Two regions can be observed in the image; near the droplet edge where pores seem completely saturated; this region extended $\simeq$ 500 μm from the drop edge (blue shading in Figure 6.8). The remaining region was only partially saturated by the penetrating fluid. The degree of saturation decreased as one moves further from the drop edge. The penetrating fluid was now present only in the form of films in the regions between the fibres. Here large pores remained unsaturated in the midst of smaller filled pores (red shading).

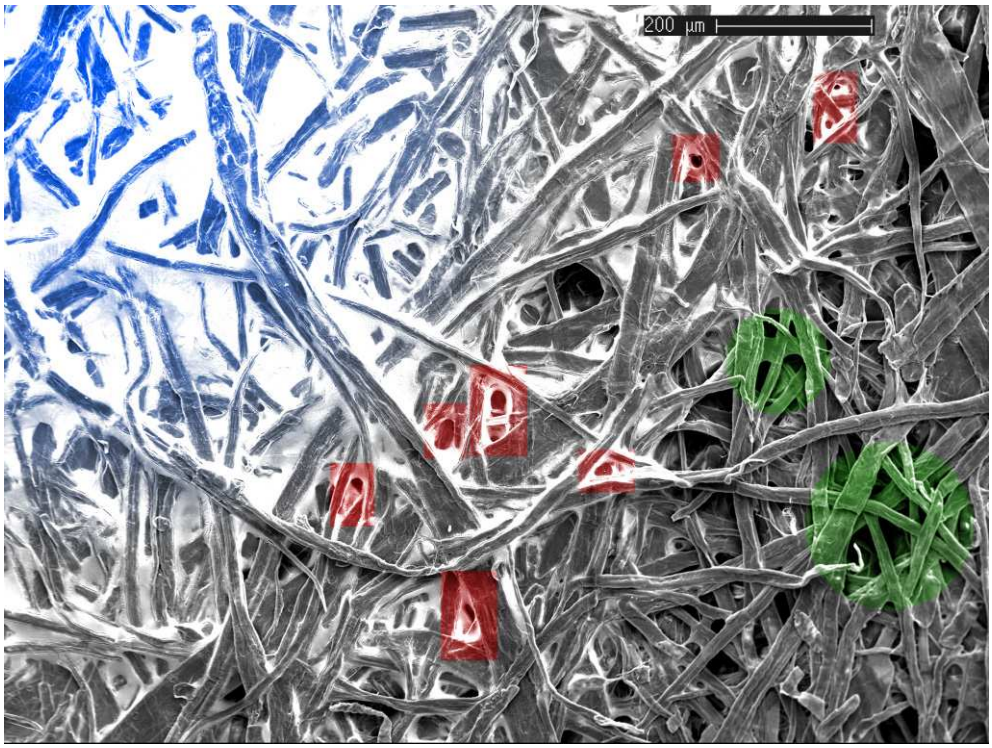

Figure 6.8: *Low magnification image showing the fluid configuration at the paper surface. A region of saturation exists (shaded blue) near the droplet (upper left of the image). The remaining regions exhibiting the presence of fluid are partially saturated. Red shading shows regions where pores exhibit partial filling. Green shading illustrates regions where the surface pores diverge to large openings.*

Figure 6.9 shows a typical fluid distribution in the midst of the completely saturated region. One observes that pores at the surface were not all filled and fibres at depth were still visible from the surface. The fluid did not tend to wet the upper surface of the paper fibre; the fluid interface instead seemed to preferentially wet the fibre edges and became pinned along the fibre edge.

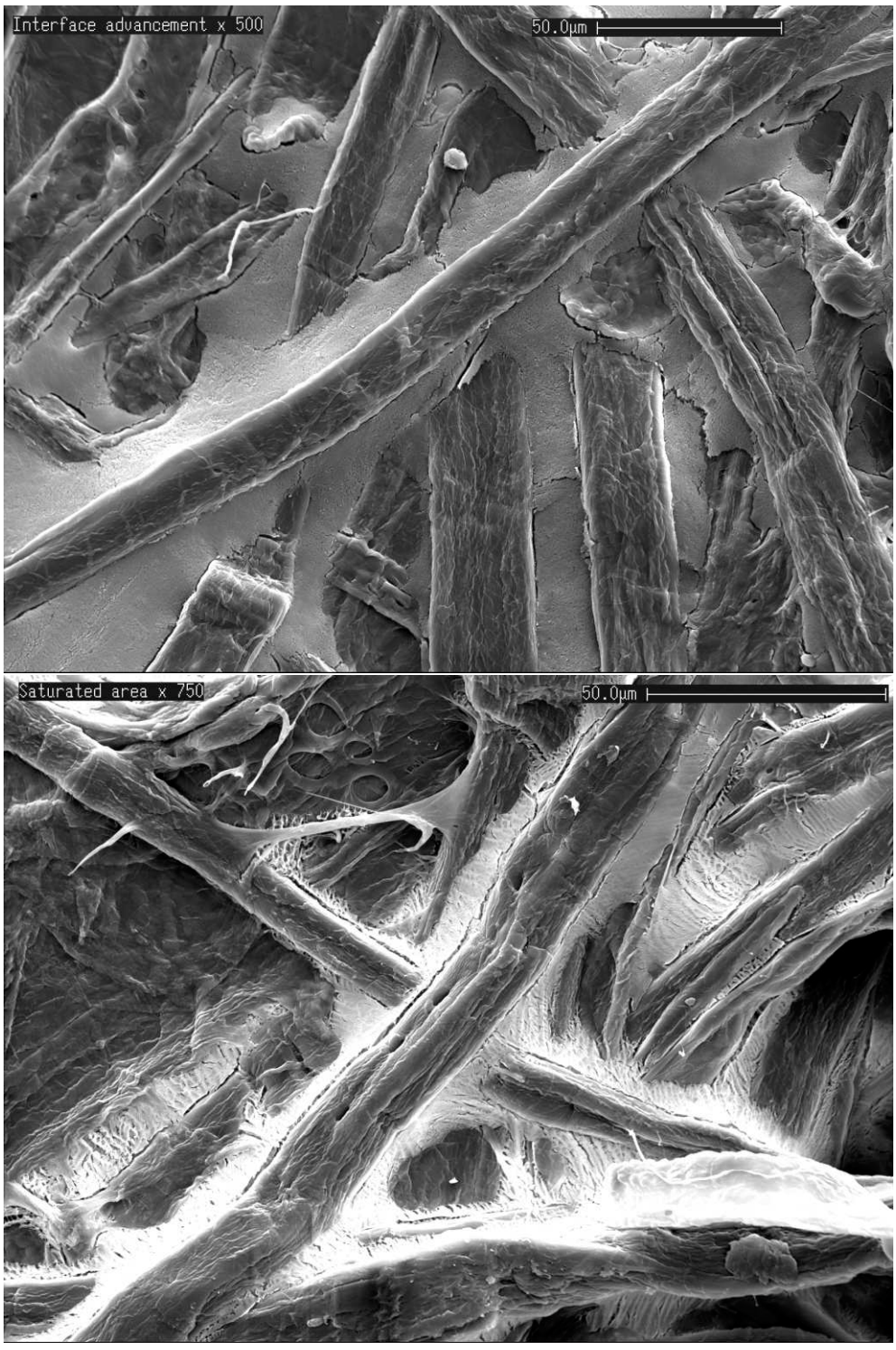

Figure 6.9: *The typical fluid distribution in the midst of the saturated zone. One observes that pores at the surface are not all filled and fibres at depth are still visible to the surface.*

Figure 6.10 is a higher resolution image showing a fluid configuration just outside the partially saturated region. The fluid primarily filled the pores which lay between the edges of fibres (red shading) and did not wet the upper fibre surface. The presence of films can be observed along channels formed by fibre overlap (blue shading) which interconnect many of the filled pores. Larger surface pores remained unfilled (yellow shading), however some edges of the large pores exhibited a presence of a liquid wetting film.

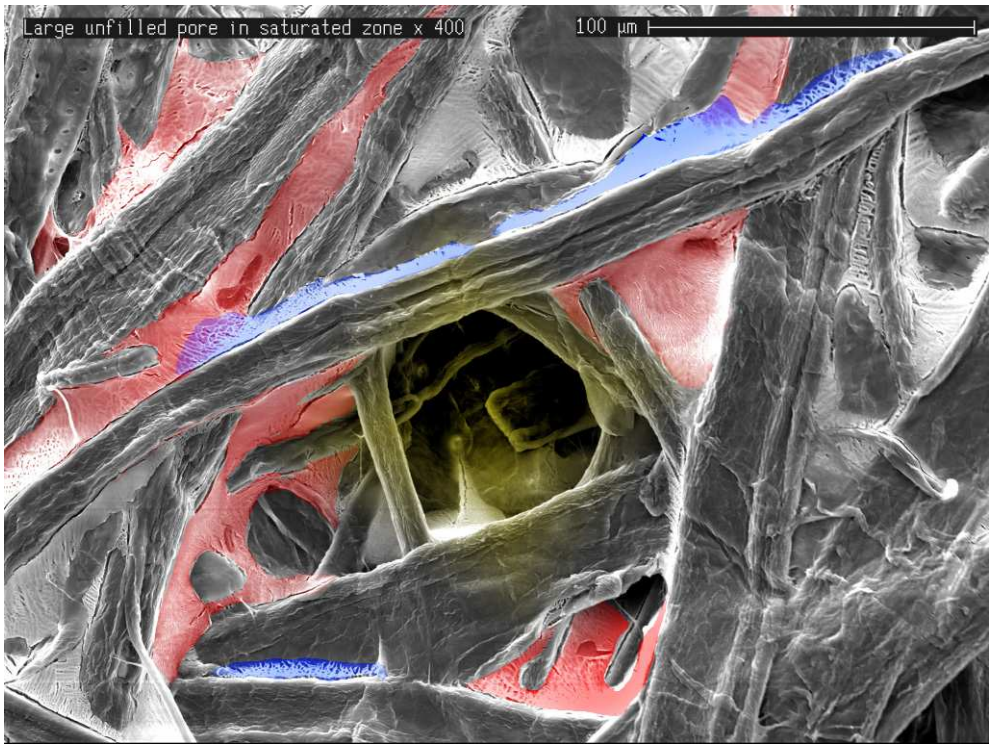

Figure 6.10: *Higher magnification image of the fluid configuration inside the partially saturated zone. This image appears on the front cover of the Journal of Pulp and Paper Science Vol. 29 No. 4 (123 - 131) April 2003 (Roberts et al., 2003)*

Further away from the droplet edge a number of interesting fluid configurations within the pore space can be observed. In the top image of Figure 6.11 completely filled pores between fibre edges can be observed (red shading), and the presence of seemingly disconnected fluid films along channels formed by fibre overlap scattered throughout the rest of the image (green shading). The bottom image in Figure 6.11 shows pore filling from thickening films on the edges of pores. A curious fluid configuration (yellow) within a pore lying 3 - 4 fibres below the paper surface can be observed where the pore was mostly filled, but a partial disk of air punctures the center of the pore. Several of these partially filled pores are visible, recall Figure 6.8 red shaded area. A close up of this configuration is shown in Figure 6.12. Figures 6.10 & 6.11 show filling of a pores from films at three different layers indicating that film flow occurred throughout the paper sheet.

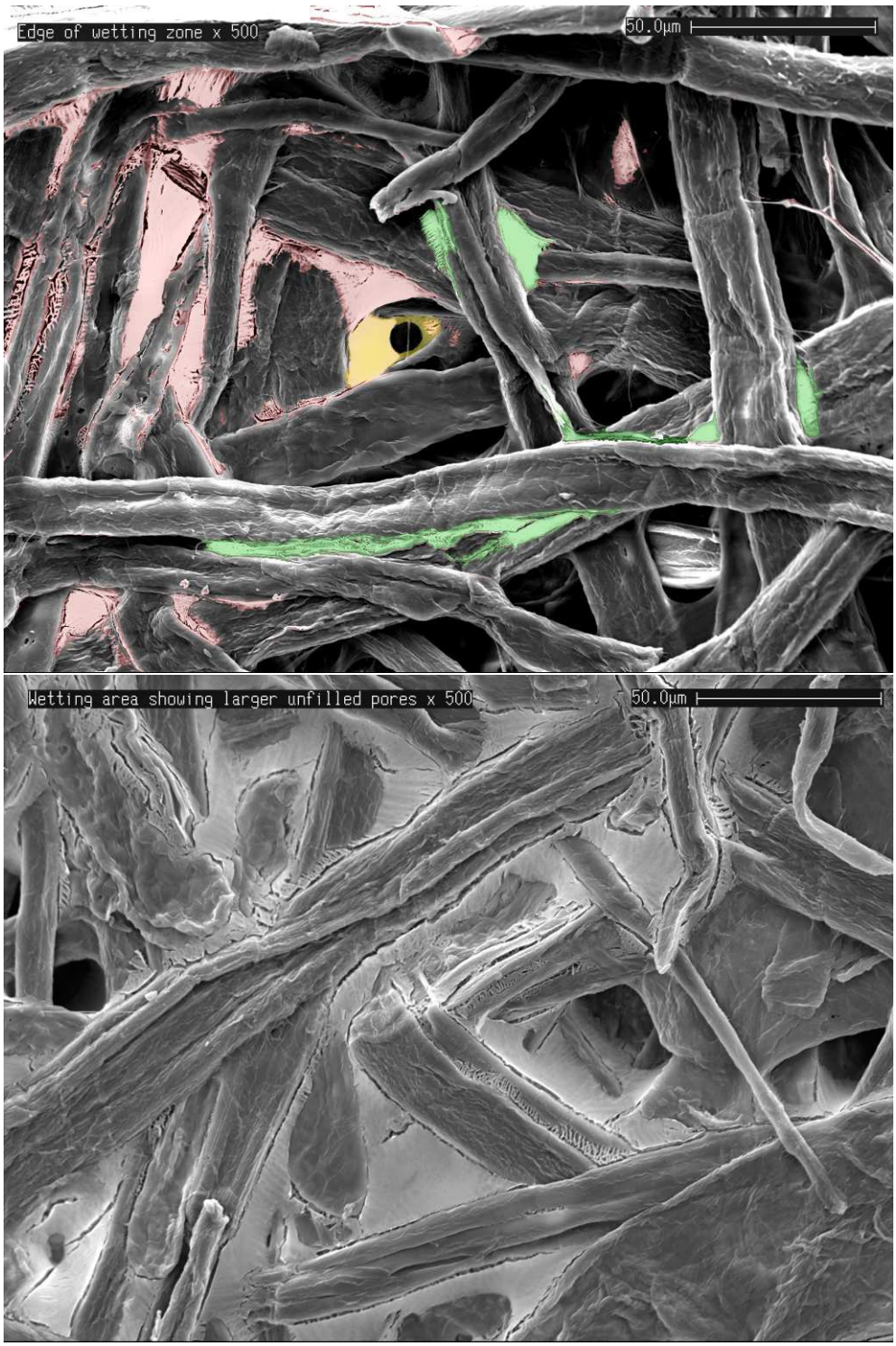

Figure 6.11: *Fluid configurations within the partially saturated zone. The top image has been colourised to highlight the fluid flow. The yellow section highlights the metastable state just prior to snap off, the red shows filled pores and the green shows film flow along inter-fibre channels. The bottom image shows films thickening on the edge of a pore leading to pore filling.*

In Figure 6.13 shows a smaller pore (red) with a pore size of $\simeq 10$ μ m completely filled with the wetting fluid and a larger neighbouring pore of size $\simeq 20$ μ m (green) which only exhibited a presence of films along the edges.

Figure 6.14 was taken further out from the drop edge. In this region the wetting fluid was present solely as films along channels formed by fibre overlaps (blue) and as films wetting edges and corners of the pore (red).

At the outer edge of the partially saturating zone film flow occurred only along fibre intersects (Figure 6.15). Only a small amount of flow could be seen along the fibre surface roughness and no flow into fiber pits (arrow in the top image).

From the experimental results it could be concluded that film flow was a major mechanism for transport of the wetting fluid. Bulk flow through the pores was not generally observed.

6.3.1.1 Cryo-2-photon laser confocal microscopy

Although SEM gave some indication of fluid imbibition at depth, it was only away from the droplet. It was necessary to investigate fluid flow under the droplet as well as below the surface of paper. To do this required the use of CLSM.

The images presented in this section are stereo composite images from all the slices acquired in a complete acquisition and should be viewed with green/red anaglyphic glasses included in the back of this thesis (Appendix **??**) to give a 3D effect. Full movies of the sequential slices are also attached in a CD (Appendix **??**). The interpretation of the CLSM images is more complex than those of cryo-SEM as fibres do not attenuate and all that is seen is the fluorescence of the liquid.

To help in interpreting the CLSM data an image is shown at the edge of the partially saturated zone approximately 200 μm from the edge of the droplet (Figure 6.16) a fibre is indicated by the arrow marked ”A”. Note there is no strong fluorescence on the surface of the fibre and also it is not possible to discern any detail on the fibre surface. This indicated that there is no liquid actually within the fibre itself. This particular fibre was about 35 μm below the surface of the paper. Note the strong lines of fluorescence shown by the arrow marked ”B”. This fluorescence came from films of liquids along the edges of fibres indicating fluid flow in fibre overlap channels. The arrow marked ”C” in this image shows an unfilled void space surrounded by thickened films of liquid. The depth of this void space was between 12 and 20 μm below the surface of the paper. An equivalent SEM image albeit on the surface is the top image of Figure 6.14. The movie of this CLMS image is #109.

The middle image in Figure 6.16 is now under the droplet and also shows strong fluorescence along the edges of fibres (arrow marked ”A”) as well as thickening of these films (arrow marked ”B”) lying 28 μm under the surface of the paper. Note there was no clear detail of the fibre surface again indicating that there was no flow within the fibre itself. The fluores-

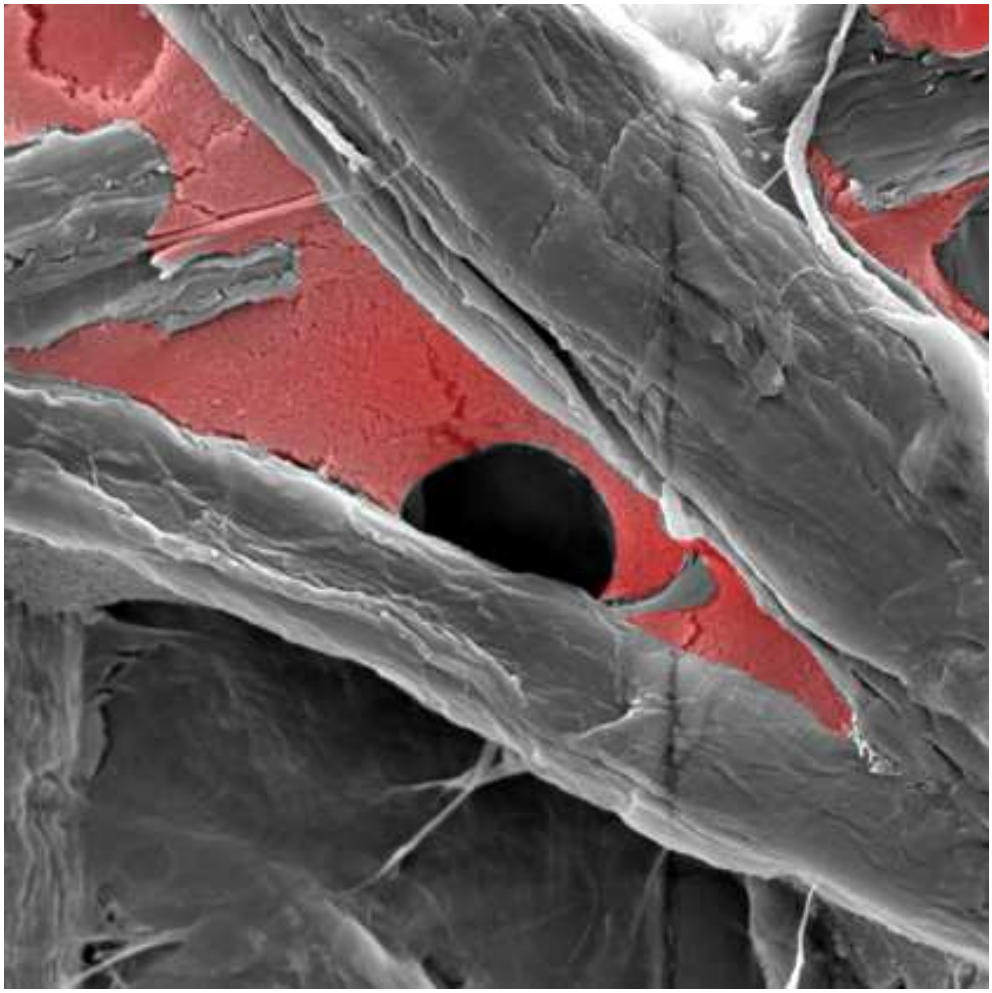

Figure 6.12: *Close up of a partially filled pore exhibiting pinning of the meniscus on the pore wall. As a result it was unlikely that snap-off would have occurred in this particular pore.*

cence seen along edge of fibres was actually visualised from underneath the fibres where they contacted adjacent fibres creating overlap channels. One can also observe unfilled void spaces below the droplet (arrow marked ”C”). The movie of this image is #106 in the attached CD.

The bottom image in Figure 6.16 is at the edge of the droplet where the arrow ”A” shows a small amount of fluorescence on the droplet surface which was about 10 μm above the paper surface at this particular point. The arrow marked ”B” highlights the scenario observed in the top image of Figure 6.12 *i.e.* pinning of the meniscus of a thickening film onto the pore wall. This occurred approximately 15 μm below the surface of the paper. The arrow marked ”C” shows thickening of films out from the fibres. The movie of this particular image is #94 and is in the attached CD.

The top image in Figure 6.17 is located at the edge of the droplet which can be seen with the arrow marked ”A”. The droplet was 15 sections deep *i.e.* 38 μm thick. It clearly shows strong fluorescence along the edges of fibres indicating film flow in fibre overlap channels (arrow marked ”B”) and film thickening (arrow marked ”C”) in exactly the same manner as that shown in red shading in the SEM image Figure 6.11. The movie of all the sections of this image is #114.

Figure 6.17 shows a number of lenses in different pores with trapped air in between them as shown by the arrow marked ”A”. This is analogous to that observed in the SEM image Figure 6.12. Note that the fibre was actually 10 μm below the lens of liquid highlighted by the arrow further emphasising the fact that filling of pores can occur at many different levels. The movie of this image is #167.

This result leads to the conclusion that even under the droplet and below the paper surface, the primary mechanism of fluid penetration into unsized papers was through liquid films along channels formed by fibre overlaps. The fibres themselves could not be clearly distinguished indicating that the fluid had not penetrated the fibres. What was particularly significant was that film flow, film thickening and large unfilled pores could be seen underneath the droplet as well as away from the droplet below the paper surface.

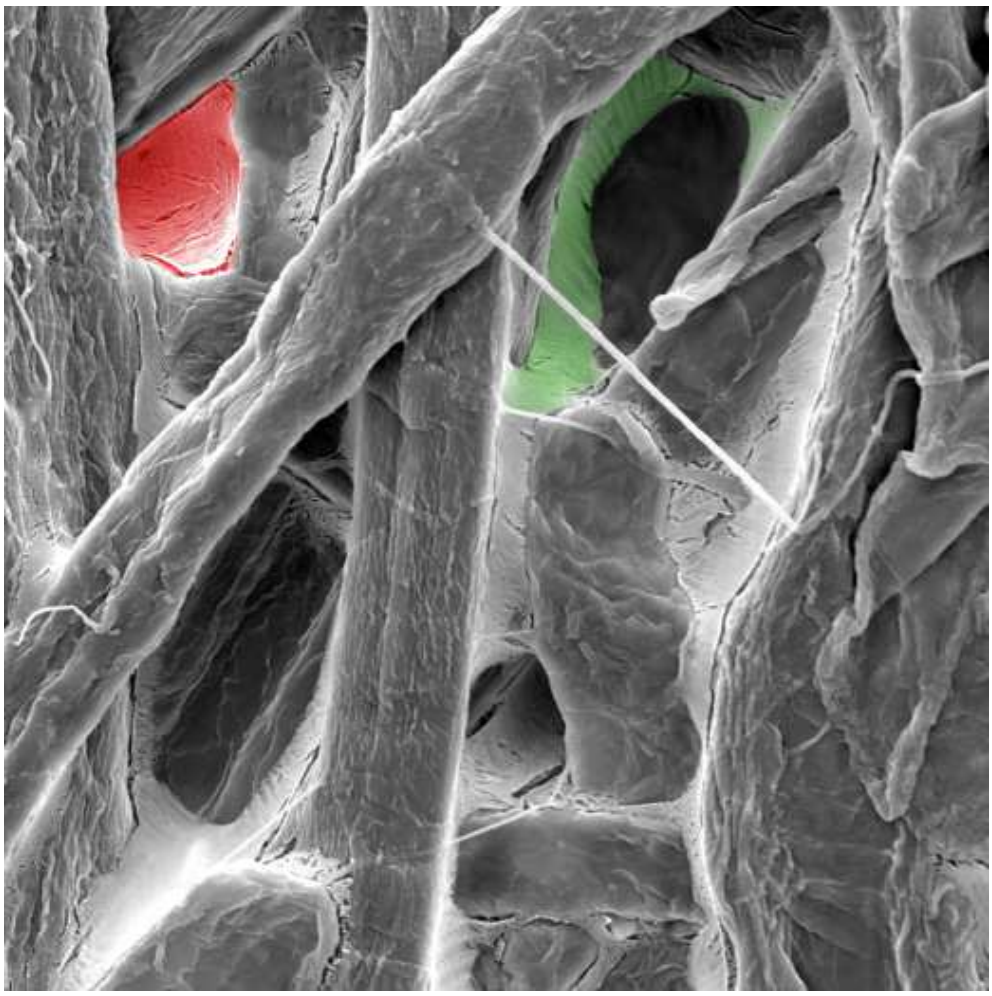

Figure 6.13: *A small pore (red) with a pore size of $\simeq$ 10 µm completely filled with the wetting fluid and a larger neighbouring pore of size $\simeq$ 20 µ m (green) which only exhibits a presence of films along the edges.*

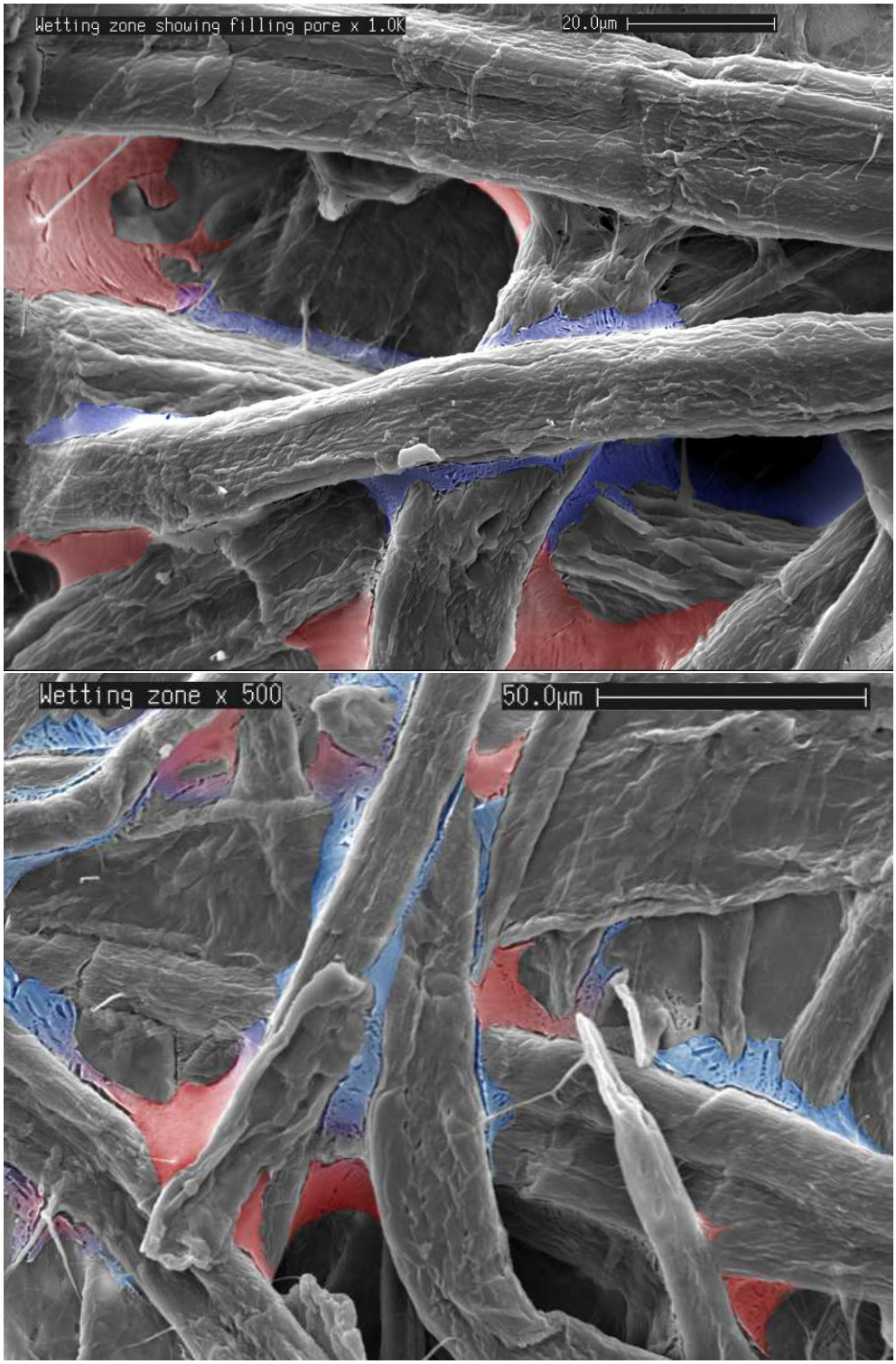

Figure 6.14: *Two examples of fluid configuration in regions far from drop edge. The wetting fluid was present solely as films along channels formed by overlapping fibres (blue) and as films wetting corners of the pores (red).*

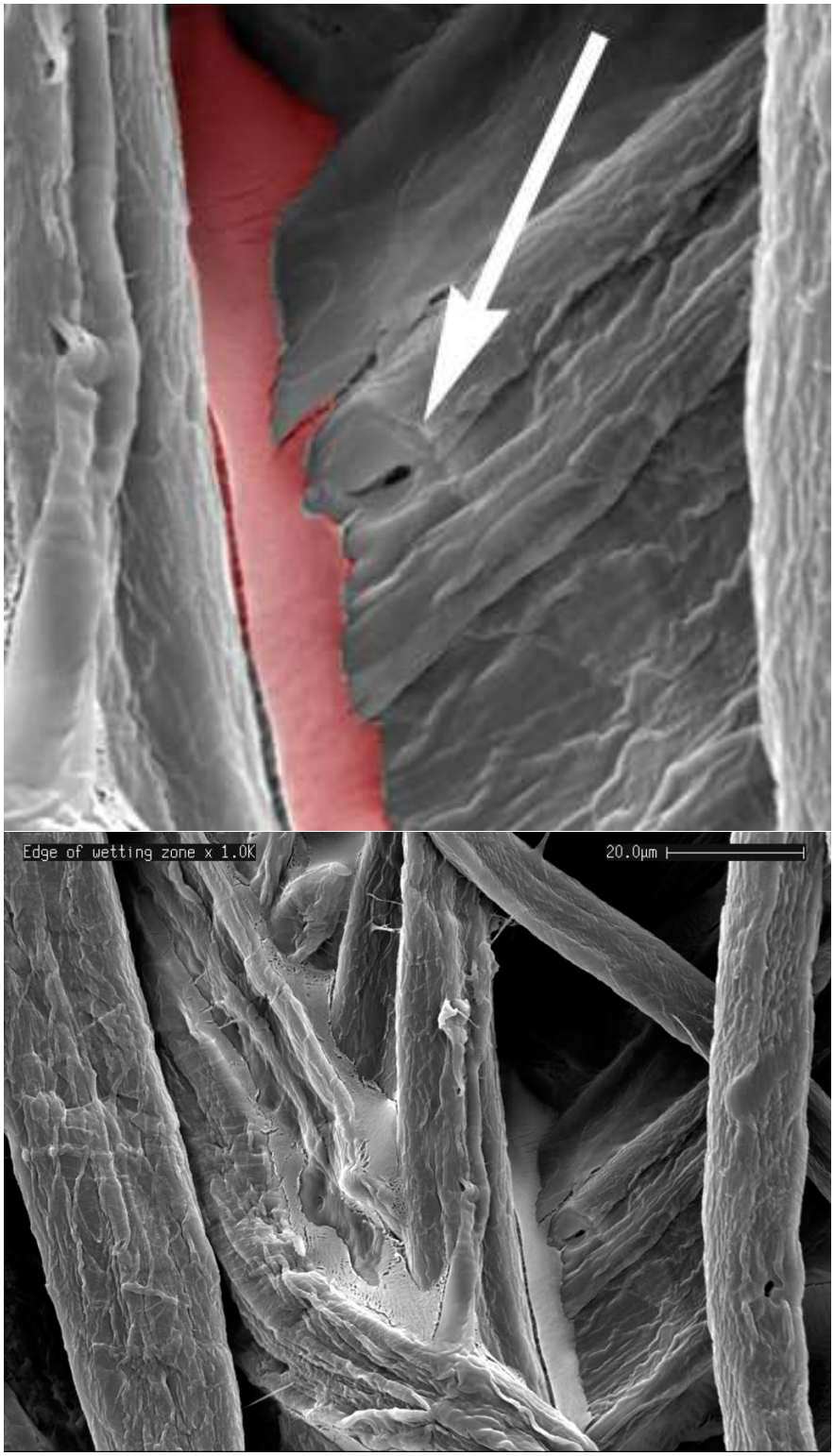

Figure 6.15: *At the outer edge of the fluid only film flow was observed along fibre intersects. The top image has been colourised to highlight film flow and is a closeup of the bottom image. The arrow highlights a bordered pit that appears to have no visible liquid beneath it.*

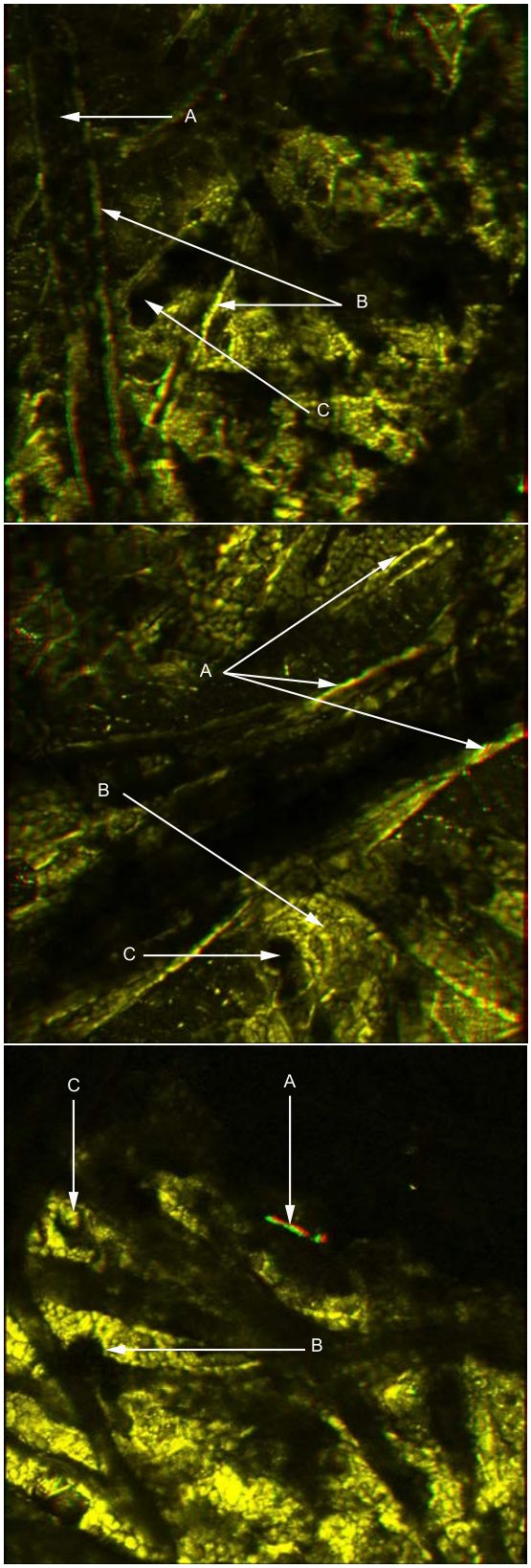

Figure 6.16: *Stereo images showing, Top: film flow occurring along edges of fibres analogous to that seen in Figure 6.14, Middle: thickening of films as seen in Figure 6.11 and Bottom: pinning of the meniscus and pore filling away from the droplet edge as seen in Figure 6.12.*

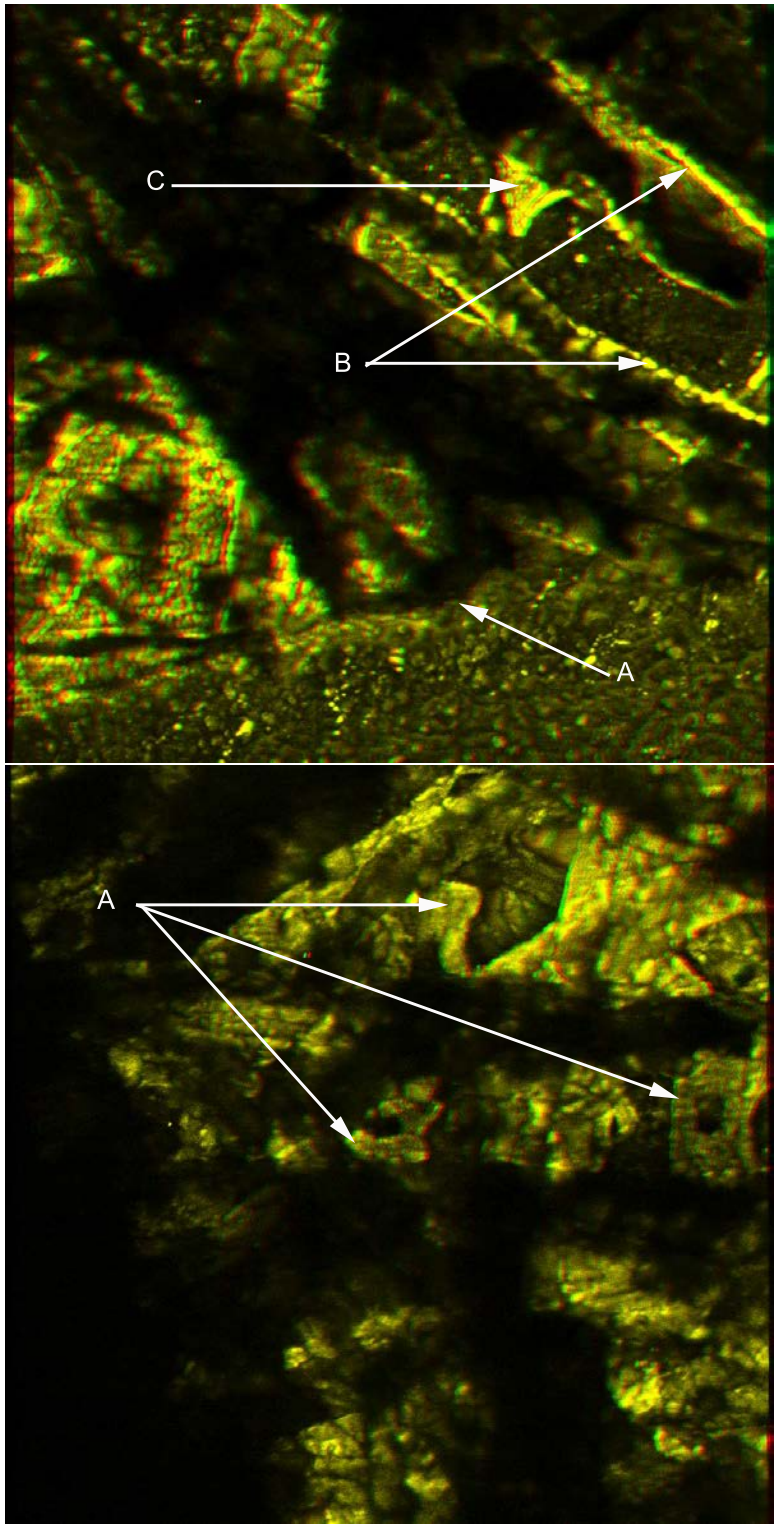

Figure 6.17: *Stereo images showing, Top: film flow adjacent to the droplet and Bottom: pore filling occurring from films from interfibre channels at different depths in the paper. Note the lenses of liquid forming at the different levels*

6.3.2 Decor papers

6.3.2.1 Cryo-SEM

Decor papers are designed to saturate. They are unsized and unlike the laboratory paper samples considered previously, contained large amounts of various organic and inorganic fillers and dyes. They are much more complex in structure than the laboratory papers imaged in Section 6.3.1 and can use fibrous material other than that originating from wood. Decor papers can vary considerably in weight, and density as was established in Chapter 4. In this section fluid penetration processes into the range of decor papers studied in Chapter 4 were visualised. It was observed as with laboratory papers that the primary mechanism of imbibition was via film flow in inter-fibre channels.

Figure 6.18 *a* is the decor paper Beech clearly showing film thickening about to result in the filling of a pore in exactly the same manner as is shown in the SEM image of imbibition into a laboratory paper Figure 6.13 . Figure 6.18 *b* is the decor paper Black. The image shows film flow along fibre overlap channels as well as clear evidence of film thickening and large unfilled pores as was observed in the bottom image of Figure 6.11. Figure 6.18 *c* is the decor paper Folkstone Grey showing pore filling as a result of film thickening as well as unfilled voids as shown in the SEM image Figure 6.8. Figure 6.18 *d* is of the decor paper Fog showing film thickening and pore filling in the partially saturated zone. Note the pores between the fibres were mostly filled, however some of the larger pores were not. In these cases note that the meniscus of the imbibing liquid had pinned to the edge of the pore thus it was unlikely that these pores would ever have filled. This is analogous to the image of fluid imbibing into the laboratory paper in the bottom image in Figure 6.11. Note the very large differences in the sizes of individual fibres some appearing to be softwood and others hardwood fibre and how this had no effect on the imbibition mechanisms described. Figure 6.18 *e* is a high magnification image of the decor paper Storm showing incomplete pore filling. This was similar to those unfilled pores in Figure 6.18 *a* and again shows clearly how the meniscus of the liquid was pinned to the sides of the pore wall. Figure 6.18 *f* is the decor paper Alpine White. As was discussed in Chapter 4 this paper had the highest ash (filler) content and was very different in structure to the laboratory papers discussed in Section 6.3.1. All of these images show typical fluid distribution away from the droplet similar to that shown in Figure 6.8.

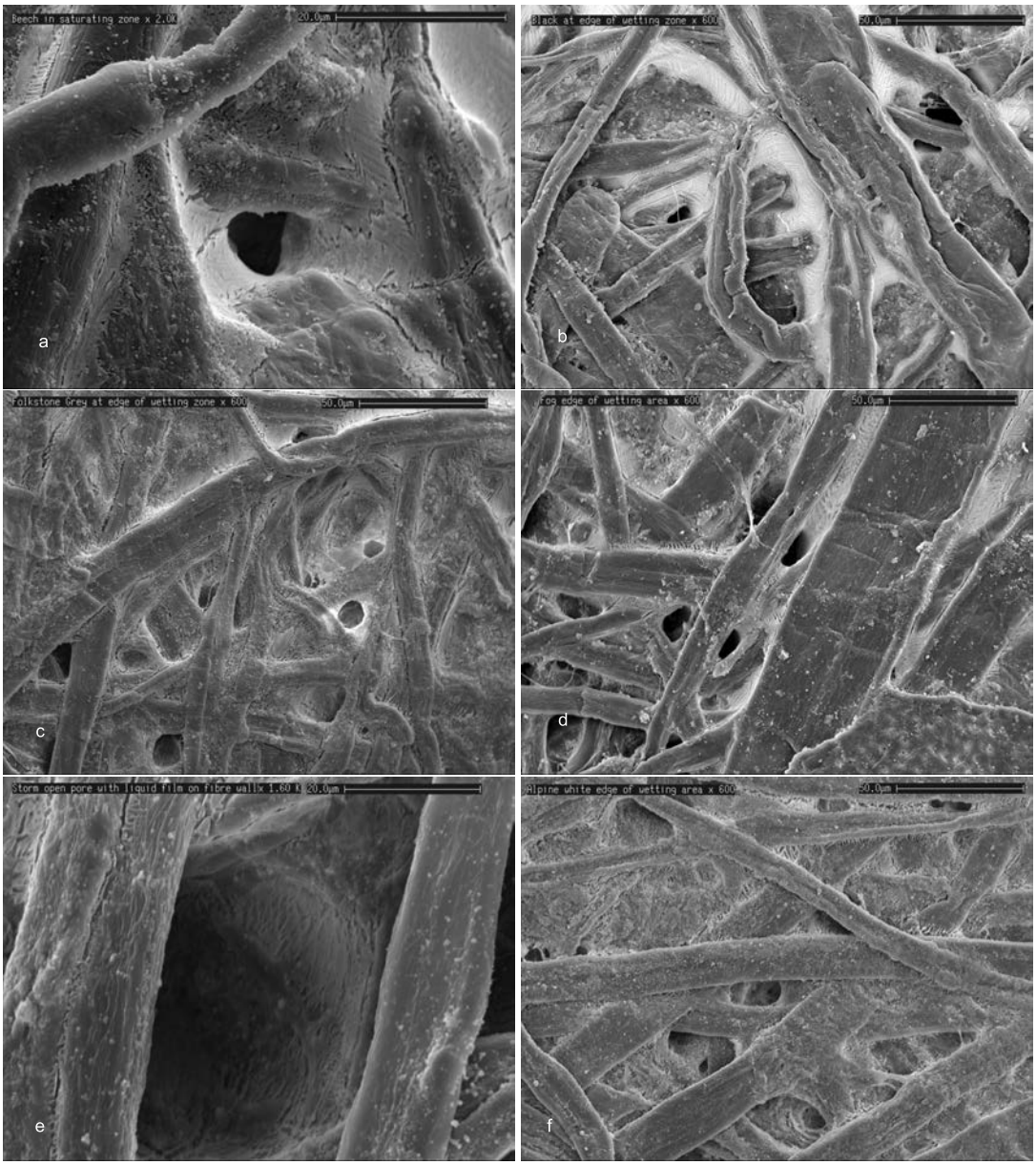

Figure 6.18: *Images of decor papers at various stages of wetting:* a)*; Beech showing pore filling from adjacent interfibre films in the fully saturated zone,* b)*; Black at the edge of the partially saturated zone showing transition from film thickening to pore filling,* c)*; Folkstone Grey showing pore filling at the edge of the partially saturated zone from interfibre films,* d)*; Fog showing edge of saturating zone, note pore filling from film flow notwithstanding the very small pore sizes,* e)*; a closeup of film thickening surrounding a pore in Storm and* f)*; Alpine White a highly filled very dense paper in the saturating zone showing interfibre film flow and unfilled pores.*

6.3.2.2 Cryo two-photon confocal microscopy

The top image in Figure 6.19 is a cryo CLSM image of the decor paper Streetlight which was a high ash paper (Table A.2) with most of the image being under the droplet. This is also clear if one scans through the movie #134 where one can quite clearly see the surface and extent of the droplet. From both the 3D composite image and from the movie one can clearly see that under the droplet there were unfilled voids that had films of liquid surrounding them (arrows marked ”A”). One can also see film thickening that had progressed to a certain stage but would not fill the pore (arrow marked ”B”). One can also see that smaller pores had been filled underneath the droplet (arrow marked ”C”). This is exactly what is seen in the top image of Figure 6.11.

The middle image in Figure 6.19 is also the decor paper Streetlight showing fluid distribution in the partially saturated zone about 150 μm from the edge of the droplet. This shows small filled pores (arrow marked ”A”) and larger unfilled pores resulting from various stages of pore filling resulting from film thickening (arrows marked ”B”). The fluid distribution shown was analogous to that shown in the cryo-SEM images in Figure 6.11. The movie of this image is #143.

The bottom image in Figure 6.19 is also the decor paper Streetlight at the transition from the fully saturated to the partially saturated zone *under the droplet*. This image has most of the mechanisms demonstrated with cryo-SEM (Figure 6.11) including film thickening (arrow marked ”A”), pore filling (arrow marked ”B”) and larger unfilled pores (arrow marked ”C”), *under the droplet*. The movie of this acquisition sequence is #144.

The top image in Figure 6.20 is the decor paper Alpine White in the saturated zone below bulk liquid which is 30μm thick showing a large unfilled pore surrounded by a thick film of fluid (arrow marked ”A”) analogous to that shown in the bottom image in Figure 6.11. It also shows a film of liquid (arrow marked ”B”) whose meniscus was pinned to a fibre wall as was shown in Figure 6.12. The movie of this image is #122. The bottom image in Figure 6.20 is the decor paper Beech showing large unfilled pores at the edge of the droplet shown by arrows marked ”A”. It also showed that fibres coming out from underneath the droplet had no evidence of surface flow (arrow marked ”B”) which was demonstrated in the cryo-SEM image Figure 6.9. The movie of this image is #141.

Some of the decor papers could not be imaged due to the fluorescence of their dyes. However cryo CLSM of all the decor papers imaged confirmed that the mechanisms of fluid flow is by films.

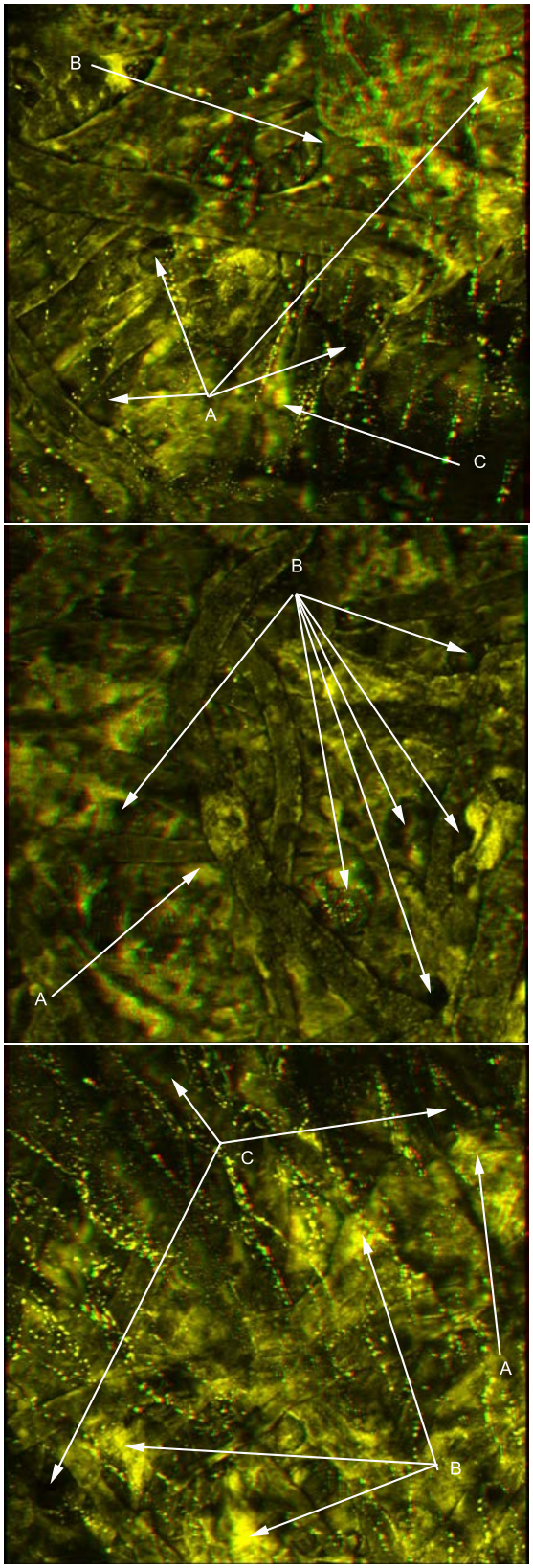

Figure 6.19: *Stereo images of the decor paper Streetlight showing, Top: unfilled voids below edge of droplet, Middle: unfilled voids below edge of droplet and film flow just out from droplet edge, Bottom: all morphologies of fluid flow underneath the middle of the un-depleted droplet.*

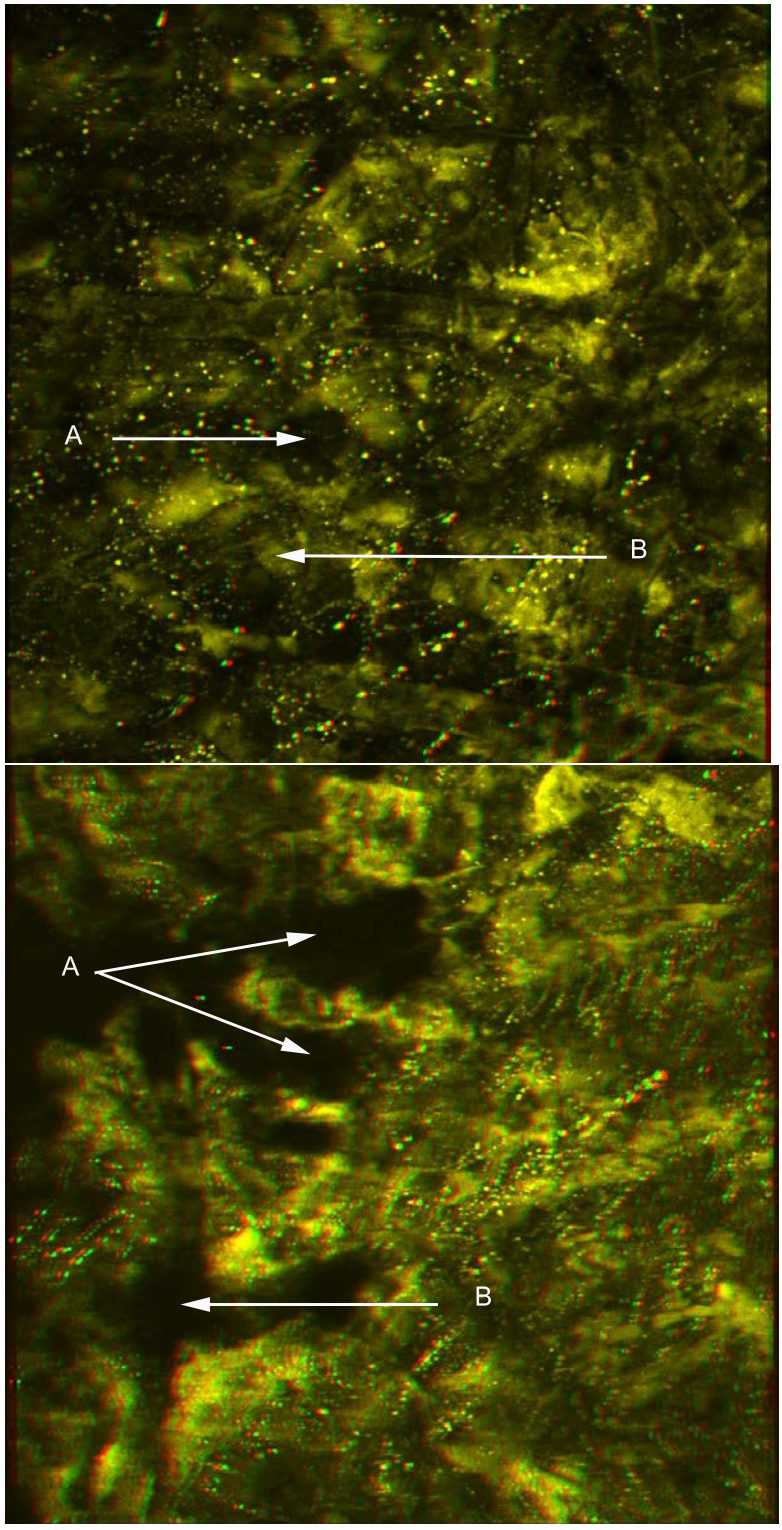

Figure 6.20: *Stereo images of decor papers showing, Top: Alpine White showing pore filling from thickening films & unfilled voids below 30 µm of bulk liquid, Bottom: Beech showing unfilled voids below edge of droplet and film flow just out from droplet edge.*

6.3.3 Pore-scale modelling of observations

In this section two phase flow modelling is reconciled with the experimental observation that the capillary penetration into a range of unsized papers was primarily associated with the flow of the wetting fluid in the form of bulk liquid films along channels formed by fibre overlaps and was not observed as bulk flow in the pores. A description of the pore morphology is given for all potential flow paths within paper. Then a mechanistic description of two-phase flow is developed within each pore morphology. Calculation of the flow rates associated with penetration down fibre overlap channels is shown to be consistent with the film flow mechanism observed experimentally.

6.3.3.1 3D Pore Morphology of Paper

The following are descriptions for the potential flow paths for the wetting fluid which exist within the fibre network at different length scales;

- flow within the bulk pores,
- flow along channels formed by fibre overlaps,
- flow along crevices formed by indentations and surface roughness of the fibres, and
- flow within the intra-fibre pores.

In this section the images in Section 6.3.1 are used to help describe these various fluid pathways on a paper fibre network, to define the length scale associated with these different pathways, and to discuss the continuity of the pathways within the sheet.

The size of pore openings within unfilled paper was highly variable. A number of different pore sizes are evident at the surface of the paper in Figure 6.8 and range from $\simeq$ 20 - 50 μm. Moreover, the cross section along a single pore can vary enormously. On penetration down 1 - 2 fibres into the paper sheet $\simeq$ 10 μm in depth, the pore size suddenly diverges. This pore morphology is evident in the regions shaded green in Figure 6.8. One also observe the presence of sharp dislocations in the pore openings when considering a cross-sectional view of a paper sheet; see, for example, Figures in Hasuike et al. (1992); Samuelsen et al. (2001).

Fluid penetrating from small pores at the surface must bridge across large pore openings; bulk penetration of fluids into the pore space was therefore characterised by converging and diverging pores, and pores exhibiting large discontinuities Kent and Lyne (1989a,b). A schematic of the inter-fiber pore space is given in Figure 6.21 (a). Due to the large number of fibre overlaps which partition the pore space into many domains, the pores are highly interconnected.

A second potential flow path for the wetting fluid was along channels formed by fibre overlaps. The morphology of these potential flow paths was not simple to determine. Hasuike et al. (1992) performed a very careful geometric evaluation of a paper sheet in 3D based on serial

sections at 2 μm spacing (Hasuike et al., 1992). Statistics on the number of fibres contacting each fibre was calculated for 138 fibres over a 200 μm^2 area. They observed a huge degree of entanglement and interconnection of fibres. The fibres, and therefore the channels generated via fibre overlaps, lie almost exclusively parallel to the sheet. Hasuike et al. (1992) observed minimal migration of fibres perpendicular to the sheet axis. They observed that almost all of the upper and lower surface of a paper fibre was in contact with other fibres and they measured approximately 80 fibres contacting the surface of a fibre for every 1 *mm* in length. As most fibres are 1 *mm* in length or longer, this represents a huge degree of fibre entanglement. With respect to the fibre cross section they observed often more than 2 fibres bonded to each fibre (Figure 10 of Hasuike et al. (1992)). This high degree of fibre overlap which is evident in all the experimental figures shown in Section 6.3.1 is sketched schematically in Figure 6.21(b) and (c). From these sketches in 3D and in cross-section one can identify the *pore geometry* that emerges due to fibre overlap in Figure 6.21(d). From the cross section it can be observed that the overlap of fibres leads to the formation of many small channels. Flow along these channels can be approximated as a corner flow problem down an open channel of angle $\alpha < 90^o$. The exact size and channel angle α was not given explicitly in Hasuike et al. (1992) and they are difficult to discern from the SEM images. Based on the cross-sectional images and given that the fibre thickness was $\simeq$ 5-10 μm and the fibre width was $\simeq$ 15 μm, an estimate of the channel depth was $r \simeq 1 - 3\mu m$. The flow channels formed by fibre overlap form an *extremely dense* interconnected network of potential flow paths (see Figure 6.21(b)).

A third potential flow path was based on flow along the roughness or curvature on the surface of a fiber. A typical fibre does not exhibit a purely convex shape, but can exhibit both an indentation due to fibre collapse and roughness in the cross section (Figure 6.21(e)). One can approximate this flow path by an open channel flow. Here the angle α associated with indentations $\alpha_i >> 90^o$ and roughness, $\alpha_r \simeq 90^o$ are both large, with the crevice size small, $r < 1$ μm. These potential flow pathways, which one observes along most fibres, intersect with the fibre overlap channels; the pathways however are quite long, and do not exhibit the strong degree of interconnectivity observed in the fibre overlap channels.

A schematic of an intra-fibre pore is shown also in Figure 6.21(e). An estimation of < 0.5 μm for the intra-fibre pore size can be given by consideration of cross sectional images of the fibre web. The pore geometry can be approximated as eye-shaped. These pores do not form a continuous pore systems throughout the fibre web; the ends of each fibre do not intersect. Flow through a fibre pore would reach the end of the pore and to continue to penetrate would need to penetrate across the pores; this is analogous to flow along a small pore reaching a large discontinuity.

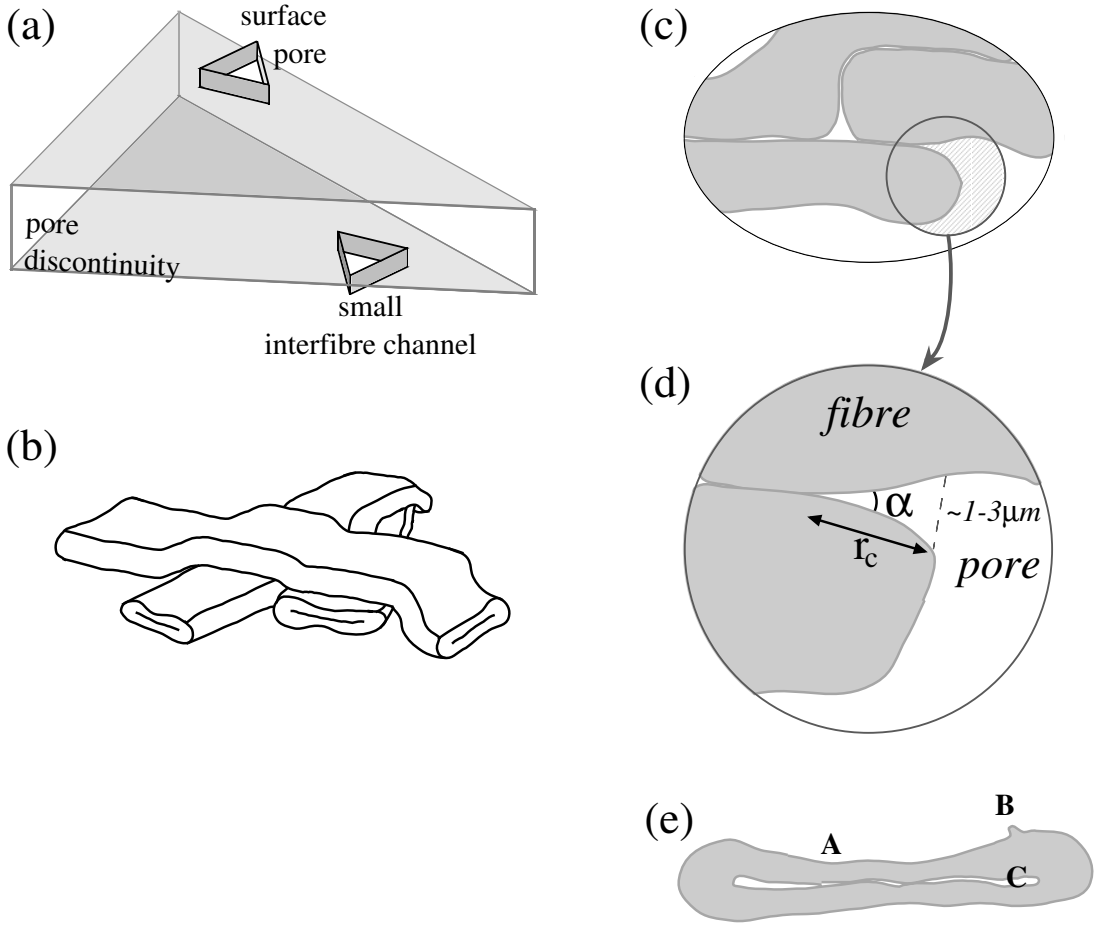

Figure 6.21: *(a) A schematic of the typical pore geometry in paper sheet; a (small) surface pore opening which opens up to a significantly larger pore. (b) Illustration of the fibre bonding state observed in 3D; note the large degree of entanglement and interconnection of the fibres. Flow channels formed by fibre overlap therefore form a highly interconnected pore space. (c) illustrates a typical fibre cross section picture. The high degree of fibre overlap was reinforced. (d) The open channel pore geometry that was generated by fibre overlap. (e) Illustration of the indentations (A) and roughness (B) that are observed on a fibre surface and (C) the intra-fibre pore.*

6.3.3.2 Mechanisms of displacement in porous networks

Pore scale mechanisms observed during penetration of a wetting fluid may be described using the terminology first introduced by Lenormand et al. (1983). There are two distinct types of advance. The first is piston-like where the fluid advances as a meniscus occupying the centers of the pore space. In the second, the wetting fluid flows along crevices in the pore space filling pores in advance of the wetting front. Based on the simplified pore descriptions the two types of advance are illustrated (Figures 6.22 & 6.23). Although the pore scale morphology of paper is much more complex, these simple illustrations give one a better understanding of the penetration mechanisms observed experimentally.

The simplest type of fluid motion in a network of pores is piston-type motion; the meniscus is inside a channel and the wetting (fluid) phase displaces the non-wetting phase (air) Fig (6.22(a)). The filling of a network of intersecting channels of variable aspect, as is the case for paper webs (Figure 6.21(a)), is more complex than flow down a single channel. In particular, the presence of pores at junctions of flow channels and sharp dislocations in the network, lead to very different flow processes. As discussed in Lenormand et al. (1983); Senden et al. (2000) the filling of these junctions and discontinuities depends on the capillary (displacement) pressures associated with meniscus advancement. This includes the fluid distribution within the pores (e.g., the number of neighbouring channels filled with wetting fluid) and the contact angle and pore size (Lenormand et al., 1983; Senden et al., 2000). The primary result is that only when the majority of pores at a junction are filled with a wetting fluid can the meniscus continue to penetrate via a frontal advance (Figure 6.22(b)). In other configurations where neighbouring pores at the junctions remain filled with non-wetting fluid (air) (Figure 6.22(c)) or the meniscus reaches a discontinuity (Figure 6.22(d)), the fluid configuration remains stable and continued displacement *can only take place by a film-flow mechanism*. For example, a fluid meniscus advancing down the smaller pores in Figure 6.21(a), a fluid configuration similar to that illustrated in Figure 6.22(d), will not advance beyond the junction to the large pore opening (discontinuity) (Kent and Lyne, 1989a,b). The principal radii of curvature at a discontinuity are infinite, therefore the capillary pressure or driving force for further advancement is zero.

The only mechanism for fluid to advance beyond discontinuities like those illustrated in Figure 6.22(c-d) is via film flow. If the frontal meniscus cannot advance down a pore the wetting fluid will flow as a film along the edges of the pores. Based on the illustration in Figure 6.21(d), Figure 6.23(b) illustrates a representative pore cross-section that includes a pore of radius R and open channels of depth d. A simple schematic of the channel with a uniform cross section and partially filled with the wetting fluid is given in Figure 6.23(b). Assuming the capillary is sufficiently long compared to its diameter, the capillary pressure across the liquid meniscus in the edge can be calculated as

$$P_c = \sigma / r_c cos(\theta + \alpha/2), \tag{6.1}$$

where θ is the contact angle of the fluid at the solid interface, α is the opening angle of the crevice and r_c is the distance between the liquid/solid contact lines. This implies that for fluid to advance down the crevice $P_c > 0$, $0^o \leq (\theta + \alpha/2) \leq 90^o$. As the channels formed by fibre overlaps have $\alpha < 90^o$, it can be expected that most wetting fluids will spontaneously penetrate along these flow paths. Progressive penetration of the wetting phase along a channel is driven by the interfacial configuration; if the film is thinner, the curvature of the liquid meniscus in the edge is increased, and consequently the capillary pressure is higher. Figure 6.23(c) illustrates the penetration of the wetting liquid along a channel of depth d formed by the fibre overlaps (similar to that observed experimentally in Figure 6.15). If fluid is available the films will continue to thicken until the channel fills completely, $r_c^1 = r_c^2 = d$ in Figure 6.23 (c).

At the channel/pore interface (Figure 6.23(d - f)), depending on the edge configuration, the films will either continue to swell or become pinned. An angle α_e is defined as the angle formed by the edges of the pore near the pore/channel interface. If the channel geometry associated with a fibre overlap opens to a flat discontinuity ($\alpha_e = 180^o$) or to an angle ($\alpha_e > 180^o$), one would expect the fluid interface to be pinned and observe no thickening of the film beyond the channel depth d, ($r_c \leq d$) as illustrated in Figure 6.23(d - e). However, if the opening at the pore edge has an $\alpha_e < 180^o$ (Figure 6.23(f)), continued, albeit slower, film thickening into the pore may be observed.

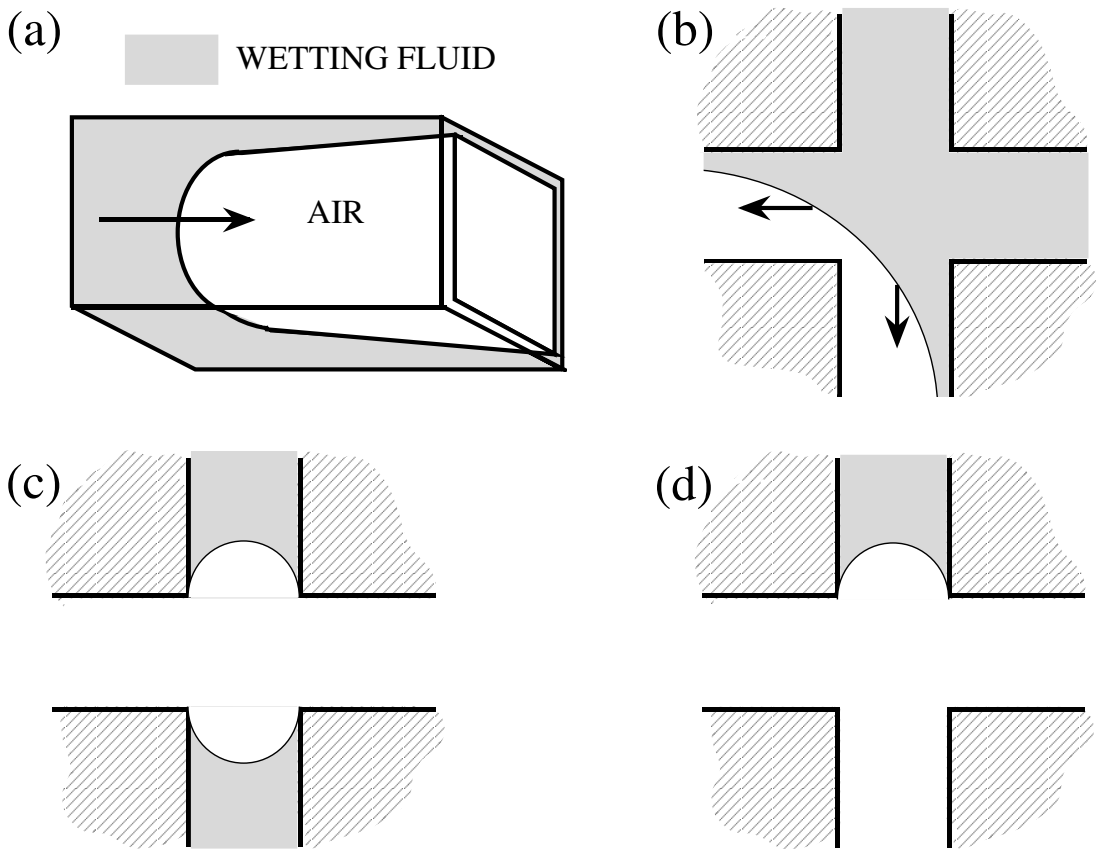

Figure 6.22: *Interfacial configurations corresponding to different fluid penetration mechanisms; (a) piston displacement, (b-d) penetration across pore boundaries and discontinuities. In case (b) the fluid can continue to advance, but in cases (c) and (d) the fluid configuration will remain stable.*

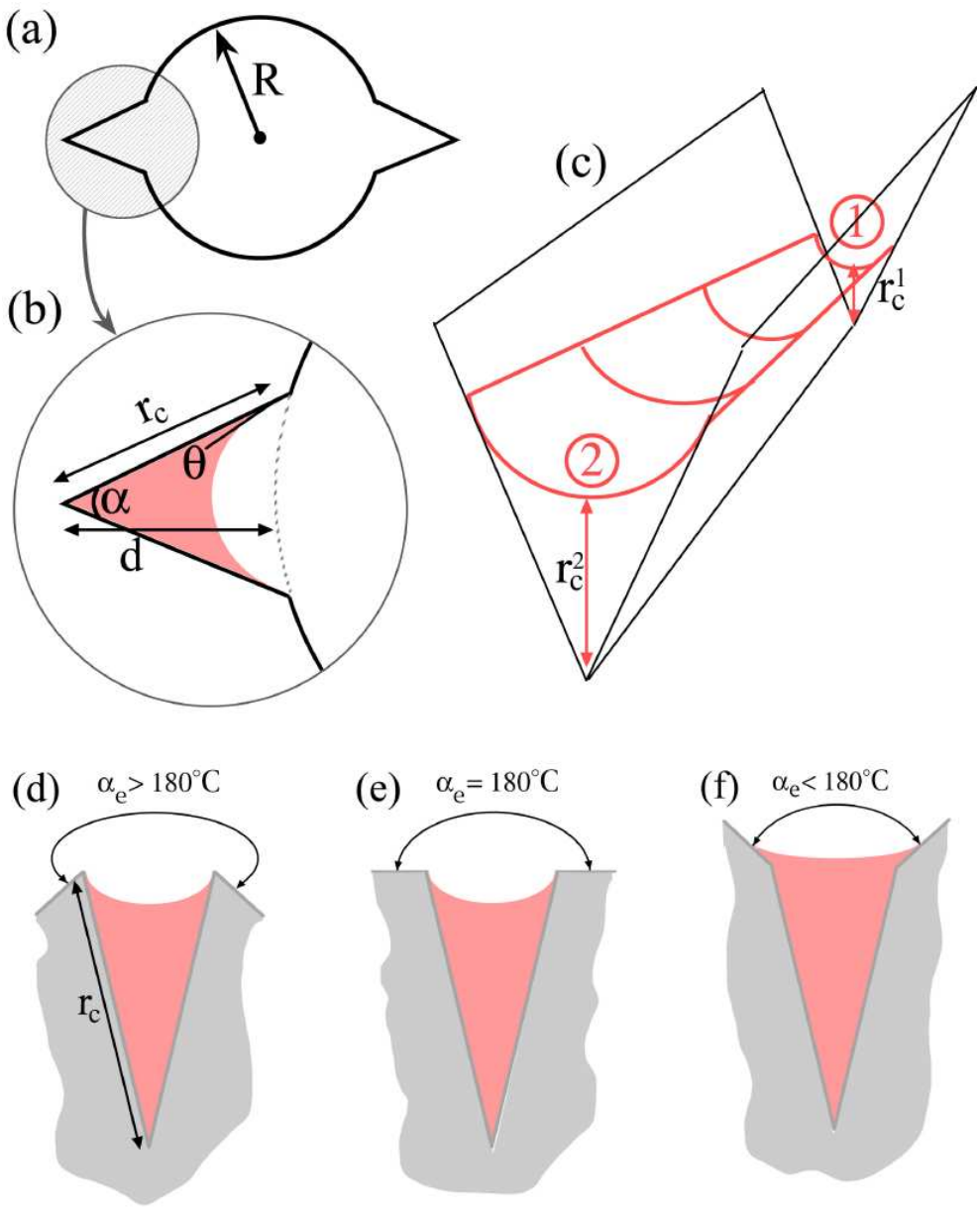

Figure 6.23: *(a) A simple illustration of a pore with two small fibre overlap channels; (b) gives a more detailed view of the channel geometry. In (c) the free penetration of a film along a channel was illustrated; a gradient in the thickness of the film along the edge of uniform cross-section is illustrated ($r_c^2 > r_c^1$). Because of this variation in thickness the capillary pressure at location (1) is greater than at location (2) $P_c^1 > P_c^2$ via Eqn. (1). Since the pressure of the non-wetting phase (air) is the same at the two locations the fluid will tend to penetrate along from (2) to (1). (d - f) show the fluid configuration at the edge of a channel after filling is complete. In (d - e) $\alpha_e \geq 180^o$ and the interface will not thicken beyond the channel depth r_c and will instead remain pinned at the channel/pore edge. In (f) as the effective channel angle $\alpha_e < 180^o$, one would observe a continued thickening mechanism.*

It was expected that the typical pore/channel interface would exhibit an angle $\alpha_e < 180^o$. Hasuike et al. (1992) showed that the average number of fibre bonds expressed with respect to the fibre cross section was ≥ 2. A cross sectional view of the pore geometry at the edge of a fibre in cross-section can therefore exhibit channels which lie in close proximity (Figure 6.24(a)-(b)). Since fibres viewed in cross section exhibit primarily a convex shape and are aligned perpendicular to the sheet axis, the pore/channel interface was highly likely to exhibit $\alpha_e < 180^o$. As shown in Figure 6.23(f), for a pore/channel interface exhibiting an $\alpha_e < 180^o$, the films will continue to thicken beyond the channel edge. The advancement of the wetting fluid via thickening films can therefore lead to the intersection of the menisci in the two channels; Configuration (2) in Figure 6.24(b) results. The merged menisci will now accumulate as a growing collar within the channel cross section and will only stop at a new discontinuity in the pore morphology (Configuration (3) in Figure 6.24(b)). This partial pore filling along the edge of a pore via films was observed in several experimental images (see e.g., some regions shaded blue in Figure 6.14).

If the pore cross section was small enough and/or the advancing films within a pore are thick enough, eventually, the wetting fluid can come into complete contact with the channel wall and an unstable non-wetting fluid (air) filament was created within the pore which spontaneously thins and *snaps-off* (Lenormand et al., 1983). The wetting fluid now completely fills the pore (Figure 6.24(c)). The experimental images illustrate this mechanism in progress. The partially saturated pores highlighted in Figure 6.8 (red shading), 6.11 (yellow shading) and 6.12 are all *very* close to having become completely filled; only one fibre edge remains in contact with the air (non-wetting phase) and the pore exhibits a small circular hole near the pore center. On continued film advancement the pore would be completely filled. Numerous pores completely filled via film flow are evident in Figure 6.8; a close up of a pore that has filled via film flow is shown in Figure 6.13 (red shading).

In Figure 6.13 it is noted that the small pore (shaded red) is filled, while the larger pore (green) has only fluid films along the edges of the pore. This observation is completely consistent with a fluid displacement pattern mediated by film flow. Pore filling fed by films that gradually thicken, via snap-off, is heavily weighted to the smaller pores; schematically, it is shown in (Figure 6.24(d)) that a larger pore with the same film thicknesses as the pore in (c) does *not* form an unstable air filament and instead remains partially wet along the pore edges. This is observed experimentally in Figure 6.13. The pore shaded green is very near the smaller filled red pore and would have similar film thickness. This pore however has not been completely filled. This can be observed on a larger scale in Figure 6.8 throughout the partially saturated zones where smaller pores can be seen being filled while the larger pores remain only partially wet along the edges.

It is important to note that the pores filled by a snap-off (film flow) mechanism do *not* have to be connected to the main wetting front via filled pores. While still connected to the droplet,

they are instead fed via films flowing along the dense interconnected network of fibre overlap channels. The filled (red) pore in Figure 6.13 is surrounded by many unfilled pores, and can only have filled via a film flow mechanism.

This scenario, that the primary pore filling mechanism in the paper network is via fluid films, allows a reconciliation of flow modelling with the experimental observations given in Section 6.3.1. Nearer the droplet edge, within the saturated zone (see upper left of Figure6.8 and Figure 6.9), films along inter-fiber channels will be thicker; this enables even the largest pores to fill via a film flow (snap-off) mechanism. That the filling of the pores originates from channels formed by fibre overlap, which lie almost exclusively parallel to the sheet, is consistent with the fluid configuration observed in the saturated zone. Here the apparent pinning of the wetting fluid to the edge of the fibres can be observed with no tendency to wet the upper surface of the fibre. In the region of partial saturation, it can be observed that the smallest pores are filled while the larger pores remain partially wet by films. Far from the droplet edge the genesis of pore filling, films alone, are observed.

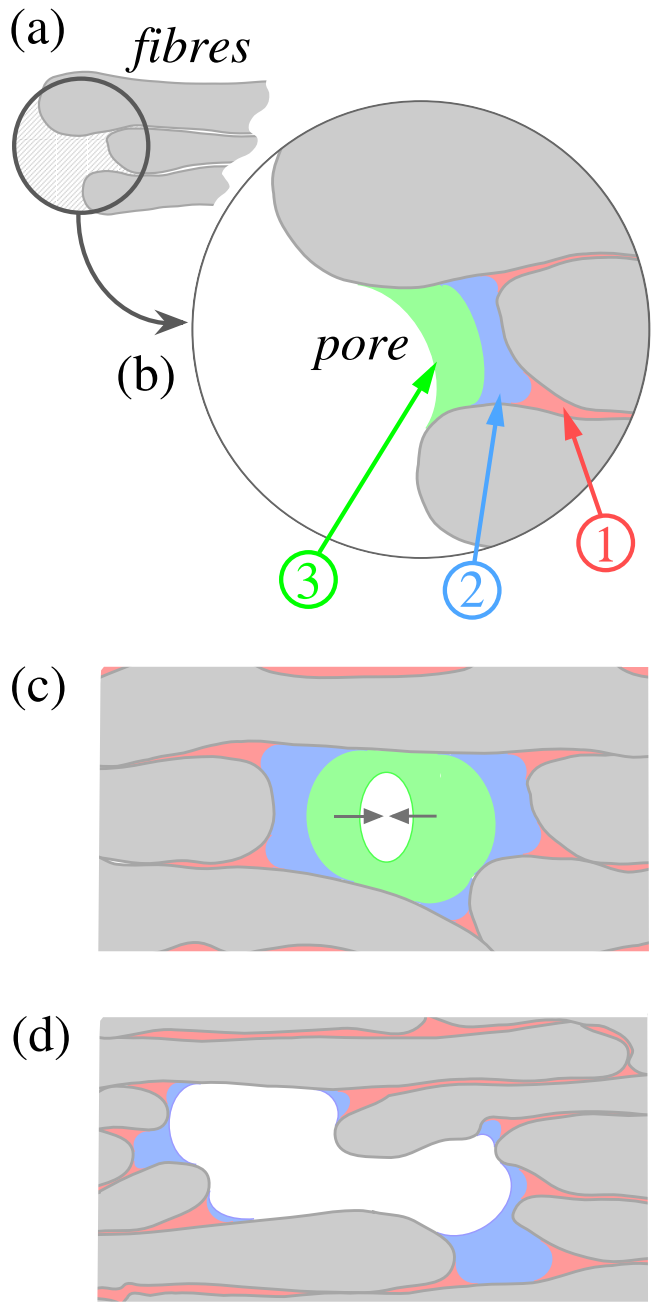

Figure 6.24: *(a) A schematic of a fibre cross section with two neighbouring fibres; this leads to two fibre overlap channels being close to each other. (b)shows a wetting fluid configuration where in (1), the fluid fills the two fibre overlap channels and in (2), the menisci have merged. This wetting fluid can advance down the inter-fiber pore as a growing collar and will stop when reaching a discontinuity within the pore (3). For a small pore (c) the advancement of one or two growing collars (2) can lead to the wetting fluid forming a film around the full circumference of the pore (3). When this occurs the pore will spontaneously fill with the wetting fluid (snap-off). (d)illustrates a large pore which exhibits the same degree of film thickening as the small pore in (c). In this case the same amount of film thickening leads to only partial wetting of the pore edges but no pore filling was observed (compare two pores in Figure 6.13.)*

Only a minimal amount of flow was observed along the roughness of the paper fibre. Figure 6.15 shows a small film advancing down an indentation in the cellulose fibre cross-section. The advancement is very small ($\simeq 10$ μm) compared to the advancement along the fibre overlaps $\simeq 1$ *mm*. The reason for this small advancement can be due to several factors. Firstly, the indentation in a fibre due to collapse exhibits a large angle α which greatly reduces the driving force P_c for flow (Eqn. 1). As discussed in Senden et al. (2000), there is no simple relationship between P_c and fluid advance, so one cannot predict the relative advance along different (coupled) flow paths. However, a reduced P_c can have a significant retardation effect on the local flow mechanisms. There is no flow observed down intra-fibre pores; Figure 6.8 exhibits no qualitative evidence of fibre swelling and at higher magnifications (Figure 6.15) no flow is observed into the fibre pits or any liquid present beneath the pits.

6.3.4 Relative flow rates along flow paths

This section discusses the relative flow rates that could be observed along different flow pathways. It could be expected from simple fluid mechanical considerations that film flow through small channels formed by fibre overlaps rather than meniscus displacement via bulk pores would significantly limit the volume imbibed and the spatial extent of fluid advance into the paper sheet. It is shown here that the experimentally observed rate of penetration was in fact consistent with a film flow process along the inter-fiber pores and was significantly slower than expected if the primary flow mechanism is based on meniscus flow down the bulk pores.

The prediction of two-phase liquid flow in a chaotic network of interconnected pores with channels was still an enormously challenging problem. Even studies of liquid flow along a *single* channel of arbitrary opening α can only be solved numerically (Ransohoff et al., 1987). Consider first the simplest flow solution; a conventional prediction based on Lucas-Washburn theory. Here one approximates the pores or channels as cylindrical capillaries of diameter r. The pressure of the wetting fluid at the paper surface is constant, and the capillary pressure in each pore is given by Laplace's equation: $P_c = 4\gamma/r$. The volume flow rate q in each capillary is related to the pressure drop and the length l of imbibition of the wetting fluid along a capillary by Poiseuille Law, which leads to the classical result of Washburn:

$$l = 1/2[\frac{\gamma r}{\mu}]^{1/2} t^{1/2} \tag{6.2}$$

According to this classical result the distance of fluid imbibition along an inter-fiber capillary of radius R, l_R should be considerably further than the fluid penetration along the fibre-fibre crevice with spacing d, l_d; $l_R/l_d = \sqrt{R/d}$. For the paper fibre web, there are bulk inter-fiber pores with R $\simeq$ 20 - 50 μm. It was assumed experimentally that a dynamic snapshot of imbibition over the first second of fluid contact time was being observed. Using Eqn. 6.2, and assuming that flow in the inter-fiber pores is not hindered by the presence of discontinuities,

it is expected the fluid would have advanced a distance $l \simeq 2-3$ *cm* over that one second of fluid contact. However this degree of advance was not observed experimentally; in fact the fluid advances only $\simeq$ 1-2 *mm* from the drop edge in the first second of fluid contact. This observation further reinforces that flow along the inter-fiber pores cannot be the major flow path for the penetrating fluid.

As discontinuities hinder bulk flow, the flow of films along channels becomes most favourable. From Equation 6.2 and assuming the fibre overlap channels can be approximated by a cylinder of diameter $r \simeq$ 1-3 μm, the fluid advance via film flow would be expected to extend $l \simeq$ 4-7 *mm* over the first second of contact. This was still faster than observed experimentally but much closer to experimental observations. A better prediction for the fluid advance down fibre overlap channels will come from solving for the flow of the wetting phase along an edge or intersection of two planes at a crevice angle α (see Figure 6.23(c)).

Predictions based on a hydraulic diameter approximation for flow of a wetting fluid at a sharp corner have been made previously (Lenormand et al., 1983). It was assumed $\alpha = 90^o$, and that the pressure drop in the non-wetting phase was negligible, that the radius of curvature along the axial direction, the plane parallel to the fluid film, was very large, and that the shape of the meniscus in the cross section was circular. The solution for this geometry was given by Lenormand et al. (1983):

$$l = .056[\frac{\gamma r}{\mu}]^{1/2} t^{1/2}, \tag{6.3}$$

Eqn. 6.3 predicts a penetration depth an order of magnitude smaller than predicted by Eqn. 6.2. For channels of r $\simeq$ 1-3 μm a fluid advance of $\simeq$ .5-.8 *mm* would be expected. This was slightly less than the extent of fluid penetration observed experimentally. Ransohoff et al. (1987) numerically solved the full Navier-Stokes equations along a corner channel as a function of corner geometry, angle and roundedness, contact angle, and surface fluid-air shear viscosity at the gas-liquid interface. They found that the hydraulic radius method could overestimate flow resistances somewhat and also showed that flow along corners at $\alpha < 90^o$ could be faster by a factor of 2 - 3. This result would give a prediction of l completely consistent with experimental observations.

Given that the fibre overlaps form a dense network of interconnected channels, and the experimentally observed flow rate was accurately matched by a film flow scenario, it was clear that these fibre overlap channels form the major conduits for flow in the paper fibre network.

6.3.5 Sized papers

6.3.5.1 Introduction

Sized papers were studied in order to visualise fluid flow over much longer time scales. In doing so it was possible to visualise a mechanism of imbibition that would not have been

possible with unsized papers *i.e.* intra-fibre flow.

It is a daunting task for a paper maker to provide a paper that will print well with all ink jet printers on the market. Even if this were confined to four-color dye-based ink jet systems, ink surface chemistry varies considerably from one manufacturer to another. The paper must absorb the aqueous vehicle rapidly without allowing dye penetration or spread. Similarly, with fountain solution in offset lithographic printing, surface chemistry varies from one supplier to another, but it is important that the paper absorb the fountain solution before the following color is laid down to avoid ink refusal. The use of water based inks in flexography requires papers with controlled ink holdout in order to achieve optimum print density without smear or set off. For uncoated papers this requires an accurate understanding of the mechanism for penetration of aqueous liquids into the surface pore structure, with a particular need to understand the role of sizing agents used in the paper industry to make paper more hydrophobic.

Cellulose fibres used for paper making are naturally hydrophilic and can be rapidly wetted by water and aqueous liquids such as water-based printing inks. Most paper and paperboard is sized, or made more hydrophobic, because of end-use requirements regarding interaction with aqueous liquids. For example, sizing is required to prevent wicking and bleeding of water-based inks when printed on plain paper, and sizing is used to prevent penetration of milk or juice into the otherwise unprotected internal edge in a liquid packaging carton. Alkyl ketene dimer (AKD) is widely used as a sizing agent in the paper industry. In this section cryo-SEM technique and cryo-confocal techniques were used to visualize water penetration into papers sized with AKD.

6.3.5.2 Cryo-SEM

SEM observations showed that when droplets had 20 minutes to penetrate the sized paper before freezing there appeared to be no flow of any magnitude in any of the SEM images analysed (Figure 6.25). Figures 6.26 – 6.29 clearly show no film or any other form of flow at all after droplet placement on the rough side of the 80 gsm photocopy paper. The images show the distribution after a short interval of 2 seconds prior to freezing (Figure 6.27), and a longer interval of 30 seconds (Figures 6.26, 6.28 & 6.29). There is no qualitative difference between images. The images provided no evidence of flow along the fibre overlap channels nor along surface roughness of the fibres. The fluid remained pinned at the surface of the paper, along the edges of fibre overlaps and on the rough surface of the fibres. There was no flow at all in the pores.

However when the droplets were placed on the paper for even longer, (30 min) there was evidence of the beginning of film flow in interfibre channels (Figure 6.30*B*). This indicates that there was very little surface flow with sized papers and there was no evidence of other flow mechanisms. This was in strong contrast to flow mechanisms previously described for unsized

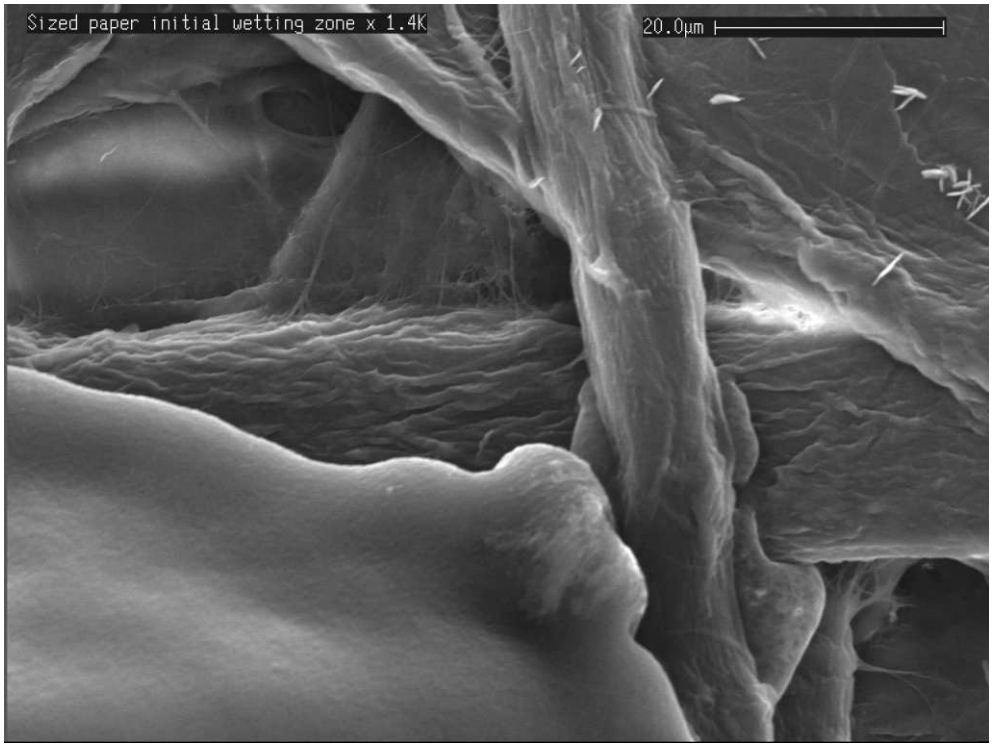

Figure 6.25: *High magnification image of an unfilled sized laboratory kraft paper BL-8 with the droplet of fluid in the bottom left quadrant of the image which was frozen 30 seconds after placement. Note the apparent high contact angle of the liquid on the surface of the fibres.*

papers.

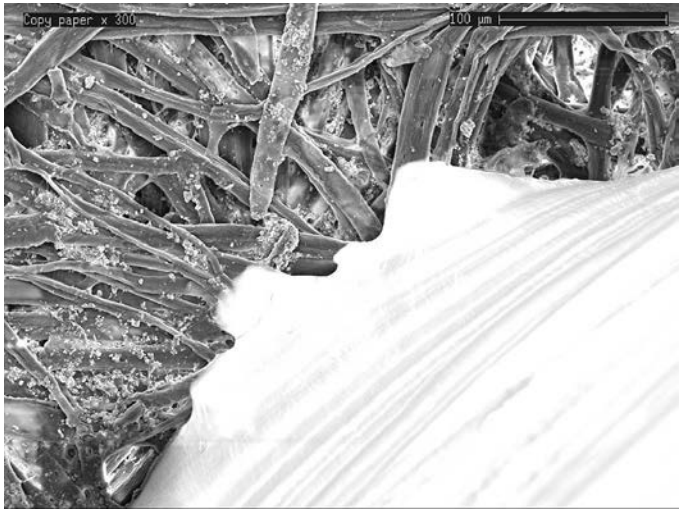

Figure 6.26: *SEM secondary electron image of fluid droplet frozen 30 seconds after placement onto sized copy paper.*

Figure 6.27: *SEM secondary electron image of fluid droplet frozen 2 seconds after placement onto sized copy paper.*

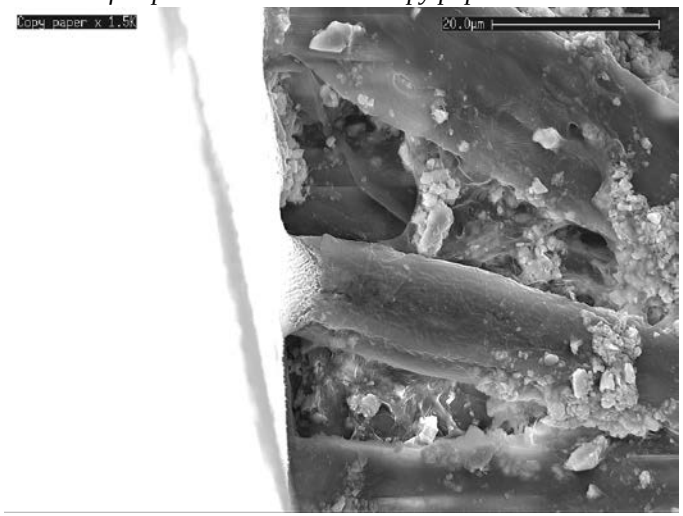

Figure 6.28: *SEM secondary electron image of fluid droplet frozen 30 seconds after placement onto sized copy paper.*

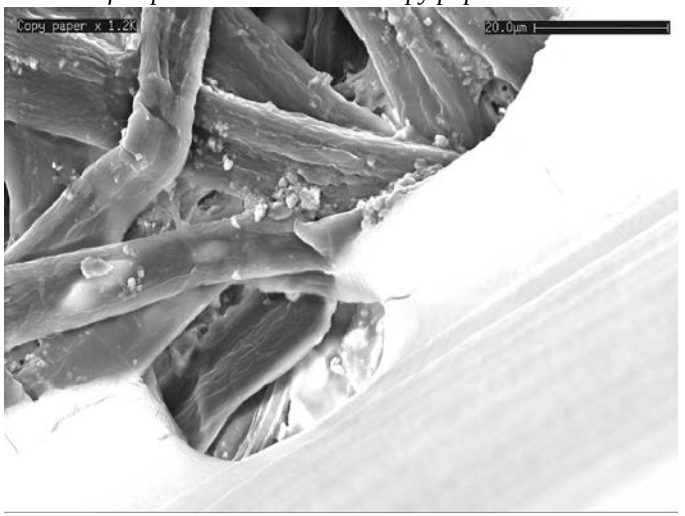

Figure 6.29: *SEM secondary electron image of fluid droplet frozen 30 seconds after placement onto sized copy paper.*

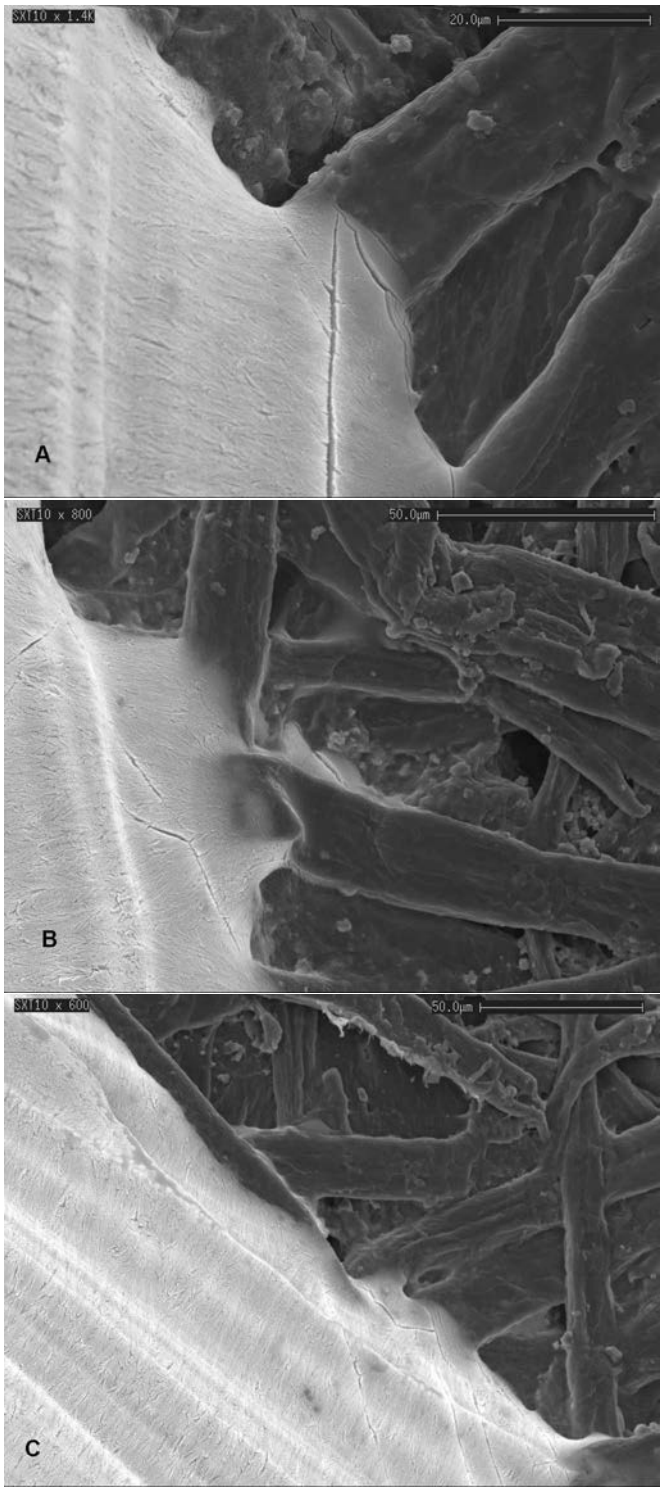

Figure 6.30: *Images of sized copy paper with droplets left 30 minutes prior to freezing. Image B shows the beginnings of film flow in interfibre channels.*

Figure 6.31 are SEM images of droplets frozen 20 minutes after placement on sized paper in secondary electron and backscatter mode where evidence was seen of the slow movement of fluid away from the droplet edge within fibres. In Figure 6.31(*b*) a "halo" of CsI can be observed within the liquid from backscattered electrons from within the fibres that extend about 100 - 200 μm from the edge of the droplet. In Figure 6.31 the images give no evidence for either bulk or film flow within the pores.

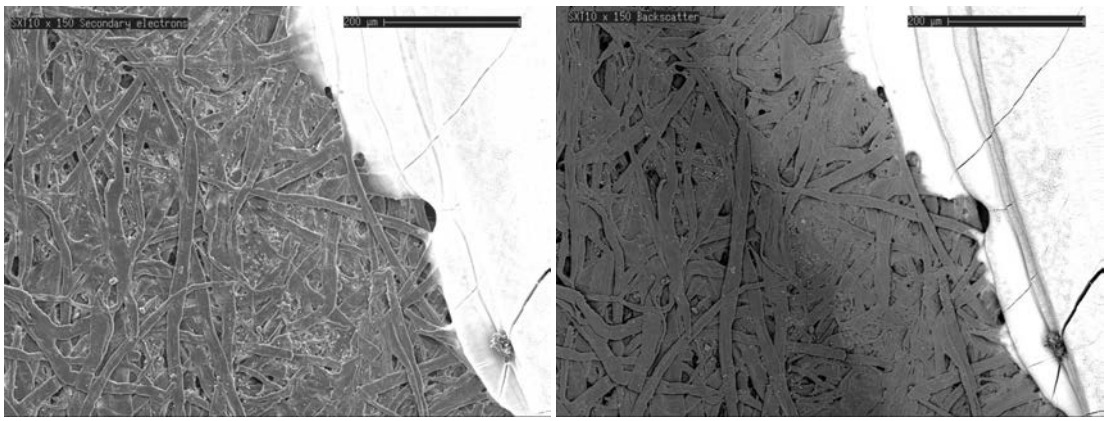

Figure 6.31: *SEM images of fluid penetration into BL-8 after 20 minutes of contact, left: secondary electron mode and right: backscattered electron mode.*

This is illustrated more clearly in Figure 6.32, which shows a magnified subsection away from the droplet edge. This highly magnified image provides no evidence of bulk meniscus liquid flow in an area where there appeared to be liquid present within the fibres. These results indicated that fluid did advance, albeit very slowly, from the droplet edge. The mechanism of fluid advance was, unlike unsized papers, based on flow within the fibres themselves. This is confirmed in Figure 6.33 which is an edge image of the paper near the droplet showing that no fluid was present within the inter-fibre pore space.

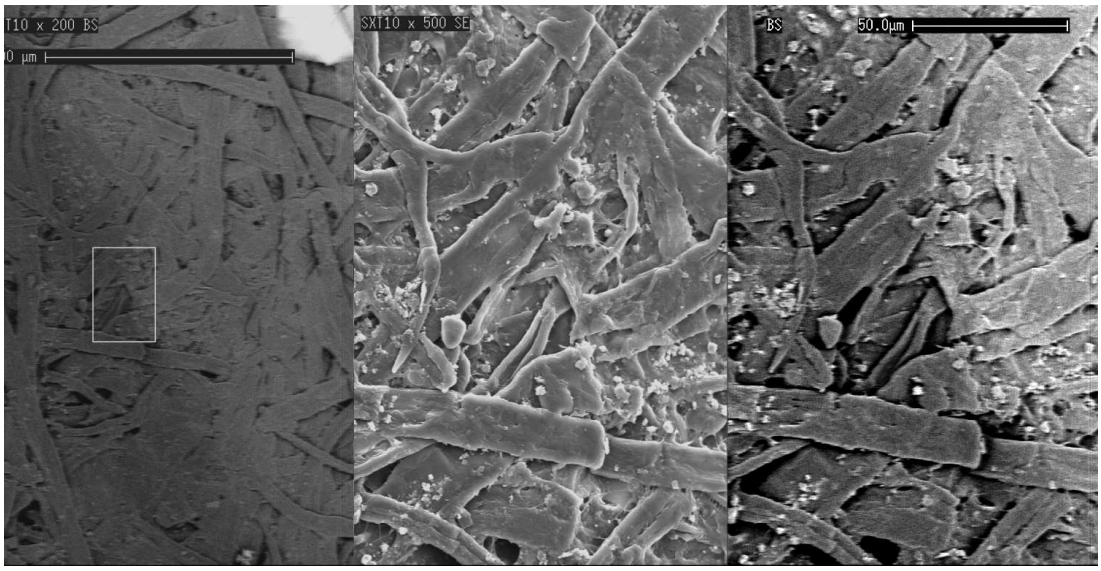

Figure 6.32: *Higher magnification images of Figure 6.31 at higher magnifications. The two right handed figures are in secondary and backscattered mode respectively. No presence of bulk fluid or film flow in pores was observed.*

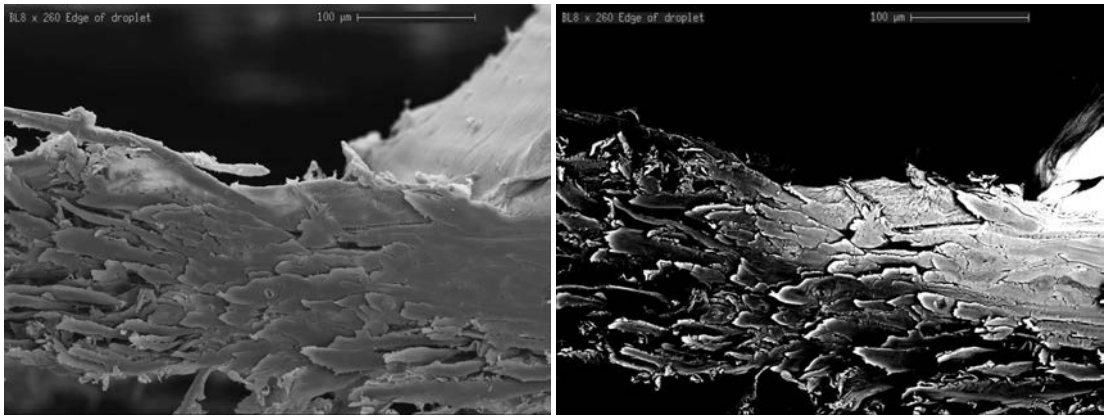

Figure 6.33: *Further evidence that there was no presence of fluid within pores. Here an edge image with the droplet shown on the far right in Figure 6.32 in secondary electron and backscattered modes. This edge image clearly shows that within the pores no fluid was present.*

6.3.5.3 Cryo two-photon laser confocal microscopy

Due to the background fluorescence of commercial laser copy paper, all cryo-confocal microscopy studies on sized papers were performed on BL-8, a sized unfilled laboratory paper. Droplets were placed on the paper for 10 minutes prior to freezing. In Figure 6.34 three stereo cryo-confocal images of the fluid distribution within BL-8 near the edge of the fluid droplet are shown. The fibre structure is clearly shown in the image and even the roughness on the fibre surface was clearly evident. This was in complete contrast to the CLSM images shown in Figure 6.16 illustrating the penetration of liquid imbibition into saturating papers where the only fluorescence came from films and where the fibres could not be distinguished (Figure 6.34). The movies of these images are #155, #154 & #153 respectively on the attached CD. As there was no natural background fluorescence from the raw paper fibres it is concluded that the fluorescence was due to liquid having penetrated into the fibres. As the surface definition of the fibre is excellent (e.g., the roughness of the fibre is observed), it could also be concluded that the fibre walls were penetrated and that there was no surface flow. The movement of the fluid away from the edge of the droplet was very slow so that after 10 minutes the fluid front was only 200 μm from the droplet. This is also shown in the cryo-SEM image Figure 6.31. It is also observed that only the surface fibres fluoresced. Confocal images at depth within the paper and under the droplet ($>$2 - 3 fibres deep) exhibit no fluorescence indicating that the liquid penetration was limited to surface fibres. This is the same as shown in cryo-SEM image Figure 6.33 where the presence of liquid in fibres appears not to completely penetrate the sample.

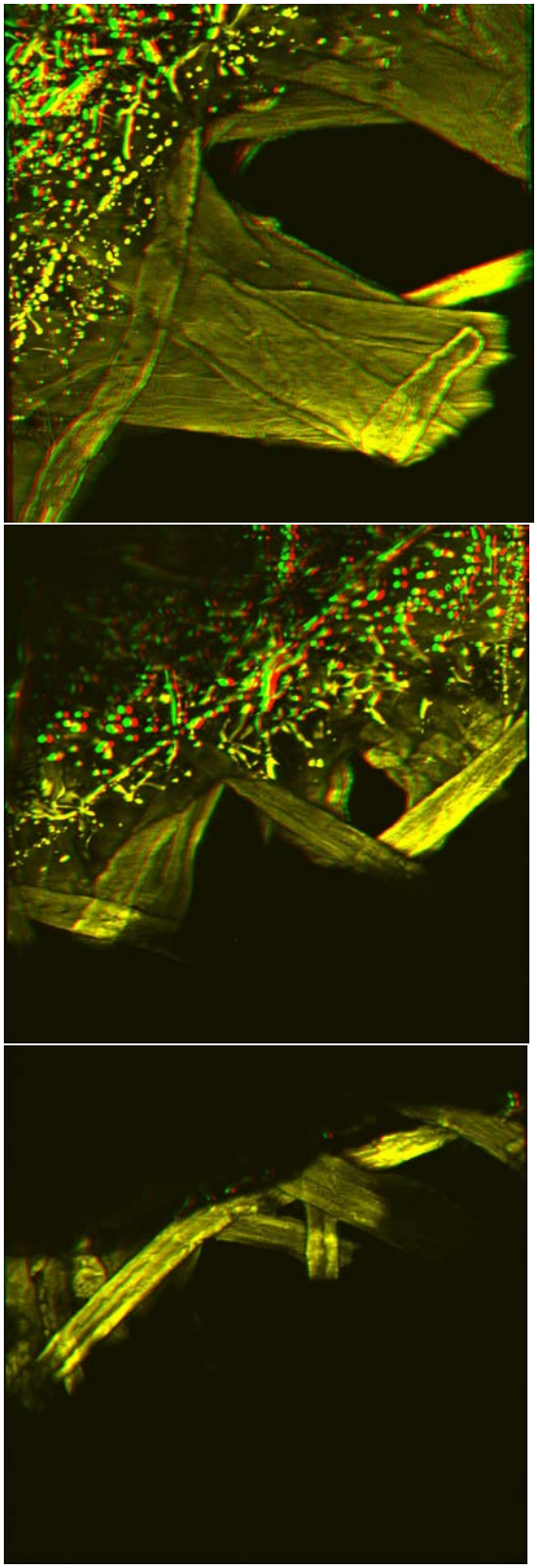

Figure 6.34: *Stereo cryo confocal images of BL-8 laboratory made sized paper near the droplet edge showing fluid flow of a length scale up to 200 µm within the fibre especially in the top image. The droplet of the penetrating liquid was in the top left hand quadrant in all images. The image size is 250 x 250 µm.*

As flow within the fibres is the only mechanism of fluid penetration being observed in the sized paper, it remained to be determined where in the fibres the fluid was located. Figure 6.35 is a stereo 3D reconstruction showing that no fluid was present within the fibre lumen as there was no strong fluorescence observed through the bordered pits. However viewing the bordered pit in 3D, the wall of the fibre on the other side of the pit can be discerned in clear detail indicating that the fluid was actually in the adjacent fibre wall itself and not lying between the pit and the adjacent fibre wall *i.e.* not within the lumen or on the surface of the fibre wall. The movie of this image is #156.

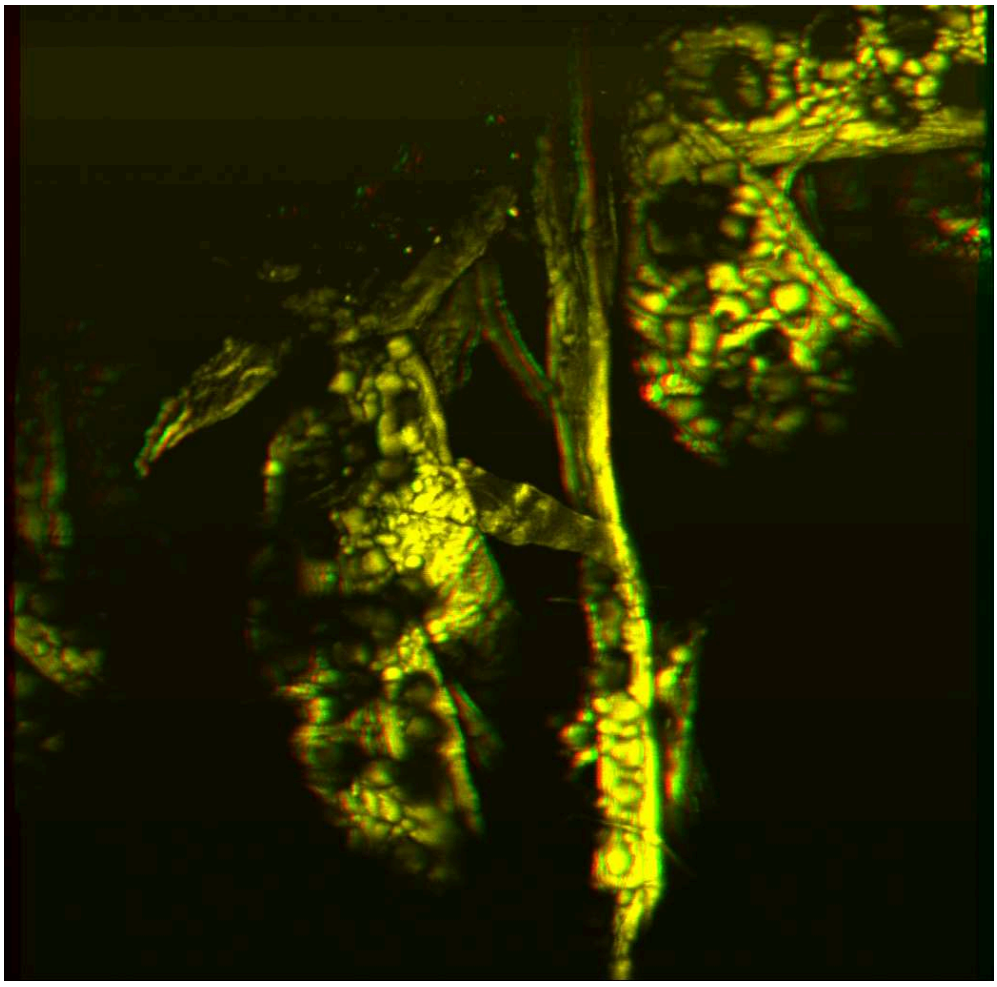

Figure 6.35: *Stereo cryo confocal images of BL-8 laboratory sized paper where one can observe the opposite wall of the fibre through an unaspirated bordered pit, showing that there was not bulk liquid present in the lumen of the fibre*

6.3.5.4 EDXA analysis

EDXA analyis conducted on the sample imaged in Figure 6.31b confirmed that the "halo" observed was in fact CsI indicating the presence of the imbibing liquid. It further confirmed that there was no CsI beyond the "halo" which extended 200 μm from the droplet edge.

The presence of liquid flow in fibres only near the surface was also confirmed by analysing a cryo-microtomed edge of sized paper with EDXA using SEM. This showed CsI distribution in the same penetration study of BL-8. Figure 6.36 illustrates an edge image of BL-8 with surface fluid (upper surface) and fibres near surface (X) and at depth (Y). EDXA analysis of the fibres indicated the presence of CsI in fibre X, while the deeper fibre Y exhibited no CsI peak at all. The EDXA spectra are shown in Figures 6.37 top (point X) and bottom (point Y) respectively.

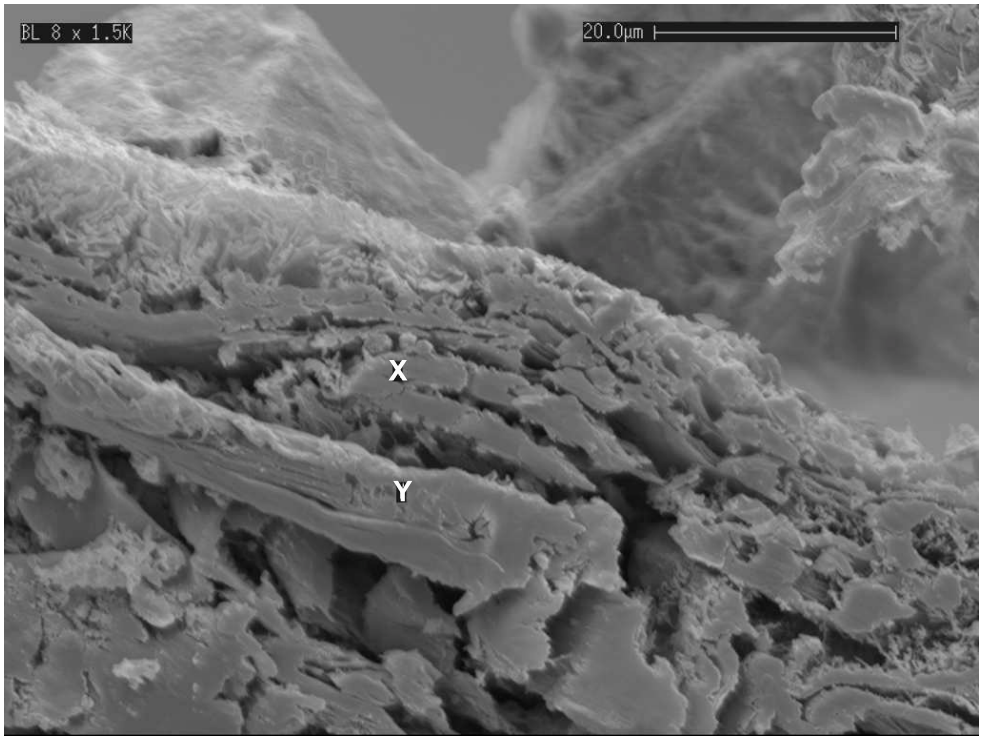

Figure 6.36: *SEM image of the edge of sized paper near the droplet edge. EDXA analysis confirmed the presence of CsI within the fiber near the surface* (X)*, but no presence of CsI within the lower fiber* (Y).

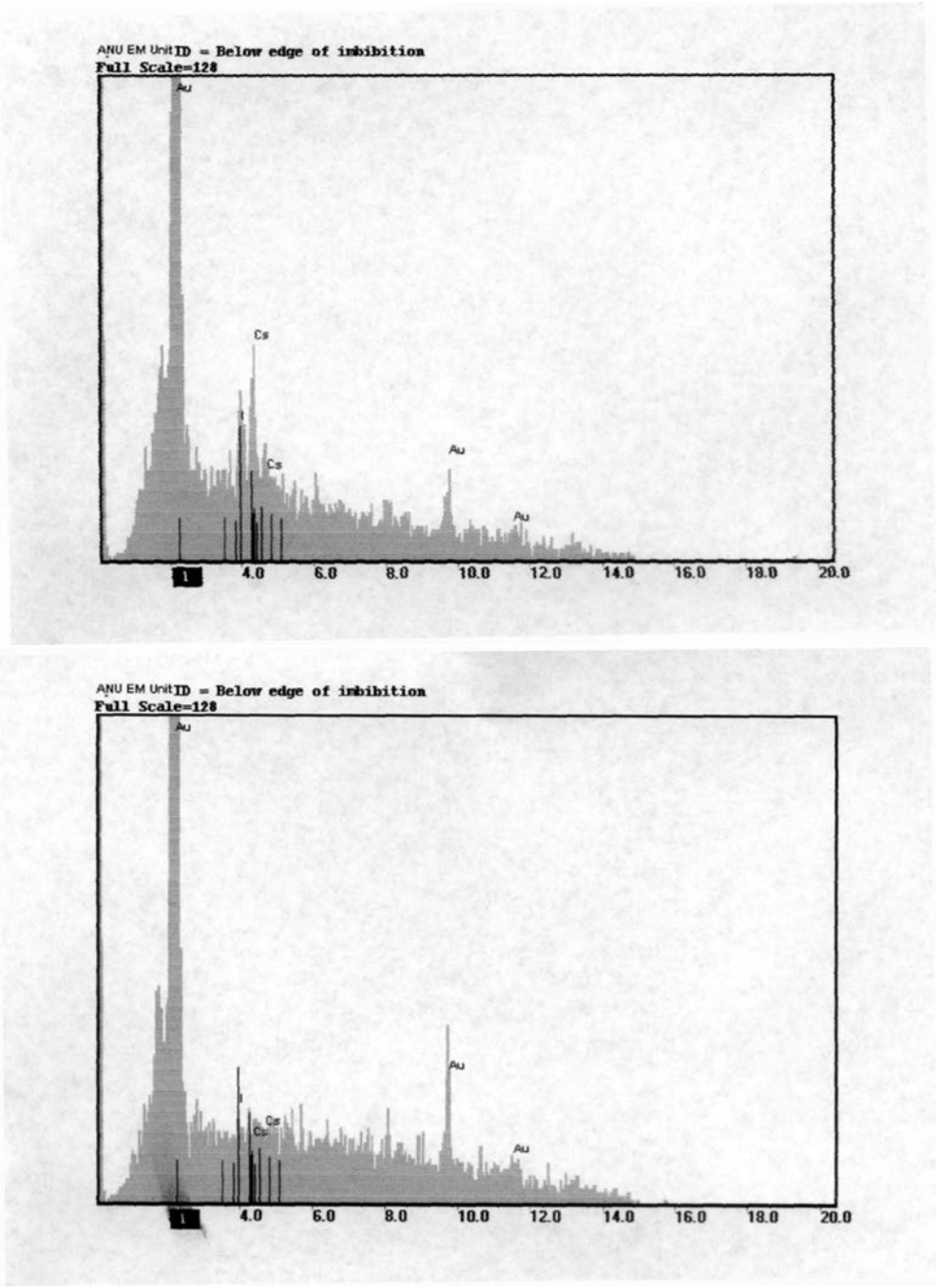

Figure 6.37: *EDXA spectra, Top: in wall of surface fibre just underneath droplet (X in Figure 6.36), and Bottom: in wall two fibres below surface (Y in Figure 6.36). The caesium peaks at point X are clearly illustrated in the top image.*

Further evidence of the presence of liquid occurring only in the fibre wall as opposed to the fibre lumen was provided by the cryo-SEM edge image Figure 6.38. Here EDXA indicated the presence of CsI in the fibre walls (X) and in the edge of the lumen (Y). However there was no evidence of bulk liquid flow at all in the particular lumen itself that would have led to the presence of CsI at point Y in Figure 6.38 other than through flow in the walls of the fibre. These results showed that any liquid that penetrated into the fibre walls in sized paper did not flow through the lumen. The EDXA spectra are Figure 6.39 top (point X) and bottom (point Y) respectively.

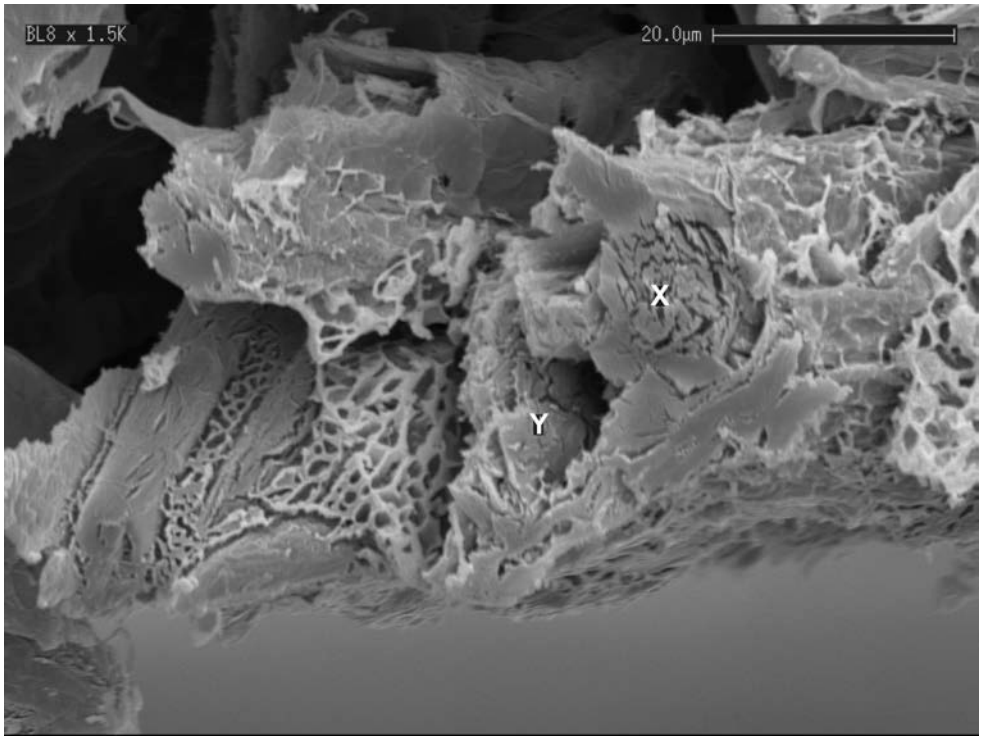

Figure 6.38: *Edge cryo-SEM image of BL-8. EDXA analysis confirmed the presence of CsI within the fiber wall at* (X)*, and on the edge of the lumen* (Y) *however there was no evidence of bulk liquid in the lumen itself.*

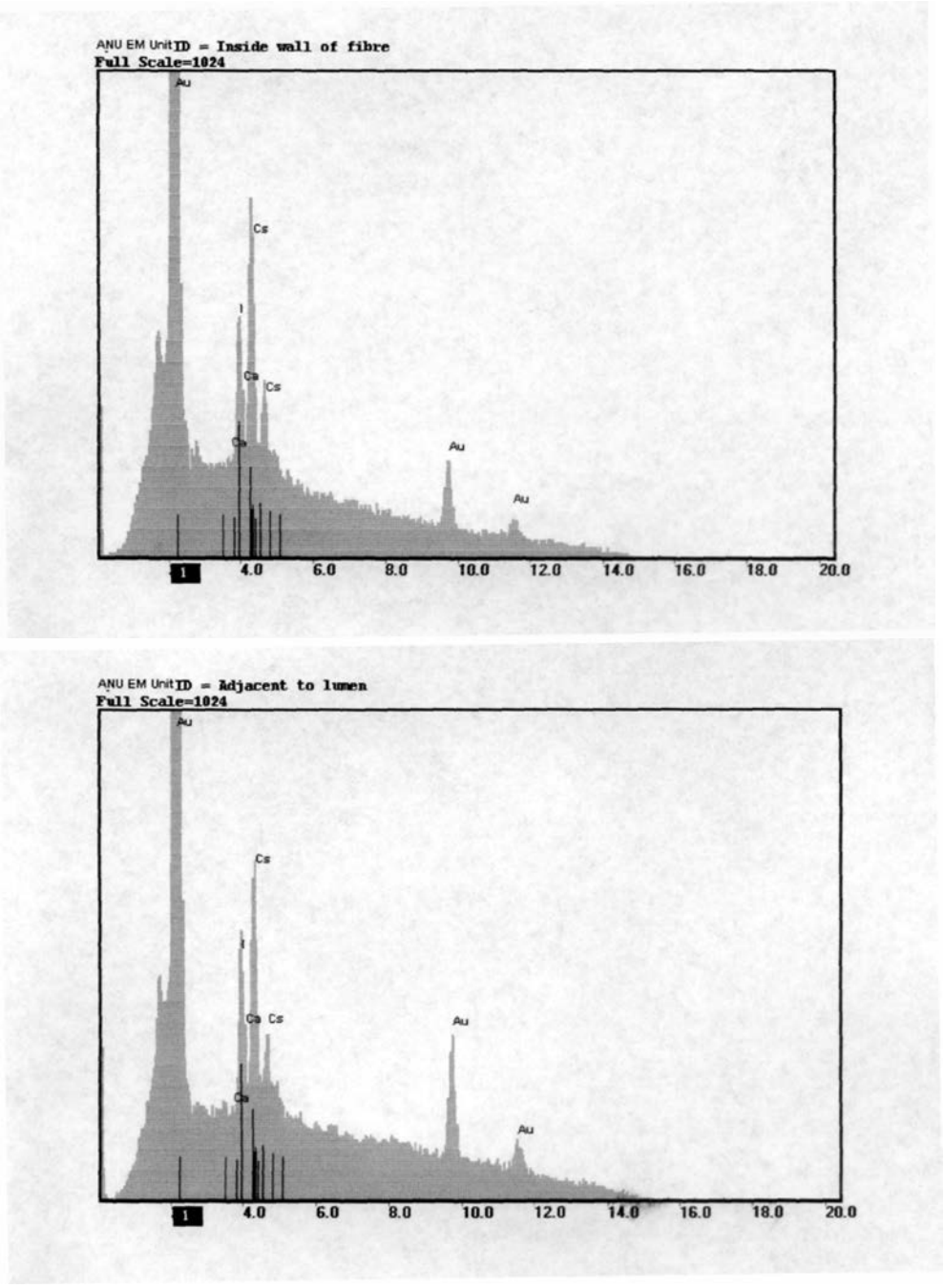

Figure 6.39: *EDXA spectra, Top: in wall of fibre just underneath droplet (X in Figure 6.38), and Bottom: on the edge of the lumen of the fibre just below the droplet (Y in Figure 6.38)*

6.4 Discussion

The structure of the pore space of paper together with local surface energy considerations are the chief determinants of fluid penetration processes. Understanding these relationships and their implications for paper performance will help in the design of products and troubleshooting problems. In this section the limitations of the work and implications of film flow processes to industrial problems of interest will be discussed.

6.4.1 Viscous effects

In all the cases observed experimentally the penetration into unsized paper was determined by capillary forces. Fluid penetration would be strongly effected if fluid was applied to the sheet under pressure (e.g., printing nip, etc.). One would in this case expect the wetting fluid to be driven down the pores. However, when pressure was released capillary transport would again dominate the flow mechanisms, and any excess fluid and fluid within pores would continue to penetrate via films.

6.4.2 Implications to fluid distributions within sheets

Flow along channels and the filling of pores away from the wetting front into unsized papers had a dramatic effect on the resultant fluid phase distribution. This is of great interest as the optimisation of resin penetration into decor paper was a major focus of this thesis. Experiments on a range of industrial decor papers which exhibited a wide range of pore structure and variations in their fibre and filler content were performed. The fluid penetration observed was similar to that shown previously for pure cellulose paper (see Figure 6.18). Flow down the inter-fiber channels and partially filled pores were all evident.

As discussed previously the fluid penetration that resulted from the filling of pores originating solely from fibres aligned parallel to the sheet would lead to a wetting fluid configuration that was made up of lenses, with the fluid films oriented preferentially along the fibre edges (e.g., the fluid configuration as shown in Figure 6.13). Therefore an understanding of fluid flow mechanisms in paper could then lead to an understanding of what aspects of paper structure affect the rate of fluid flow. The effect of fillers is dealt in for more detail in Chapter 7.

6.4.3 Implications to printing interactions

The identification of the mechanisms of fluid movement in paper is important not just in the application of the knowledge to just decor papers. Even though this thesis did not consider the penetration of very small amounts of liquids into paper, the mechanisms of fluid movement will be the same for much smaller volumes commonly found in printing. In most printing applications the amount of fluid added is significantly less than that considered in the cryo

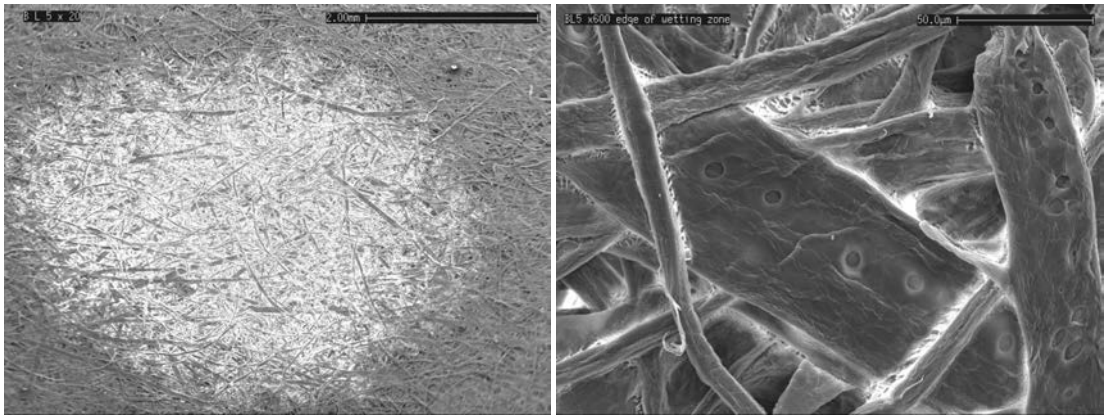

Figure 6.40: *Figure showing the presence of films in an unfilled unsized laboratory paper only both near the droplet center (a) whole droplet (b) after a 3 µl droplet penetrated paper.*

experiments described in this thesis. In Figure 6.40 examples of fluid penetration of a small droplet of 3μl into paper are shown. In this system the whole droplet penetrated within the $\simeq 1$ second of fluid contact time. The penetration of fluid exhibited similar film flow characteristics as seen previously; one now observes *no zone of complete saturation* right across the depleted droplet. Even in the original center of the droplet, flow was observed solely along inter-fiber channels and no filling of the smallest pores is observed. Given that most printing applications use orders of magnitude less fluids, one might expect that in many printing applications the imbibing fluid will never fill pores. This has been noted previously by Gregerson et al. (1994, 1995) who studied ink distribution on and around surface fibres for flexography printed newspaper. They observed (Figure 10 in (Gregerson et al., 1995)) no ink spreading into voids, but significant penetration of the surface structure via ink absorption into the inter-fiber voids.

6.4.4 Sizing effects

The penetration of droplets onto commercial copy (sized) paper was also considered. It was thought (Garnier et al., 1999) that the sizing agent preferentially sits at the intersections of fibres within sized paper; given that film flow down channels formed by fibre overlap was the preferred flow mechanism. The presence of sizing agents within channels would certainly impede the advancement of the wetting fluid. Experiments on sized paper illustrated this. In Figures 6.26, 6.28 & 6.29 the droplet edge on sized paper was observed *30 seconds* after drop application. The fluid did not advance and stayed on the fibre surface and no channel flow was observed.

The results given in Section 6.3.5 illustrated the dramatic effect sizing had on the penetration of aqueous liquids into paper. While unsized paper exhibited fast penetration of fluid primarily along channels formed by fibre overlaps and more slowly along crevices and surface

roughness of the fibres, in sized paper only a single potential flow path was observed; flow within the fibre walls. The implications of the current work to a better understanding of the effect of sizing on fluid penetration are discussed.

AKD must be present on all fibre surfaces: Where the AKD sits within the fibre web is an important question that has been debated for many years in the literature. Sizing takes place after the AKD is exposed to elevated temperatures in the dryer section of the papermachine. In order for sizing to be effective it is universally accepted that AKD must sinter and spread on the fibre surfaces. The extent and physical/chemical reason for this redistribution remains controversial. Garnier et al. (1999) found that AKD did not completely spread and wet model cellulose surfaces and concluded that AKD vapours adsorb on the surface of fibres during papermaking . Isogai (1999) found that sizing increased with heat treatment and related this to melting and spreading of the sizing compounds over the fibre surfaces. Seppanen et al. (2000) found that AKD only partially wetted cellulose in kraft pulp handsheets and that further spreading of AKD molecules occurred by surface diffusion in the form of an autophobic monolayer precursor from the foot of the AKD particle, the rate of spread being temperature dependent and was shown to be quite slow ($10^{-11} m^2$/s). The results in this chapter lead to the conclusion that whatever the mechanism for the spread and anchoring of AKD on the fibre surfaces, it was present over the entire fibre surface and was not simply present as randomly placed hydrophobic patches within the web. This was true for both the sized laboratory sheets and the commercial copy paper.

Senden et al. (2000) showed that in unsized paper, there are many potential flow paths for the wetting fluid; it was shown that the two mechanisms primarily observed are flow along channels formed by fibre overlaps and to a lesser extent, flow along crevices formed by indentations and surface roughness on the fibre walls. It was also shown, based on work by Hasuike et al. (1992) that the flow channels formed by fibre overlaps form an extremely dense interconnected network of potential flow paths. If the AKD was randomly present within only a fraction of the fibre overlap regions this would in no way impede the flow of fluids along this network of channels. This can be illustrated by considering an analogy based on percolation theory (Sahimi, 1994).

Imagine first that all the bonds of the paper fibre network are potential channels for the flow of the fluid from the surface into the sheet. Consider a simple case, where the fibre network is approximated by a highly connected network of these potential channels based on a 12-connected lattice (the cubic-close-packed network). This network is illustrated in Figure 6.41. Now suppose that some of these fibre channels have the presence of AKD in them, while others are free to conduct water films. It would be desirable to know what proportion of the fibre channels would have to be sized in order to stop flow of the fluid from the surface across and into the paper sheet. In other words what sizing efficiency in terms of proportion of overlap channels made hydrophobic is required to stop flow from occurring into the full sheet.

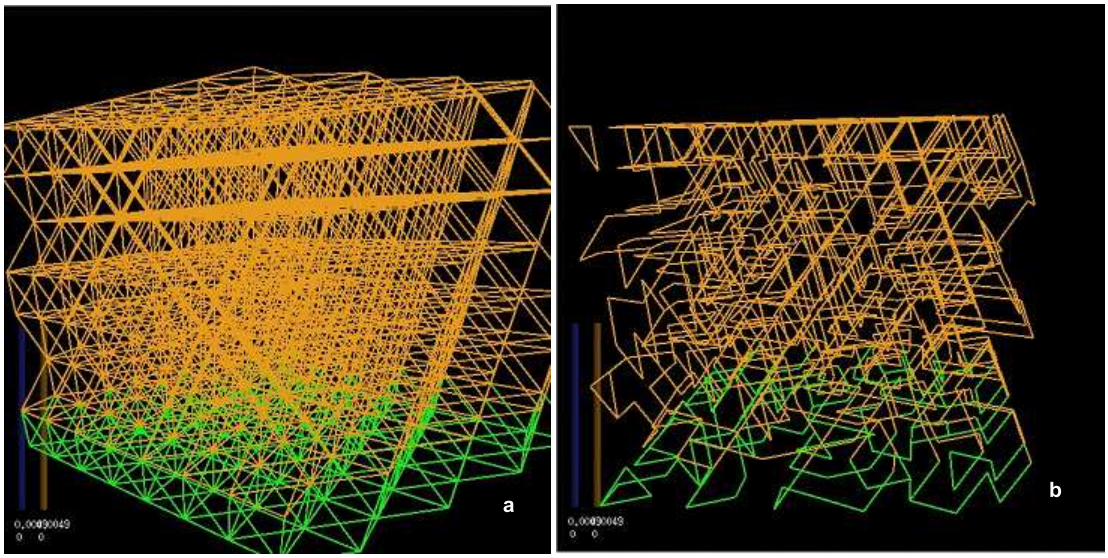

Figure 6.41: *Illustration of (a) a highly interconnected network of channels and (b) the same network with 80% of the channels removed. Here only the remaining channels which span the system are shown;* i.e.*, those that could conduct fluid from top to bottom of the sheet. Clearly having a large proportion of channels hydrophobised randomly would not lead to effective sizing.*

It is assumed that the AKD is randomly placed on a proportion x of the channels; *i.e.*, x are hydrophobised, while (1-x) channels remain open to flow (hydrophilic). Percolation theory enables the exact proportion x required to be closed to flow to stop the droplet from spreading within the sheet. The proportion x required to be closed to flow is 88%. If, for example 20 percent of the channels remained water wetting, these wetting channels would remain interconnected and the inter-fibre channel flow would continue unabated; Figure 6.41(b) shows an example of the system of Figure 6.41(a) with 80% of the (hydrophobic) channels removed. There remains a strongly interconnected network of hydrophilic pores within the network. If one considered a system where 95% of the channels were removed it would no longer conduct fluid throughout the sheet. However, the hydrophilic regions while disconnected on the scale of the full sheet, *would* exhibit small regions where the fluid, on contact, may penetrate locally into the sheet (e.g., locally in patches to 2 - 3 fibres in depth). While it is certainly an oversimplification to consider a paper sheet as a highly ordered network of channels, similar results were obtained on completely random networks (e.g., Voronoi tessellation Voronoi (1908)).

Given the experimental results where no penetration away from the droplet front was observed for the sized papers, it is believed that this strongly indicated that there was effectively 100 percent coverage of the fibres on the mesoscopic length scale ($\simeq$ 1 micron). Recall Figures 6.26, 6.27, 6.28 & 6.29 where the dramatic pinning of the fluid droplet was observed along the surface of fibres after *20 minutes* of contact time. All fibres exhibited crevices formed by indentations due to fibre collapse and surface roughness of the fibres. Thousands of these small

channels were in contact with the droplet and were potential pathways for the fluid penetration along the fibre surface. Again, no indication was seen of surface flow along *any* of these channels. This indicated that all these potential pathways must be hydrophobised. Given that the majority of the fibre surface was either rough or part of an overlapping channel, it can be concluded that the hydrophobic AKD must be effectively present on the whole surface.

The results and observations discussed above are limited to a mesoscopic ($>$ micron) scale. Clearly there are molecular scale processes occurring which are not addressed. One problem that should be considered is why the fluid seems to penetrate the fibre walls after sizing. Regardless how the AKD is deposited, there will be defects present. Defects exist at all length scales, from molecular to microscopic. They may be as subtle as chain disorder, or be represented by macroscopic voids. Their size and prevalence can lead to increased vapour diffusion or bulk fluid transport across the sizing barrier.

Chapter 7

Effects of filler on the rate of imbibition in paper

The effect of fillers on the the mechanism of fluid imbibition are presented in this chapter.

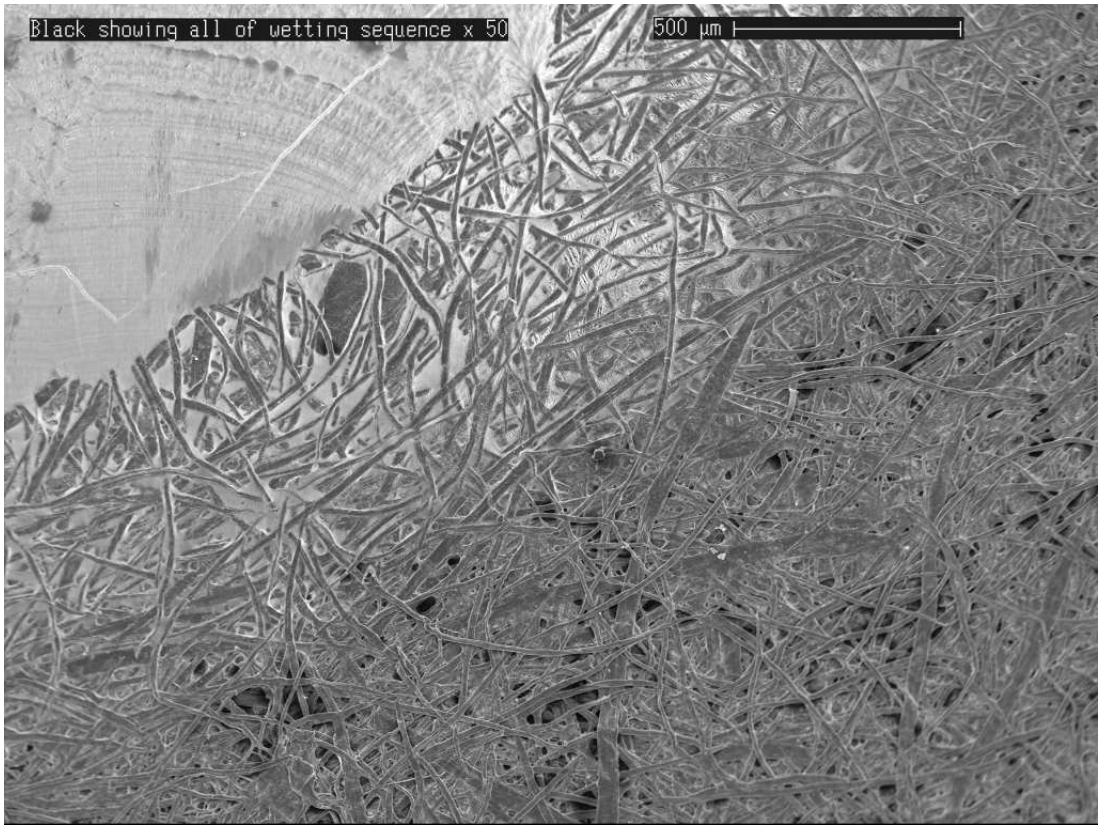

Low magnification cryo-SEM image showing complete wetting sequence of Black decor paper showing liquid droplet through to dry paper.

7.1 Introduction

In the previous Chapter the mechanisms of fluid imbibition for simple cellulosic sheets were identified along with the potential morphologies for flow paths. The mechanism of fluid flow was shown to be by films in channels formed by fibre overlaps. Many papers include the addition of fillers. Fillers are added to paper for opacity and brightness improvement especially for papers used for printing (Biermann, 1996; Laufmann, 1998; Phipps, 2001). While there has been much study of the effect of coating layers on fluid flow into paper (Gate and Windle, 1973; Gate et al., 1973; Garey et al., 1973; Gane et al., 2001; Groves et al., 2001; Grant et al., 1974; Huang and Lepoutre, 1998; Elftonson and Strom, 1995; Lepoutre, 1976; Lepoutre and Rezanowich, 1977; Lepoutre, 1978; Lepoutre and de Grace, 1978; Lepoutre et al., 1979; Lepoutre and Inoue, 1985; Lepoutre, 1989; Lafaye et al., 1987), there have been few studies of the effect of fillers on fluid flow in unsized filled papers. The aim of this chapter is to determine how the modification of paper structure by the inclusion of fillers affects the rate of fluid imbibition in unsized laboratory papers.

Two filler types are studied, precipitated calcium carbonate (PCC) and talc. A range of filler loadings are considered. All papers were made with the same pulp type, manufacturing conditions and basis weight. Two liquids were used in combination with the use of plasma treatment of the papers to identity any possible liquid/paper effects. All papers were examined using SEM and cryo-SEM, and with a new high speed video microscopy method.

It is shown that the major flow path for fluid imbibition remains the fibre overlap channels. It is further shown that the addition of fillers can affect the pore structure and impact on the rates of imbibition of liquids into paper. The major effects of the addition of PCC filler to paper is the enhancement of the connectivity between inter-fibre channels at different depths within the paper. This led to faster flow in the z direction. In the case of the addition of talc filler to paper flow was reduced in the x & y directions. This may be due to the poorer wettability of the talc.

7.2 Materials and methods

7.2.1 Experimental materials

7.2.1.1 Paper samples

Two replicates of laboratory sheets with a bleached furnish of 70% hardwood and 30% softwood blend pulp refined to 500 CSF[1] were made at International Paper's laboratory at Tuxedo Park NY using a Canpa Dynamic Sheet Former to a target basis weight of 75 GSM. The sheets were pressed at 0.5 and then 1 bar between 2 blotters and dried under restraint at 114°C. The

[1] Canadian Standard Freeness, a measure of the drainage rate of water from pulp

different types of filler incorporated were scalenohedral PCC and talc with variable amounts of filler; 0%, 7.5%, 15% and 30%. Paper samples for the high speed saturation experiments were randomly taken from within and between each paper type using a 25mm diameter wad punch. The paper samples were stored in a room of fixed temperature and humidity (20°*C* and 50% rh).

7.2.1.2 Liquid types

Two liquids were used, water with 0.1% w/w ammoniacal copper sulphate, and isopropanol (Aldrich) with 0.1% w/w iodine (the dyes added to increase contrast). The surface tension of the isopropanol solution with iodine dye was 21.2 mJm^{-2} and the water solution with copper sulphate was 70.6 mJm^{-2}, both being almost identical to the surface tensions of the undyed liquids.

7.2.2 High speed video microscopy

The relative reflectance method for determining rates of liquid penetration into decor papers used in Chapter 4, was only effective in determining rates of saturation of fairly viscous liquids such as DEG (having a similar rheology to UF resin) where saturation rates were measured at 30 fps. Quantifying imbibition rates of low viscosity liquids into unsized papers required faster rates. A new method was developed that was suitable for imbibition of aqueous solutions and other wetting liquids of similar viscosity. The technique involved placing a 15 μl droplet on a *Teflon* cylinder with a diameter of 4.5 mm using a Gilson micro-pipette ($1 - 200$ μl) and raising the droplet very slowly until it touched the bottom side of the paper. Imaging was carried out using a CCD camera at 300 fps, the image was split by a triangular prism so that two images could be obtained. One image was of the cross section of the spreading droplet on the bottom side of the paper, enabling the exact moment of fluid contact with the paper to be determined and the second view is of the top side of the paper where changes in reflectance during saturation were measured (Figure 7.1). The video sequence was acquired until the droplet was depleted, usually $4 - 5$ seconds. The variables analysed were rate of saturation and rate of subsurface spread. Rate of saturation was determined by counting the number of frames till the droplet had penetrated to the other side of the paper, but before strike through of the liquid occurred on the other side of the paper. Stills from the video output and graphs in Figure 7.1 show the full sequence of wetting; before the droplet touches the paper (Figure 7.1 a & f), as soon as droplet touch occurs (Figure 7.1 b & g), full saturation but before the beginning of subsurface spread (Figure 7.1 c & h), immediately after saturation when strike-through of liquid begins to occur on the top surface of the paper (Figures 7.1 d & i) and at the end of the sequence and liquid has spread below the surface nearly all the way across the sample (Figure 7.1 e & j). As the paper sheet begins to saturate, the light intensity decreases.

***Table 7.1**: Average thicknesses for all papers.*

Paper type	**Thickness (μm)**
No filler	126
Talc 7.5%	124
Talc 15%	120
Talc 30%	112
PCC75%	127
PCC15%	128
PCC30%	122

After complete saturation, fluid pools up on the top side of the paper within the droplet spread area. Where pooling occurs one now observes an increase in light intensity. Time to saturation was determined by manually advancing each frame until the increase in light intensity shown in Figure 7.1 i x = 130 became apparent due to pooling. This time was defined as the full saturation time. The data was then corrected for the thickness of the paper samples (Table 7.1) and converted into a rate (mm/s).

The rate of sub-surface spread was the rate of spread of liquid in the plane of paper after saturation had occurred (analogous to wicking of a liquid) and is described in Figure 7.2. The fast rate initially is associated with the rapid rate of imbibition in the z direction. The subsurface rate was determined by using a fitted polynomial curve with the first order coefficient being the rate of spread (mm/s) (Equation 7.1 & Figure 7.2). Full details of the development of the method are attached as Appendix D. It would have been desirable to measure the volume loss of the droplet as a function of time by measuring the sectional area of the droplet below the paper. However this was not possible as the paper warped during saturation as can be seen in Figure 7.1 j and as such the relative droplet area potentially visible from the side was obscured. No accurate measure of droplet cross-section could therefore be obtained.

A similar approach to the one describe above was used by Oliver et al. (1994) using a dynamic sorption apparatus which enabled study of individual ink jet drops as they spread and penetrated various porous substrates. In that case the side and top of a penetrating drop was imaged with two cameras and presented through a screen splitter to enable both drop views to be captured side by side but with a video acquisition rate of only 30 fps.

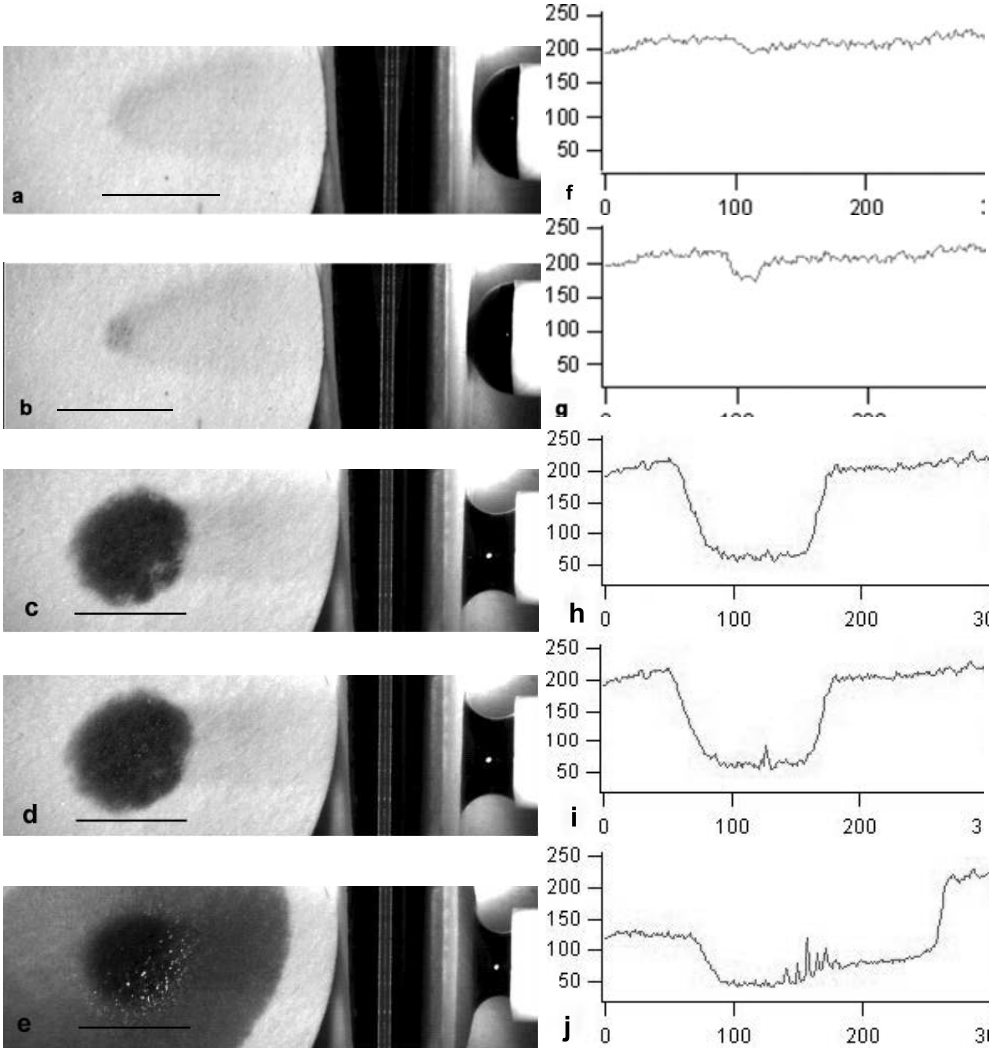

Figure 7.1: *Sequence of images (left) and light intensity profiles (right) showing: a & f just before droplet touch, b & g at droplet touch, c & h full saturation, d & i just after saturation showing strike-through of liquid on top surface note spike in graph at about point 130 showing increased reflection from strike-through liquid and e & j full spread after droplet depletion. Note the changing reflectance values at the point "130" on the x axis. The "halo" visible in the top image is a shadow cast by the collar from one of the light sources. The y axis of the graphs is the intensity of the light reflected off the top side of the paper the scale being 0 = black and 255 full white. The x axis is the number of pixels in the image. The line on the graph is 4.5 mm long and is equivalent to the diameter of the Teflon collar. The changing amount of reflected light was calculated for each frame by subtracting the light intensity of the dry paper before droplet touch from the light intensity of each consecutive frame during the complete wetting sequence giving a graph of droplet spread and change of reflectance over time. The time between consecutive images was 0.003 s.*

$$y = K_0 + K_1 x + K_2 x^2 \tag{7.1}$$

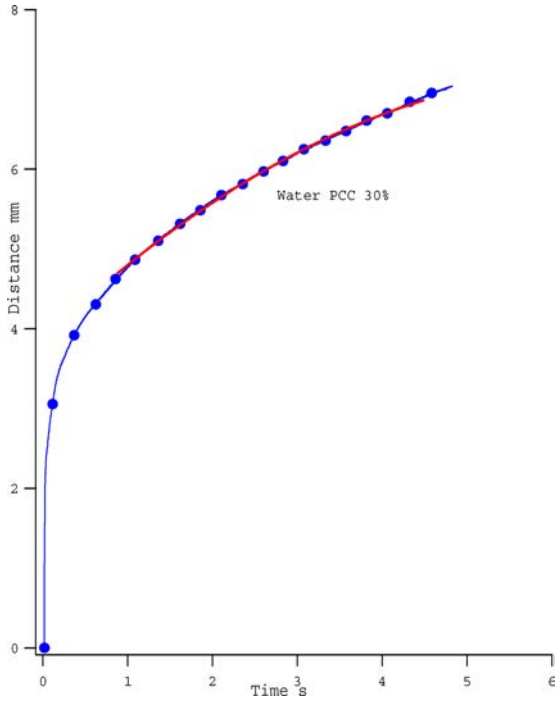

Figure 7.2: *Fitted curve (2nd order polynomial) (red) of the wetting sequence of PCC30 (30% PCC) imbibed with water (blue). The initial steep section on the graph relates to the saturation within the droplet edge and hence is extremely rapid. K_1 in Equation 7.1 is the coefficient used to determine average subsurface spread.*

7.2.3 Plasma treatment

One of the aims of this chapter was to determine the effect of different fillers on the rate of liquid imbibition and to identify the mechanisms causing the differences. Plasma treatment (Shohel, 1987) was used in an attempt to remove the effects of any chemical heterogeneity from either fibres or filler. This would have allowed the investigation of the role of pore structure alone in fluid penetration studies. However as is shown later plasma treatment strongly affected the wettability of fibres but seemed to minimally affect the fillers. A brief review of the effect of plasma treatment on fibres was presented in Section 2.2.3 in Chapter 2.

The plasma reactor used was powered by a ENI Power Systems HPG2 RF generator using a microwave plasma of 135 kHz at a power of 30W (Figure 7.3). A vacuum in the chamber of 0.15 Torr was achieved and water vapour admitted into the plasma reactor. The length of treatment was 60 s. Extending the treatment had no affect on the rates of imbibition. Imme-

***Figure 7.3**: Plasma reactor setup including chamber and RF generator*

diately after treatment the chamber was allowed to equilibrate to atmospheric conditions and the samples which had been treated in a Petri dish were covered by glass and transferred to the high speed video microscopy apparatus.

All samples within each treatment were plasma treated together to ensure there was no variability in the plasma treatment effect. The order of the wetting experiments themselves was randomised to ensure no bias due to ageing. To determine if an ageing effect after plasma treatment affected the rate of imbibition, a batch of the same paper type, Control A (an unfilled paper) was plasma treated. Half of the samples were wetted as soon as possible after plasma treatment and the other half were kept one hour before wetting. There was no significant difference in the rate of imbibition between the two batches. This confirmed results by Chan Tang and Bosisio (1980); Carlson et al. (1995). As all wetting experiments were conducted within 15 minutes of plasma treatment ageing was not considered a factor in the results.

7.2.4 Mercury intrusion porosimetry

The mean pore diameter of a porous material is often considered the primary indicator of liquid penetration rates. Mercury intrusion porosimetry (MIP) (Rucinski et al., 1986; Webb and Orr, 1997; Johnson et al., 1999) was used to determine average pore diameter. From the volume of mercury intruded into the paper sample and using the Lucas-Washburn equation the pore volume and diameter can be inferred.

The instrument used was a Micromeritics Mercury Intrusion Porosimeter Autopore III

model 9410[2]. The sample of 300 mm x 20 mm which had been weighed was rolled up with nylon mesh[3] and placed in a No. 11 P5 bulb penetrometer having a stem volume of 1.836 mL. The penetrometer was then sealed, weighed and placed into the vacuum port of the porosimeter. A final vacuum of 50 μmHg was applied to the sample for 15 min. Mercury was allowed to flood into the penetrometer at a pressure of 0.004 mPa. The assembly plus mercury was then weighed. The sample was then placed into the high pressure port of the porosimeter. The high pressure regime was limited to 11.15 mPa to avoid any risk of damaging or dislocating fibres. Each pressure setting between 0.004 mPa to 11.15 mPa (40 steps in logarithmic increments) was held for 10 seconds to determine incremental intruded volume. Schoelkopf et al. (2003) used an equilibration time of 60 s for throat diameters down to 0.004 μm.

7.2.5 SEM imaging

The techniques to image the raw papers using SEM were the same as described in Chapter 3 and the techniques for cryo-SEM were fully described in Chapter 6.

7.2.6 Statistical analysis of data

Design of experiments and statistical analyses are as detailed in Chapters 3 & 4. Significant results are presented in tabular form (Tables E.1, & E.2) and for ease of interpretation in line graphs.

The treatment structure affecting rate of imbibition into paper in this chapter was; liquid type, water or isopropanol, plasma treated or not, whether filler was present or not, if filler present the type, talc or PCC and filler amount, 0, 7.5, 15 & 30%.

7.3 Results

7.3.1 Macro effects of filler and plasma treatment on fluid flow

Data for saturation rate is summarised in Figure 7.4 and Table 7.2. One significant effect is that the addition of PCC increased the saturation rate of water in both the plasma treated and untreated samples. There was a dramatic increase in the penetration rate for PCC-loaded paper ($>$ 100% increase with increasing filler content). In contrast the addition of talc had no significant effect on the saturation rate of water in either plasma treated or untreated talc filled papers. Plasma treating led to an increase in water saturation for all papers.

The data also shows the addition of PCC enhanced the saturation rate of isopropanol whereas the addition of talc had little effect. Plasma treating had no effect on the imbibition rate of isopropanol with increasing levels of PCC. Plasma treating appeared to have a negative

[2]The software controlling the equipment was Micromeretics Instrument Corporation 9410 version 2.0.

[3]As used in retail fruit packaging to enable the mercury to penetrate within the roll of paper in the penetrometer.

effect on saturation rate of isopropanol in talc filled papers at 30% addition rate and no effect in unfilled papers.

Figure 7.6 shows a series of video still images at 0.015 seconds after droplet contact for both isopropanol and water in unfilled, 30% PCC and 30% talc filled papers, none of which had undergone plasma treatment. The images clearly show that after this time delay, liquid had only saturated across a limited number of regions for all the paper types except for 30% PCC filled paper saturated with water which had almost fully saturated the paper which is consistent with Figure 7.4.

Data for subsurface spread is summarised in Figure 7.5 and Table 7.3. The major significant effect was that the addition of talc slowed down the rate of subsurface spread of water in both plasma treated and untreated papers. The spreading rate of water in the PCC filled paper exhibits a slight increase ($\sim$10%). At higher addition levels of PCC plasma treatment had very little effect on the subsurface spread rates of water. Plasma treatment appeared to affect the rate of subsurface spread of isopropanol at the highest rate of addition of talc. There were no other affects on the rate of subsurface spread of isopropanol.

Table 7.4 shows that the addition of fillers reduces average pore diameter as determined by MIP and that for an equivalent amount of filler addition the pore sizes in PCC papers are substantially smaller than those filled with talc.

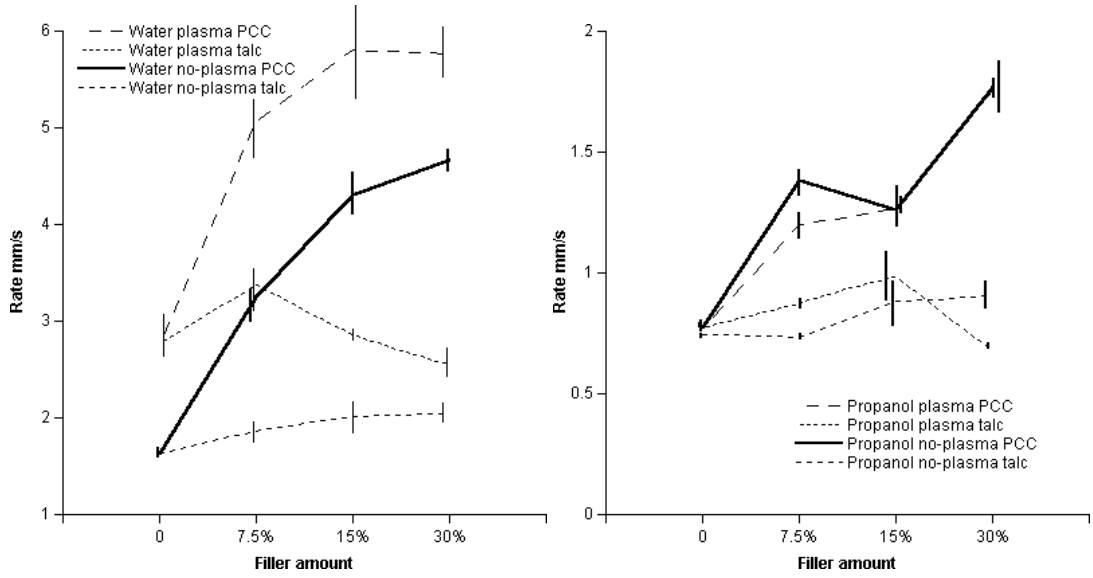

Figure 7.4: *Graphs showing the effect of plasma treatment, filler type and amount on the saturation rates of a) water and b) propanol. The graphs show standard error bars between replicates.*

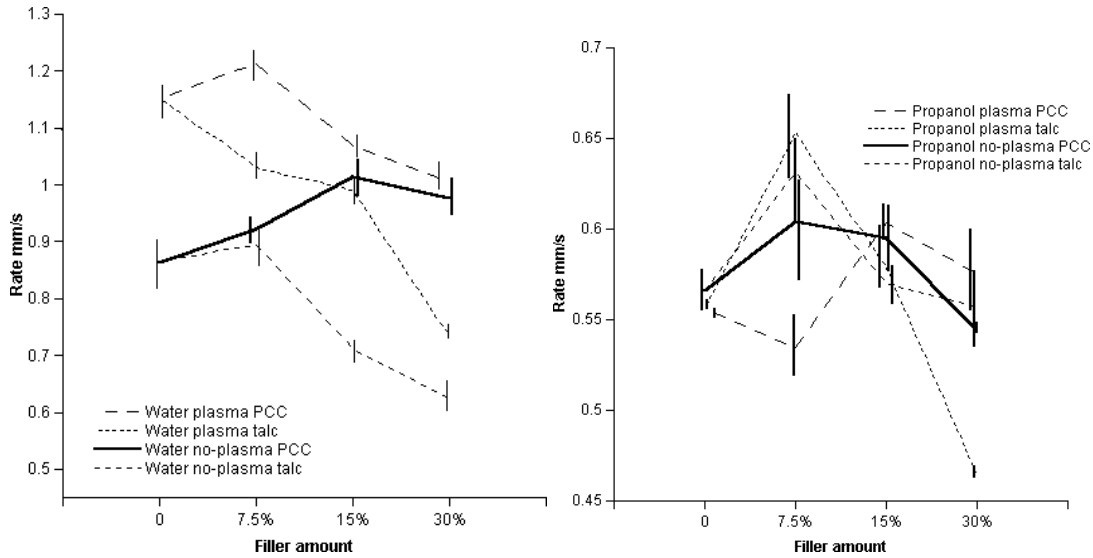

Figure 7.5: *Graphs showing the effect of plasma treatment, filler type and amount on the rate of sub-surface spread of a) water and b) propanol. The graphs show standard error bars between replicates.*

***Table 7.2**: Saturation rate raw data (mm/s)*

Liquid type	Plasma treatment	Filler type	Filler amount			
			0	**7.5%**	**15%**	**30%**
Propanol	Yes	None	0.77			
Propanol	Yes	PCC		1.2	1.26	1.75
Propanol	Yes	Talc		0.87	0.98	0.68
Propanol	No	None	0.74			
Propanol	No	PCC		1.38	1.26	1.76
Propanol	No	Talc		0.73	0.88	0.91
Water	Yes	None	2.76			
Water	Yes	PCC		5.07	5.81	5.766
Water	Yes	Talc		3.37	2.86	2.55
Water	No	None	1.62			
Water	No	PCC		3.24	4.30	4.66
Water	No	Talc		1.86	2.01	2.06

***Table 7.3**: Sub surface spread raw data (mm/s)*

Liquid type	Plasma treatment	Filler type	Filler amount			
			0	**7.5%**	**15%**	**30%**
Propanol	Yes	None	0.55			
Propanol	Yes	PCC		0.53	0.60	0.57
Propanol	Yes	Talc		0.65	0.57	0.46
Propanol	No	None	0.56			
Propanol	No	PCC		0.60	0.59	0.54
Propanol	No	Talc		0.63	0.57	0.55
Water	Yes	None	1.15			
Water	Yes	PCC		1.21	1.06	1.00
Water	Yes	Talc		1.03	0.99	0.73
Water	No	None	0.86			
Water	No	PCC		0.92	1.01	0.97
Water	No	Talc		0.89	0.71	0.62

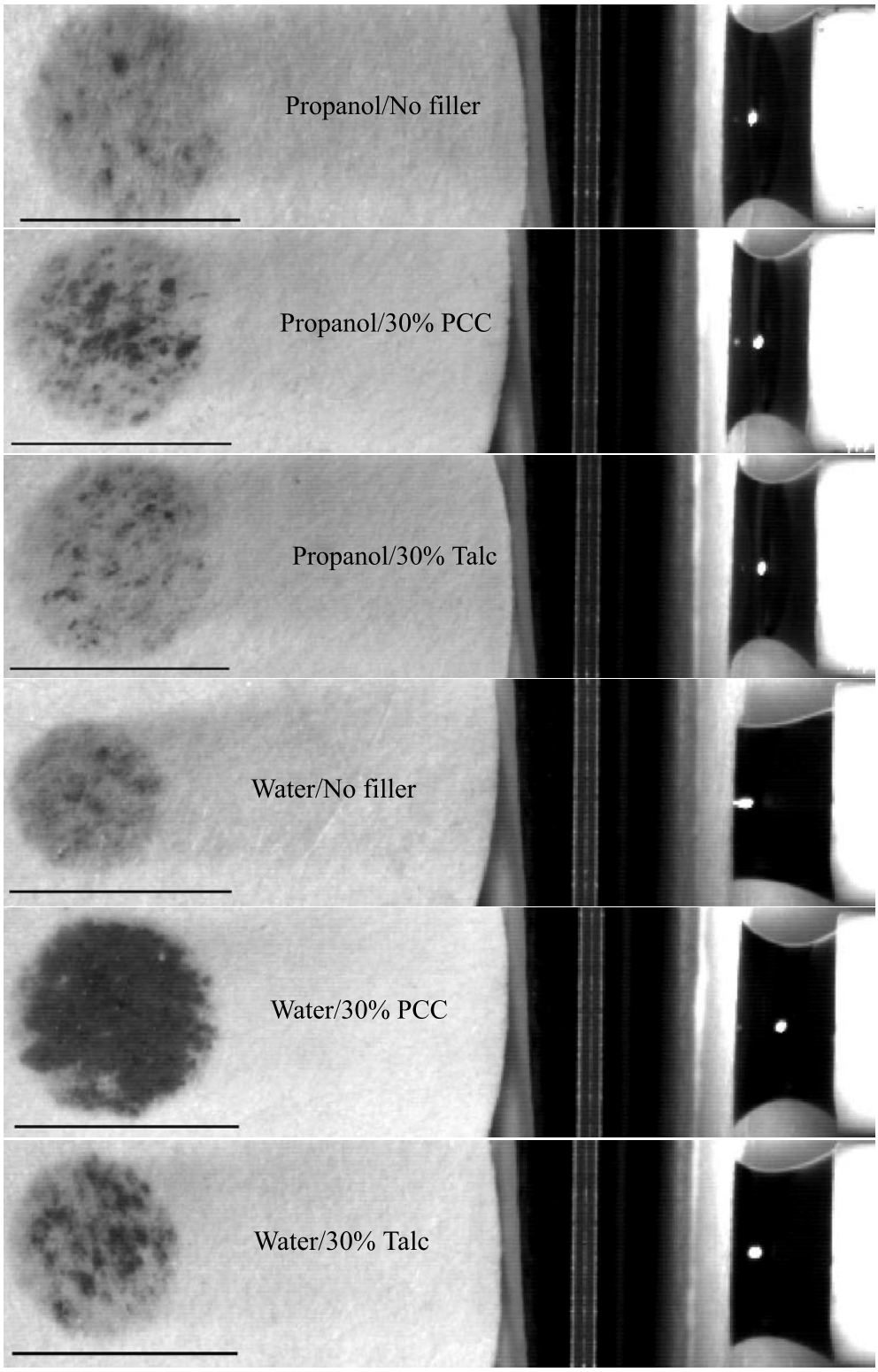

Figure 7.6: *Series of images showing the degree of saturation after 0.015 seconds. Note the differences in level of saturation and hence rate of imbibition in the* z *direction. Scale bar is 4.5 mm*

***Table 7.4**: Average and predicted pore diameter obtained from mercury intrusion porosimetry.*

Paper type	**Average pore diameter (μm)**	**Predicted pore diameter (μm)**
No filler	4.12	n/a
Talc 7.5%	3.86	4.06
Talc 15%	3.54	4.01
Talc 30%	3.47	3.9
PCC75%	3.64	4.06
PCC15%	2.95	4.01
PCC30%	2.20	3.9

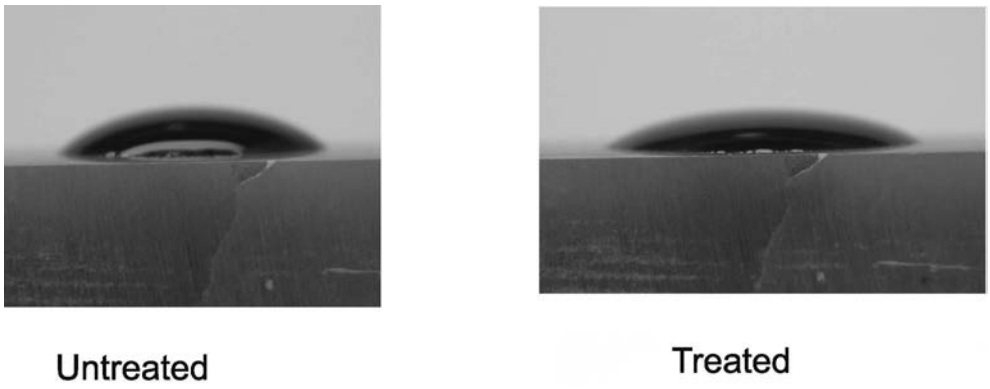

***Figure 7.7:** Images of water droplets on talc before and after plasma treatment showing that plasma treatment had very little effect.*

Wettability can be associated with the apparent contact angle of a liquid on a surface such that the more wettable the surface the lower the liquid contact angle. To test the effects of the wettability of both fillers on fluid imbibition in filled papers, a large crystal of calcite (calcium carbonate) and a piece of metal chalk (talc) were wetted with both isopropanol and water and contact angles determined. Both water and isopropanol spread very rapidly on the calcite crystal such that there was no measurable contact angle. It was assumed that the contact angle for plasma treated calcite would also be close to 0°. Isopropanol also spread very rapidly over the talc with no measurable contact angle and plasma treating was found to have no effect. Water however did give a measurable contact angle on talc and plasma treating was found only to have little effect on it (Figure 7.7). The surface energies of calcium carbonate, talc and cellulose are detailed in Table 7.5 (Yildirim, 2001).

Plasma treating of unfilled papers resulted in a higher degree of pore infilling as evidenced by there being fewer unfilled pores (Figure 7.8) than in untreated unfilled paper (Figure 7.19). From Figures 7.4 & 7.5 one can see the significant positive effect on imbibition rates of plasma treating of cellulose fibres in unfilled papers.

***Table 7.5**: Surface energies.*

Material	**Surface energy (mJm^{-2})**
Cellulose	44
PCC	48
Talc	31.7

Figure 7.8: *Low magnification image of wetting of an unfilled plasma treated paper. Note that there are fewer unfilled pores than in untreated papers (Figure 7.19).*

7.3.2 SEM observations of the distribution of filler

Figures 7.9 & 7.10 show high magnification images of particles of PCC and talc in paper. PCC is smaller 2 - 3 μm and has a more complex scalenohedral like shape, whereas talc is plate-like and being up to 20 μm in extent and (1 μm) in thickness.

Figures 7.11, 7.13 & 7.15 are SEM images of papers filled with 7.5%, 15% & 30% PCC respectively and Figures 7.12, 7.14 & 7.16 are SEM images of papers filled with 7.5%, 15% & 30% talc respectively. It is clear that the distribution of the fillers differs. With PCC filled papers the filler tends to aggregate into large clumps up to 30μm in diameter and is heterogeneously distributed throughout the paper (Figure 7.15). Many fibre surfaces exhibit no filler coverage while others show a complete coverage. In some cases these large aggregated clumps of PCC are located in larger pores and could bridge across pores. The effect of this is to "break" up these larger pores. This was not the case for talc filled papers where the filler tended to be concentrated around the edges rather than within the pores (Figure 7.16). Figure 7.18 is a schematic of the distribution of fillers at a larger scale.As a result it had a much lower impact on changing pore sizes (Table 7.4).

Table 7.4 also shows the impact of fillers on pore diameter by predicting the pore sizes if the filler is distributed around the edge of the pores such as occurred with talc. This assumes that the pores are spherical in shape and that the filler is distributed homogeneously around edges of the pores. For talc filled papers the assumption of even coverage of filler agrees with

the data. However the predictions for PCC filled pores strongly overestimate the actual sizes. This reinforces the observation that PCC aggregates in pores and tends to break the pore up into much smaller volumes. Figure 7.17 shows a schematic diagram of the way the different filler particles distribute at a pore scale.

7.3.3 SEM observations of the effect of filler on the spreading of liquids

To better understand the effect of fillers on imbibition in paper a study was undertaken using cryo-SEM. Figures 7.19 - 7.22 are images of unfilled paper. Only data for untreated paper with water as the saturating fluid are shown. One notes that in unfilled paper the fluid is present in the form of films in the inter-fibre channels as was seen in Chapter 6. One also notes that the fluid does not completely invade the largest pores. As described in Chapter 6, in unfilled papers the advancing fluid invades all pores via films and a pore saturates by the thickening of these advancing films. The smaller pores are therefore completely invaded, but the largest pores remain only partially wetted along the edges.

With filled papers irrespective of the type or amount of filler, fluid advanced in the form of films along inter-fibre channels. Figures 7.23 - 7.26 show imbibition of fluid in paper filled with 7.5% PCC. Unlike unfilled paper, very few pores remain unfilled behind the wetting front. In the top left hand corner of Figure 7.25 one can see a pore containing PCC particles being invaded with the wetting fluid (arrow marked A). Note the difference between the filling pore in Figures 7.25 (arrow A) and the filling pore in the centre of Figure 7.22. The former is being invaded through filler whereas the latter is being invaded through thickening films on all the edges surrounding the pore. Figure 7.26 further shows how readily particles of PCC wet. A clump of particles on the *surface* of a fibre has been completely imbibed (arrow A). Note the adjacent areas on the surface of the same fibre are dry.

Figures 7.27 - 7.30 show imbibition of fluid in a paper filled with 7.5% talc. There are less unfilled pores behind the wetting front than unfilled paper. Figure 7.29 shows an almost filled pore where the liquid appears to be pinned on a large particle of talc within the pore (arrow marked A). Note also a thickening film in an inter-fibre channel that appears to be pinned on a large particle of talc (arrow B). Figure 7.30 also shows the phenomenon of the wetting fluid appearing to pin on talc particles.

Figures 7.31 - 7.34 show wetting of a paper filled with 15% PCC. As with papers filled with 7.5% PCC, there are almost no unfilled pores between the edge of the droplet and the wetting front (Figure 7.33). Where PCC is in a pore that is in contact with the wetting fluid, one observes penetration into the filler (arrow A). Where there are particles of PCC in an inter-fibre channel there seems to be no pinning of the film of wetting fluid as with talc (arrow B). Figure 7.33 shows detail of pore filling immediately behind the wetting front. Figure 7.34 shows again the wetting liquid imbibing into the clump of PCC (arrow A).

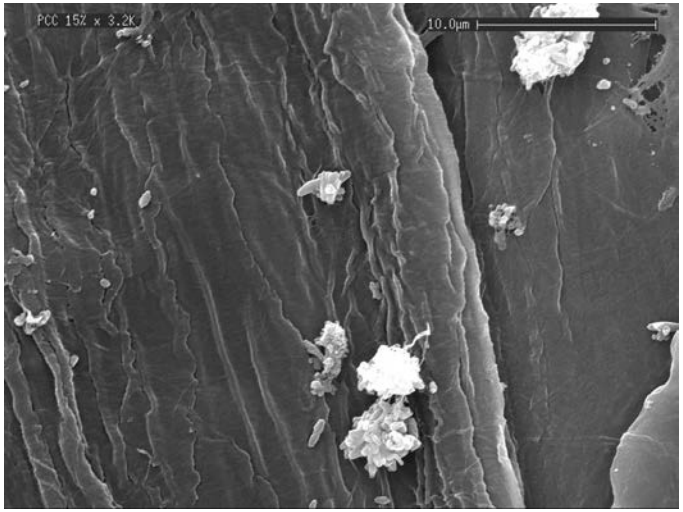

Figure 7.9: *High magnification image of individual PCC particles in a paper with 15% PCC. Note complex scalenohedral but overall roughly spherical shape.*

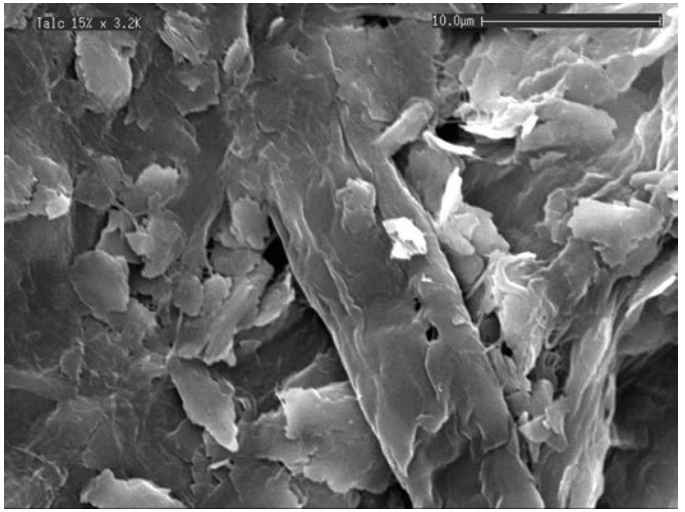

Figure 7.10: *High magnification image of individual talc particles in a paper with 15% talc. Note the plate-like structure of the particles with relatively smooth surface and very rough edges.*

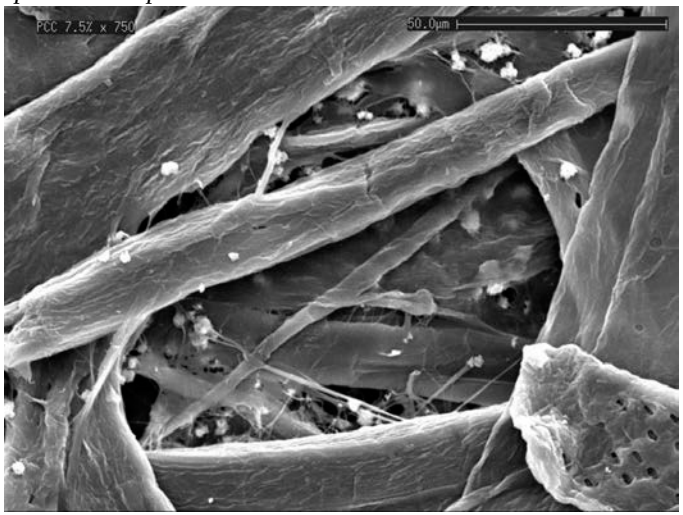

Figure 7.11*: SEM images of laboratory paper with 7.5% PCC.*

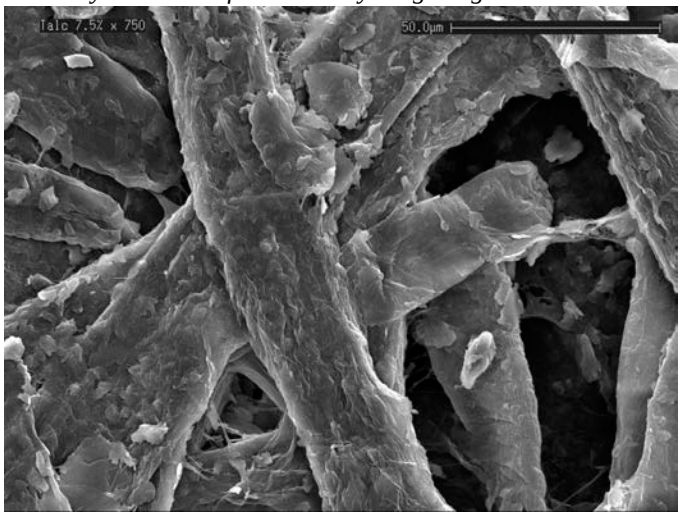

Figure 7.12*: SEM images of laboratory paper with 7.5% talc.*

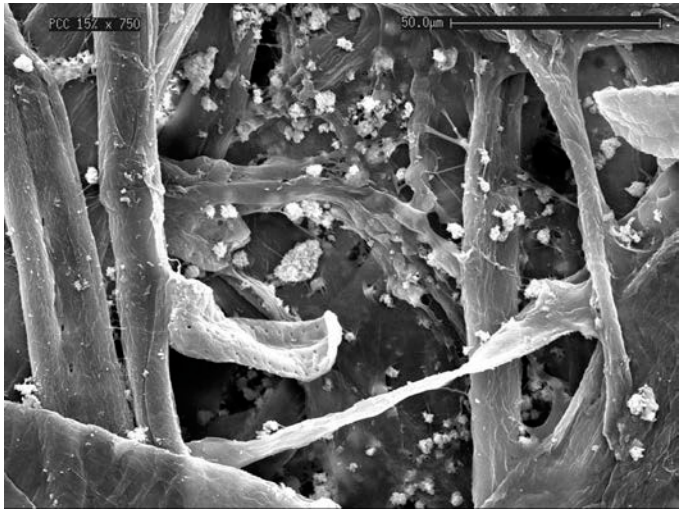

***Figure 7.13**: SEM images of laboratory paper with 15% PCC.*

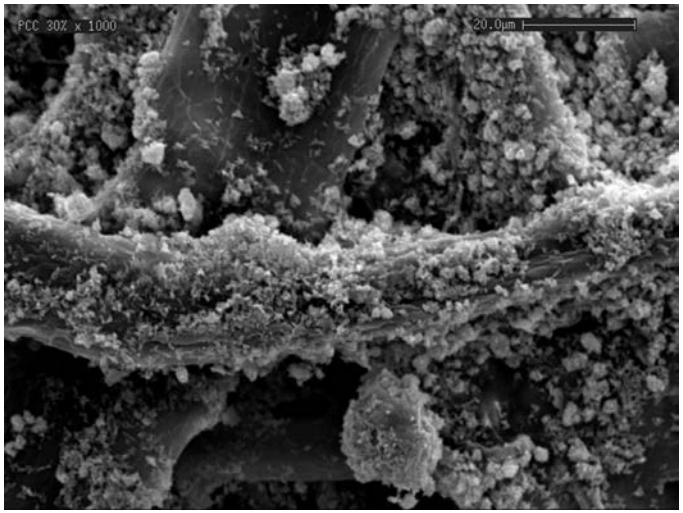

***Figure 7.15:** SEM images of laboratory paper with 30% PCC. Note tendency for the PCC particles to aggregate into clumps in pores.*

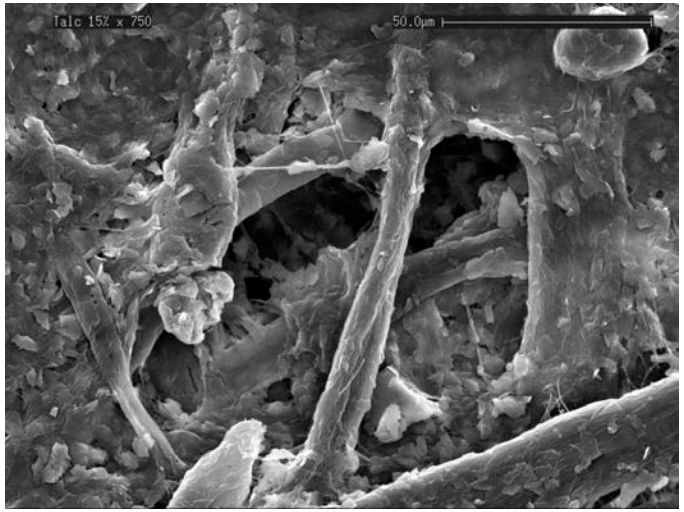

***Figure 7.14**: SEM images of laboratory paper with 15% talc.*

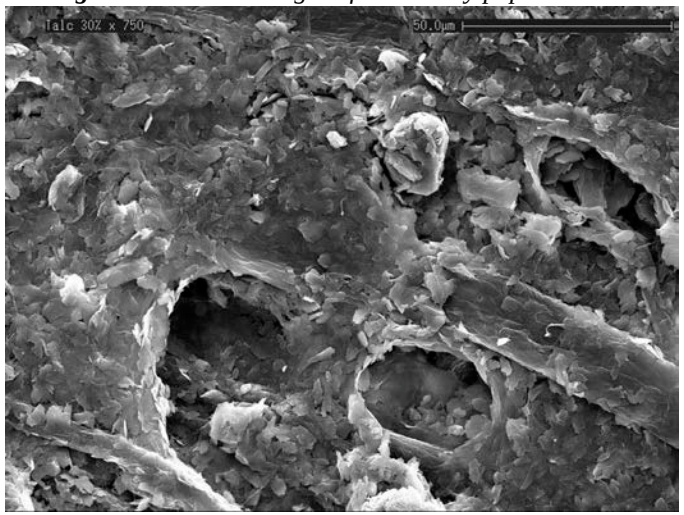

***Figure 7.16:** SEM images of laboratory paper with 30% talc. Note tendency for the talc particles to be distributed around and not in the larger pores.*

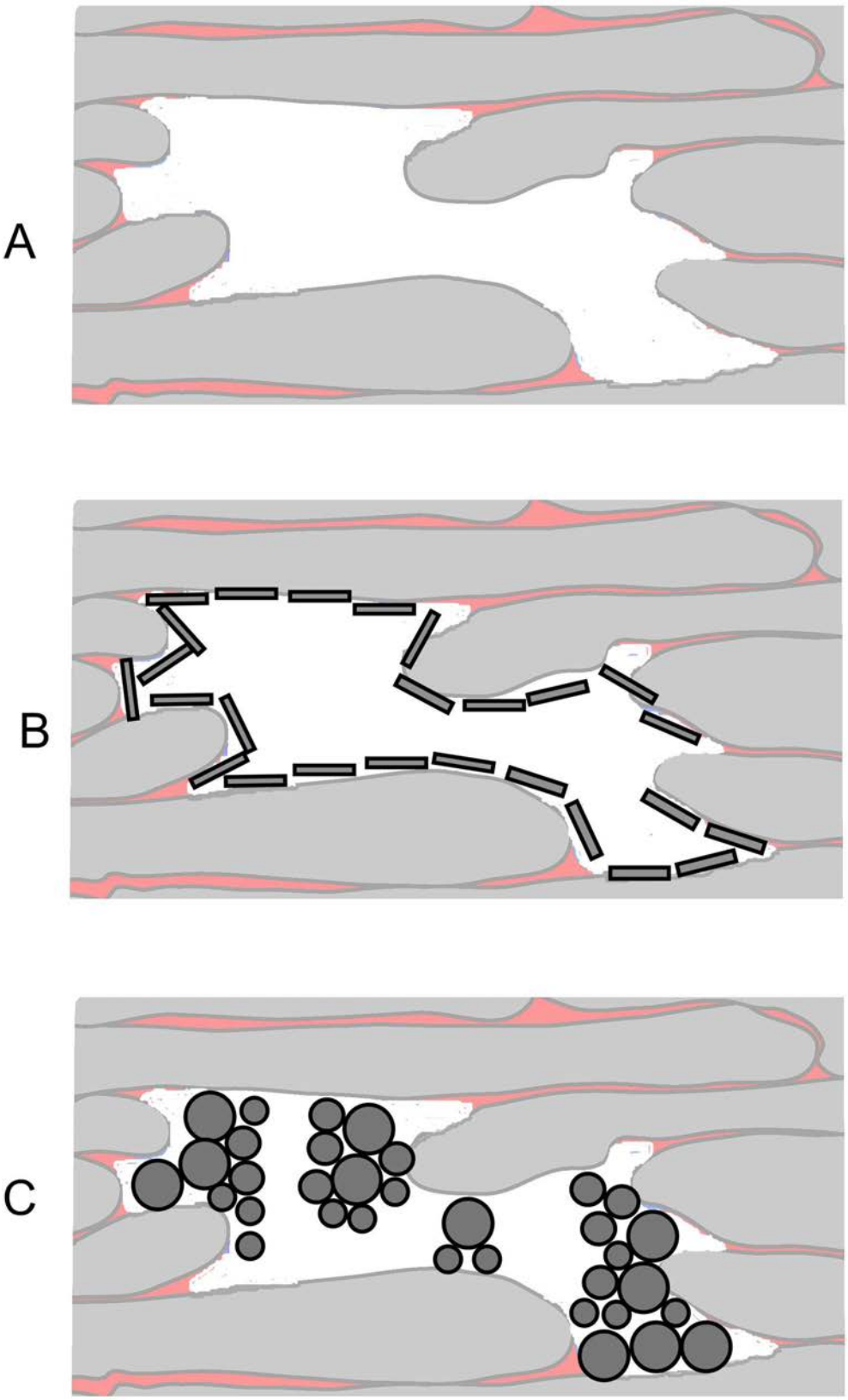

Figure 7.17: *Schematic showing the distribution of filler particles at a pore scale; a) unfilled paper, b) paper filled with talc and c) paper filled with PCC. Note distribution of PCC particles in clumps in larger pores and the distribution of talc particles around the edges of larger pores.*

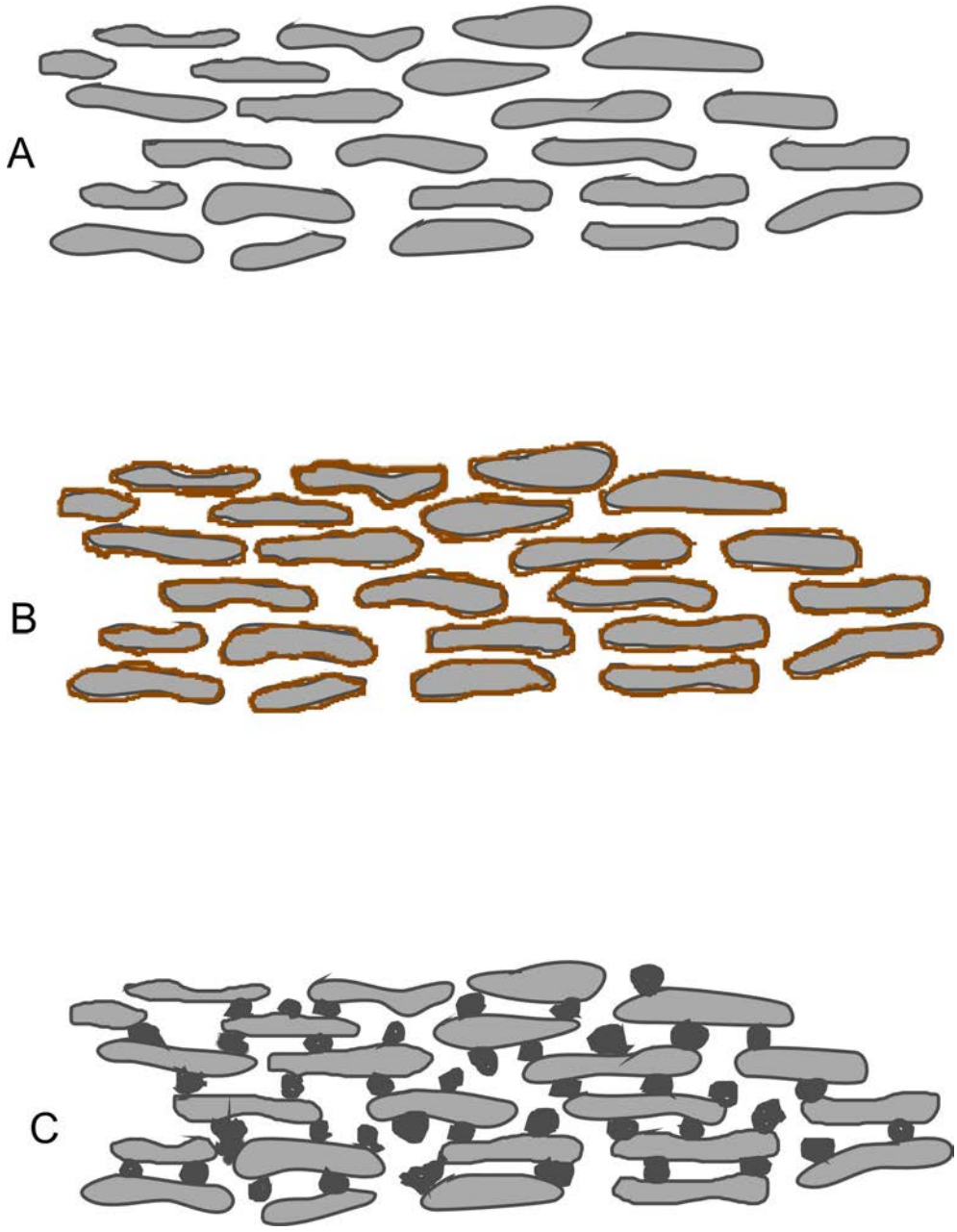

Figure 7.18: *Schematic showing the distribution of filler particles at a larger scale; a) unfilled paper, b) paper filled with talc and c) paper filled with PCC.*

Figures 7.35 - 7.38 show wetting of a paper filled with 15% talc. In Figure 7.35, unfilled pores are evident behind the fluid front. Figure 7.37 is a higher magnification image at the wetting front and shows what appears to be pinning of a film by a particle of talc (arrow A). The particle of talc appears completely surrounded by the wetting fluid yet the liquid has not spread over the particle. This is also shown in Figure 7.38 (arrow A) where it can be clearly seen that a particle of talc is stopping the spreading of a film prior to pore filling.

Figures 7.39 - 7.42 show wetting in a paper filled with 30% PCC. Figures 7.41 and 7.42 show the influence that the particles of PCC have on the filling of pores by the wetting fluid. Note that in Figures 7.41 & 7.42 the invading liquid follows the distribution of the particles of PCC. Note also in Figure 7.42 that where there are PCC particles on the surface of the fibre they imbibe the wetting fluid.

Figures 7.43 - 7.46 show wetting in a paper filled with 30% talc. There are still larger unfilled pores behind the wetting front. Figure 7.44 shows what appears to be the impeding pore filling (arrows marked A). Figure 7.45 shows a large pore with talc distributed around the edge remaining empty. Figure 7.46 shows a thickening film being pinned on particles of talc.

Flow along films is evident as the main mode of fluid advance in all of the papers imaged, irrespective of filler type or amount.

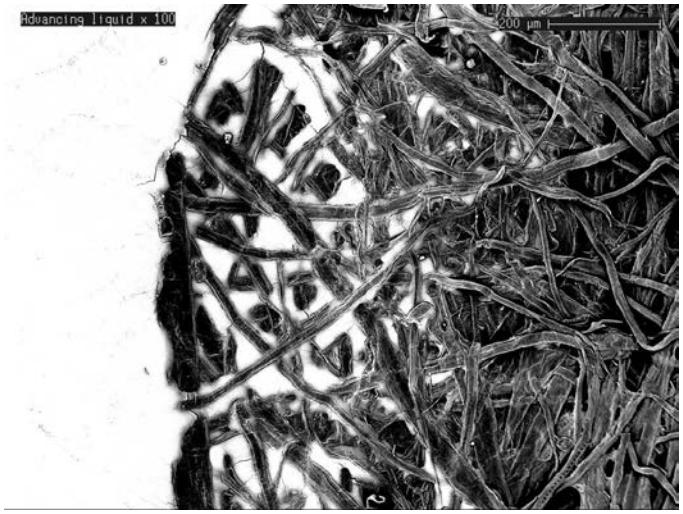

Figure 7.19: *Low magnification image of wetting of a paper with no filler.*

Figure 7.20*: Higher magnification image of a paper with no filler.*

Figure 7.21*: High magnification image of an unfilled paper.*

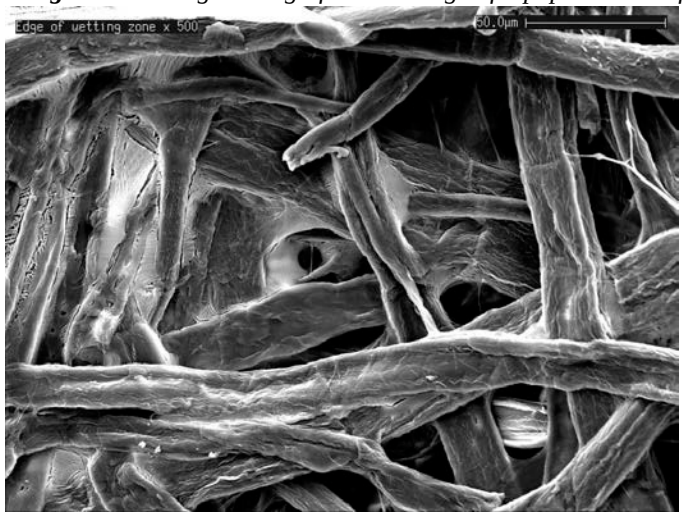

Figure 7.22*: Higher magnification image of an unfilled paper.*

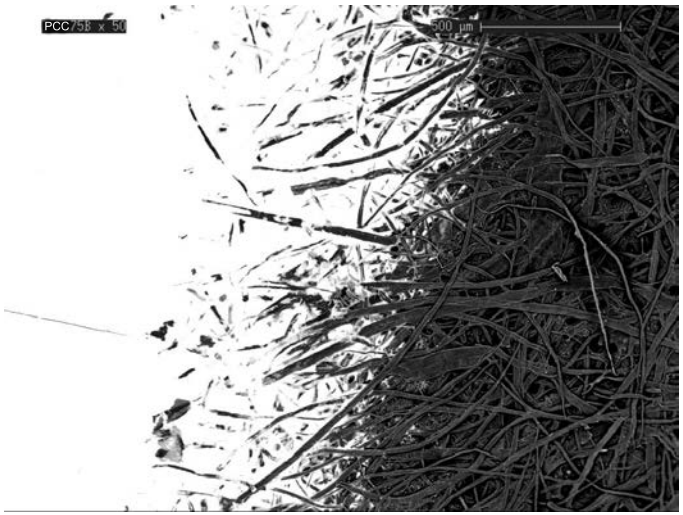

Figure 7.23: *Low magnification image of wetting of paper filled with 7.5% PCC. Arrows marked A show unfilled pores.*

Figure 7.24: *Higher magnification image of a 7.5% PCC filled paper showing infilling of pores.*

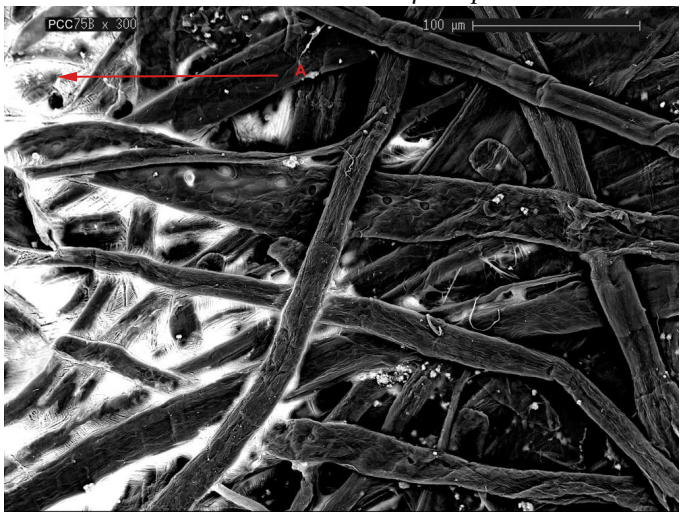

Figure 7.25: *Wetting of a 7.5% PCC filled paper showing showing few unfilled pores. Note impact of filler on filling of pores (arrow marked A).*

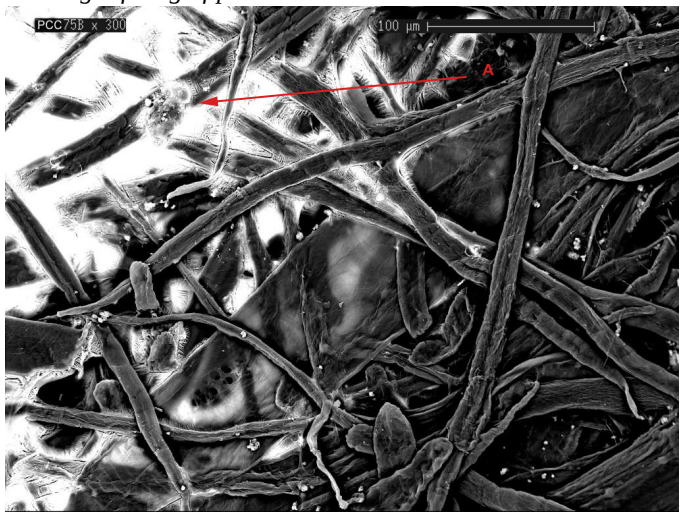

Figure 7.26: *Wetting of a 7.5% PCC filled paper showing showing pore filling right at edge of wetting area. Note wetting of particles of PCC on fibre surface (arrow marked A)*

Figure 7.27: *Low magnification image of wetting of paper filled with 7.5% talc. Note unfilled pores in comparison to Figure 7.23. Arrows show unfilled pores behind wetting front.*

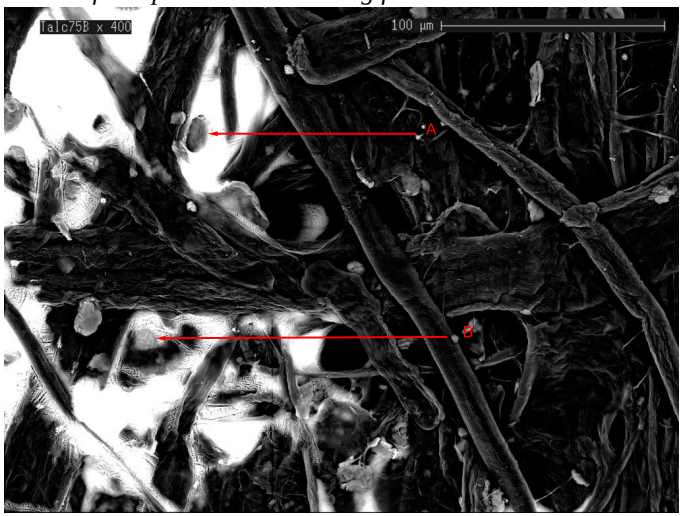

Figure 7.29: *High magnification image of a 7.5% talc filled paper showing pore filling only at edge of wetting area. Fluid filling a pore appears to be pinned on a talc particle (arrow A) and a thickening film in an inter-fibre channel also appears pinned on a talc particle (arrow B).*

Figure 7.28: *Higher magnification image of a 7.5% talc filled paper showing more detail of pore filling.*

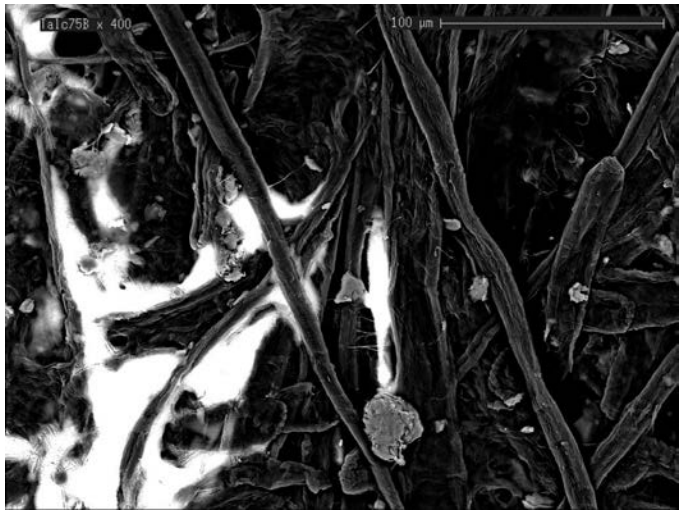

Figure 7.30: *7.5% talc filled paper showing fluid propagation by films.*

Figure 7.31: *Low magnification image of wetting of paper filled with 15% PCC.*

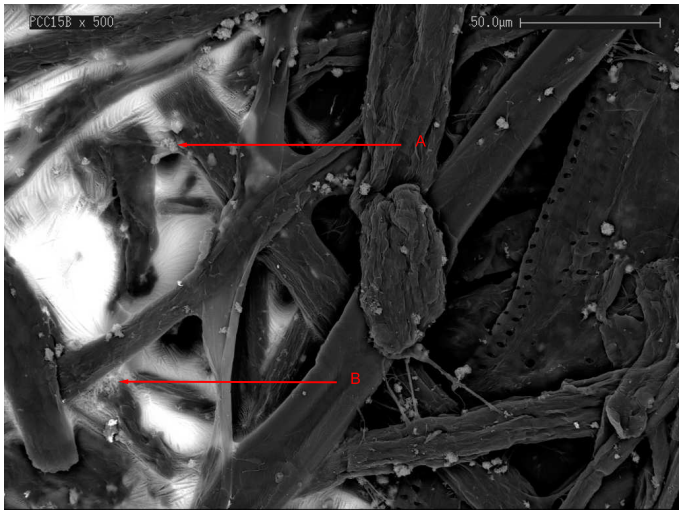

Figure 7.33: *High magnification image of a 15% PCC filled paper showing pore filling at very edge of wetting area.*

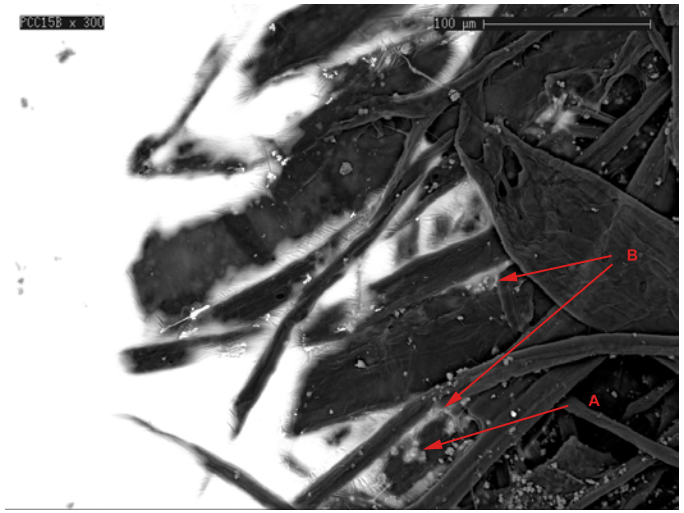

Figure 7.32: *Higher magnification image of a 15% PCC filled paper showing film flow at edge of wetting area. Arrow A shows particles of PCC being readily wet and arrow B shows particles in a fibre overlap channel where pinning of fluid flow is evident.*

Figure 7.34: *Higher magnification image of a 15% PCC filled paper showing film flow at very edge of wetting area. Arrow A shows the influence of aggregated PCC particles in the filling of pores.*

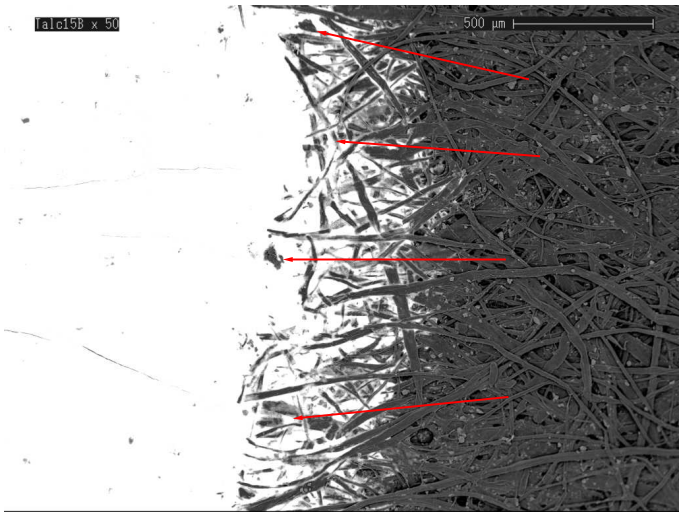

Figure 7.35: *Low magnification image of wetting of paper filled with 15% talc.*

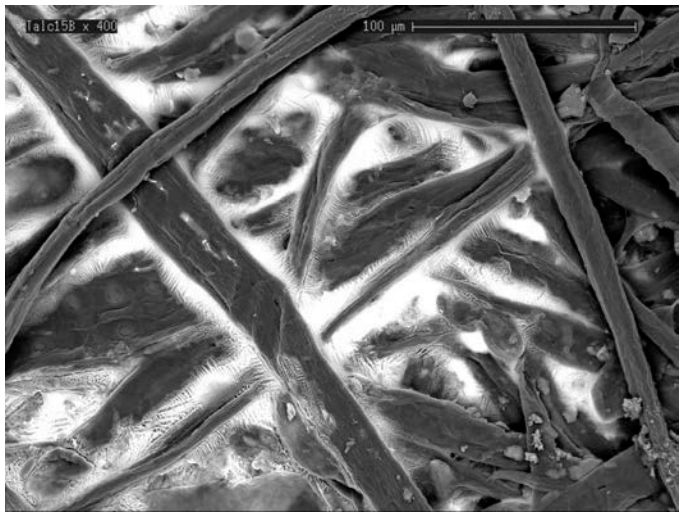

Figure 7.36: *Higher magnification image of a 15% talc filled paper showing more detail wetting.*

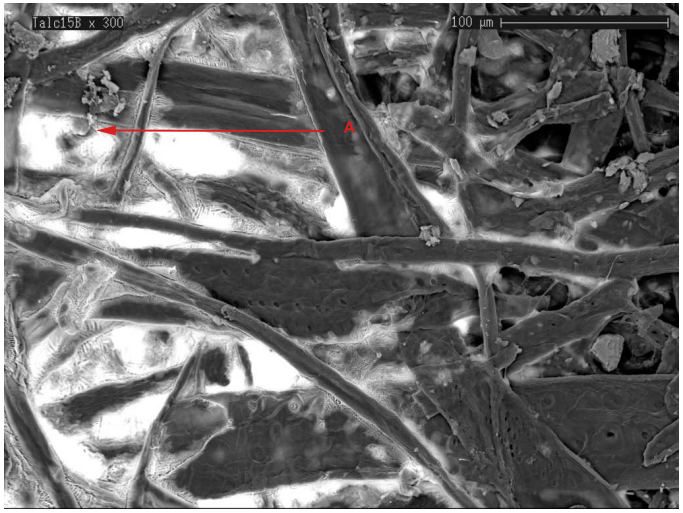

Figure 7.37: *High magnification image of a 15% talc filled paper showing few unfilled pores. Arrow A shows liquid filling a pore pinned on the edge of a particle of talc.*

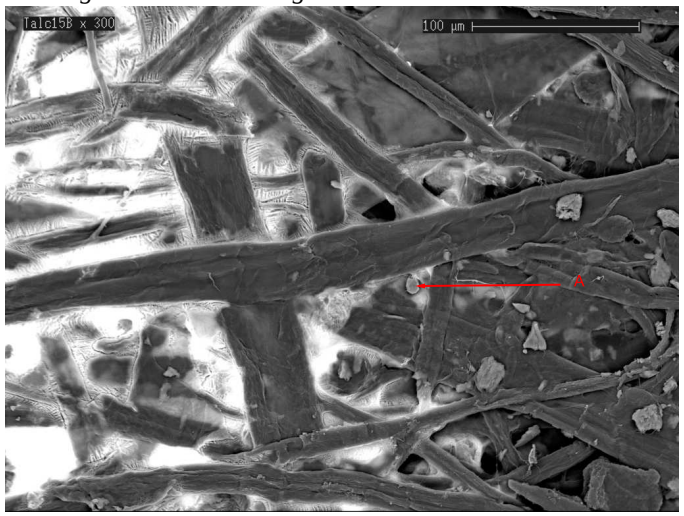

Figure 7.38: *Higher magnification image of a 15% talc filled paper showing unfilled pores near edge of wetting area. The arrow marked A again shows the effect of a particle of talc impeding pore filling.*

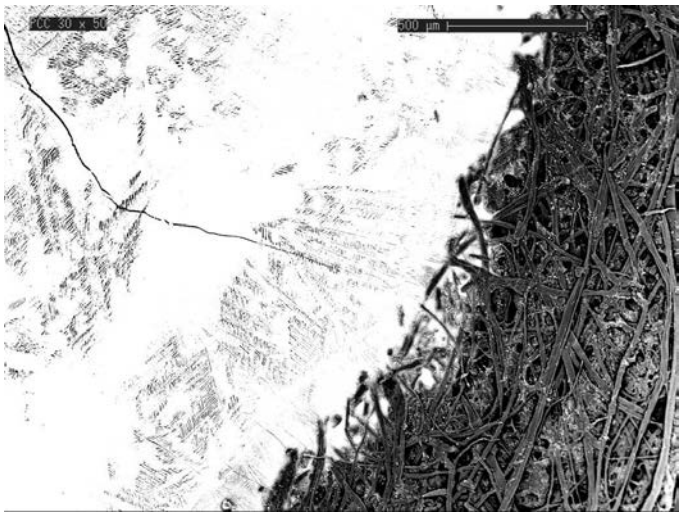

Figure 7.39: *Low magnification image of wetting of paper filled with 30% PCC.*

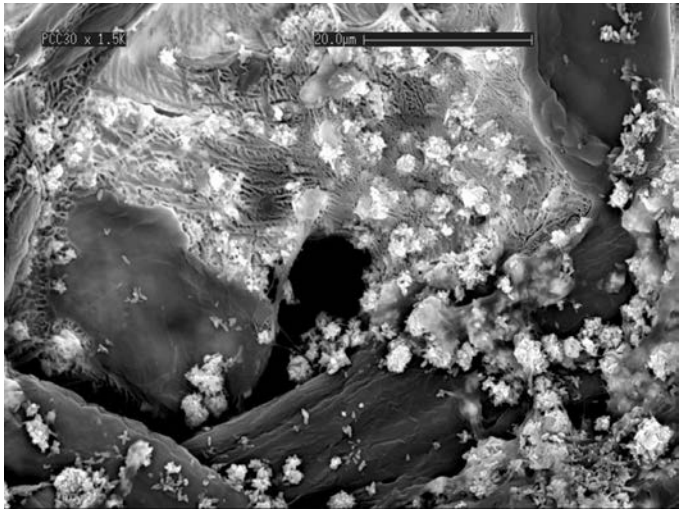

Figure 7.41: *High magnification image of a 30% PCC filled paper showing more detail of imbibition into clumps of particles. Note the pattern of imbibition exactly follows the distribution of particles.*

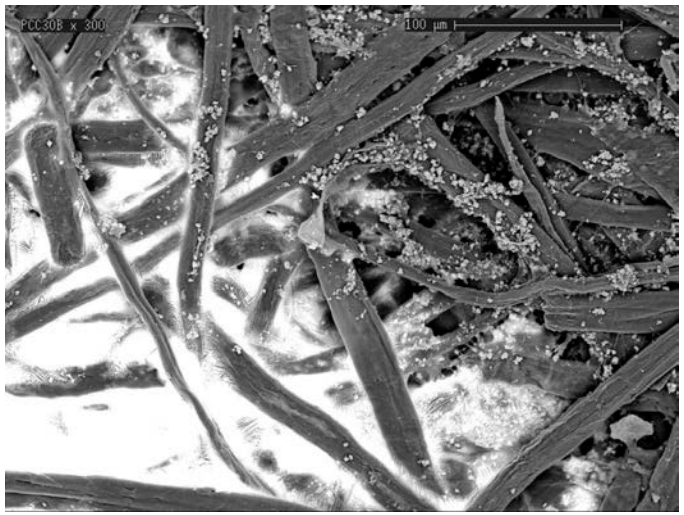

Figure 7.40: *Higher magnification image of a 30% PCC filled paper showing few unfilled pores .*

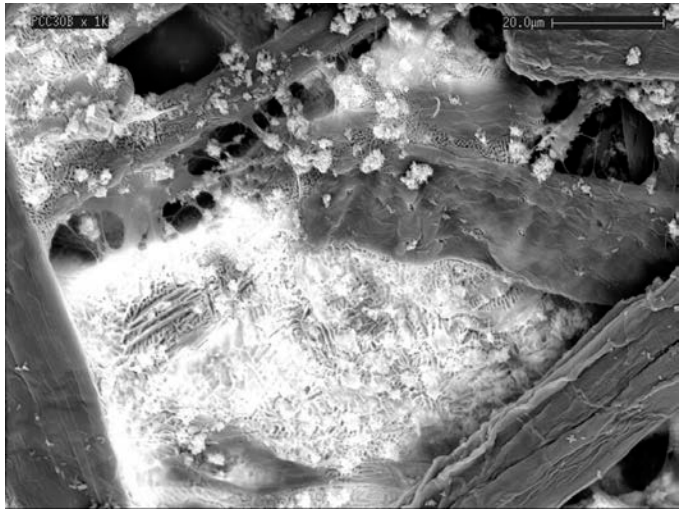

Figure 7.42: *Higher magnification image of a 30% PCC filled paper showing more detail of imbibition of clumps of particles.*

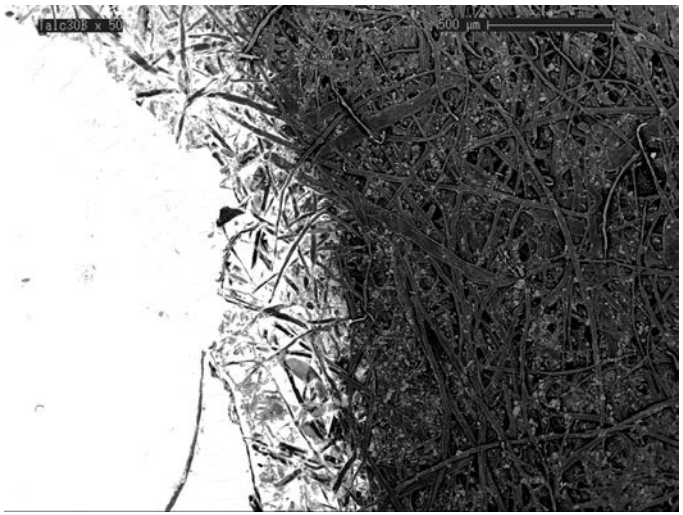

Figure 7.43: *a) Low magnification image of wetting of paper filled with 30% talc.*

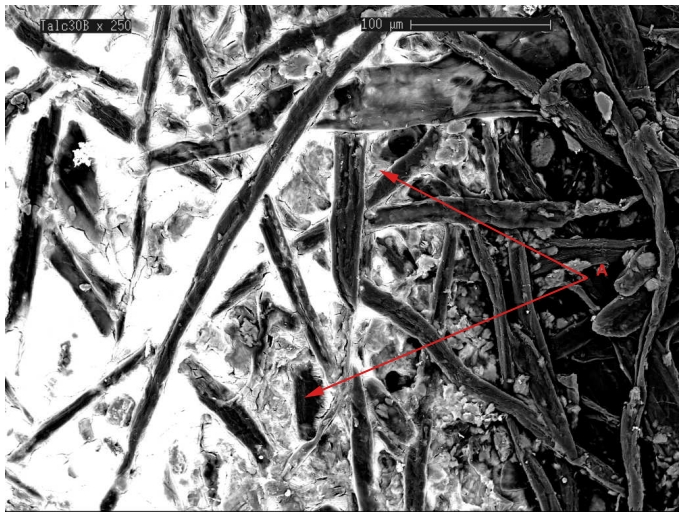

Figure 7.44: *Higher magnification image of a 30% talc filled paper showing the edge of the wetting area.*

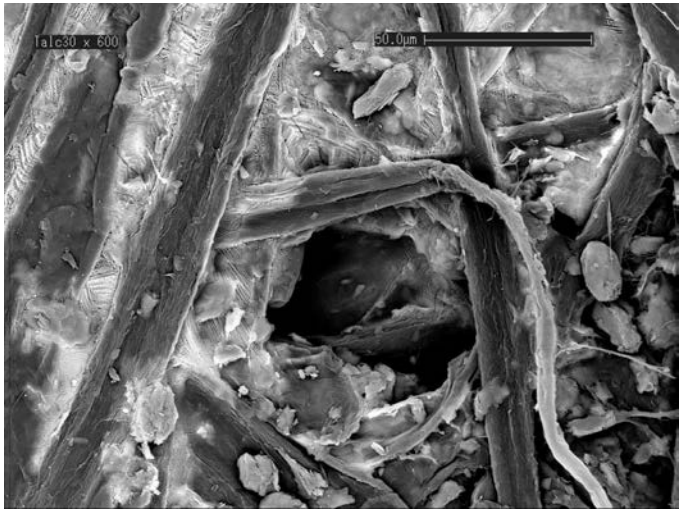

Figure 7.45: *High magnification image of a 30% talc filled paper showing more detail of pore filling.*

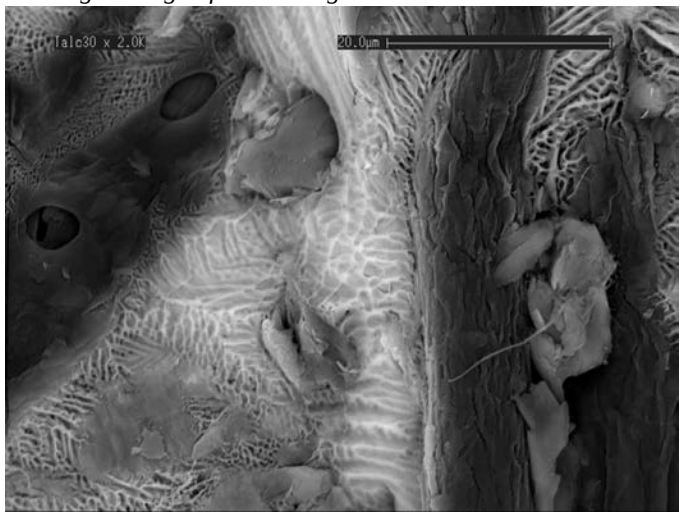

Figure 7.46: *Higher magnification image of a 30% talc filled paper showing more detail of filling of pores. Arrows marked A show the impact of particles of talc on impeding pore filling.*

7.4 Discussion

A number of conclusions can be drawn from the data;

1. Whether a paper is filled or not and irrespective of the type of filler added to the paper, the mechanism of liquid imbibition in paper is by capillary pressure driven films in fibre overlap channels Figures 7.23, 7.30, 7.31, 7.36, 7.40 & 7.44 are examples of both of the filler types and all of the amounts and represent what was observed in all SEM images.

2. The type of filler significantly affected the paper structure. PCC aggregated into clumps heterogeneously distributed throughout the paper and could break up pores (Figure 7.15) Talc was more homogeneously distributed in the paper and was not seen to aggregate in clumps, and was often located around the edges of pores (Figure 7.16). As a result for an equivalent amount of filler, the sizes of pores in a PCC filled paper were considerably smaller than those in papers filled with talc (Table 7.4). In fact the pore morphology of a talc filled paper and an unfilled paper were similar. The distribution of both fillers is demonstrated schematically in Figure 7.17 showing the impact of the two fillers at a pore scale and Figure 7.18 showing the impact on a larger scale.

3. The Lucas-Washburn equation, cannot describe fluid imbibition rates in filled paper. The addition of PCC to paper resulted in smaller pores, but also faster rates than unfilled and talc filled papers (Figures 7.4 & 7.5). The Lucas-Washburn equation would have predicted the opposite.

4. The addition of PCC increased rates of imbibition of water in all directions but particularly in the *z* direction. It also increased the rate of imbibition of isopropanol in the *z* direction. In PCC filled papers most pores behind the wetting front are infilled (Figures 7.39 - 7.42).

5. The addition of talc in papers reduced rates of imbibition of water in the *x & y* directions in paper and had no effect on the rate of imbibition of water in the *z* direction (Figures 7.4 & 7.5).

To explain the observed differences in the fluid penetration results for the talc and PCC-filled papers, the differences in the pore morphology and surface energy characteristics are examined. The increase in rates in the *z* direction due to PCC addition and the filling of the pores behind the fluid front for both water and isopropanol can be both attributed to the change in the pore morphology. Fluid invaded the larger inter-fibre pores because of the tendency of PCC to aggregate into clumps and breakup the larger pores into smaller pores (Figure 7.15). This is further verified by MIP data for PCC filled paper where the mean pore size is 50% that of unfilled paper. These clumps of PCC form a sub-network of small interconnected channels

within the larger inter-fibre pores. These inter-particle channels would be approximately ~ 2 microns in diameter given that the particles themselves are ~ 2 - 3 microns in diameter. These are significantly smaller than the pores formed by the fibre web structure ($\sim$ 50 microns). The resultant capillary pressure for invasion into these smaller porous regions is extremely favourable according to the Laplace equation $P_c = 2\lambda/r$. Thus the capillary pressure in these small voids would be at least one order of magnitude greater than that formed by inter-fibre pores themselves and may compete with the penetration of inter-fibre channels (dependent of course on the local morphology on the channel). This explains the observation that regions rich in PCC are quickly and completely invaded by the wetting fluid (Figures 7.4, 7.41 & 7.42). Smaller pores can then be completely invaded by thickening films (Figure 7.47C).

The tendency for fluid to saturate quickly through a PCC filled sheet in the *z* direction is then explained by considering the effect of this local pore bridging on the potential flow path of the wetting fluid at the scale of the full sheet. For an unfilled sheet, it is well known that the fluid path through the sheet is extremely tortuous due to the strong preferred alignment of fibres in plane (Figure 7.48A). The bridging of the pores by PCC greatly decreases the tortuosity of the flow path in the *z* direction (Figure 7.48C) by connecting inter-fibre channels at different depths in the paper. As PCC loading is increased, the tortuosity further decreases. This is consistent with the data in Figure 7.4. PCC also decreases the tortuosity of the flow path laterally, but due to the fibre alignment the effect is only minimal (Figure 7.5).

The effects of talc on imbibition of water cannot be attributed to pore morphology. Particles of talc were primarily distributed around the edges of pores and did not aggregate in clumps within pores thus there would have been little impact on the resultant pore morphology. Thus there was no opportunity for the formation of sub-networks of potential flow paths in larger pores as was the case with PCC. Therefore the connectivity between different levels of inter-fibre channels would not have been enhanced with the addition of talc. One can see the effect of the distribution of talc on the tortuosity of flow paths for unfilled and talc filled papers are similar. This is shown at a pore scale in Figure 7.47B and on a larger scale in Figure 7.48B. This is consistent with the data in Figure 7.4 showing no increase in imbibition rates in the *z* direction.

There are two potential reasons for this reduction in subsurface flow rate with talc filled papers to have occurred (Figure 7.5). The first is that with increasing levels of talc, the density of fibre in the paper would have been reduced. This would have resulted in a lower density of fibre-overlap channels which could have had an effect on the rate of lateral flow.

The second and most probable cause for this reduction in subsurface imbibition rate with the addition of talc is related to the wettability of the talc particles themselves. It was shown in Figures 7.29, 7.36, 7.38 & 7.46 that the wetting liquid appeared to pin on particles of talc and not wet as effectively as fibres. The flat surface of talc particles are uncharged and are slightly hydrophobic and have a lower surface energy than either cellulose or PCC (Table 7.5). Thus

some particles of talc located in fibre-overlap channels may impede the rate of spreading of films (Figure 7.38 arrow marked A) explaining the reduced rate of subsurface spread of water.

When isopropanol was placed on a solid talc surface, it spread spontaneously with no apparent contact angle. This would explain why in Figure 7.5 there was no change in the rate of subsurface spread of isopropanol in talc filled papers with increasing levels of filler in contrast to the rate of subsurface spread of water reducing.

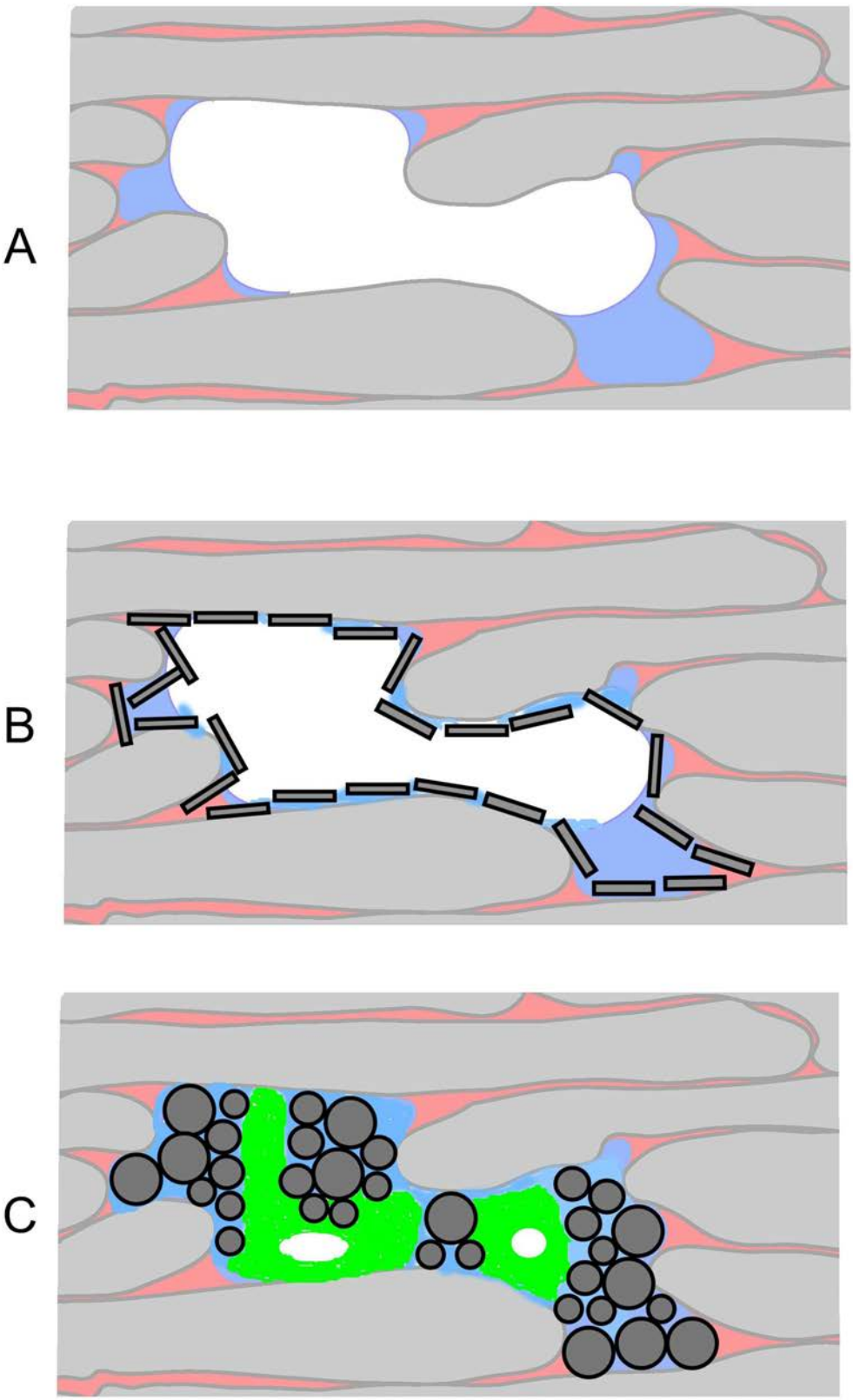

Figure 7.47: *Schematic comparing the effects of different fillers with the infilling of large pores, A: no filler, B: talc and C: PCC. The schematic is of a vertical section through paper.*

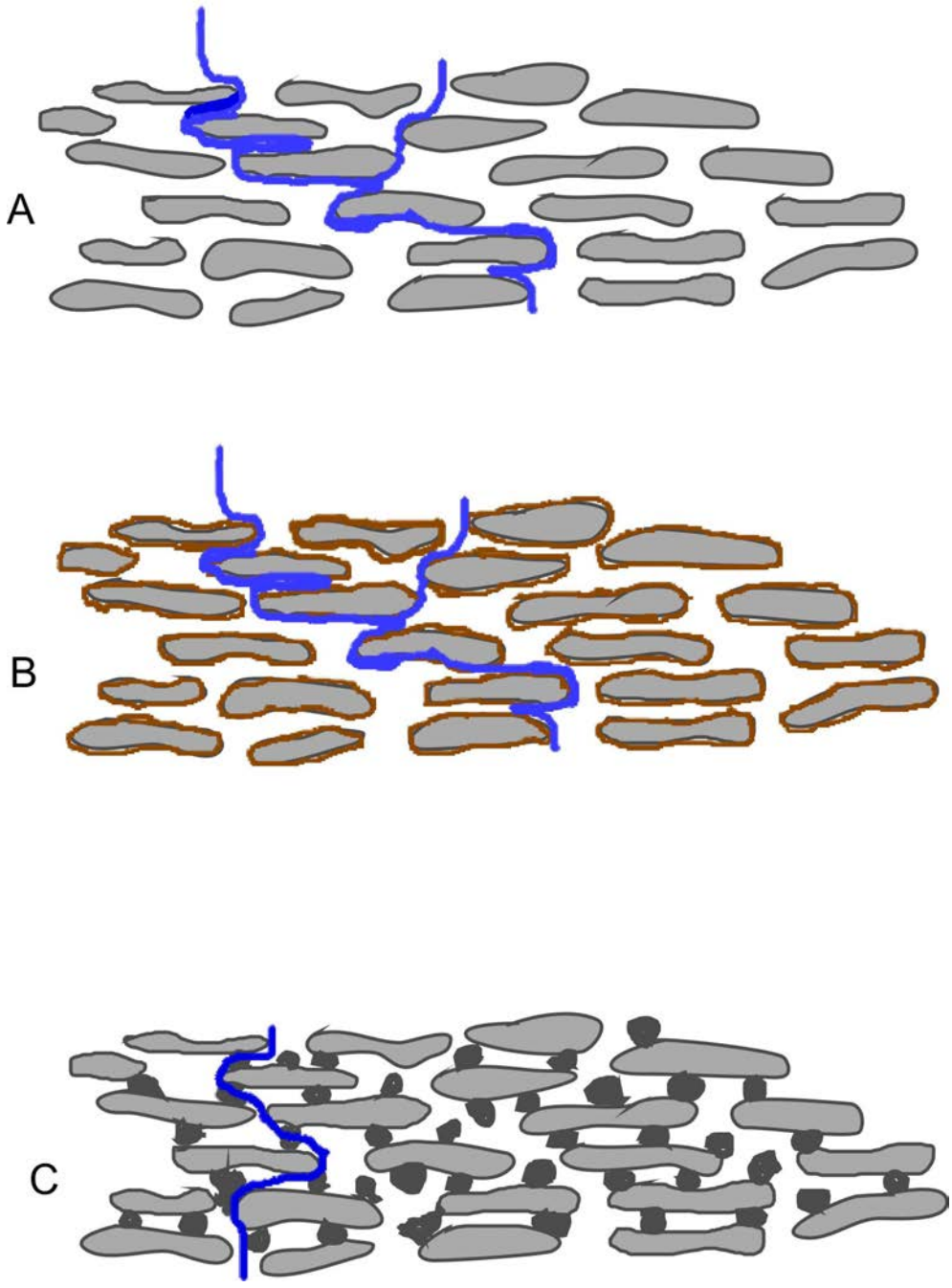

Figure 7.48: *Schematic of potential flow paths of liquid in A) unfilled, B) papers filled with talc and C) papers filled with PCC showing little difference in the tortuosity of flow paths between talc filled and unfilled papers and a significantly reduced tortuosity for PCC filled papers.*

Chapter 8

Discussion on decor papers

This chapter interprets the behaviours of the decor papers tested in Chapters 3 & 4 with the findings of Chapter 5 - 7. In this discussion chapter the initial industrial problem is analysed in terms of the new vision of paper gained.

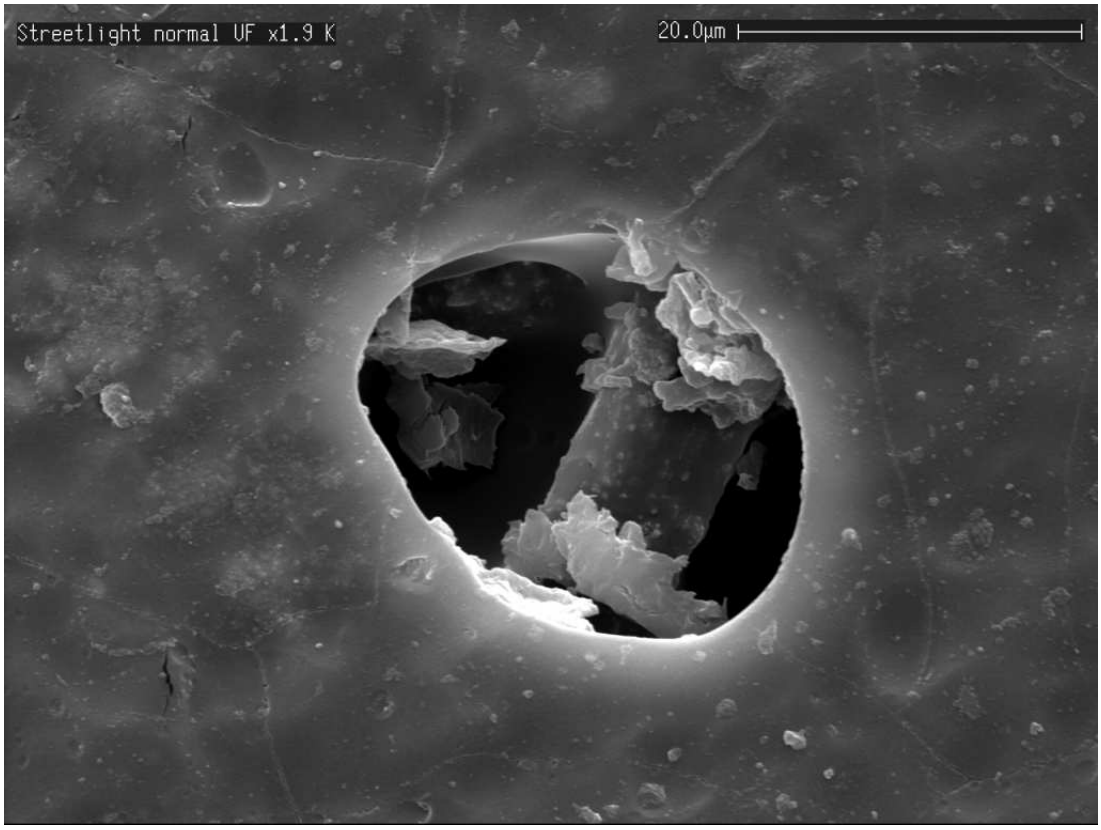

High magnification image of an unfilled pore in Streetlight caused by migration of MF resin away from the surface of the paper. Note unresinated fibre.

8.1 Introduction

From this thesis one now has sufficient understanding to tackle the "paper effect" identified between the different decor papers studied in Chapters 3 & 4. The effect that fillers have on both pore morphology and rate of fluid imbibition in decor papers is summarised here. The fillers used in the decor papers are identified and their effects on pore structure determined. These are then related to the imbibition performance of the decor papers established in Chapter 4, the mechanism of imbibition having been established in Chapter 6. The key is to consider the way film flow is influenced by inter-fibre channels, filler morphology and distribution.

The decor papers were analysed using mercury intrusion porosimetry to determine average pore diameter, visualised using SEM to examine filler distribution and pore morphology, and analysed using EDXA to identify the types of filler used. Fluid imbibition data used was based on the rate of imbibition of diethylene glycol to the point of 50% saturation.

8.2 Structure of decor papers and implications for imbibition

Initially the rate to 50% saturation appears to be related to the average pore diameters of the decor papers (Figure 8.1) *i.e.* the paper with the smallest pore size, Alpine White, saturated fastest and the papers with the largest average pore diameter, Black, Fog and Storm saturated slowest. However, there are some interesting inconsistencies. Folkstone Grey, New England Elm and Streetlight have small average pore diameters, however, they also have relatively slow rates of imbibition to 50% saturation. This reinforces the point made in Chapter 7 that pore size alone is too simplistic in predicting the rate of fluid imbibition.

In Chapter 4 the density of decor papers was found to relate to both the rate of fluid imbibition (Figure 4.42) and the production of defects in pressed LPM panels (Figure 4.8). Density was also very strongly related to the filler content of the decor papers (Figures 4.6). The filled decor papers studied (Kraft being the only unfilled decor paper) were re-examined under high magnification SEM and with EDXA analysis[1] in order to determine the type of fillers in the paper. This showed that all the papers contained TiO_2 except for Black, confirming the findings in Chapter 3 obtained using Raman microscopy. Figures 8.3, 8.5 & 8.9, show that particles of TiO_2 have a spherical or block-like shape and are < 1 μm in size. It has a very high surface energy (90 mJm^{-2}) making it hydrophilic. In addition, EDXA analysis showed that all papers except for Folkstone Grey and Streetlight also contained kaolin (aluminium silicate $Al_2Si_2H_4O_9$) which has a similar surface energy (Yildirim, 2001; Burry and Keller, 2002) to TiO_2, and a plate like structure similar to talc (Figures 8.5 & 8.13). It is proposed that the different amounts of TiO_2 and kaolin,[2] but most importantly their distribution affected rates of

[1] Voillot et al. (1990) also used EDXA and SEM to report on the distribution of fillers and pigments in the *z* direction in paper.

[2] as measured by their filler contents

imbibition (Table 8.1).

Papers that imbibed fastest to 50% saturation (Figure 8.1), Alpine White and Beech had the highest filler contents, 41% and 33% respectively and had very few large open voids on their surfaces (Figures 8.2 & 8.4). These papers also had very small average pore diameters, 0.77 and 1.05 μm respectively. High magnification images of these papers (Figures 8.3 & 8.5) show that the filler is distributed as clumps in pores of the paper. It is believed that the effect of the addition of TiO_2 filler would have been analogous to the addition of PCC to the laboratory papers investigated in Chapter 7, bearing in mind the TiO_2 particles being smaller. The small voids between the particles in the clumps of aggregated TiO_2 would have been readily invaded by the imbibing fluid due to higher capillary pressures, enhancing fluid flow in the *z* direction due to the increased connectivity of inter-fibre channels at different depths in the paper.

Storm was one of the slowest to saturate to 50% (Figure 8.1). This is readily explainable by the large *unfilled* pores, (Storm having the largest average pore diameter 1.63 μm Figure 8.14 & 8.15) and a relatively low amount of filler (22%). This would have resulted in relatively poor connectivity between inter-fibre channels at different depths within the paper, which as shown in Chapter 7 would not enhance fluid flow in the *z* direction.

Two papers had very similar filler contents, Fog; 26% and New England Elm; 29%, however, there was a large difference in the rate of imbibition to 50% saturation (Figure 8.1), with New England Elm saturating faster than Fog. The filler in Fog is primarily located on the fibres and *not* in the inter-fibre pores (Figures 8.8 & 8.9). This explains the larger average pore diameter (1.25 μm). The filler distribution in New England Elm appeared to be more concentrated within the pores and this could result in and a reduction of the average pore diameter (1.03 μm) and more importantly greater connectivity between inter-fibre channels and so explaining the greater rate of imbibition in the *z* direction (Figures 8.12 & 8.13).

Folkstone Grey and Streetlight also had very similar amounts of filler (34 & 35% respectively) and yet had different average pore diameters, (0.86 μm & 1.06 μm respectively). They saturated at different rates, Folkstone Grey being faster (Figure 8.1). Folkstone Grey had fewer larger pores that contained little filler (Figures 8.10, 8.11), than did Streetlight which had a much higher occurrence of large pores that contained little filler (Figures 8.16 & 8.17). Folkstone Grey therefore could have had greater connectivity of inter-fibre channels in the *z* direction than Streetlight. This reinforces the argument of the importance of fillers on pore morphology affecting connectivity of the inter-fibre channel network.

The fact that pore size alone is not a good determinant of rates of imbibition can be illustrated by comparing Streetlight and Beech. They have almost identical filler amounts as well as average pore diameters yet Beech saturated much faster. This is again attributed to the distribution of fillers, in Beech being located in the larger pores (Figures 8.4 & 8.5) and in Streetlight on the fibre surfaces and not in the larger pores (Figures 8.16 & 8.17). It also appears as though Folkstone Grey and Streetlight saturated more slowly due to the absence

of kaolin which is highly wetting. It is interesting to note that even though similarly shaped to talc, it appears to have had the opposite effect on imbibition due to the wettability of the particles.

The identification of film flow in papers, followed by thickening and snap-off which depend on the local geometry of the channels and adjacent void space, enabled the solution of a puzzling result from Chapter 4. There it was shown that some papers initially saturated rapidly to 50% saturation (Figure 4.30) and then slowly to 95% saturation (Figure 4.31), and there appeared no obvious relationship between the two. Papers in this category, Black, New England Elm and Beech had particular morphological characteristics that were different from the other decor papers tested. Black and New England Elm had a wide range of pore diameter distributions caused by the presence of very large voids throughout the paper. As was shown in Chapter 6 the smaller pores would have filled rapidly resulting in rapid saturation to 50%. The larger pores would have filled much more slowly, resulting in the slower saturation rate to 95%. This can also be seen by examining the SEM micrographs of saturating decor papers in Figure 8.18, where it is shown that the papers that were the slowest to saturate to 95% had large unfilled surface and subsurface pores in the fully saturated zone (Black & Storm), compared to those that saturated much faster to 95% saturation (Alpine White, Folkstone Grey and Fog) which had very few.

Beech on the other hand had a similar saturation behaviour, but in this case caused by an entirely different morphological feature. Due to the heterogeneous distribution of filler which was concentrated just below the paper surface (shown in the edge image of the paper in Chapter 3 Figure 3.43), there were quite small pores on and just below the surface which would have filled rapidly explaining the very fast initial rates of saturation to 50%. Toward the centre of the paper, however, the pores were much larger due to the absence of filler *i.e.* pore size varied in the *z* direction as opposed to the larger pores being spread throughout the paper like those described immediately above. These larger pores would have filled much more slowly resulting in a slower rate of imbibition to 95% saturation.

The results relating aspects of paper structure with the addition of filler were very significant as they enable one to determine what factors make a decor paper suitable for resin impregnation and LPM pressing, which was one of the original aims of the thesis. The elimination of larger pores due to the distribution of fillers, which was shown in Chapters 7 & 8 to increase connectivity in the inter-fibre channel network (thus enhancing fluid flow in the *z* direction) is important as rate of fluid imbibition was found in Chapter 4 to be directly related to the generation of LPM defects (*i.e.* open surface voids on pressed LPM). The fillers should aggregate into clumps, and should be hydrophilic and of a shape to enable the close association of filler particles to create higher capillary pressures for imbibing liquids. Therefore the particle shape should be spherical or close to it. The other recommendation made for the manufacture of decor papers, is that calendaring should be totally avoided because this operation

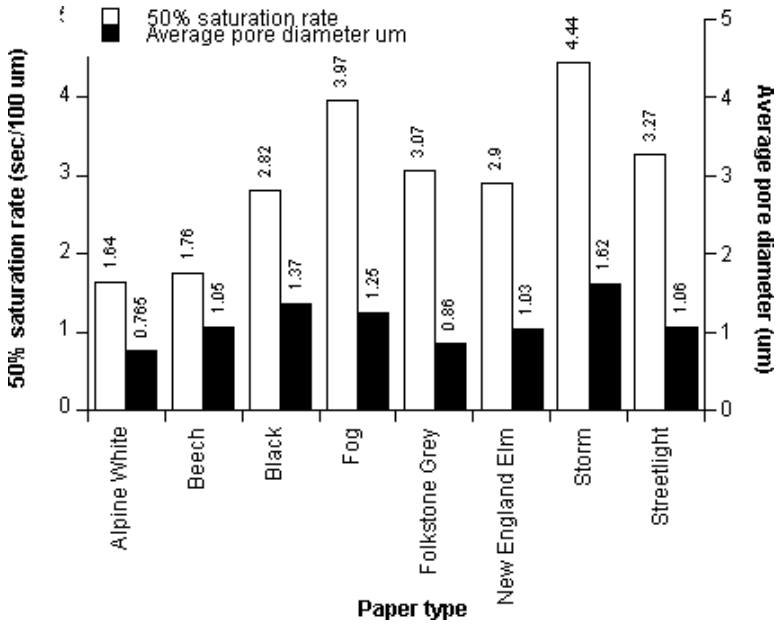

Figure 8.1: *Graphs showing the relationship between average pore diameter determined by mercury intrusion porosimetry and saturation rate to 50%.*

creates smaller pore sizes on the surface of the paper compared to those in the core of paper creating discontinuities which would require external pressures for fluids to penetrate (Lyne, 1976). Ideally the pore sizes should reduce with paper depth which conflicts with Schnieder (1997a) who discussed the advantages of calendering to reduce resin uptake. This is totally refuted and backs up the author's personal experience in an industrial situation where it was shown that these papers are not at all suitable for the production of LPM panels.

Table 8.1*: Filler content of decor papers.*

Paper type	Filler content (%)
Alpine White	41
Beech	33
Black	14
Fog	26
Folkstone Grey	34
New England Elm	29
Storm	22
Streetlight	35

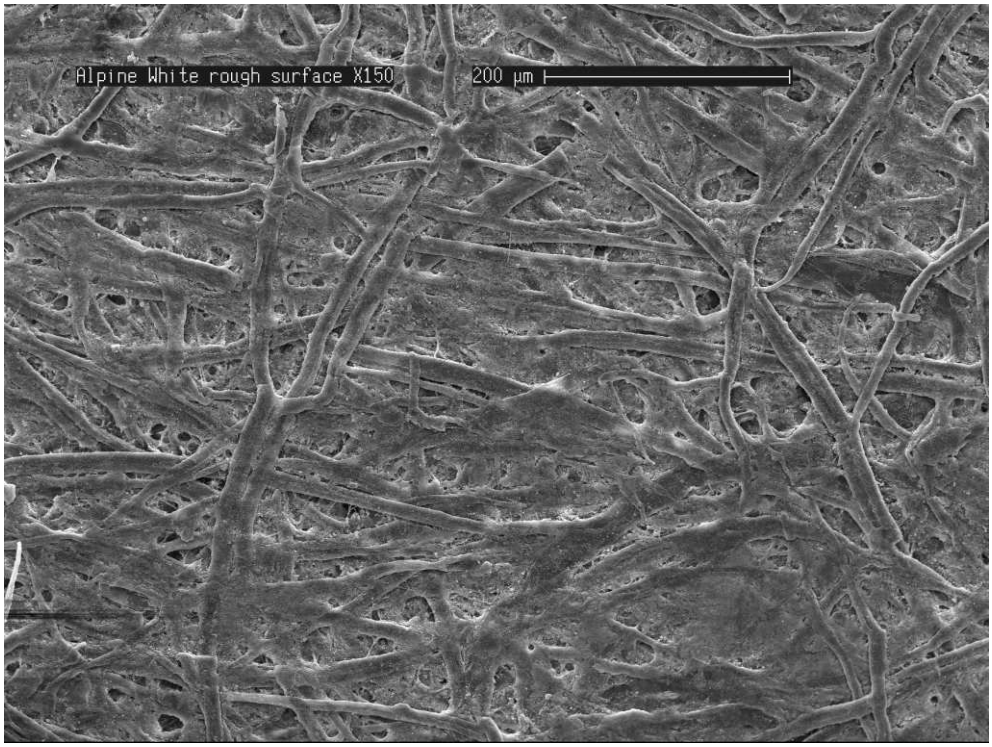

Figure 8.2: *Low magnification SEM image of unresinated Alpine White showing distribution of filler. Note even distribution of pore sizes with no large pores.*

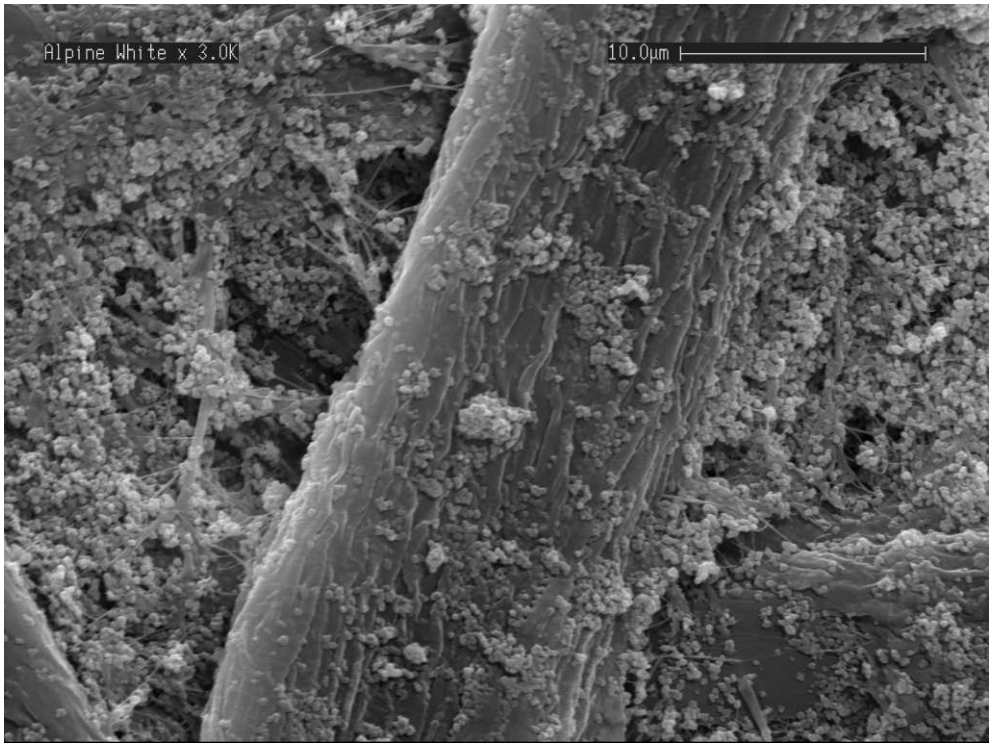

Figure 8.3: *High magnification SEM image of unresinated Alpine White (x 3K) showing filler particles. The particles of filler do not appear clumped.*

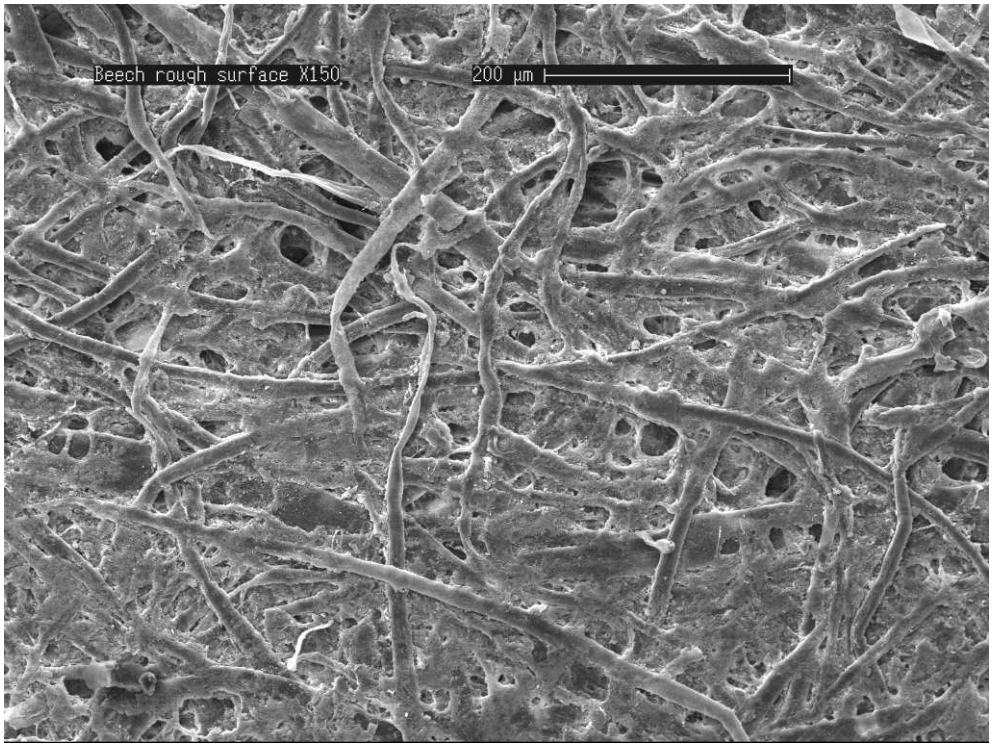

Figure 8.4: *Low magnification SEM images of unresinated Beech showing distribution of filler. Note larger pores.*

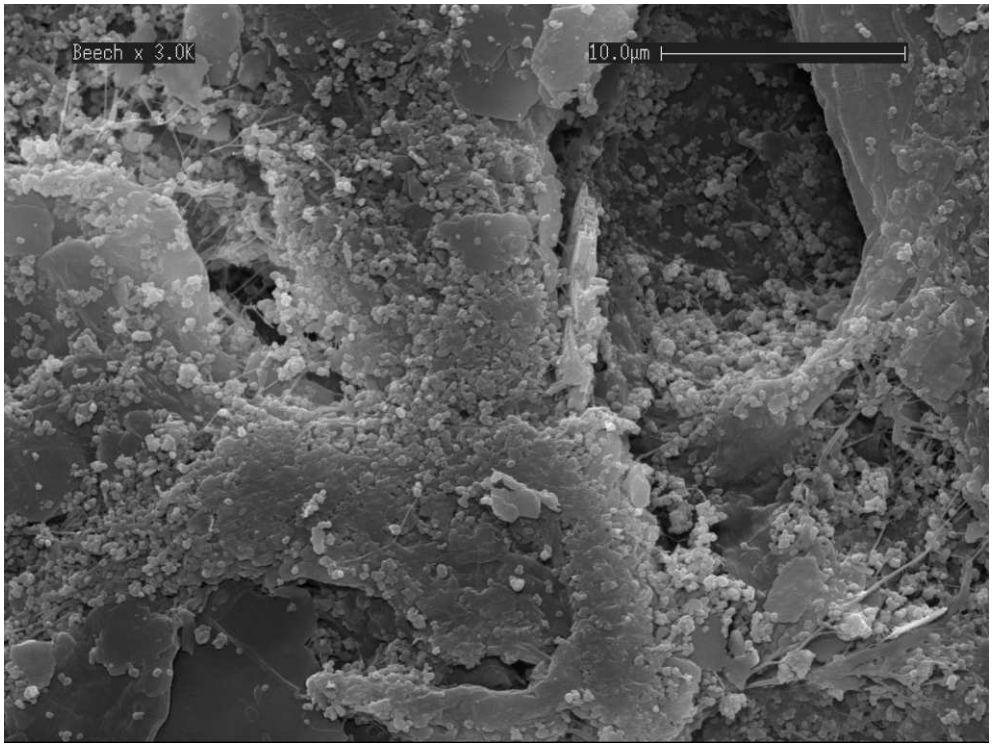

Figure 8.5: *High magnification SEM images of unresinated Beech showing filler particles. The particles appear aggregated on fibre surfaces.*

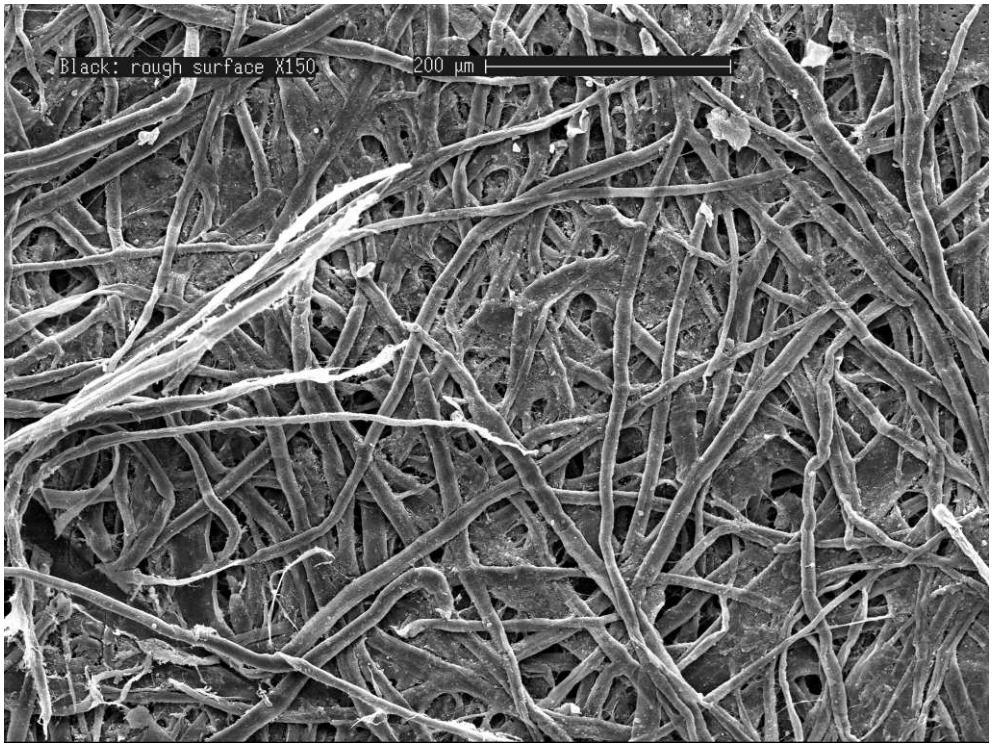

Figure 8.6: *Low magnification SEM images of unresinated Black showing distribution of filler. Note very open structure of the paper with large pores.*

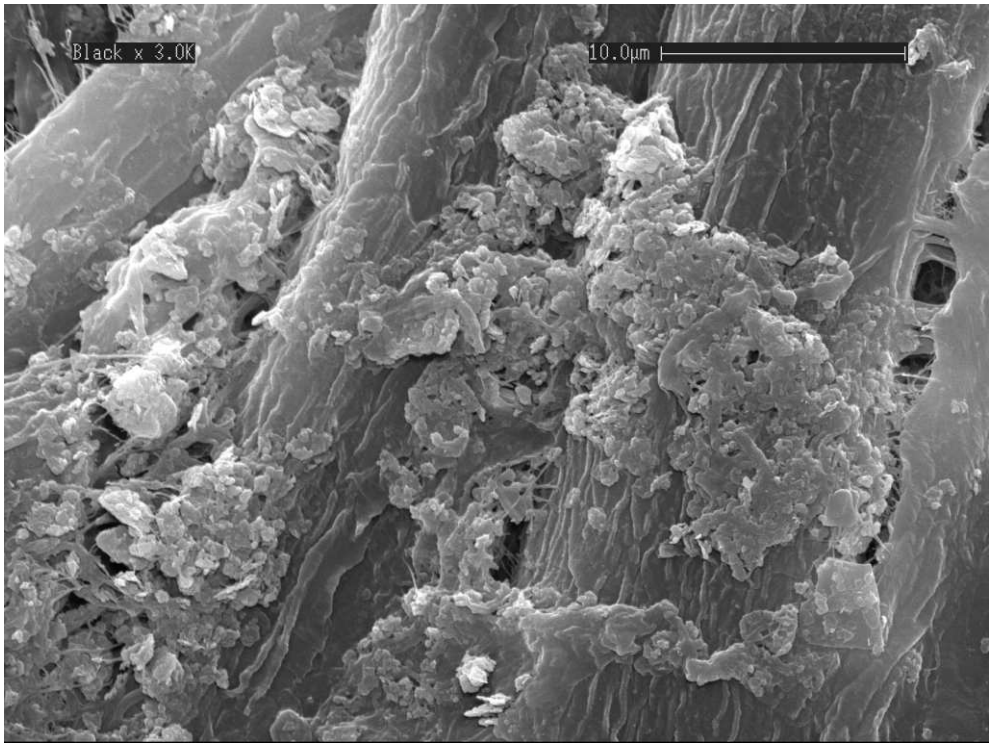

Figure 8.7: *High magnification SEM images of unresinated Black showing filler particles. The particles appear aggregated on fibre surfaces.*

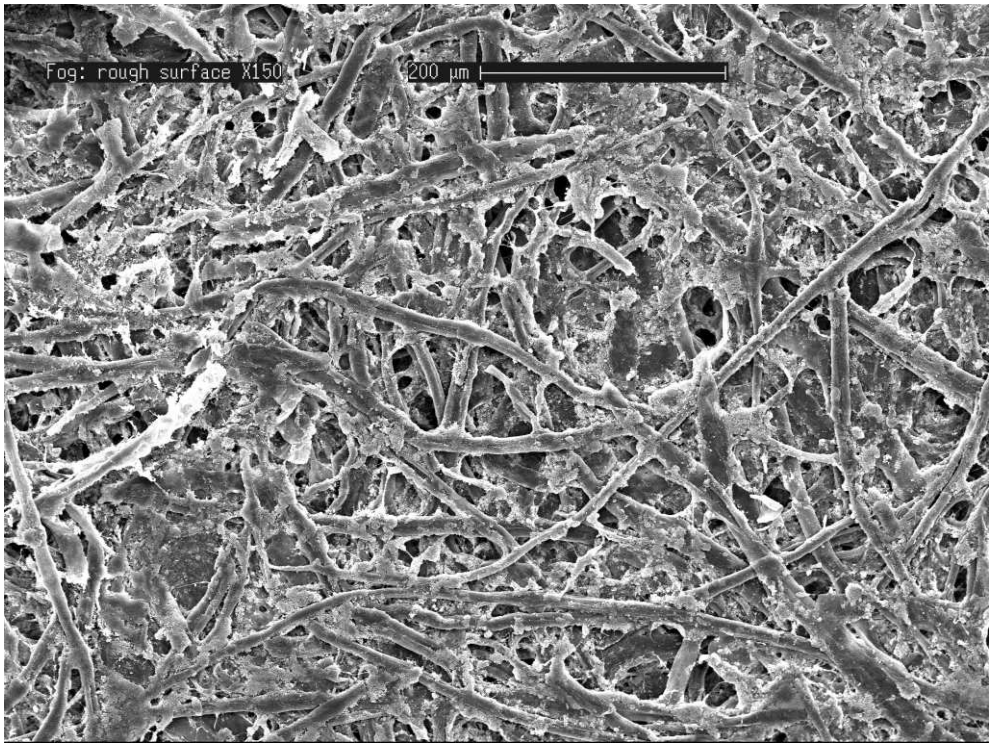

Figure 8.8: *Low magnification SEM images of unresinated Fog showing distribution of filler. Note very heterogeneous distribution of filler and the higher frequency of larger pores.*

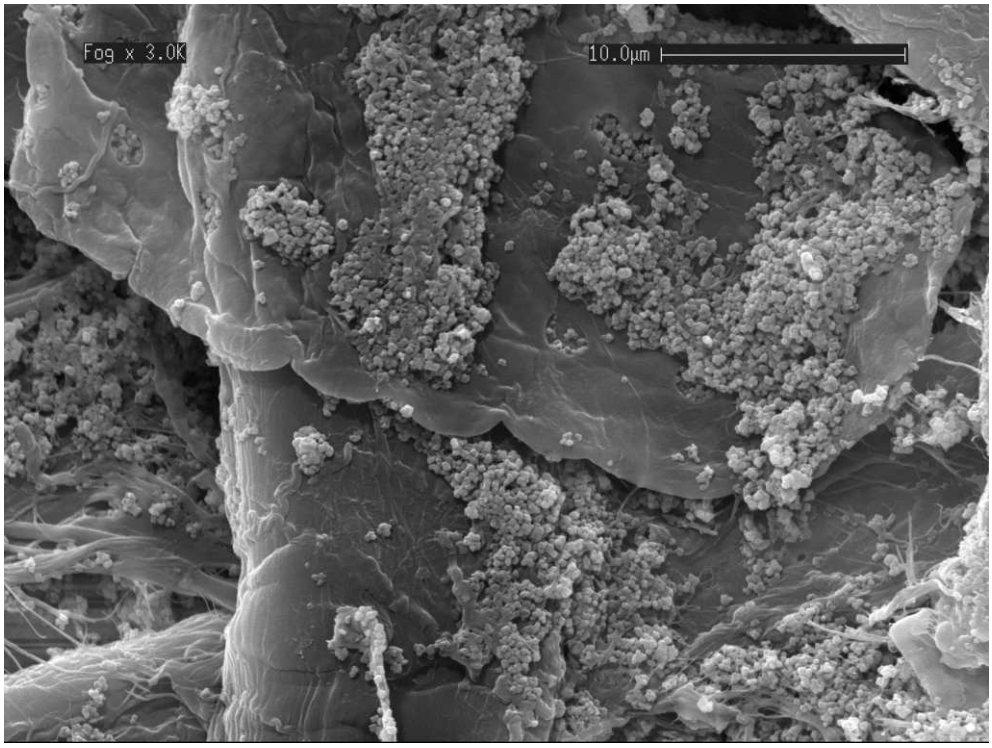

Figure 8.9: *High magnification SEM images of unresinated Fog showing filler particles. Particles appear clumped in the pores.*

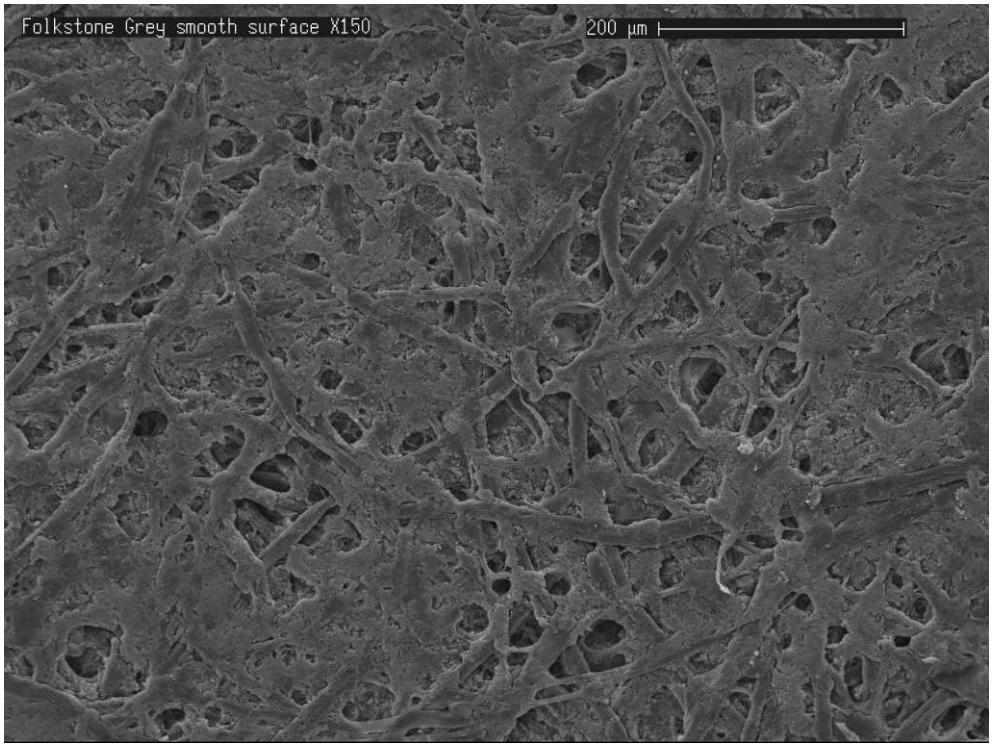

Figure 8.10: *Low magnification SEM images of unresinated Folkstone Grey showing distribution of filler. Note presence of larger pores and concentration of filler near the surface.*

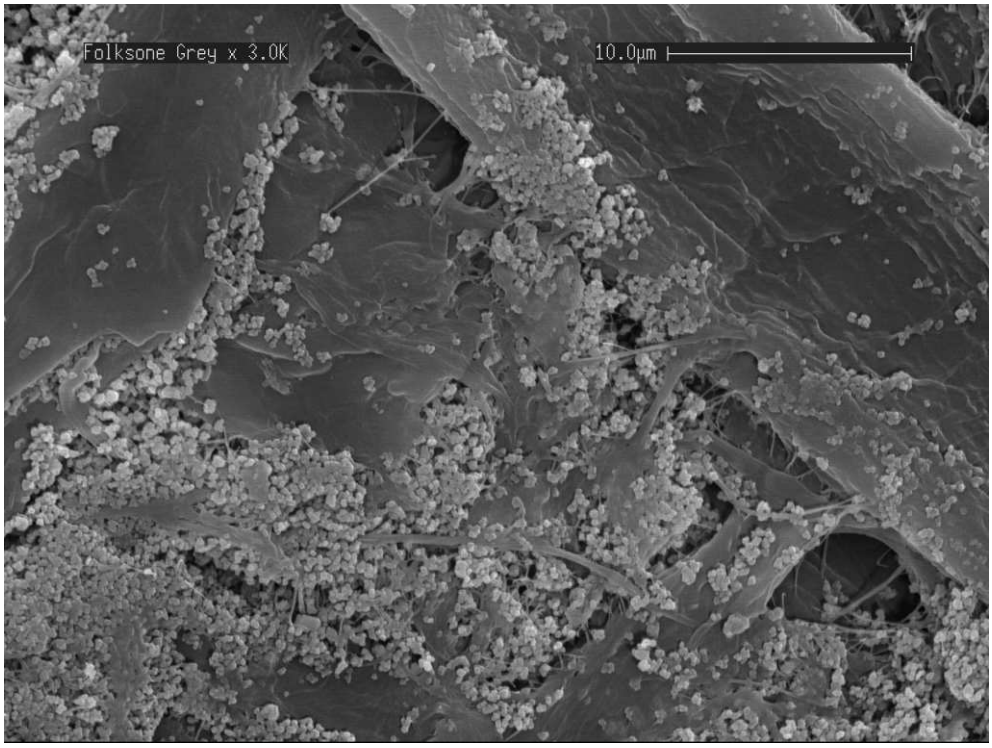

Figure 8.11: *High magnification SEM images of unresinated Folkstone Grey showing filler particles. Particles appear clumped in the pores.*

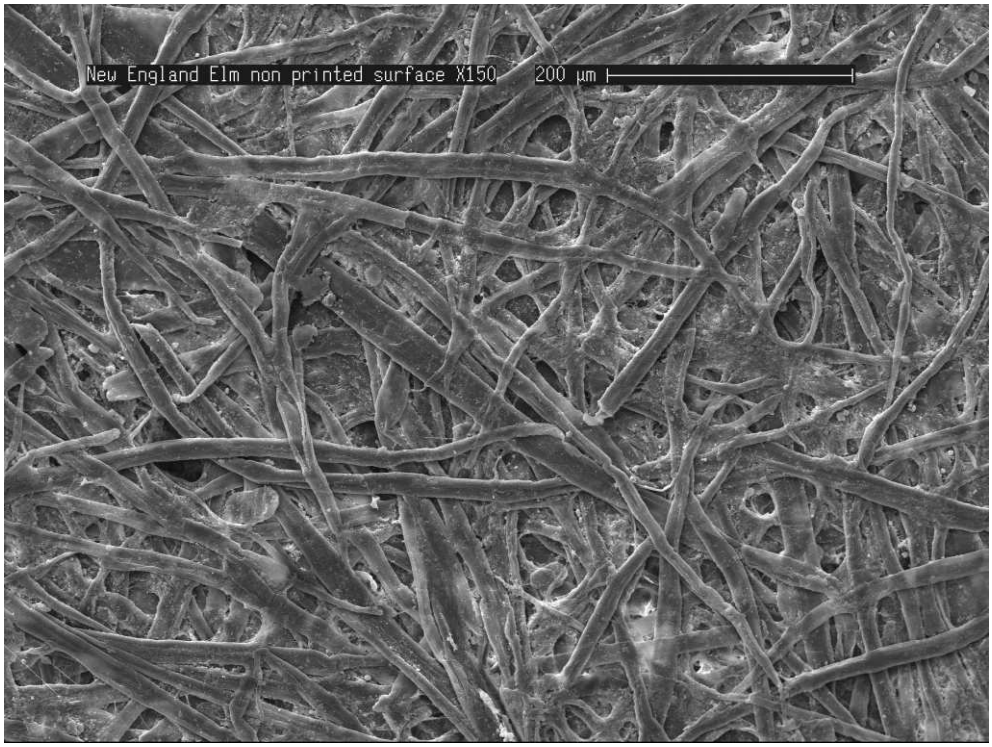

Figure 8.12: *Low magnification SEM images of unresinated New England Elm showing distribution of filler. Note presence of larger pores and concentration of filler near the surface.*

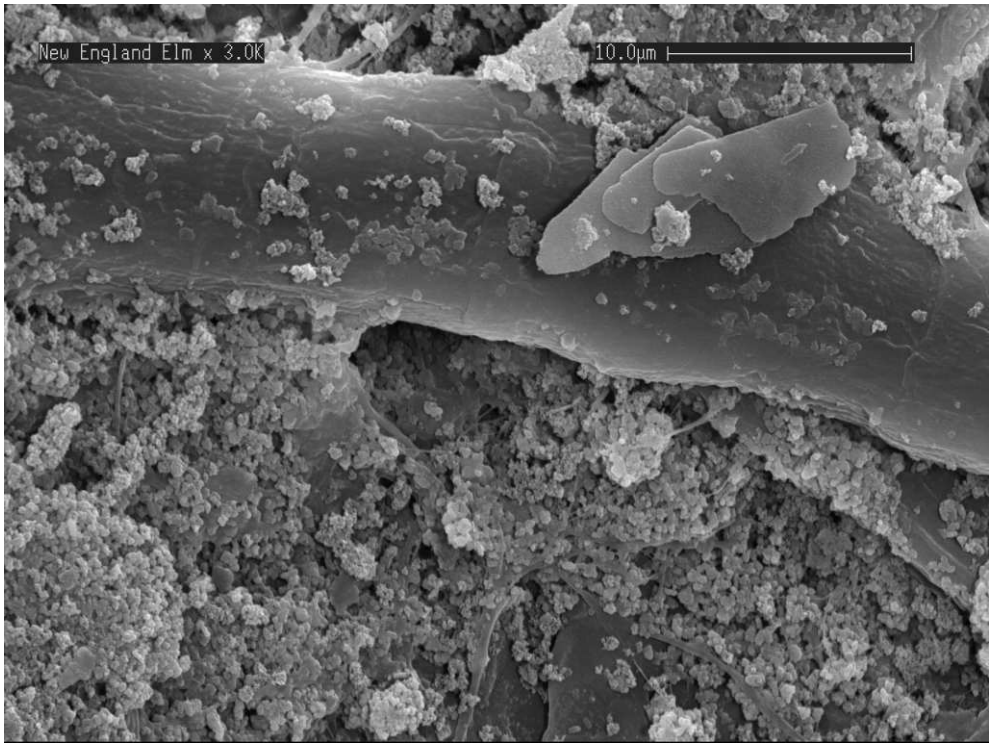

Figure 8.13: *High magnification SEM images of unresinated New England Elm showing filler particles. Note plate-like kaolin particles and concentration of filler particles in pores.*

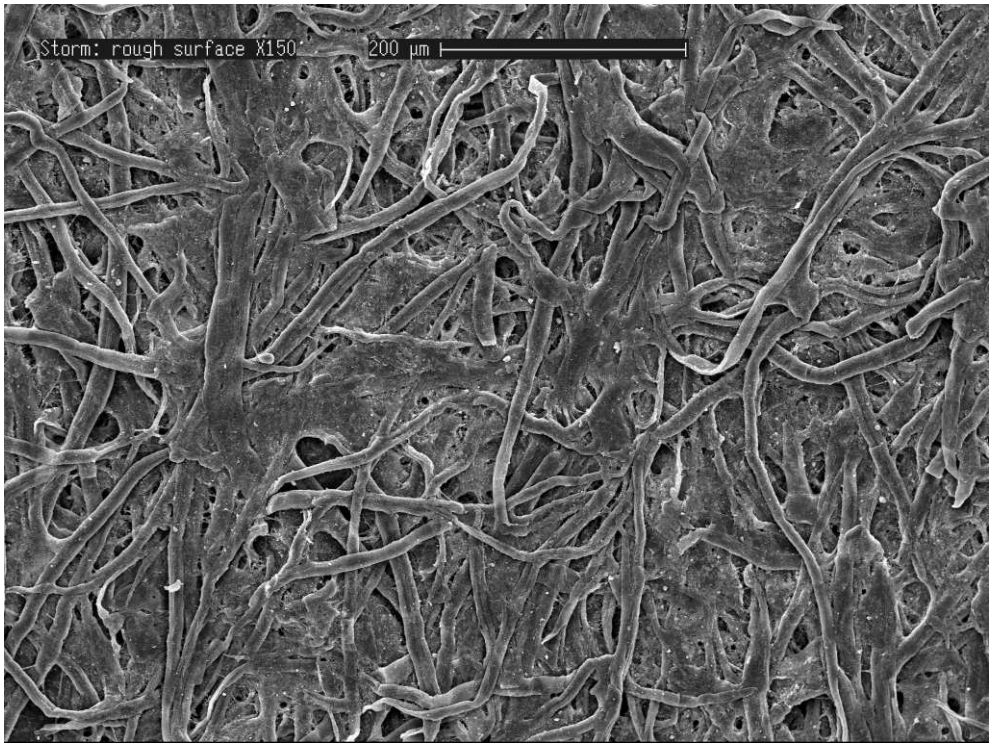

Figure 8.14: *Low magnification SEM images of unresinated Storm showing distribution of filler and the very open structure of the paper.*

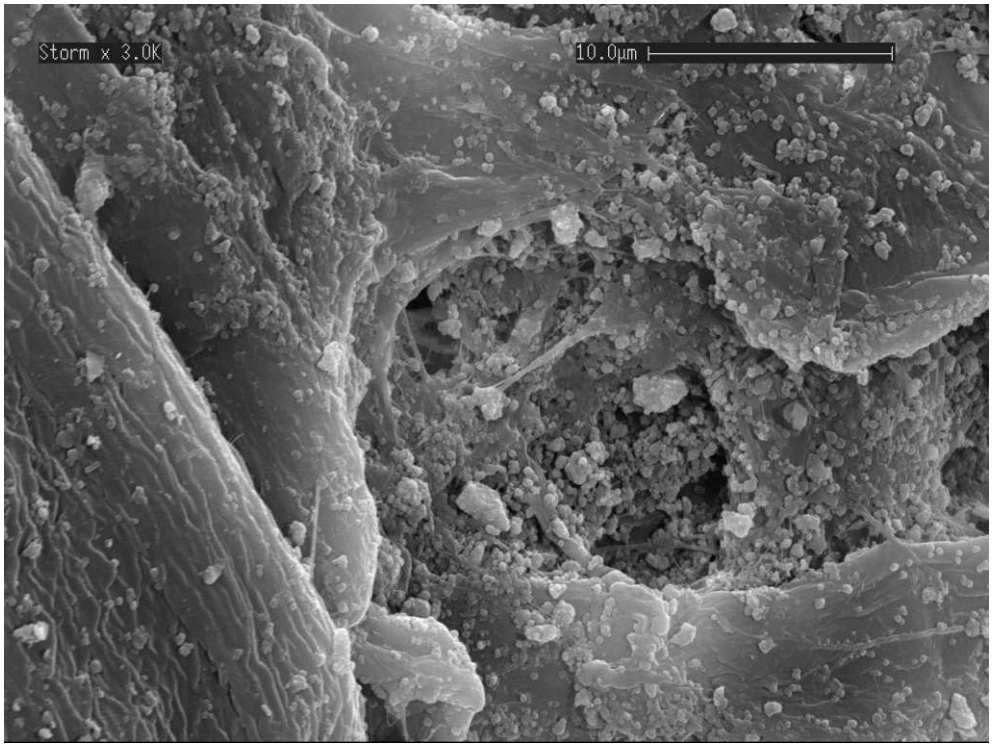

Figure 8.15: *High magnification SEM images of unresinated Storm showing filler particles, which appear heterogeneously distributed.*

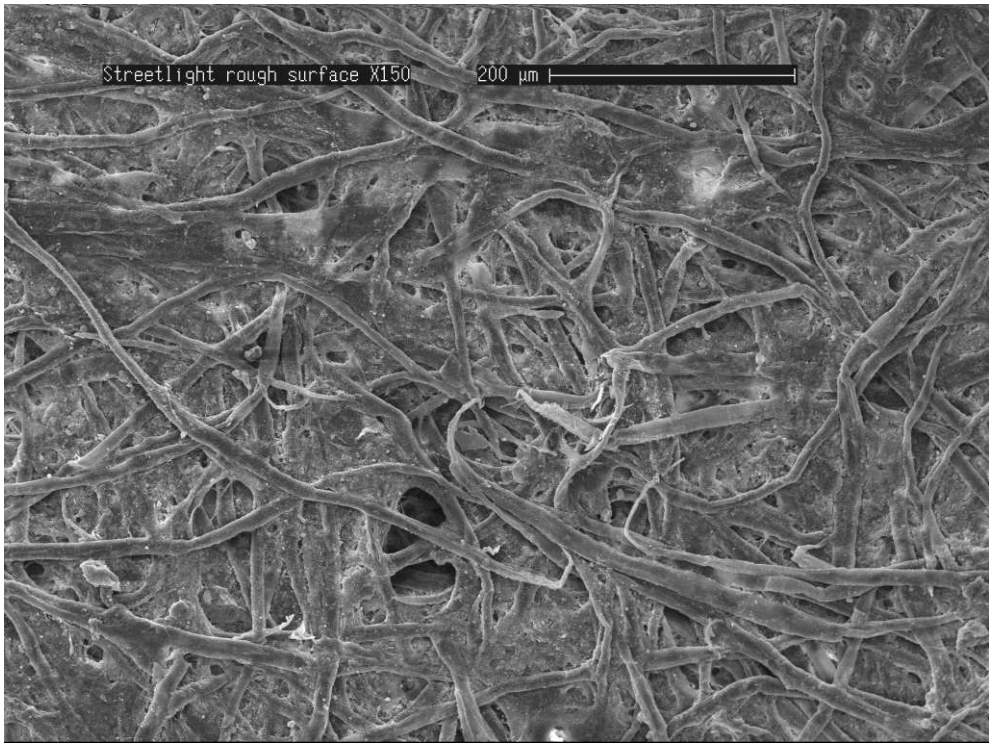

Figure 8.16: *Low magnification SEM images of unresinated Streetlight showing distribution of filler and the presence of very large pores.*

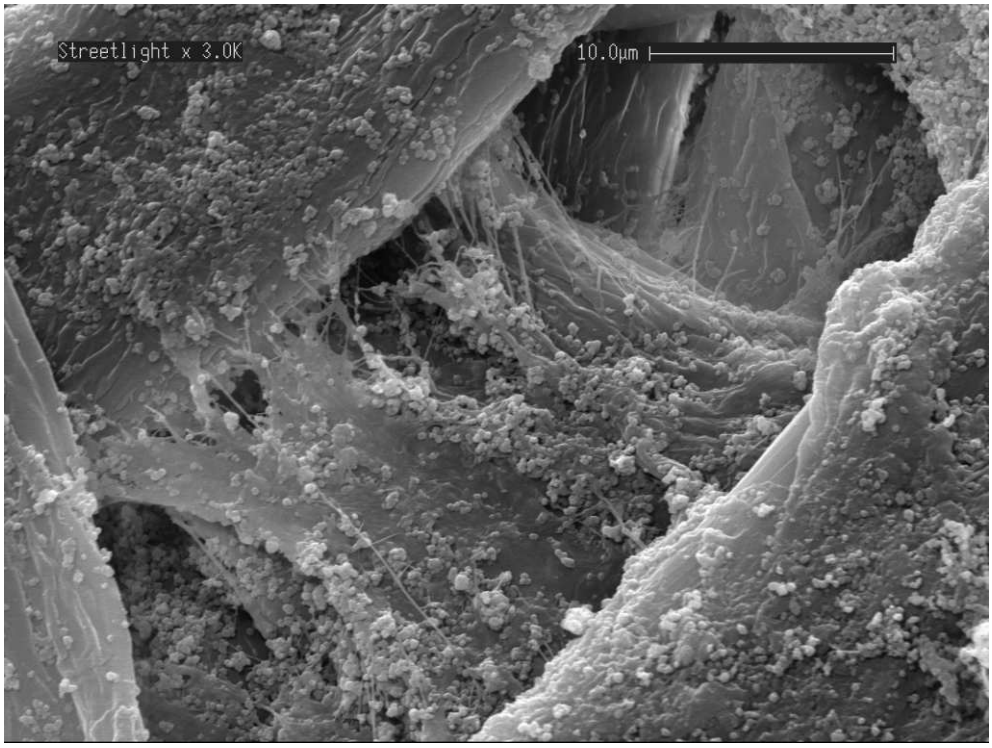

Figure 8.17: *High magnification SEM images of unresinated Streetlight showing filler particles, which appear heterogeneously distributed.*

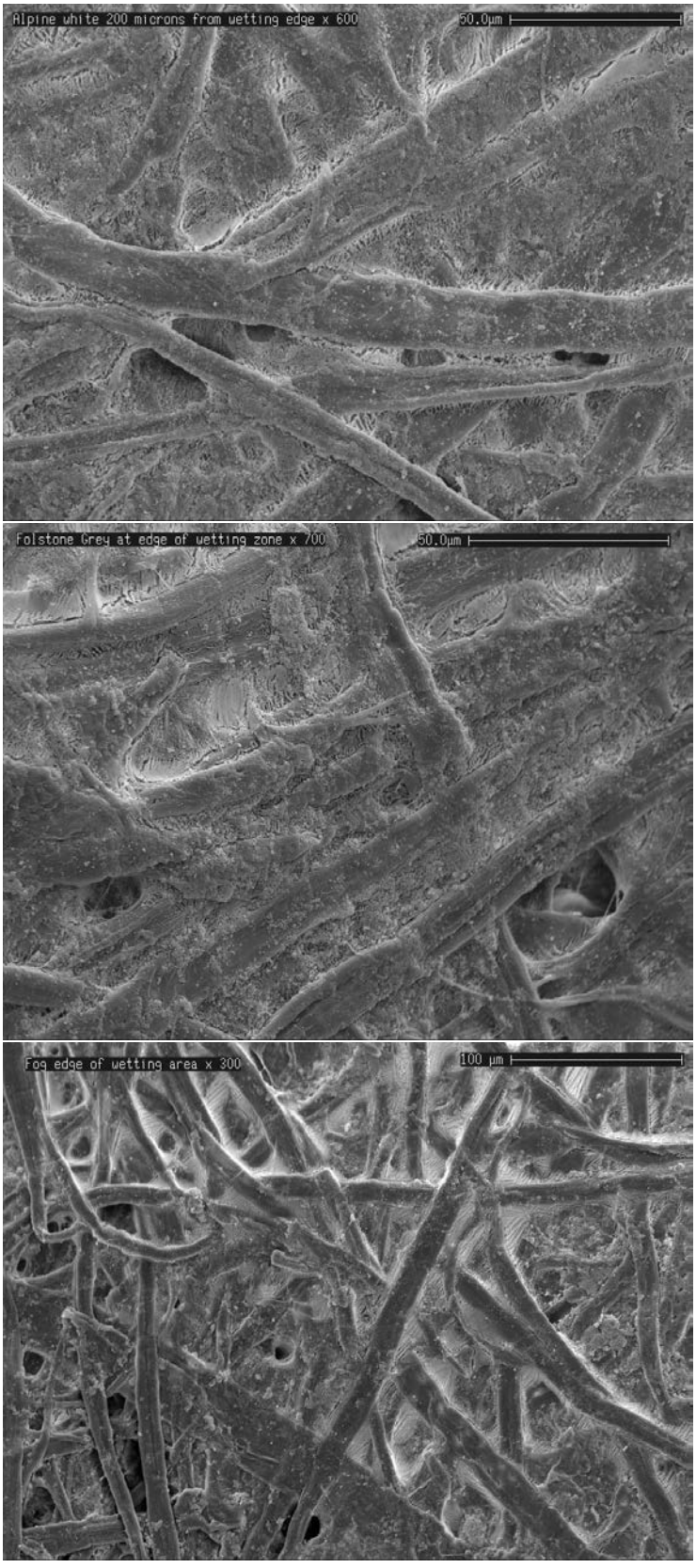

Figure 8.18: *Cryo-SEM images in the saturated zone showing the comparison of papers with no large unfilled voids: from top-bottom; Alpine White, Folkstone Grey, and Fog.*

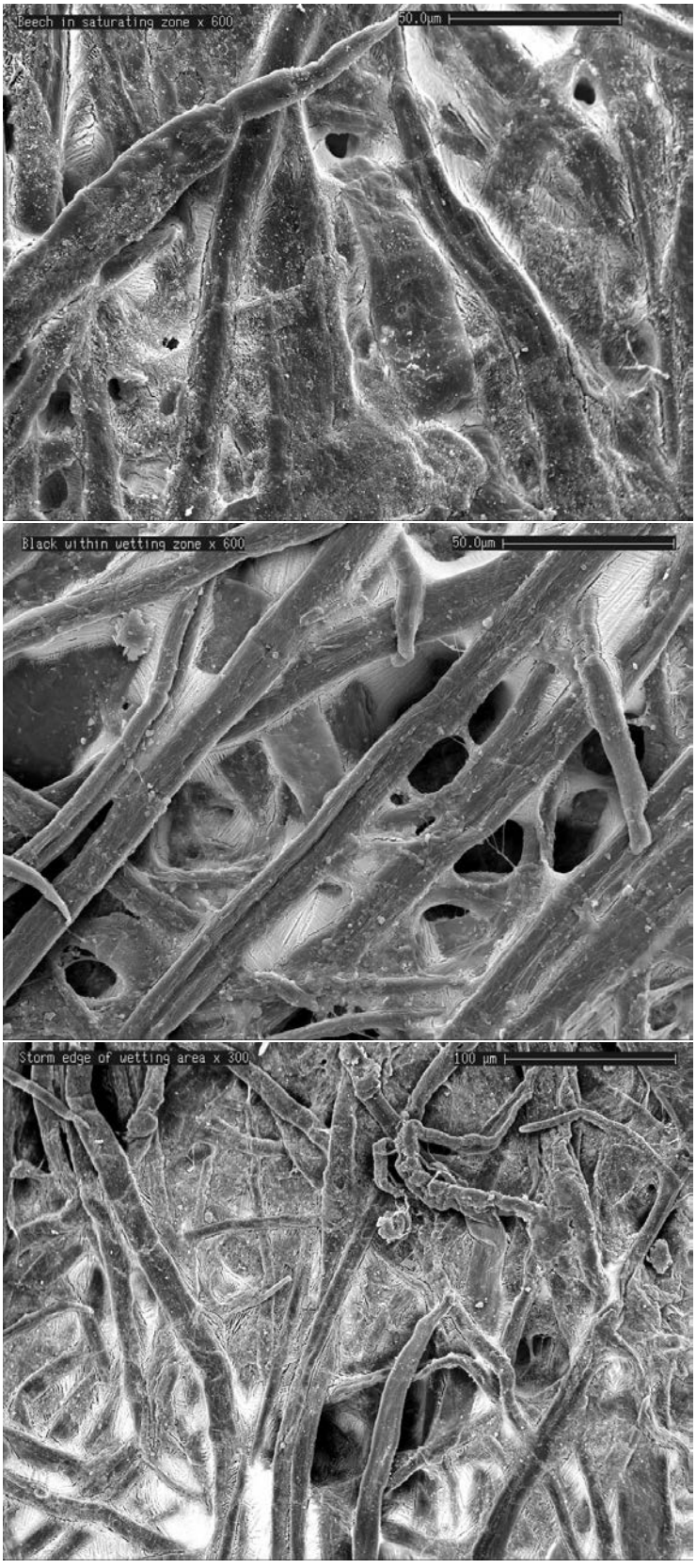

Figure 8.19: *Cryo-SEM images in the saturated zone showing the comparison of papers with large unfilled voids: from top-bottom; Beech, Black, and Storm. These papers had the slowest rates of imbibition to 95% saturation.*

8.3 Conclusion

The “paper effect” determined in Chapters 3 & 4 appeared to be most closely linked to the distribution of fillers within decor papers. While filler content and average pore diameter can in some cases relate to rate of fluid imbibition, it is the distribution of the filler, the affect pore morphology and consequently the connectivity of the inter-fibre channel network that is the key factor in determining rates of fluid imbibition in decor papers.

Chapter 9

Conclusions

This Chapter discusses the main findings of the thesis in relation to the aims and introduces areas of future research.

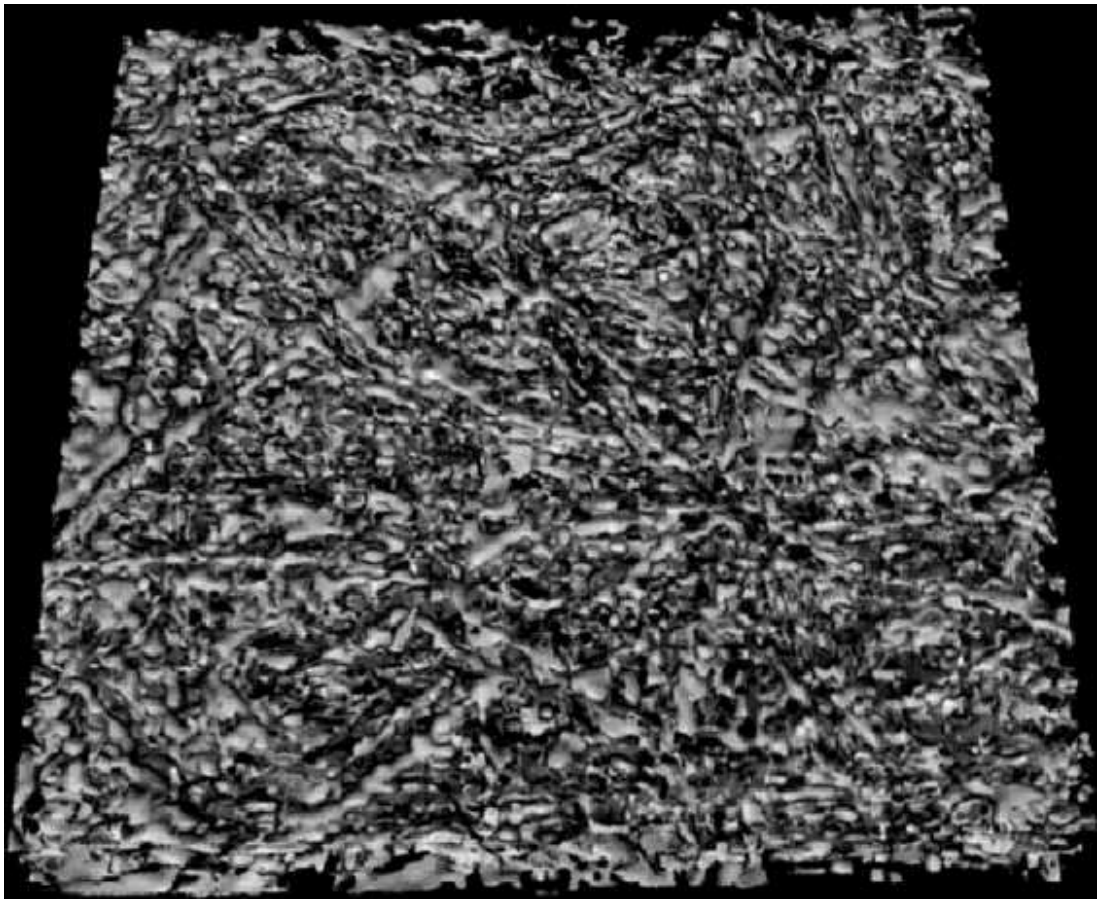

Reconstructed image obtained using x-ray micro computed tomography showing the void space of an unfilled laboratory paper. The image is of mercury intruded into paper after undergoing mercury intrusion porosimetry.

The project had its genesis in an industrial process problem that was costing the author's company millions of dollars each year in lost revenue, namely the production of defects in LPM. In trying to solve the problem locally, help was sought from suppliers of the decor paper, resins and even the equipment suppliers themselves. As this proved fruitless an extensive literature search was undertaken with the result that there was little information available on how to solve the problem or even the exact nature of the problem.

Through research in this thesis, the nature of the problem was identified, and also its causes, these being related to two fluid flow issues of the resins used in the impregnation of decor papers. Insufficient flow of the saturating urea formaldehyde resins resulting in unfilled voids in the centre of the paper followed by excessive flow of the melamine formaldehyde resins into these unfilled pores in the centre of the paper leading to unfilled voids on the surface of the pressed papers.

This then led to the bulk of the research in the thesis, that being to identify the kinetics of fluid flow in paper, a topic that has been studied for decades. By far the majority of this research has revolved around the Lucas-Washburn (Lucas, 1918; Washburn, 1921) equation where the mechanism of fluid imbibition is by bulk meniscus flow through the pores in paper and where surface tension drives flow. The pores were described as being equivalent to cylindrical capillaries with an average size in order for the model to work. This of course is far from the reality of the geometrical complexity of paper. The Lucas-Washburn model would thus predict a greater rate of flow in larger pores and that these as a result would fill first (Windle et al., 1970). However, it was demonstrated in this thesis that the initial rapid liquid penetration in paper described by Napier (1964) was actually filling of the smallest pores first. The research in this thesis also refuted the fundamental assumption of the Lucas-Washburn model, that of bulk meniscus flow, by demonstrating that in fact fluid imbibition in paper is dominated by capillary pressure driven film flow through channels formed by overlapping fibres. These channels form a dense and connected network and as such provide preferential pathways for fluid flow throughout the paper.

As part of the research in this thesis insights have been gained into the mechanisms of flow in certain internally sized papers which has led to the refuting of a long held belief that flow *within* fibres occurs in fibre lumens in the form of bulk meniscus flow. In fact flow was found to occur in the walls of fibres.

Previously, it had been believed that the primary purpose of the addition of fillers to paper was only to increase the opacity of the paper (Biermann, 1996; Phipps, 2001). However, it was also demonstrated in this thesis that the addition of fillers had an effect on the morphology of the pores in paper as well as on the rate of fluid imbibition into paper. It was found they have no effect on the *mechanism* of fluid flow, but dependent on filler type, had an effect on firstly, the degree to which the inter-fibre channels were connected and as a consequence, on the *rate* of film flow in these channels. The mechanism of flow was still dominated by capillary

pressure driven films. The research on the effect of fillers also led to an understanding of the behaviours of the decor papers studied earlier in the thesis.

Therefore as a result of the research conducted for this thesis, we now have a greater understanding of the kinetics of fluid flow in paper and this has ramifications for fundamental research on the physics of fluid flow in porous media in general. We also now know exactly what happens in that first half a second in the impregnation process of decor papers that previously was unknown and now understand what makes an effective saturating decor paper and conversely what it is that makes one less effective. Research from this thesis has relevance for most areas of paper use, *i.e.* printing, personal products, packaging, and barrier type products such as food containers given that most uses of paper involve some interaction with a liquid.

Using the techniques described in this thesis it would be possible to study the imbibition of complex fluids (including resins and inks) into paper. The use of the X-ray micro-computed tomography (CT) apparatus developed in the laboratory at Applied Mathematics would be an invaluable tool in this research. The following image, reconstructed from the x-ray micro CT acquisitions involving saturating papers, shows the potential of the technique for future research (Figure 9.1).

An example of serial tomographic sections of dry paper is attached as *PCC75A coronal.mpg* and a rendered simulated 3D movie of laboratory paper is attached as the file *paper.avi*.

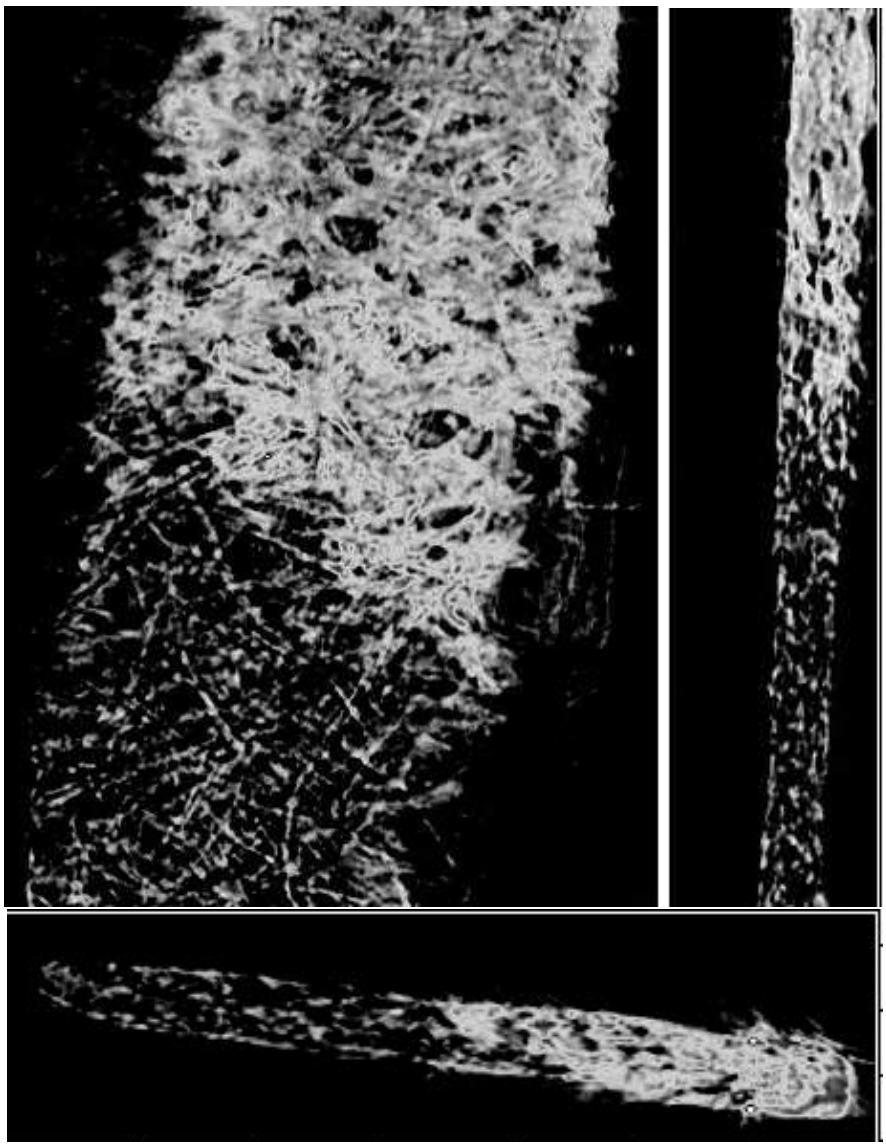

Figure 9.1: *Images reconstructed from the x-ray micro CT of wetting an unfilled laboratory paper with 1-eicosene doped with OsO_4 showing trapping of air in the saturated zone as well as liquid in the form of films in unfilled saturating kraft paper, confirming what was seen in Chapter 6 using CLSM. The brighter areas in the image show the distribution of the liquid. The left image is the coronal section, the right image is the sagital section and the bottom image is the transverse section of the same sample. Note the filled paper has less trapping than the unfilled paper.*

Bibliography

Adam, W. and Kamutski, W. (1993). *Kunstoffe Plastics*, volume 83/10. Hanser Publishers, Munich.

Adamson, A. (1960). *Physical Chemistry of Surfaces*. Interscience Publishers, Inc., New York.

Arledter, H. (1957). Factors influencing the oil and resin solutions penetration rate, absorbency and the resin pickup of absorbent papers. *Tappi J*, 40(7):513–519.

Aspler, J. (1993). Interactions of ink and water with the paper surface in printing. *Nordic Pulp and Paper Journal*, 8(1):68–74.

Aspler, J., Davis, S., and Lyne, M. (1984). The dynamic wettability of paper: Part I. the effect of surfactants, alum and ph on self sizing. *Tappi J.*, 67(9):138–131.

Aspler, J., De Grace, J., Beland, M., Maine, C., and Piquard, L. (1993). Transfer and setting of water based ink. Part II: pH, water absorbency and uncoated paper structure. *Journal of Pulp and Paper Science*, 19(5):J203–J207.

Aspler, J. and Lyne, M. (1984). The dynamic wettability of paper: Part II. influence of surfactant type on improved wettability of newsprint. *Tappi J.*, 67(10):96–99.

Bico, J. and Quere, D. (2003). Precursors of impregnation. *Europhysics Letters*, 61(3):348–353.

Biermann, C. (1996). *Handbook of pulping and papermaking second edition*. Academic Press San Diego, 2nd edition.

Blunt, M. (1997). Effects of heterogeneity and wetting on relative permeability using pore level modeling. *Society of Petroleum Engineers Journal.*, (2):70–87.

Blunt, M., King, M., and Scher, H. (1992). Simulation and theory of two-phase flow in porous media. *Physical Review A*, 46(12):7680–7699.

Bottin, M., Schreiber, H., Klemberg-Sapieha, J., and Wertheimer, M. (1984). Modification of paper surface properties by microwave plasmas. *Journal of Applied Polymer Science: Applied Polymer Symposium*, (38):193–200.

Brecht, W. (1962). *Formation and Structure of Paper*, volume 1. Technical Section of the British Paper and Board Makers Association London ed. Bolam, F.

Bristow, J. (1961). Factors influencing the gluing of paper and board. *Svensk Papperstidning*, 64(21):775–796.

Bristow, J. (1986a). *Paper Structure and Properties: International fiber Science and Technology Series No 8 ed. Bristow, J.A. and Kolseth, P*. Marcel Dekker inc. New York.

Bristow, J. A. (1967). Liquid absorption into paper during short time intervals. *Svensk Papperstidning*, 70(19):623–629.

Bristow, J. A. (1968). The absorption of water by sized papers. *Svensk Papperstidning*, 71(2):33–39.

Bristow, J. A. (1971). The swelling of paper during the sorption of aqueous liquids. *Svensk Papperstidning*, 74(20):645–652.

Bristow, J. A. (1986b). *Paper Structure and Properties: International fiber Science and Technology ed. Bristow, J.A. and Kolseth, P.* 8. Marcel Dekker inc. New York.

Brown, P. and Swanson, J. (1971). Wetting properties of cellulose treated in a corona discharge. *Tappi. J.*, 54(12):2012–2018.

Buchanan, J. and Lindsay, R. (1962). *Formation and Structure of Paper*, volume 1. Technical Section of the British Paper and Board Makers Association London ed. Bolam, F.

Burry, W. and Keller, S. (2002). Effects of dehydration on the apolar surface energetics of inorganic paper fillers. *Journal of Chromatography A.*, 972(2):241–251.

Capitani, D., Proietti, N., Ziarelli, F., and Segre, A. L. (2002). NMR study of water-filled pores in one of the most widely used polymeric material: The paper. *Macromolecules,*, (35):5536–5543.

Carlson, G., Strom, G., and Annergren, G. (1995). Water sorption and surface composition of untreated or oxygen plasma-treated chemical pulps. *Nordic Pulp and Paper Research Journal No. 1*, 10(1):17–23.

Centonze, V. and Pawley, J. (1995). *Handbook of biological confocal microscopy*, chapter 36, pages 549–567. Plenum Press New York, 2nd edition.

Chan Tang, T. W. and Bosisio, R. G. (1980). Enhanced wettability of cellulose strips treated in a microwave plasma. *Tappi J.*, 63(3):111–113.

Chen, K. and Scriven, L. (1990). Liquid penetration into a deformable porous substrate. *Tappi J.*, 73(1):151–161.

Chen, X., Kornev, K., Kamath, Y., and Neimark, A. (2001). The kinetics of wicking of liquid droplets into yarns. *Textile Research J.*, 71(10):862–869.

Climpson, N. and Taylor, J. (1976). Pore size distributions and optical scattering coefficients of clay structures. *Tappi 59 (7)*, 59(7):89–92.

Cobb, R. M. and Lowe, D. V. (1934). A sizing test and sizing theory. *Paper Trade J.*, 98(12):43.

Cramm, R. and Bibee, D. (1982). The theory and practice of corona treatment for improving adhesion. *Tappi J.*, 65(8):75–78.

Cussons, T. (1997). The penetration of paper by resins; II the characterisation of resins and papers. Internal report Borden Chemicals.

Cutshall, K. (1990). The nature of paper variation. *Tappi J.*, 73(6):81–90.

Danino, D. and Marmur, A. (1994). Radial capillary penetration into paper: limited and unlimited liquid reservoirs. *Journal of Colloid and Interface Science*, 166:245–250.

Davis, P. and Smith, D. (1989). Using NMR spectroscopy to analyze the pore structure of coatings. *Tappi J.*, 72(5):85–89.

Denk, W., Piston, D., and Webb, W. (1995). *Handbook of biological confocal microscopy*. Plenum Press New York, 2 edition.

Denk, W., Strickler, J., and Web, W. (1989). Two photon laser microscopy. US Patents and Trademarks Office no. 5,034,613.

Dickson, A. (2000a). The quantitative microscopic analysis of paper cross-sections. *Appita Journal*, 53(4):292–295.

Dickson, A. (2000b). The quantitative microscopic analysis of paper cross-sections: sample preparation effects. *Appita Journal*, 53(5):362–366.

Dollish, F., Fately, W., and Bentley, F. (1973). *Characteristic Raman frequencies of organic compounds*. John Wiley and Sons New York.

Dong, M. and Chatzis, L. (1995). The imbibition and flow of a wetting liquid along the corners of a square capillary tube. *Journal of Colloid and Interface Science*, 172:278–288.

Duchesne, I. and Daniel, G. (1999). The ultrastructure of wood fibre surfaces as shown by a variety of microscopic methods - a review. *Nordic Pulp and Paper Research Journal*, 14(2):129–139.

Ebrahimzadeh, P. (1998). Effect of impregnation on mechanosorption in wood and paper studied by dynamic mechanical analysis. *Wood Science and Technology Vol. 32*, 32:101–118.

Echlin, P. (1992). *Low-Temperature Microscopy and Analysis*. Plenum Press, New York.

Eklund, D. and Salminen, P. (1986). Water transport in the blade coating process. *Tappi J.*, 69(9):116–119.

Eklund, D. and Salminen, P. (1987). Water sorption in paper during short times. *Appita Journal*, 40(5):340–346.

Elftonson, J. and Strom, G. (1995). *Proceedings Tappi Coating Fundamentals Symposium*. TAPPI Press Atlanta GA.

Enzenberger, W. (1961). On the surface finishing of particleboard with resin impregnated paper layers. *Holz als Roh-und Werkstoff*.

Enzenberger, W. (1968). *Particleboard Manufacture and Application*. Pressmedia Ltd. Sevenoaks Kent UK.

Forsberg, P. and Lepoutre, P. (1994). Environmental scanning electron microscope examination of paper in high moisture environment: Surface structural changes and electron beam damage. *Scanning Microscopy*, 8(1):31–34.

Fredericks, P. (1996). Raman spectroscopy. *Testing Technology*, (7):6–9.

Furo, I. and Daicic, J. (1999). NMR cryoporometry: A novel method for the investigation of the pore structure of paper and paper coatings. *Nordic Pulp and Paper Research Journal*, 14(3):221–225.

Gane, P. A. C., Matthers, G. P., and Schoelkopf, J. (2001). *Coating imbibition rate studies of offset inks: A novel determination of ink-on-paper viscosity and solids concentration using the ink tack force-time integral*. TAPPI Press Atlanta GA.

Gane, P. A. C., Matthews, G. P., Schoelkopf, J., Ridgway, C. J., and Spielmann, D. C. (2000). Fluid transport into porous coating structures: some novel findings. *Tappi J.*, 83(5):77–78.

Garey, C., Leekley, R., Hultman, J., and Nagel, S. (1973). Determination of pore size distribution of pigment coatings. *Tappi J.*, 56(11):134–138.

Garnier, G., Bertin, M., and Smrckova, M. (1999). Wetting dynamics of alkyl ketene dimer on cellulosic model surfaces. *Langmuir*, 15:7863–7869.

Gate, L., Windle, W., and Hine, M. (1973). The relationship between gloss and surface microtexture of coatings. *Tappi J.*, 56(3):61–65.

Gate, L. F. and Windle, W. (1973). *The Fundamental Properties of Paper Related to its Uses: Transactions of the Symposium held at Cambridge, September 1973*. Technical Section, British Paper and Board Makers' Association. London.

Gindl, W., Dessipri, E., and Wimmer, R. (2002). Using UV-microscopy to study diffusion of melamine-urea-formaldehyde resin in cell walls of spruce wood. *Holzforschung*, 56(1):103–107.

Goel, A., Tzanakakis, M., Huang, S., Ramaswamy, S., Choi, D., and Ramaroa, B. (2001). Characterization of the three-dimensional structure of paper using x-ray microtomography. *Tappi J.*, 84(5).

Grant, G., Clifton, G., and Sheppard, J. (1974). Coating distribution using microtome sectioning and neutron activation analysis. *Tappi J.*, 57(4):127–130.

Gregerson, O. W., Johnson, P. O., and Helle, T. (1994). *International Printing and Graphic Arts Conference, Halifax*.

Gregerson, O. W., Johnson, P. O., and Helle, T. (1995). Small-scale topographical variations of newsprint surfaces and their effects on printing ink transfer distribution. *Journal of Pulp and Paper Science*, 21(10):J331–J336.

Groves, R., Matthews, G., Heap, J., McInnes, M., Penson, J., and Ridgway, C. (2001). *The Science of Papermaking. Transactions of the 12th Fundamental Research Symposium, Oxford*, volume 2.

Hardy, W. (1919). The spreading of fluids on glass. *Phil. Mag.*, 38(49).

Hardy, W. (1936). *Sir William Bate Hardy Collected Papers*. Cambridge University Press.

Hasuike, M., Kawasaki, T., and Murakami, K. (1992). Evaluation method of 3-D geometric structure of paper sheet. *Journal of Pulp and Paper Science*, 18(3):J114–J120.

Heady, R. (1997). *The wood anatomy of Callitris Vent (Cupressaceae): an SEM study*. PhD thesis, The Australian National University.

Hill, C., Hedren, A., Meyers, G., and Koutsky, J. (1984). Raman spectroscopy of urea-formaldehyde resins and model compounds. *Journal of Applied Polymer Science*, 29:2749–2762.

Howarth, P. and Schindler, M. K. (1985). *Papermaking raw materials. Transactions of the Eighth Fundamental Research Symposium held at Oxford September 1985*, volume 2. Mechanical Engineering Publications Limited, London.

Hoyland, R. (1977). *Fibre-Water Interactions in Paper-Making; Transactions of the symposium held at Oxford*. Technical Section, British Paper and Board Makers' Association, London.

Hoyland, R. W., Howarth, P., and Field, R. (1973). *The Fundamental Properties of Paper Related to its Uses. Transactions of the Symposium held at Cambridge*. Technical Section, British Paper and Board Makers' Association, London.

Huang, T. and Lepoutre, P. (1998). Effect of basestock surface structure and chemistry on coating holdout and coated paper properties. *Tappi J.*, 81(8):145–152.

Hung, J. Y., Nelson, R. W., and van Eperen, R. H. (1969). Remarks on the surface receptivity and roughness of paper as these relate to liquid film application. *Tappi J.*, 52(9):1732–1734.

Inoue, S. (1995). *Handbook of biological confocal microscopy*, chapter 1, pages 1–17. Plenum Press New York.

Isogai, A. (1999). Mechanism of paper sizing by alkyl ketene dimers. *Journal of Pulp and Paper Science*, 25(7):251–255.

Jalbert, J. (1991). *Polymers, Laminations and Coatings, A Tappi Press Anthology of Published Papers 1986 - 1991*. TAPPI Press Atlanta, Ga.

James, C., Rees, A., and Plummer, M. (1998). Applications fo the scanning electron microscope to the study of australian newpsrint mills papers: product evolution and development. *Appita Journal*, 51(4):267–273.

Jang, H. F., Robertson, A. G., and Seth, R. S. (1991). Optical sectioning of pulp fibers using confocal scanning laser microscopy. *Tappi Journal*, 74(10):217–219.

Jang, H. F. and Seth, R. S. (1998). Using confocal microscopy to characterize the collapse behavior of fibers. *Tappi Journal*, 81(5):167–173.

Jayme, G. and Rohman, E. N. (1965). Quantitative determination of the melamine resin content of wet-strength papers. *Das Papier*, 19(12):832–841.

Johnson, R., Abrams, L., Maynard, R. B., and Amick, T. J. (1999). Use of mercury porosimetry to characterize pore structure and model end-use properties of coated papers - part i optical and strength properties. *Tappi J.*, 82(1):239–251.

Kallmes, O. and Corte, H. (1960). The structure of paper; 1. the statistical geometry of an ideal two dimensional fiber network. *Tappi J.)*, 43(9):737–752.

Kent, H. and Lyne, M. (1989a). *Fundamental of papermaking: Transactions of the ninth Fundamental Research Symposium Vol. 2 held at Cambridge*. Mechanical Engineering Publications, London.

Kent, H. and Lyne, M. (1989b). On the penetration of printing ink into paper. *Nordic Pulp and Paper Research Journal*, 4(2):141–145.

Ketoja, J., Kananen, J., Niskanen, K., and Tattari, H. (2001). *The Science of Papermaking. Transactions of the 12th Fundamental Research Symposium, Oxford*. The Fundamental Research Society, Bury, Lanscashire.

Kettle, J., Matthews, P., Ridgway, C., and Wagberg, L. (1997). *The Fundamentals of Papermaking Materials: Transactions of the 11th Fundamental Research Symposium Cambridge*, volume 2. Pira International.

Kibblewhite, R. and Bailey, D. (1988). Measurement of fibre cross-section dimension using image processing. *Appita Journal*, 41(4):297–303.

Kibblewhite, R. and Brookes, D. (1977). Dimensions and collapse behaviour of kraft and bisulphite fibres in wet pulps and 'in situ' in handsheets. *Appita Journal*, 31(2):111–118.

Kohl, W., Frei, J., and Trethaway, B. (1996). Characterization of the cure process in melamine-formaldehyde laminating resin using high-pressure differential scanning calorimetry. *Tappi J.*, 79(9):199–205.

Kornev, K. and Neimark, A. (2001). Spontaneous penetration of liquids into capillaries and porous membranes revisited. *Journal of Colloid and Interface Science*, 235:101–113.

Kraske, D. (1960). Methods for the analysis of the physical structure of clay-starch coating films. *Tappi J.*, 43(1):73–82.

Lafaye, J., Gervason, G., Maume, J., and Piette, P. (1987). The effect of coating with surfactant on quality and offset printability. *Tappi J.*, 70(8):43–49.

Larson, R., Scriven, L., and Davis, H. (1977). Percolation theory of residual phases in porous media. *Nature*, 268:4409–413.

Laufmann, M. (1998). Fillers for paper - a global view. Technical report, Presented at the PTS-Seminar Wet End Operations - Vorgange in der Siebpartie Munich.

Lemasters, J. J., Chacon, E., Zahrebelski, G., Reece, J. M., and Nieminen, A. (1993). *Optical Microscopy Emerging Methods and Applications*, chapter 12, pages 339–354. Academic Press, Inc. San Diego.

Lenormand, R., Touboul, E., and Zarcone, C. (1988). Numerical models and experiments on immiscible displacements in porous media. *J. Fluid Mech.*, 189:165–187.

Lenormand, R. and Zarcone, C. (1984). *59th Annual Technical Conference and Exhibition of the Society of Petroleum Engineers*. American Institute of Mining, Metallurgical, and Petroleum Engineers.

Lenormand, R., Zarcone, C., and Sarr, A. (1983). Mechanisms of the displacement of one fluid by another in a network of capillary ducts. *J. Fluid Mech.*, 135(99):337–353.

Lepoutre, P. (1976). Paper coatings; structure-property relationships. *Tappi J.*, 59(12):70–75.

Lepoutre, P. (1978). Liquid absorption and coating porosity. *Paper Technology and Industry*, (11):298–301.

Lepoutre, P. (1989). *Progress in Organic coatings*. Number 17. Elsevier.

Lepoutre, P. (1990). On wetting time. *Nordic Pulp and Paper Research Journal No. 4*, 5(4):200.

Lepoutre, P. and de Grace, J. (1978). Ink transfer characteristics and coating structure. *Paper Technology and Industry*, (11):301–304.

Lepoutre, P., DeGrace, J., and Mangin, P. (1979). Printability of coated papers, influence of coating absorbency. *Tappi J.*, 62(5):33–36.

Lepoutre, P. and Inoue, M. (1985). Influence of surfactant on the gluing of coated board. *Tappi J.*, 68(3):114.

Lepoutre, P. and Rezanowich, A. (1977). Optical properties and structure of clay latex coatings. *Tappi J.*, 60(11):86–91.

Lindquist, B., Lee, S., and Coker, D. (1996). Medial axis analysis of void structure in three-dimensional tomographic images of porous media. *J. Geophys. Res.*, 101(B4):8297–8310.

Lindquist, B., Venskatarangan, A., Dunsmuir, J., and Wong, T. (2000). Pore and throat size distributions measured from synchrotron x-ray tomographic images of fontainbleau sandstones. *J. Geophys. Res.*, 105(9):21509–21528.

Liukkonen, A. (1997). Contact angle of water on paper components:sessile drops versus environmental scanning electron microscope measurements. *Scanning*, 19:411–415.

Lloyd, M. D. and Dickson, A. R. (2000). Effect of calendering speed on sheet structure and paper properties. *Appita Journal*, 53(2):487–493.

Loebl, J. (1985). *Instruction Manual for Langmuir Minitrough*.

Lucas, R. (1918). Ueber das zeitgesetz des kapillaren aufstiegs von fleussigkeiten. *Kolloid-Z*, 23:15–22.

Lyne, B. (1976). Machine-calendering: implications for surface structure and printing properties. *Tappi J.*, 59(8):101–106.

Lyne, L. and Madsen, V. (1964). An apparatus for the measurement of liquid penetration into porous webs at a press nip. *Pulp and Paper Magazine of Canada*, 65(12):T523–T527.

Lyne, M. (1993). *Transactions of the tenth fundamental research symposium held at Oxford*. Pira International Leatherhead UK.

Lyne, M. and Aspler, J. (1982). Wetting and the sorption of water by paper under dynamic conditions. *Tappi J.*, 65(12):98–101.

Maloney, T. and Paulapuro, H. (1998). Hydration and swelling of pulp fibers measured with differential scanning calorimetry. *Nordic Pulp and Paper Research Journal*, 13(1):31–36.

Mark, R., Habeger, C., Borch, B., and Lyne, M. (2002). *Handbook of Physical Testing of Paper*, volume 1. Marcel Dekker, Inc., 2nd edition.

Marmur, A. (1988). Drop penetration into a thin porous medium. *Journal of Colloid and Interface Science*, 123(1):161–169.

Marmur, A. and Cohen, R. (1997). Characterization of porous media by the kinetics of liquid penetration: the vertical capillaries model. *Journal of Colloid and Interface Science*, 189:299–304.

Matthews, P. (2000). Computer modelling of fluid permeation in porous coatings and paper - an overview. *Nordic Pulp and Paper Research Journal*, 15(5):476–485.

Minsky, M. (1957). Microscopy apparatus US patent no. 3013467. *US Patents and Trademarks Office*.

Napier, J. (1964). Liquid penetration into paper. *Paper Technology*, 5(3):275–280.

Nguyen, H. and Durso, D. (1983). Absorption of water by fiber webs: an illustration of diffusion transport. *Tappi J.*, 66(12):76–79.

Oliver, J. and Mason, S. (1976). *The Fundamental Properties of Paper Related to its Uses. Transactions of the Symposium held at Cambridge, September 1973*. Technical Section, British Paper and Board Makers' Association.

Oliver, J. F., Agbezuge, L., and Woodcock, K. (1994). A diffusion approach for modelling penetration of aqueous liquids into paper. *Colloids and Surfaces A: Physicochemical and Engineering Aspects.*, 89.

Otieno-Alego, V. (2000). *Radiation in Art and Archeometry*. Elsevier, Amsterdam, The Netherlands.

Pan, Y. L., Kuga, S., , and Usuda, M. (1988). An ultrasonic technique to study wetting and liquid penetration of paper. *Tappi J.*, 61(7):119–123.

Phillip, J. (1978). Adsorption and capillary condensation on rough surfaces. *The Journal of Physical Chemistry*, 82(12):1379–1385.

Phipps, J. (2001). Choosing fillers for optimum paper properties: understanding the compromises. *Paper Technology*, pages 37–41.

Pizzi, A. (1983a). *Wood Adhesives Chemistry and Technology*, volume 1. Marcel Dekker, Inc. New York.

Pizzi, A. (1983b). *Wood Adhesives Chemistry and Technology*, volume 2. Marcel Dekker, Inc. New York.

Potter, S. and Fraser, S. (1999). A two-photon laser-scanning confocal fluorescence microscope. Caltech unpublished.

Price, D., Osborn, R., and Davis, J. (1953). A liquid penetration test for measuring the sizing of paper. *Tappi J.*, 36(1):42–46.

Ransohoff, T. C., Gauglitz, P. A., and Radke, C. J. (1987). Snap-off of gas bubbles in smoothly constricted noncircular capillaries. *AIchE Journal*, 33(5):753–765.

Ransohoff, T. C. and Radke, C. J. (1988). Laminar flow of a wetting liquid along the corners of a predominantly gas-occupied noncircular pore. *Journal of Colloid and Interface Science*, 121(2):392–401.

Rapp, A., Bestgen, H., Adam, W., and Peek, R. D. (1999). Electron energy loss spectroscopy (EELS) for quantification of cell-wall penetration of melamine resin. *Holzforschung*, 53(2):111–117.

Reaville, E. and Hine, W. (1967). Measurement of sizing. *Tappi J.*, 50(6):262–270.

Ridgway, C. and Gane, P. (2002). Controlling the absorption dymnamic of water-based ink into porous pigmented coating structures to enhance print performance. *Nordic Pulp and Paper Research Journal*, 17(2):119–129.

Robards, A. W. and Sleytr, U. B. (1985). *Low temperature methods in biological electron microscopy*, volume 10 of *Practical methods in microscopy*. Elsevier, Amsterdam.

Roberts, R. J., Senden, T. J., Knackstedt, M. A., and Lyne, M. B. (2003). Spreading of aqueous liquids in unsized papers is by film flow. *Journal of Pulp and Paper Science*, 29(4):123–131.

Rucinski, K., Caronia, A., and McNeil, R. (1986). Filter media characterization by mercury intrusion. *Tappi J.*, 69(11):121–123.

Rye, R., Mann Jr, J. A., and Yost, F. (1966). The flow of liquids in surface grooves. *Langmuir*, 12(2):555–565.

Sahimi, M. (1994). *Applications of percolation theory*. Taylor & Francis Ltd London.

Salminen, P. (1988). Water transport into paper - the effect of some liquid and paper variables. *Tappi J.*, 71(9):195–200.

Samuelsen, E., Gregersen, O., Houen, P., Helle, T., Raven, C., and Snigerev, A. (2001). Three-dimensional imaging of paper by use of synchrotron x-ray microtomography. *Journal of Pulp and Paper Science*, 27(2):50–53.

Sapieha, S., Wrobel, A., and Wertheimer, M. (1988). Plasma-assisted etching of paper. *Plasma Chemistry and Plasma Processing.*, 8(3).

Scandinavian Pulp Paper and Board Testing Committee (1964). Water absorbency of sized paper and paperboard by the cobb method. *Svensk Papperstidning*, 67(19):J203–J207.

Scheepers, M., Gelan, J., Carleer, R., Adriaensens, P., Vanderzande, D., Kip, B., and Brandts, P. (1993). Investigation of melamine-formaldehyde cure by fourier-transform raman-spectroscopy. *Vibrational Spectroscopy*, 6(1):55–69.

Scheepers, M., Meier, R., Markwort, L., Gelan, J., Vanderzande, D., and Kip, B. (1995). Determination of free melamine content in melamine-formaldehyde resins by raman-spectroscopy. *Vibrational spectroscopy*, 9(2):139–146.

Schnieder, C. (1997a). *Forum Zukunft, Resin and paper basic research provides new data*, pages 15–29. Technocell Dekor, Gunzach, Germany.

Schnieder, C. (1997b). *Forum Zukunft, Resin and paper basic research provides new data*, pages 47–55. Technocell Dekor, Gunzach, Germany.

Schoelkopf, J., Gane, P., Ridgway, C., Spielmann, D., and Matthews, G. (2003). Imbibition behaviour of offset inks part 1: Gravimetric determination of oil imbibition rate into pigmented coating structures. *Tappi J.*, 2(6):9–13.

Schoelkopf, J., Gane, P. A. C., Ridgway, C. J., and Matthews, G. P. (2000a). Influence of inertia on liquid absorption into paper coating structures. *Nordic Pulp and Paper Research Journal*, 15(5):422–430.

Schoelkopf, J., Ridgway, C., Gane, P., Matthews, G., and Spielmann, D. (2000b). Measurement and network modeling of liquid permeation into compacted liquid blocks. *Journal of Colloid and Interface Science*, 227:119–131.

Seidl, R. J. (1949). Paper and plastic overlays for veneer and plywood. *Forest Products Research Society*, pages 23–32.

Seiler, C. (1957). Penetrating and saturating qualities of kraft papers. *Tappi J.*, 40(10):200A–203A.

Senden, T., Knackstedt, M., and Lyne, M. (2000). Droplet penetration into porous networks: role of pore morphology. *Nordic Pulp and Paper Research Journal*, 15(5):554–563.

Seppanen, R., Tiberg, F., and Valignat, M. (2000). Mechanism of internal sizing by alkyl ketene dimers (akd): The role of the spreading monolayer precursor and autophobicity. *Nordic Pulp and Paper Research Journal*, 15(5):452–458.

Shohel, J. (1987). *Encyclopedia of Physical Science and Technology*, volume 10. Academic Press.

Smith, K. (1959). Scanning electron microscopy in pulp and paper research. *Pulp and Paper Magazine of Canada December*, 60(12):T367–T371.

Sok, R., Knackstedt, M., Sheppard, A., Pinczewski, W., Lindquist, W., Venskatarangan, A., and Paterson, L. (2002). Direct and stochastic generation of network models from tomographic images; effect of topology on two phase flow properties. *Transport in Porous Media*, 46:345–371.

Stannet, V. T. and Williams, J. L. (1977). *Fibre-Water Interactions in Paper-Making*. Transactions of the symposium held at Oxford.

Sun, Z., Ibrahim, A., Oldham, P., Schultz, T., and Connors, T. (1997). Rapid lignin measurement in hardwood pulp samples by near-infrared fourier transform raman spectroscopy. *J. Agric. Food Chem.*, 45(8):3088–3091.

Suranyi, G., Gray, D., and Goring, D. (1980). The effect of corona discharge on wettability of aged corrugating medium. *Tappi J.*, 63(4):153–154.

Swanson, J. and Cordingly, S. (1959). Surface chemical studies in pitch, II the mechanism of the loss of absorbency and development of self sizing in papers made from wood pulps. *Tappi J.*, 42(10):812–819.

Sweerman, A. (1961). A new approach to the measurement of roughness and porosity of paper. *Tappi J.*, 44(7):172A–175A.

TAPPI (1992). *TAPPI Test Methods*. TAPPI PRESS Atlanta GA.

Tiberg, F., Zhmud, B., Hallstensson, K., and von Bahr, M. (2000). Capillary rise of surfactant solutions. *Phys. Chem. Chem. Phys.*, 2(22):5189–5196.

Ting, T. H. D., Chiu, W. K., and Johnston, R. E. (1997). Network changes in paper under compression in the z-direction: the effect of loading rate and fibre wall thickness. *Appita Journal*, 50(3):223–229.

Ting, T. H. D., Johnston, R. E., and Chiu, W. K. (2000). Compression of paper in the z-direction the effects of fibre morphology, wet pressing and refining. *Appita Journal*, 53(5):378–384.

Tsien, R. and Waggoner, A. (1995). *Handbook of biological confocal microscopy*. Plenum Press New York, 2nd edition.

Van den Akker, J. and Wink, W. (1969). Mechanisms of liquid-phase movement of water through paper. *Tappi J.*, 52(12):2406–2410.

Van der Wulp, K. (1995). *The process of making 3-D reconstructions from LSCM data*. Dept. of Physiology, U.B.C.

Verhoeff, J., Hart, J., and Gallay, W. (1963). Sizing and the mechanism of penetration of water into paper. *Pulp and Paper Magazine of Canada*, 64(12):T509.

Voillot, C., Gravier, M., Ramaz, A., and Chaix, J. (1990). The use of x-ray image processing to analyze the z-direction distribution of fillers and pigments. *Tappi J.*, 73(5):191–193.

Voronoi, G. (1908). Nouvelles applications des paramèteres continus *à* la thèorie des formes quadratiques. *J. Reine Agnew. Math*, 134:198–207.

Washburn, E. W. (1921). The dynamics of capillary flow. *Physical Review Vol.*, 17(3):273–283.

Webb, P. and Orr, C. (1997). *Analytical methods in fine particle technology*. Micromeritics Instrument Corporation.

Wilhelmy, L. (1863). Uber die abhngigkeit der kapillaritts-kon-stanten des alkohols von substanz und gestalt des benetztenfesten krpers. *Ann. Physik*, 119(6).

Williams, G., Drummond, J., and Cisneros, H. (1994). A microscopic approach for examining fiber and paper structures. *Journal of Pulp and Paper Science*, 20(4):J110–J114.

Williams, G. J. and Drummond, J. G. (2000). Preparation of large sections for microscopical study of paper structure. *Journal of Pulp and Paper Science*, 26(5):188–193.

Windle, W., Beazley, K., and Climpson, M. (1970). Liquid migration from coating colors 2. the mechanism of migration. *Tappi J.*, 53(12):2232–2236.

Wink, W. and Van den Akker, J. (1957). A new apparatus and procedure for determining the surface receptivity and roughness of paper as these relate to liquid film applications. *Tappi J.*, 40(7):528–536.

Winspear, S. (1979). The characterization of liquid acceptance by paper. *Appita Journal*, 33(1):25–32.

Xu, L. and Parker, I. (1999). Correction of fluorescence attenuation with depth in fibre and paper images collected by confocal laser scanning microscopy. *Appita Journal*, 52(1):41–44.

Xu, L., Parker, I., and Osborne, C. (1997). Technique for determining the fibre distribution in the z-direction using confocal microscopy and image analysis. *Appita Journal*, 50(4):325–328.

Yamazaki, H. and Munakata, Y. (1993). *Transactions of the tenth fundamental research symposium held at Oxford*. Pira International Leatherhead.

Yildirim, I. (2001). *Surface free energy characterization of powders*. PhD thesis, Virginia Polytechnic Institute and State University.

Young, R., Denes, F., Sabharcoal, H., Nelson, L., and Tu, X. (1994). *Improvement of biobased composite properties through cold plasma treatments*. Second Pacific Rim Bio-Based Composites Symposium, Vancouver, BC Canada.

Zang, Y. and Aspler, J. (1995). The influence of coating structure on the ink receptivity and print gloss of model clay coatings. *Tappi J. 78 (1)*, 78(1).

Zhmud, B., Tiberg, F., and Hallstensson, K. (2000). Dynamics of capillary rise. *Journal of Colloid and Interface Science*, 228:263–269.

Appendix A

Tables of paper and resin properties from Chapter 3

***Table A.1**: Details of papers analysed*

Paper type	**Supplier**	**Classification**	**Weight** (gsm)	**Roll no.**
Alpine White	Munksjo	Calendered, high density	72	70350/26
Alpine White	Munksjo	Calendered, high density	71	70350/29
Beech	Interprint/Arjo	Calendared print high density	69	80241/4
Beech	Interprint/Arjo	Calendared print high density	69	80286/5
Black	Technocell	Twin wire formed	72	138541/21
Black	Technocell	Twin wire formed	71	138541/12
Fog	Munksjo	Non calendared	89	68448/3
Fog	Munksjo	Non calendared	91	68448/2
Folkstone Grey	Munksjo	Calendared	80	69670/7
Folkstone Grey	Munksjo	Calendared	82	69670/2
Kraft	Westvaco	100% wood pulp absorbent paper	210 (spec)	7528/108
Kraft	Westvaco	100% wood pulp absorbent paper	210 (spec)	6578/96
New England Elm	Toppan	Heavy high density calendared	100 (spec)	189513/4
New England Elm	Toppan	Heavy high density calendared	100 (spec)	189513/5
Storm	Devon Valley Industries	Non calendared	92.6	172490/5
Storm	Devon Valley Industries	Non calendared	93	172490/1
Streetlight	Devon Valley Industries	Non calendared heavy medium density	121.6	195262/1
Streetlight	Devon Valley Industries	Non calendared heavy medium density	119	183588/5

***Table A.2**: Physical property data from suppliers*

Paper type	**Ash content**	**pH**	**Gurley porosity** (seconds)	**Klemm** (mm/10min)	**Resin pickup** (g)	**Bekk Smoothness**
Alpine White	41.1	7	28	22	95	293
Alpine White	41.5	6.6	30	21	89	297
Beech	33	6.8	17	22	n/a	163
Beech	34	6.9	19	22	n/a	162
Black	14	7.2	14	n/a	n/a	n/a
Black	13	7.1	14	n/a	n/a	n/a
Fog	26	7.2	11	28	130.0	54
Fog	26.1	7.2	16	29	130	60
Folkstone Grey	34	6.1	27	18	113	198
Folkstone Grey	35.6	6.8	31	21	101	205
Storm	22.5	7.0	17	n/a	n/a	n/a
Storm	22.5	7.2	20	n/a	n/a	n/a
Streetlight	35	7.4	19.2	n/a	n/a	n/a
Streetlight	34.5	7.0	19.4	n/a	n/a	n/a
Kraft	0.7	n/a	n/a	n/a	n/a	n/a
New England Elm	28.8	n/a	n/a	n/a	n/a	n/a

Table A.3: *Summary of identifiable compounds in uncured UF resin using Raman spectroscopy identifiable in Figure 3.46 (Hill et al., 1984).*

Compound	**Wave number**
Formalin	906 cm^{-1}
Trimethylene tetraurea	1119 cm^{-1}
Dimethylolurea	1284 & 1648 cm^{-1}
Methylenediurea	1430 cm^{-1}

Table A.4: *Summary of identifiable compounds in uncured MF resin using Raman spectroscopy identifiable in Figure 3.46 (Scheepers et al., 1993, 1995).*

Compound	**Wave number**
Melamine in-plane ring deformation	676 cm^{-1}
Melamine triazine ring breathing	975 cm^{-1}
Methylolmelamine	1460 cm^{-1}

Table A.5: *Summary of identifiable compounds in cured UF resin using Raman spectroscopy identifiable in Figure 3.47 (Hill et al., 1984).*

Compound	**Wave number**
Dimethylolurea	904 cm^{-1}
Penta methylene hexaurea	955 cm^{-1}
Formalin	1313 cm^{-1}
Dimethylolurea dimethylether	1633 cm^{-1}

Table A.6: *Summary of identifiable compounds in cured MF resin using Raman spectroscopy identifiable in Figure 3.46 (Scheepers et al., 1993, 1995).*

Compound	**Wave number**
Melamine in-plane ring deformation	676 cm^{-1}
Melamine triazine ring breathing vibration	975 cm^{-1}
Hexamethylolmelamine	1450 cm^{-1}

Appendix B

Details of relative reflectance method from Chapter 4

The saturation tests were done using diethylene glycol ($C_4H_{10}O_3$) (DEG) which has a similar viscosity and pH to that of UF resin, (18.4 s measured with a No 4 flow cup at 25°C) and a pH of 8.4. Seiler (1957) when investigating the principle effects of penetration of resins into paper ruled out the use of resins because they varied from day to day in viscosity, molecular weight distribution, and in polarity and affinity to cellulose. However although DEG does not age (unlike UF resin), it was very hygroscopic and therefore absorbed moisture from the atmosphere. For this reason the DEG was completely changed every 30 minutes during testing. Additional DEG also had to be added to the Petri dish to replace the DEG that penetrated the paper samples. In order to ensure that the viscosity of the DEG was constant it was placed in an accurately machined brass holder which was then placed in a water bath at $25 \pm 0.5°C$ (Figure 4.4). The temperature of the water bath was controlled by a B. Braun Frigomix-U with a Julabo VC temperature controller. Therefore any change in the rates of saturation would be due to paper effects (either chemical or physical). The sample of paper was placed on the DEG within the Petri dish. The paper sample floated on the liquid therefore there was no physical pressure on the penetrating liquid beside the weight of the sample. The Petri dish was placed on top of black cloth so as to minimise reflections.

A Cohu solid-state video camera[1] was fitted with a 25 mm 1:1.4 Cosmicar/Pentax lens with a 7 mm extension tube and attached to a retort stand. A Junkel and Kunkel retractable plate was placed beneath the camera so that the distance between the camera lens and plate was 155 mm. A 50 mm Petri dish containing 15 ml of DEG was placed on the base plate (Figure 4.4). Images of the Petri dish (and saturating paper) were recorded using a Sony Beta cam Umatic professional video recorder. A FOR-A VTG-33 video timer imprinted of each image with the elapsed time in hundredths of seconds. If the captured (still) images were not perfectly frozen, distortions in the image affected reflectance values, thus only new video cassettes were used to record images. It was also found that advancing the frames forwards rather than in reverse gave

[1] acquiring at 30 fps and with the automatic gain turned off

better frozen images. To eliminate changes in reflectance of samples caused by movement of the paper sample and hence washer, a thumbtack was placed upside down in the middle of the Petri dish which prevented samples (and washer) moving while floating on the liquid.

The aperture on the camera lens was adjusted to maximise the different reflected light intensity between the paper and the steel washer. Light papers such as Alpine White needed a higher f-stop and darker colours such as Black and Storm needed lower f-stop Table B.1. Setting the correct aperture was also important because too much light would cause complete saturation of the image *i.e.* no definition between washer and the saturating paper. To ensure repeatable results the intensity of the light had to be kept constant over the whole sample without any effects of shadowing. The stand onto which the camera and fibre optic source was attached could only close to an angle of about 35° so there was a significant decrease in lighting intensity from any concentrated source across the paper and most significantly across the washer that was used for the reference reflection. This problem was solved by simply using the fluorescent lights in the laboratory that provided an even illumination across the sample.

Still images of the saturating papers were obtained from the video camera and converted into a digital format for analysis with an Apple G3 Powerbook computer using Igor Pro[2]. The rate of saturation was determined by measuring the light intensity of the saturating paper surface and dividing it by the constant value of the reflected light from the washer every .03s and plotted against time (Figure B.2).

[2] v.3.1.4 Wavemetrics inc.

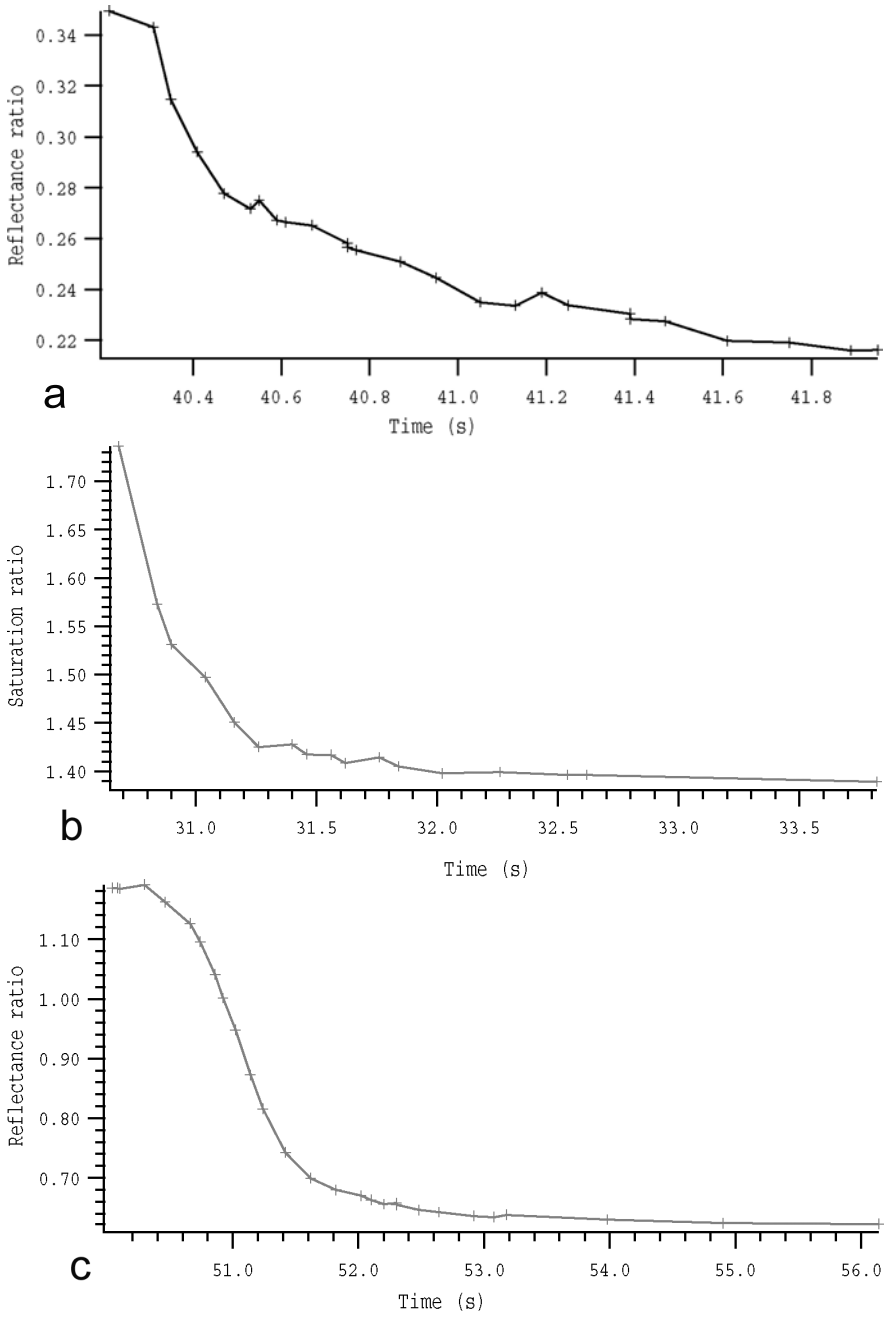

Figure B.1: *Plot of uncorrected changing reflectance ratio vs. time for a) Black, b) Folkstone Grey & c) Kraft.*

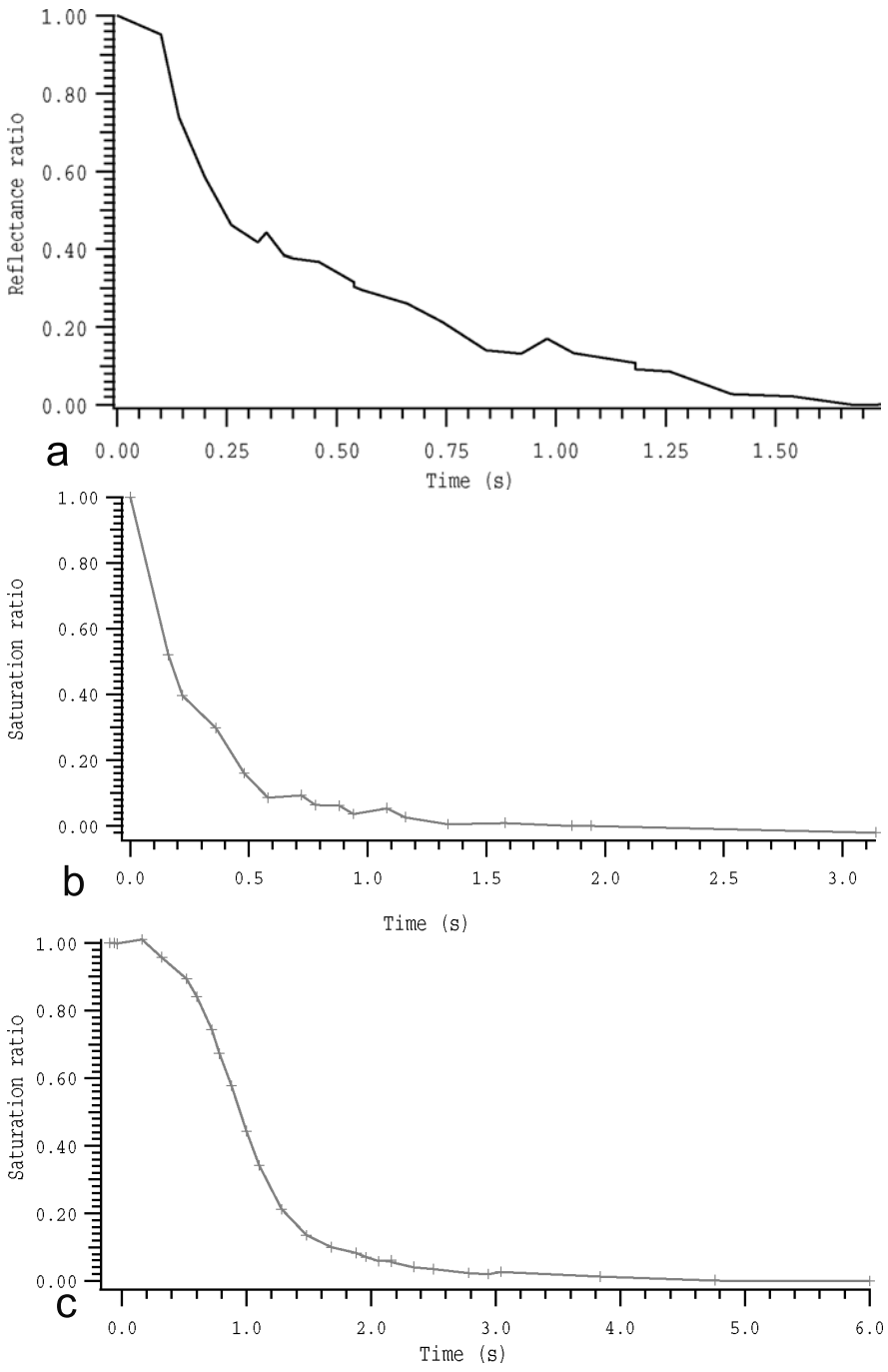

Figure B.2: *Plot of normalised changing reflectance ratio vs. time for a) Black, b) Folkstone Grey & c) Kraft.*

***Table B.1**: Aperture and calibration details for papers for reflectance method testing.*

Paper type	f-stop	calibration dry or saturated
Alpine White	f11	dry
Beech	f8	dry
Black	f5.6	dry
Fog	f11	dry
Folkstone Grey	f11	dry
Kraft	f8	saturated
New England Elm	f11	dry
Storm	f5.6-f8	dry
Streetlight	f11	dry

Paper samples were cut from paper sheets using a 32 mm circular wad punch, with the washer in the middle, then placed in the Petri dish by hand, using tweezers with the rough side of the paper orientated toward the penetrating liquid. Care was taken to ensure that the sample was placed onto the penetrating liquid as horizontally as possible. It was essential that the washers were always dry and clean before use, so they cleaned after each run with ethanol. The reflectivity of the paper and the washer had to be calibrated for each sample to maximise the difference in intensity of the reflected light from the paper and that from the washer. On all papers except for Kraft, a normalising image was obtained just prior to contact with the saturating liquid. This image was used for calibration purposes however with Kraft where there was relatively little contrast between reflected light from the washer and that from unsaturated paper, so calibration had to occur after full saturation. The video recorder was stopped at least 10 seconds after it appeared that saturation had been completed. This was necessary because full saturation could not be determined by eye.

Appendix C

Details on design and construction of cryo-cell used in CLSM from Chapter 6

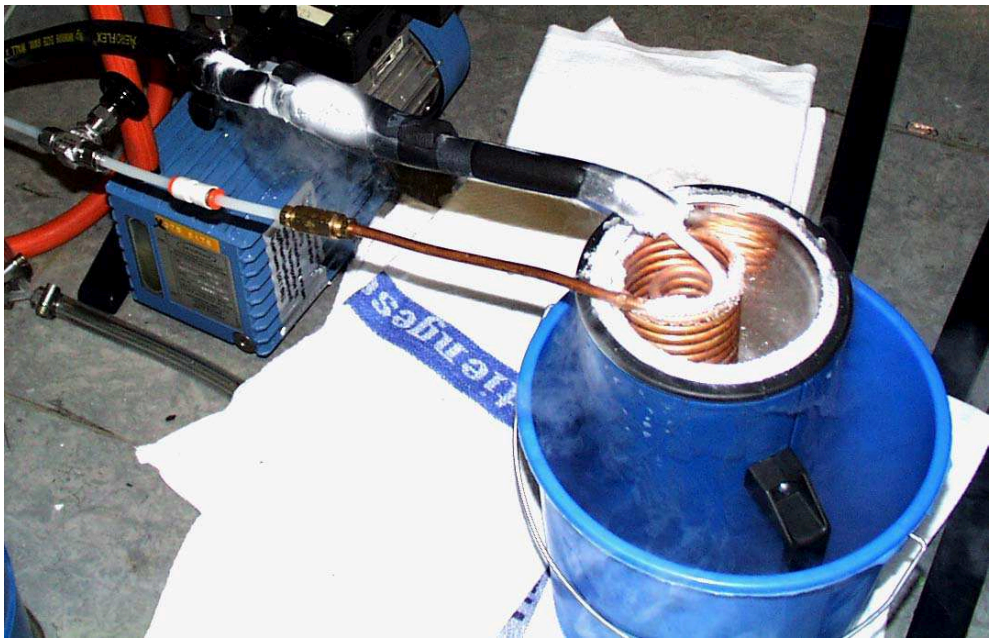

Figure C.1: Copper cooling coil placed in dewar of liquid nitrogen showing needle valve on the supply side of the nitrogen gas and the vacuum pump used for generating nitrogen slush

C.1 Cell design

The cryo-cell is based around a ring made from 180 to 250 μm sintered bronze spheres pressed into a housing machined from *Kel-F* 81 (3M) a homopolymer of chlorotrifluoroethylene (CTFE) (Figure C.1a). The material is dimensionally stable at cryogenic temperatures, well suited to

the large changes in temperature that in the experiment could be up to 100°C. The cryo-cell unit was fitted into a base plate made from *Delrin* (Dupont) an acetal resin, that was permanently fixed to the translational stage of a Leica DM IRB/E inverted CLSM (Figure 6.5). The cryo-cell was removed from the base plate to enable placement of the sample (Figure C.1b).

To enable laser excitation and imaging of the sample, a magnetic stainless steel disc which was held in place by rare earth magnets (to enable easy removal and replacement during sample placement) covered the bottom of the cell. The hollow centre of the disc was covered by a glued piece of 0.15mm optical quality microscope glass slide to contain the cold gas around the sample. In order to be able to position and focus the laser, the cryo-cell had a viewing window at the top which also had to effectively contain the cold nitrogen gas around the sample. This was made from two magnetic stainless steel hollow discs, both covered with a section cut from a microscope slides (Figure C.1c). Figure C.3 shows an assembly diagram of the cryo-cell and base plate and the engineering diagram is shown in Figure C.1.

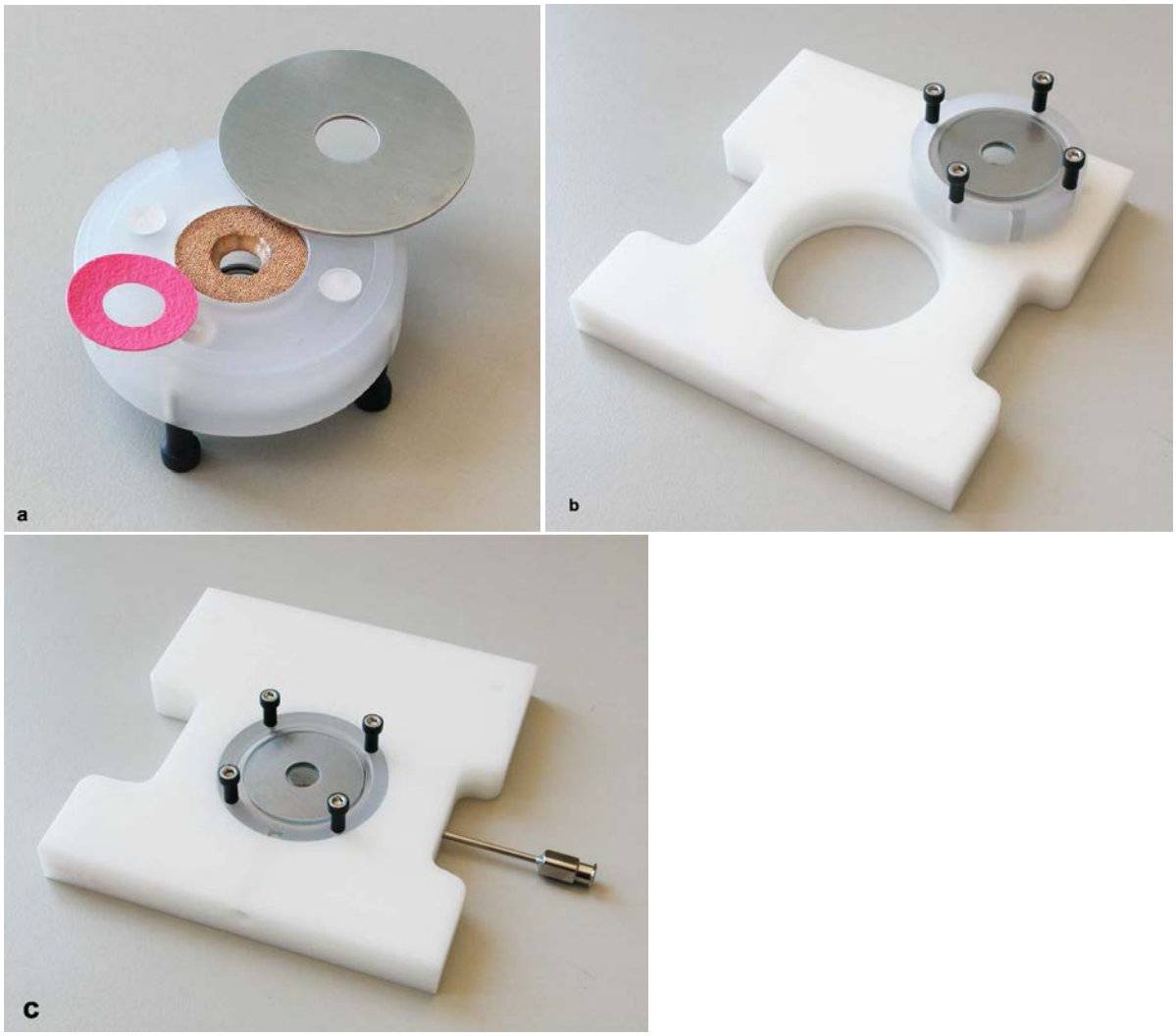

Figure C.2: *a: Image of the cryo-cell insert showing the sintered bronze ring, the rubber washer to keep sample still under high gas flow and the removable magnetic stainless steel viewing window. Note the rare earth magnets embedded in the* Kel-F. *The insert is actually upside down in the image. b: Cryo-cell insert on top of* Delrin *base, c: cryo-cell insert placed in* Delrin *base with Luer No. 12 syringe in place for N_2 cold gas input, showing top viewing port enabling laser positioning and focussing.*

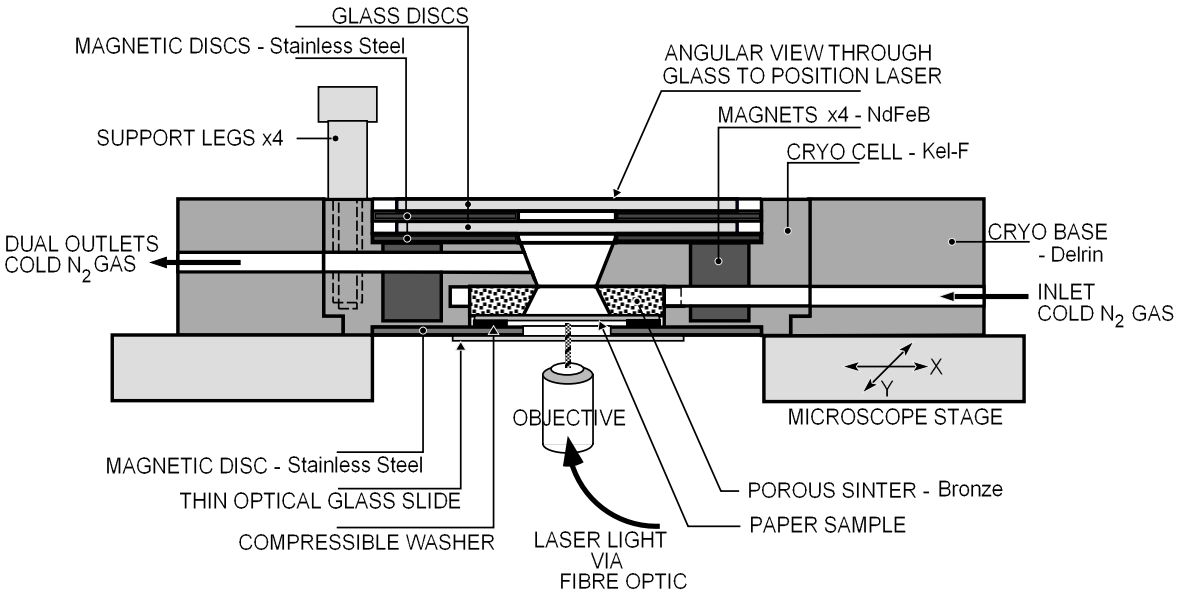

Figure C.3: Assembly diagram of cryo-cell for 2-photon laser confocal microscope

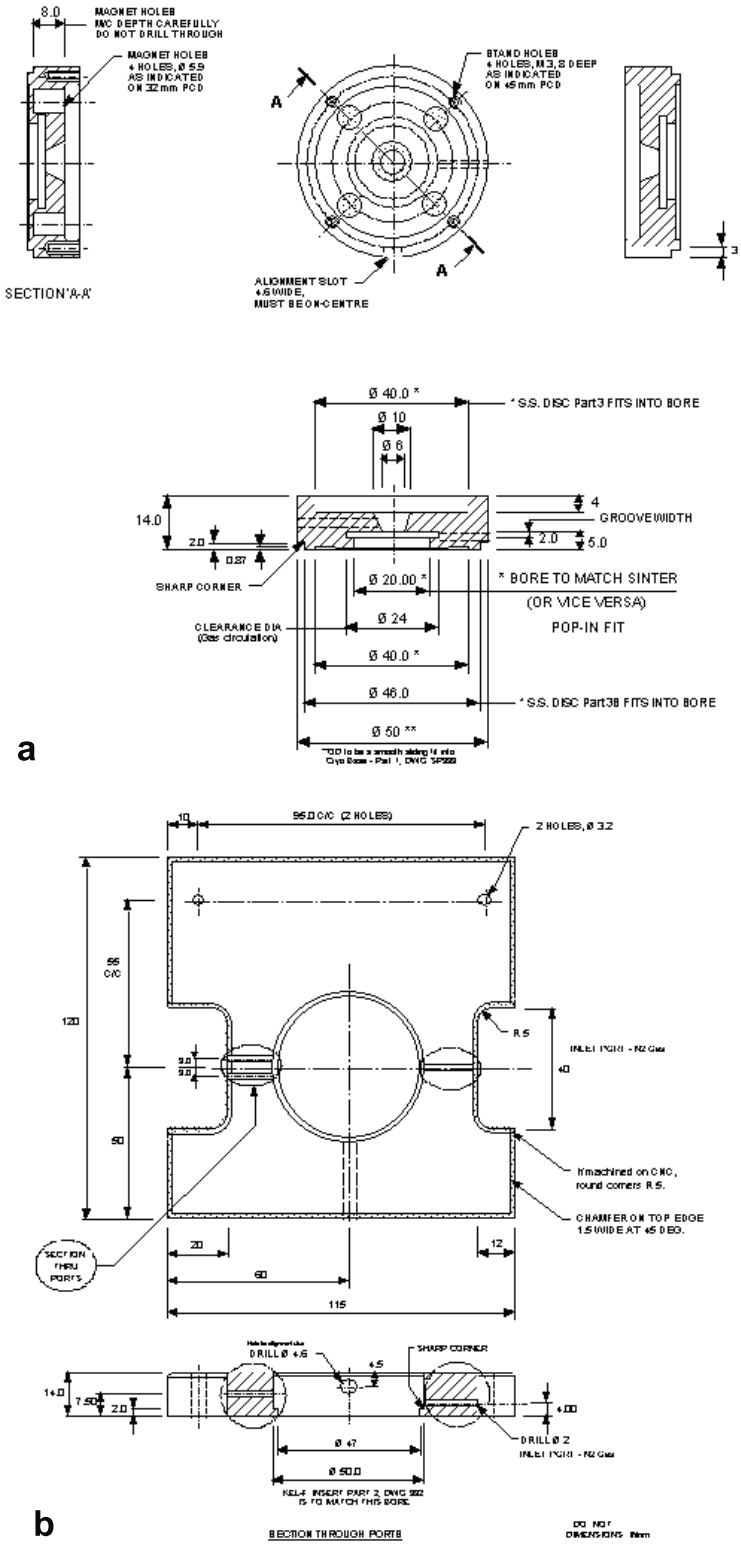

Figure C.4: *Engineering diagram of cryo-cell for 2-photon laser confocal microscope a:* Kel-F *cryo-cell insert, b:* Delrin *base.*

C.2 Use of cryo-cell

To ensure that the necessary cold temperatures were achieved and maintained within a narrow range of -60°C and -70°C ±2°C, a thermocouple wire from a Digital Multimeter Thermocouple (Omega) was placed into one of the gas exhaust ports that passed through the assembly originating from the sintered bronze ring. A gas tube was connected to the cryo-cell with a no. 12G, 50 mm steel syringe (see Figure C.1c) using a male luer fitting made of *Kel-F*. The gas tube was 6 mm OD, 4.2 mm ID nylon pipe covered by neoprene for insulation. Given the very cold temperatures of the N_2 gas (down to -120°C) a 6.5 mm OD 321 stainless steel high vacuum flexible tube (wall thickness 0.15 mm and insulated with neoprene) was used to connect the nylon pipe to the base of the cryo-cell (Figure C.2). This enabled movement of the translational stage of the microscope when locating the required fields of view which would not have been possible had nylon pipe been used as it became rigid with the temperatures associated with the cold gas. The temperature of the cold N_2 gas passing through the cell was controlled manually by a needle valve to adjust the flow achieving temperature variation during imaging of only $\pm\ 2^{\circ}C$.

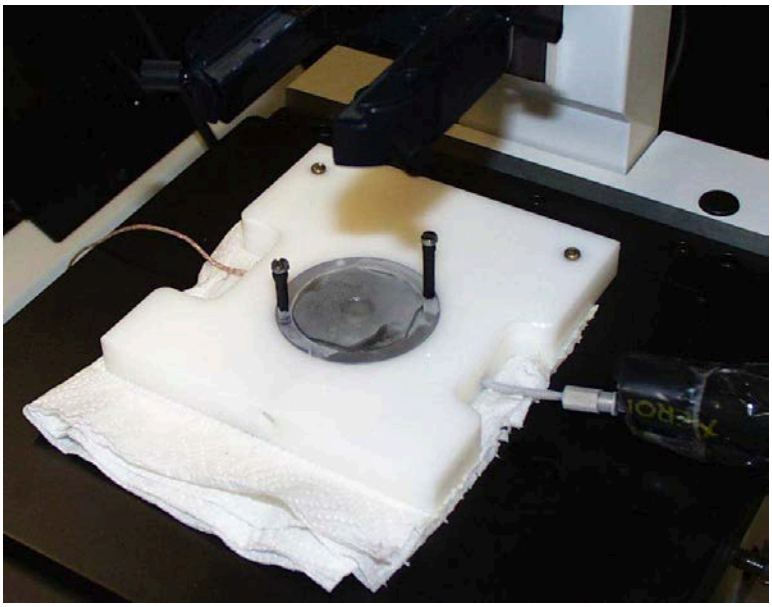

Figure C.5: *The cryo-cell in the base plate on the microscope stage, note the incoming cold gas on the R.H.S. and the thermocouple wire going into an exhaust port on the L.H.S.*

Cooling of the N_2 gas was achieved by passing the gas through a double coil made with copper pipe that was immersed in liquid nitrogen see Figure C.1. It was important to ensure that the copper cooling coil was completely covered by a large volume of liquid nitrogen. It was observed that as the liquid nitrogen in the dewar was allowed to boil off too far, the temperature of the liquid nitrogen and consequently the cold gas stream to the cryo-cell was reduced by as

much as 20°C. When the liquid nitrogen was replaced in the dewar, the temperature of the cold gas consequentially increased. Frequent topping up with small volumes of liquid nitrogen minimised temperature variation resulting in much more stable cooling gas temperatures.

Appendix D

Development of method for determination of liquid flow using high speed visualisation from Chapter 7

The apparatus developed was based around a precision dovetail slide (Figure D.1) onto which was placed a 4.5 mm Teflon. Teflon was used as it has a very low surface energy minimising the footprint of the droplet giving water a contact angle of $>90^{\circ}$ enabling the droplet to be stable both before and during imbibition. This was especially important for containing the droplet of isopropanol which had a much lower contact angle on the stub. stub that held the droplet of experimental liquid. This was driven toward the paper sample by a Philips MB 14 variable speed DC geared motor powered by a GW Laboratory DC power supply Model - GPS $-$ 3030D at a speed of 6.5 mm/min, the column being immediately stopped upon liquid contact with the bottom of the paper sample enabling the liquid to penetrate through capillary pressure alone. As the liquid penetrated the paper, the amount of reflected light off the paper changed in relation to that prior to the droplet touching the paper.

The paper sample was mounted in a 12mm wide ”C” shaped clamp, fixing the paper on three sides ensuring the paper was as flat and orthogonal to the droplet axis (Figure D.2). In order to image the top surface of the paper concurrently with the spreading droplet on the bottom surface, a 25 x 25 x 32 mm triangular prism was placed over the paper so that the image obtained was split. The long side of the prism was covered with black paper to reduce any reflected light affecting the imaging of the top surface of the paper. Half of the field of view of the camera. The high-speed digital CCD camera (Roper Scientific MegaPlus ES310 Turbo) was set up (Figure D.2) with the centre of the image being aligned with the paper sample. The camera was connected to a PIXCI D2X imaging board installed in a Windows Pentium based PC through a RS232 cable. The software used for video capture was XCAP Interactive Image Analysis Version 2.2[1]. The video rate was set at 300 fps and acquisition data

[1]EPIX Incorporated Buffalo Grove IL USA

was stored directly into the computer RAM. It was then converted into a .AVI movie format for later analysis using the wave analysis programme Igor v 4.0. (Wavemetrics Inc.) The light source was a Fiber-Lite M1 150 which had two flexible outputs, one orientated to the top side and the other to the bottom side of the paper sample (Figure D.2). was the top side and half the bottom (droplet) side of the paper sample (Figure D.2). This enabled the rate of saturation within the penetrating droplet edge as well as the rate of subsurface and droplet spread to be measured concurrently. Figure 7.1 shows the complete sequence; before the droplet touches the paper (Figure 7.1 a & e), as soon as droplet touch occurs (Figure 7.1 b & f), saturation but before the beginning of subsurface spread (Figure 7.1 c & g) and at the end of the sequence where the droplet is nearly depleted and liquid has spread below the surface nearly all the way across the sample (Figure 7.1 d & h). Soon after saturation fluid actually pooled up on the top side of the paper within the droplet spread area.

A similar approach was used by Oliver et al. (1994) using a dynamic sorption apparatus which enabled study of individual ink jet drops as they spread and penetrated various porous substrates. In that case the side and top of a penetrating drop was imaged with two cameras and presented through a screen splitter to enable both drop views to be captured side by side but only had a video acquisition rate of 30 fps.

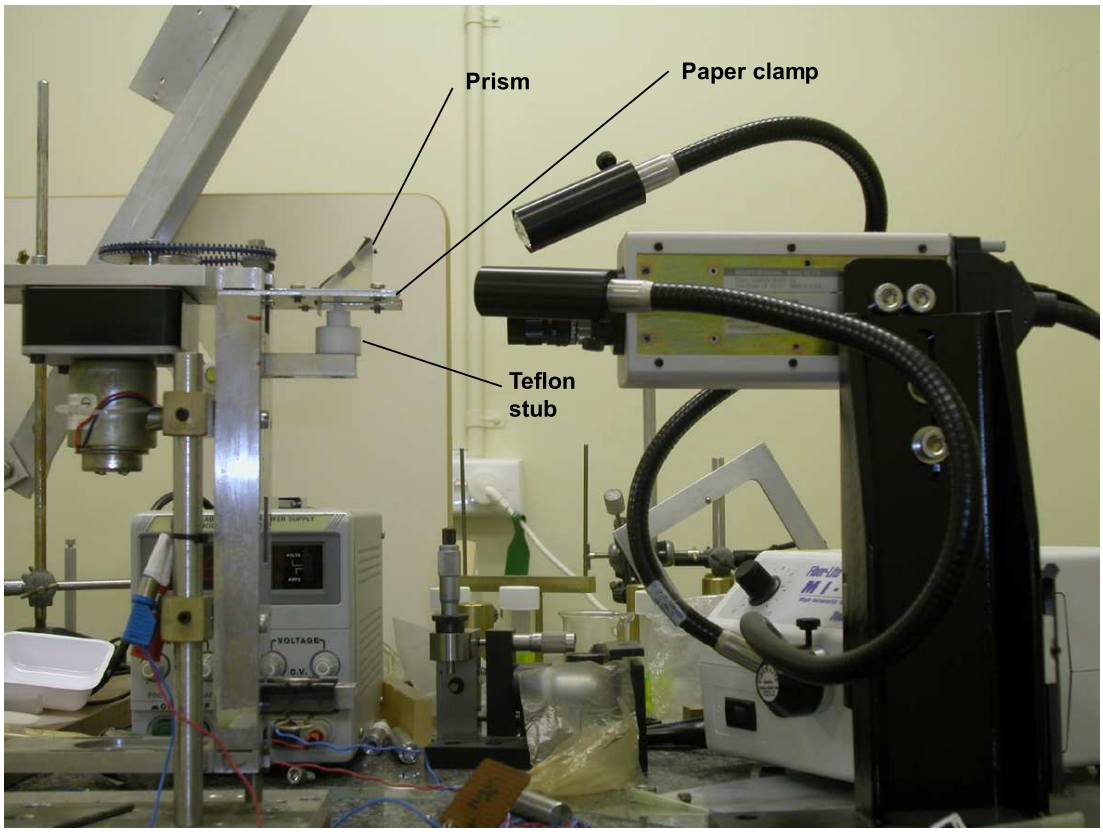

Figure D.1*: The experimental apparatus with camera, controlled voltage supply and light source.*

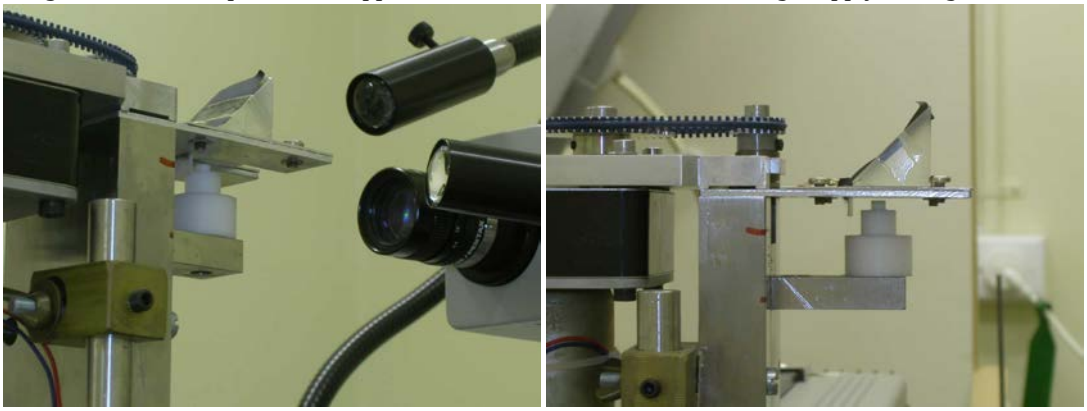

Figure D.2: *Images showing the relationship of the high speed CCD camera to the position of the sample clamp. The lights were directed above and below the sample. The sample clamp and position of the prism to split the image is also shown.*

Appendix E

Tables of data from Chapter 7

***Table E.1**: Identification of significant relationships.*(* = $p < 0.05$, ** = $p < 0.01$, *** = $p < 0.001$, NS = not significant $p > 0.05$)

Experimental factors	**Response variables**				
	Saturation rate	Subsurface spread	Saturation efficiency	Droplet spread	Printing efficiency
Liquid type	***	***	***	***	***
Presence of filler	***	NS	***	**	***
Filler type	***	***	***	NS	***
Plasma treating	*	***	NS	***	NS
Filler amount	NS	***	***	NS	NS
Liquid x plasma	*	***	NS	***	NS
Filler type x Filler amount	**	*	NS	NS	NS
Liquid x presence of filler	***	NS	**	*	*
Plasma treating x presence of filler	*	NS	NS	*	NS
Liquid x filler type	***	***	NS	*	***
Liquid x filler amount	NS	NS	NS	***	NS
Liquid x plasma x filler amount	NS	NS	NS	*	NS

***Table E.2**: Summary of significant relationships for rates of imbibition, the data being untransformed.*

Experimental factors	**Response variables**							
	Saturation rate (mm/s)				Subsurface spread (mm/s)			
Liquid type	Water	Isopropanol			Water	Isopropanol		
	3.275	1.046			0.951	0.572		
Presence of filler	Yes	No			Yes	No		
	2.388	1.475			NS	NS		
Filler type	None	PCC	Talc		None	PCC	Talc	
	1.475	3.126	1.65		0.784	0.805	0.704	
Plasma treating	Yes	No			Yes	No		
	2.456	1.864			0.804	0.719		
Filler amount	7.5%	15%	30%		7.5%	15%	30%	
	NS	NS	NS		0.811	0.767	0.685	
Presence of filler	Yes	No			Yes	No		
Propanol	NS	NS			NS	NS		
Water	NS	NS			NS	NS		
Presence of filler	Yes	No			Yes	No		
Plasma yes	NS	NS			NS	NS		
Plasma no	NS	NS			NS	NS		
Plasma	Yes	No			Yes	No		
Propanol	1.037	1.054			0.565	0.576		
Water	3.874	2.675			1.044	0.859		
Filler type	None	PCC	Talc		None	PCC	Talc	
Plasma yes	NS	NS	NS		NS	NS	NS	
Plasma no	NS	NS	NS		NS	NS	NS	
Filler amount	7.5%	15%	30%		7.5%	15%	30%	
PCC	2.727	3.162	3.490		0.819	0.82	0.775	
Talc	1.712	1.686	1.554		0.763	0.723	0.676	
Filler type	None	PCC	Talc		None	PCC	Talc	
Propanol	NS	NS	NS		0.561	0.576	0.576	
Water	NS	NS	NS		1.007	1.034	0.832	
Filler type	None	PCC	Talc		None	PCC	Talc	
Propanol plasma	NS	NS	NS		NS	NS	NS	
Propanol plasma	NS	NS	NS		NS	NS	NS	
Propanol no plasma	NS	NS	NS		NS	NS	NS	
Propanol no plasma	NS	NS	NS		NS	NS	NS	
Water plasma	NS	NS	NS		NS	NS	NS	
Water plasma	NS	NS	NS		NS	NS	NS	
Water no plasma	NS	NS	NS		NS	NS	NS	
Water no plasma	NS	NS	NS		NS	NS	NS	
Plasma	Yes	Yes	No	No	Yes	Yes	No	No
Presence of filler	Yes	No	Yes	No	Yes	No	Yes	No
Propanol	NS	NS	NS	NS	NS	NS	NS	NS
Water	NS	NS	NS	NS	NS	NS	NS	NS